KINETIC AND SPECTROSCOPIC CHARACTERIZATION OF INTERMEDIATES IN THE SOLUBLE METHANE MONOOXYGENASE CATALYTIC CYCLE: THE OLD AND THE NEW

A DISSERTATION
SUBMITTED TO THE FACULTY OF
UNIVERSITY OF MINNESOTA
BY

RAHUL BANERJEE

IN PARTIAL FULFILLMENT OF THE REQUIREMENTS
FOR THE DEGREE OF
DOCTOR OF PHILOSOPHY

ADVISER: JOHN D. LIPSCOMB

FEBRUARY 2013

Acknowledgments

This Ph.D. has been a long journey and has brought excitement and arduous moments in equal measure. It has been thus quite an adventure replete with a 'moral of the story' realization for me. Like every other journey in life, it would not have been possible without the support of people around me. Above all, I would like to thank my adviser Dr. John D. Lipscomb. Apart from his guidance, I thank him for the patience and calm that he has displayed towards my research. I accept these teachings from him with folded hands. I would also like to mention that his manner of approach of a storyteller towards a research publication or a presentation is exemplary. I would also like to thank my thesis committee members Dr. Thomas, Dr. Que, Dr. Tolman and Dr. Nelsestuen for their patience and advice. The thesis research would not have been possible without the help of my collaborators. I thank Katlyn Meier and Dr. Münck at CMU, Eric Bergeron and Dr. Proshlyakov at MSU, Dr. Park and Dr. Solomon at Stanford, Chris Pollock and Dr. DeBeer at Max Planck Institute, Dr. Vu and Dr. Que at UMN, Dr. Thomas at UMN, Dr. Austin at Bates College and Dr. Elgren at Hamilton College. The time spent in the laboratory was made enjoyable and productive by the support and help of my friends and colleagues. I shall look back fondly at the many scientific and non-scientific discussions that had permeated this time. I would like to thank Dan Renner, Dr. Kovaleva, Dr. Neibergall, Dr. Chakrabarty, Dr. Purpero, Dr. Makris, Dr. Mbughuni, Dr. Melanie Rogers, Brent Rivard and Cory Knoot. I owe a great deal to my parents for which mere words of gratitude would only be a disservice. The elements crucial to the successful completion of this thesis research, such as patience and perseverance have been their contribution. I would also like to thank my aunts and their families in Maryland for providing me with the warmth of a home in this country. This enumeration would not be complete without expressing my gratitude towards soluble methane monooxygenase. In a strange way, this mute, inanimate object has acquired an anthropomorphic character in my mind and has become a teacher for me. Through my research, I have learnt many a lesson that has precipitated my search for truth in the real and metaphysical realm. I can see now how detachment from the results of our actions (experimental results in research) can fashion an objective scientist who strives only for the truth. This Ph.D. has indeed been a doctorate in philosophy for me.

Abstract

Soluble methane monooxygenase (sMMO) catalyzes the difficult reaction of oxidative hydroxylation of methane to methanol, thereby allowing the host methanotroph to grow on methane as the sole source of carbon and energy. As methane possesses the strongest aliphatic C-H bond, the chemical mechanism of this enzyme is the epitome of oxygen activation in metalloenzymes. Exhaustive research of the catalytic mechanism of sMMO in recent years has elucidated many aspects of the chemistry occurring at the dinuclear iron active site center. These studies include the three dimensional structures of the protein components of sMMO and fairly detailed outlines of both the chemical mechanism and the method of regulatory control. The discovery of a diferric peroxo intermediate **P,** and more crucially, a high valent bis-μ-oxo diiron(IV) intermediate **Q** have provided the greatest advances in the understanding of oxygen activation in diiron oxygenases. The research described here has extended this understanding in several aspects. A long standing issue of low accumulation of enzyme reaction intermediates for spectroscopic studies has been addressed and in part solved. A new intermediate **P*** that had been proposed to exist based on kinetic studies has been trapped and characterized through spectroscopic techniques. **P*** appears to be a diferrous cluster intermediate that binds O_2 weakly with little transfer of charge density onto the oxygen atoms. This result suggests a general theme for heme and non-heme oxygen activating enzymes in which ferrous centers initially form a weak complex with O_2, which is strengthened in following steps by interactions such as stabilizing hydrogen bonds and charge donation from trans ligands. The long sought after goal of characterization of the vibrational spectrum of compound **Q** has been achieved through a time resolved resonance Raman technique. The preliminary results corroborate the diamond core structure that has been proposed for **Q**. Another putative high valent intermediate **Q'** has been discovered to arise from compound **Q** in the catalytic cycle. This is potentially a very significant finding as it seem likely that **Q'** rather than **Q** reacts directly with substrate. Following from a precedent from synthetic diiron model compound studies, it is possible that **Q'** is an open core form of the **Q** intermediate in which a reactive, terminal Fe(IV)=O moiety replaces the more stable bis-μ-oxo bridging structure.

Table of Contents

List of Tables

Chapter 1

Chapter 2

Chapter 3

Chapter 4

List of Schemes

Chapter 2

List of Figures

Chapter 1

Chapter 2

Chapter 3

Chapter 4

Chapter 5

List of Abbreviations

HAT, hydrogen atom transfer; GWP, global warming potential; AOM, anaerobic oxidation of methane; sMMO, soluble methane monooxygenase; pMMO, particulate methane monooxygenase; BDE, bond dissociation energy; AMO, ammonia monooxygenase; EXAFS, extended X-ray absorption fine structure; EPR, electron paramagnetic resonance; ENDOR, electron nuclear double resonance; MCD, magnetic circular dichroism; CD, circular dichroism; MMOH, methane monooxygenase hydroxylase component; MMOB, methane monooxygenase B component; MMOR, methane monooxygenase reductase component; ORF, open reading frame; NMR, nuclear magnetic resonance; T4mo, toluene 4-monooxygenase; DFT, density functional theory; NADH, nicotinamide adenine dinucleotide reduced; FAD, Flavin adenine dinucleotide; BADAN, 6-Bromoacetyl-2-Dimethylaminonaphthalene; hDOHH, human deoxyhypusine hydroxylase; XAS, X-ray absorption spectroscopy; QM/MM, quantum mechanics/molecular mechanics; RNR, ribonucleotide reductase; KIE, kinetic isotope effect; NRVS, nuclear resonance vibrational spectroscopy; PCR, polymerase chain reaction; LB, luria broth; IPTG, isopropylthio-β-galactoside; DEAE, diethylaminoethyl cellulose, SDS, sodium dodecylsulfate; MOPS, 3-(N-morpholino)propanesulfonic acid; HEPES, 4-(2-hydroxyethyl)-1-piperazineethanesulfonic acid; NaCl, sodium chloride; ESI-MS, electrospray ionization-mass spectrometry; DTT, dithiothreitol; RFQ, rapid freeze quench; TCEP, tris(2-carboxyethyl)phosphine; ESI-TOF, electrospray ionization-time of flight; DTNB, 5,5'-dithiobis-(2-nitrobenzoic acid); CFE, cell-free extract; VTVH, variable-temperature variable-field; *J*, exchange coupling constant; rRaman, resonance Raman; TRRR, time resolved resonance Raman; PEEK, polyether ether ketone; HPLC, high-pressure liquid chromatography;

CHAPTER 1

An introduction to the soluble methane monooxygenase system

1.1 OXYGEN ACTIVATION

This thesis research is a tale of two gases, oxygen and methane. We shall start the story with the younger of the two gases, oxygen (in terms of geological age). Life on earth started in an anaerobic climate that subsequently changed upon the advent of photosynthesis. The atmospheric concentration of oxygen rose dramatically from about <0.1% to almost contemporary levels of 21% (v/v) around 2.45 billion years ago in a time interval known as the Great Oxidation Event [1]. The use of oxygen as a terminal electron acceptor in aerobic metabolism allowed the utilization of a much larger fraction of the redox energy from reduced carbon compounds such as glucose, in comparison to anaerobic metabolism. In addition, the utilization of oxygen added to the metabolic repertoire of aerobes leading to the generation of new secondary metabolites such as alkaloids, antibiotics and novel metabolic pathways to utilize new carbon sources. Indeed, oxygen has been predicted to be associated with almost 10^3 metabolic reactions that are unique to aerobic organisms [2]. These two roles played by oxygen in aerobic organisms provided a greater evolutionary fitness compared to anaerobes and may have contributed to the emergence of complex eukaryotic life [3].

Considering that aerobic life is based upon the use of oxygen as the terminal electron acceptor, it is interesting to note that oxygen is rather unreactive towards organic molecules on its own at ambient temperature. This stability arises from the unique electron arrangement in the degenerate π^* orbitals of molecular oxygen that contain two unpaired electrons with the same spin. This leads to a triplet state (S = 1) electronic configuration for ground state oxygen whereas most organic molecules possess a singlet state electronic structure (S = 0). Reactions between singlets and triplets do not occur readily because the total spin must be conserved during any chemical process and a spin inversion is required for the triplet-singlet reaction to occur. Thus, although a reaction of organic molecules with ground state oxygen is thermodynamically favored, it is kinetically unfeasible, as such a reaction is spin-forbidden.

A solution for this kinetic sluggishness is the use of transition metal atoms in metalloenzymes to activate oxygen and facilitate a spin inversion. Transition metal atoms have unpaired electrons in their d-atomic orbitals allowing them to transfer electrons to triplet oxygen. Upon formation of a metal-oxygen bond, the metal center reduces the exchange stabilization of triplet oxygen as well

as stabilizes the singlet spin state of oxygen [4, 5]. The combined effect of stabilizing the singlet spin states and destabilizing the triplet spin states decreases the energy gap and allows for an intersystem crossing. This intersystem crossing is the essence of oxygen activation.

Oxygen chemistry revolves around its use as an electron acceptor. This is primarily because the reduction of oxygen is a very exergonic process and can be coupled to endothermic metabolic reactions (Equation 1) [6].

$$O_2 + 4H^+ + 4e^- \rightleftharpoons 2H_2O \qquad \Delta G^o = -314.6 \text{ kJ. mole}^{-1} \tag{1}$$

Oxygen activation at the metal center can lead to three oxidation states for the oxygen atom: superoxo (O_2^-), peroxo (O_2^{2-}) and oxo (O^{2-}) states. These oxidation states can be correlated to the strength of the substrate O-H, N-H and C-H bond that is oxidized by the enzyme in the catalytic cycle. This correlation is based upon the hydrogen atom transfer (HAT) reaction, which is the key step in these oxidation reactions. The kinetic rates for HAT reactions have been described well by a model based upon the Marcus cross relation function, which is a variant of the Marcus equation describing electron transfer rates [7]. The cross relation equation for a hydrogen atom transfer reaction (Equation 2) is described in Equation 3.

$$MO + RH \longrightarrow MOH + R^{\bullet} \tag{2}$$

$$k_{MO/RH} = \sqrt{k_{MOH/MO}\ k_{RH/R}\ K_{eq}\ f} \tag{3}$$

The rate constant for the HAT reaction ($k_{MO/RH}$) is correlated to the self-exchange rate constants for the two reactants ($k_{MOH/MO}$, $k_{RH/R}$), the equilibrium constant for the reaction (K_{eq}) and the factor *f*. The equilibrium constant for the reaction is dependent upon the bond dissociation free energies of the donor C-H bond and the acceptor MO-H bond. Accordingly, the oxidation of a strong C-H bond (> 90 kcal mole^{-1}) requires an oxidant with a strong basic character coupled with a large effective reduction potential, in order for the HAT reaction to be thermodynamically feasible [8]. It is relevant to note here that the basicity of the activated oxygen molecule increases in the

following order: superoxo (O_2^-) < peroxo (O_2^{2-}) < oxo (O^{2-}). The effective reduction potential of the oxidant is dependent upon the oxidation state of the metal center and activated oxygen atom.

While all members of the oxido-reductase family of enzymes with oxygen as a substrate, use it as an electron sink, the oxygenase sub-family of enzymes additionally incorporates either one or both atoms of molecular oxygen into the oxidized product. These enzymes are accordingly classified as monooxygenases and dioxygenases, respectively. An efficient way of categorizing the enzymes that activate oxygen for redox chemistry is based upon the redox state of the oxygen molecule in the key substrate reactive intermediate (either proposed or directly observed) of the enzyme catalytic cycle. In other words, this classification follows increasing levels of oxygen activation in enzymes that in turn correlates with the oxidative power of the oxidant. These categories can be described as follows –

1. Dioxygen (O_2) – The proteins in this group reversibly bind oxygen for purposes of either oxygen storage or distribution from the point of oxygen uptake in the respiratory system to the tissues in the bodies of higher multicellular organisms. The examples for such proteins are hemoglobin and myoglobin in vertebrates and hemocyanin and hemerythrin in invertebrates. It is interesting to note that nature has found different solutions for the problem of reversible binding of dioxygen with hemoglobin and myoglobin containing a heme iron center [9, 10], hemerythrin containing a non-heme diiron center [10] and hemocyanin with a dicopper center [11]. The oxygen molecule is bound in its superoxide redox form in the heme iron center containing enzymes [12] while it is bound in the peroxo redox state in the diiron and dicopper containing proteins [11].

2. Superoxo (O_2^-) – The common characteristics between the enzymes utilizing a metal superoxo reactive intermediate are –
   i.) These enzymes perform formally a four-electron oxidation without the requirement of reducing equivalents provided externally from a cofactor (e.g, α-ketoglutarate, NADH). In other words, the substrate C-H bond oxidation occurs prior to oxygen O-O bond cleavage.

ii.) The substrate C-H bonds are activated on account of being in close proximity to either a heteroatom or a π - system. This substrate activation is necessary given that metal-superoxo intermediates are mild oxidants.

The enzymes displaying such a metal superoxo reactive intermediate include non-heme diiron enzymes such as *myo*-inositol oxygenase [13], non-heme mononuclear iron enzymes such as isopenicillin N synthase [14] and non-coupled binuclear copper containing enzymes such as dopamine β-monooxygenase [15].

3. Peroxo (O_2^{2-}) – The enzymes proposed to utilize a metal peroxo intermediate as the key oxidant in the catalytic cycle have electron rich/activated substrates. Examples for this category include coupled binuclear copper containing enzymes such as tyrosinase [16] and heme enzymes such as heme oxygenase [17]. There is another group of monooxygenases where a flavin cofactor is present in lieu of a metal atom. The key oxidant in these enzymes has been demonstrated to be a hydroperoxyflavin form of the prosthetic group [18].

4. Oxo (O^{2-}) – This group of enzymes activates oxygen to its highest redox state in the active oxidant of their catalytic cycles. They do so by incorporating a pair of electrons from an accessory electron donor such as reduced nicotinamide to break the dioxygen O-O bond prior to substrate C-H bond oxidation. The high valent metal-oxo moiety formed as a result is suitable for oxidizing strong C-H bonds on account of the large basicity of the oxo group coupled with the high redox potential of the high valent metal center. The examples for this category of enzymes include α-ketoglutarate dependent monoiron enzymes such as taurine dioxygenase [19], heme enzymes such as peroxidase and cytochrome P450 [20], Rieske type monoiron dioxygenases [21] and non-heme diiron enzymes such as ribonucleotide reductase [22] and soluble methane monooxygenase [23].

The following two classes of enzymes are classified separately as they possess certain unique characteristics. While a metal-bound activated oxygen species is formed in the catalytic

cycle, these metal centers either do not transfer the oxygen to the substrate or merely serve to activate the substrate thus leading to oxygen activation on the substrate molecule.

5. Oxidase – While the enzymes in this group do not introduce any atom of dioxygen into the substrate, they do couple the oxidation of the substrate molecule to the reduction of oxygen to either hydrogen peroxide or water. The examples in this category include monocopper enzymes such as copper amine oxidase [24] and galactose oxidase [25] and multicopper oxidases such as laccase [26]. The most important example of an oxidase is cytochrome *c* oxidase where a hetero-binuclear active site composed of a heme a_3 and mononuclear copper center serve to reduce oxygen to water. This enzyme is the terminal electron acceptor at the end of the electron transport chain in aerobic cellular respiration [27].

6. Substrate mediated oxygen-activation – The enzymes in this category are characterized by an oxidized metal center (Fe^{3+}) in the reactive form of the enzyme, which thus prevents oxygen binding to the metal center. Rather, the metal center activates the substrate, leading to a direct attack of dioxygen on the carbon atom of the substrate that is ultimately oxidized in the reaction. The metal center also mediates the transfer of the second electron from substrate to dioxygen thus allowing the spin-forbidden reaction between substrate and dioxygen to occur via intersystem state crossing [28]. The enzymes in this category include the mononuclear non-heme iron enzymes such as lipoxygenase [29] and intradiol dioxygenases [28].

1.2 ROLE OF METHANE IN THE GLOBAL CARBON CYCLE

We shall now focus our attention on the other gas relevant to this thesis research, methane. Methane is a key component of the global carbon cycle and is a subject of much scientific enquiry considering its impact as a greenhouse gas. It has a global warming potential (GWP) that is almost 21 times that of carbon dioxide, which has been the primary agent behind the greenhouse warming effect since the onset of the Industrial Revolution. The greenhouse effect of methane arises because it absorbs thermal radiation from the planetary surface in the infrared region (1600-1700 nm) and solar radiation in the near-infrared region, thus trapping the energy in the atmosphere and causing a positive radiative forcing [30]. Considering its GWP, the rise in atmospheric levels of methane from 700 to 1790 ppbv (parts per billion by volume) in the time period from 1750 to 2008 is of great concern [31]. However, considering that the lifetime of methane in the atmosphere is only 11 years, a reduction in its atmospheric concentration by decreasing emissions has the greatest potential towards achieving a decrease in the global warming effect in the short-term frame.

The predominant source of methane production is anaerobic methanogenesis with the remainder arising from abiotic hydrothermal processes [32]. Anaerobic methanogenesis is undertaken by a group of archaea called methanogens, which convert C_1 compounds like CO_2 or acetate to methane. In this process, CO_2 is used as the electron sink in order to generate metabolic energy [33].

There are anthropogenic and natural processes through which the methane produced by bacteria and abiotic thermal chemistry is emitted into the atmosphere. The bulk of the methane emissions arise from anthropogenic activity and the principal sources are described below [34].

1. Natural gas – The primary component of natural gas is methane. The extraction, processing and distribution of natural gas, either on its own or associated with petroleum mining, involves a large emission of this volatile component.
2. Livestock – The digestive system of ruminants contain methanogenic bacteria and the exhaling of methane produced in this process is the second largest emission source.
3. The other sources of methane emission include anaerobic fermentation in landfills, rice fields and wastewater treatment plants by methanogens and coal mining.

The natural sources of methane emission include methane production by methanogens in wetlands, water bodies like rivers and oceans and in termite digestive tracts. Another source of methane emissions is methane gas hydrate, which is a crystalline solid composed of methane gas molecules trapped within a cage of water molecules [35]. Considering that these hydrates contain almost twice the amount of carbon as present in all fossil fuels, the destabilization of these undersea sediment and permafrost bound gas hydrates pose a significant threat to global climate warming. These gas hydrates can also conversely serve as a vast potential source of energy [36].

The sink for atmospheric methane is oxidation by hydroxyl radicals, which are produced as a result of photolysis of ozone [37, 38]. The soil based sink for methane is the aerobic metabolism of a group of bacteria called methanotrophs that use methane as a carbon source [39]. This group of bacteria and its aerobic oxidation of methane shall be discussed in greater detail in section 1.3. In more recent research, it has been observed that a significantly large fraction of methane is removed by groups of archaea executing an anaerobic oxidation of methane (AOM) [40]. These microbial colonies use either nitrate or sulfate as the electron acceptors [40, 41]. It has been also shown that the nickel-containing enzyme, methyl-coenzyme M reductase that produces methane in methanogens, catalyzes the reaction in the reverse direction in the first step of AOM [42].

1.3 METHANOTROPHIC BACTERIA

Methylotrophs are a group of bacteria that can utilize single carbon atom containing compounds as an electron source and as a sole source of carbon. Methanotrophs are a subset of this group that can assimilate this carbon from methane in a facultative and obligate fashion. This group of microorganisms occupies environmental niches in soil and water at the interface between anoxic and oxic conditions as it utilizes oxygen as the electron sink while the methane is produced by anaerobic methanogens. Thus, their common habitats include marshes, wetlands, rice paddies, freshwater lake basins and landfills.

The metabolic pathway of the methanotrophs is characterized by (a) the presence of a methane monooxygenase enzyme instrumental in converting methane to methanol and (b) a central role for formaldehyde as a metabolite in the catabolic and anabolic pathways. The metabolic pathway for the utilization of methane as an electron and carbon source is described in Figure 1.1.

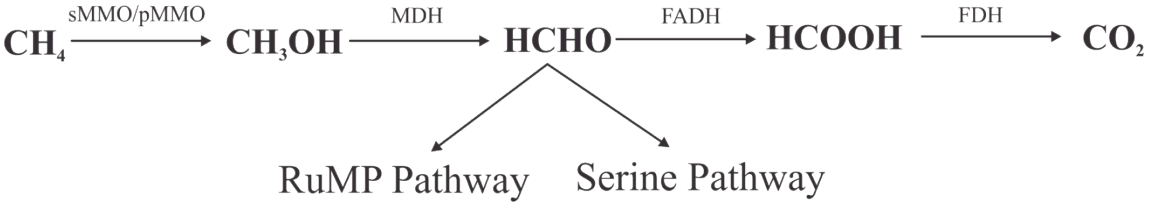

sMMO - soluble methane monooxygenase
pMMO - particulate methane monooxygenase
MDH - methanol dehydrogenase
FADH - formaldehyde dehydrogenase
FDH - formate dehydrogenase

Figure 1.1 – Metabolic pathway for the oxidation of methane in methanotrophs.

The methanotrophs are further divided into three classes depending upon the type of metabolic pathway employed to assimilate formaldehyde. Type I methanotrophs include the genera *Methylomonas* and *Methylobacter* and use the RuMP (Ribulose monophosphate) pathway. Type II methanotrophs include the genera *Methylosinus* and *Methylocystis* and use the serine pathway. There is a third class designated as type X which include genera like *Methylococcus* and are characterized by having enzymes from both metabolic pathways of assimilating formaldehyde [43].

The oxidation of methane to methanol by a soluble methane monooxygenase (sMMO) and a membrane-bound form of the enzyme (pMMO) serve as the cornerstone for the methanotroph metabolism as it is an extremely difficult reaction to catalyze. The oxidation reaction involves the cleavage of the strongest known aliphatic hydrocarbon C-H bond (BDE = 105 kcal $mole^{-1}$) [44]. We shall discuss the catalytic mechanism of these two enzymes in further detail in sections 1.4 and 1.5.

The ability of soluble methane monooxygenase enzyme to oxidize a variety of compounds including heteroatom-substituted and unsubstituted aliphatic and aromatic hydrocarbons and particularly halogenated hydrocarbons has been well demonstrated [45, 46]. Based upon this ability of the sMMO enzyme, methanotrophs have been employed for bioremediation of chemical pollutants [47, 48]. A particular emphasis has been placed upon the ability of methanotrophs to metabolize trichloroethylene, which is a major pollutant present in groundwater sources [49, 50].

1.4 PARTICULATE METHANE MONOOXYGENASE (pMMO)

The only two classes of enzymes known to perform an aerobic oxidation of methane are particulate membrane-bound methane monooxygenase (pMMO) and soluble methane monooxygenase (sMMO) [43]. A homolog of pMMO, ammonia monooxygenase (AMO), has also been demonstrated to oxidize methane in *Nitrosomonas europaea* whole cell extracts [51]. While pMMO is expressed in all methanotrophs, sMMO is observed to be present in only type II and X methanotrophs [43]. The regulation of expression between sMMO and pMMO in these methanotrophs is dependent upon the cellular copper concentration. A copper concentration ratio greater than 0.85 to 1 μmole/g (dry weight) of cells leads to an expression of pMMO in lieu of sMMO, accompanied with an expansion of the intra-cytoplasmic membranes for support of pMMO [52].

pMMO is an integral membrane protein comprised of a trimer of three subunits in an $\alpha_3\beta_3\gamma_3$ arrangement [53]. The elucidation of the identity of the metal centers in the protein has, however, been ambiguous. A multitude of spectroscopic techniques have led to varied interpretations of the metal content and arrangement of the metallocenters of the enzyme; i) a type 2 mononuclear copper center alongside a dinuclear copper cluster (based upon X-ray crystallography, EXAFS) [53, 54], ii) a trinuclear copper cluster (based upon EPR spectroscopy) [55] and a diiron center similar to sMMO (based upon Mössbauer spectroscopy) [56]. The function of the metal centers involves both electron transfer and C-H bond oxidation. The lack of a clear identification of the metal centers likely arises from the fact that during purification the enzyme suffers from a substantial loss of activity as compared to whole cell extracts, which additionally varies between preparations and research groups [57]. In addition, the physiological reductant for the enzyme has also not been identified, preventing a proper measurement of pMMO activity in purified extracts.

Two recent results, however, seem to support the hypothesis that methane oxidation occurs at a dinuclear copper cluster in pMMO. In the first research paper, the authors were able to heterologously express the soluble portion of pMMO, which contains a mononuclear type 2 copper site and a dinuclear copper cluster but not the proposed site for the diiron cluster. This portion of the enzyme was able to exhibit a marginal activity towards methane oxidation. As this protein was shown to bind 3 equivalents of copper atoms and no iron atoms, it was proposed that

methane oxidation occurs at the dicopper site [58]. In the second paper, Raman spectroscopy and density functional theory calculations were used to elucidate the active constituent of a Cu-ZSM-5 zeolite that oxidizes methane to methanol. The methane-oxidizing site in the zeolite was reported to be a mono-oxo bridged dicopper cluster [59]. This supports the hypothesis that methane oxidation can also occur at a copper center in comparison to a traditional iron-based catalysis in sMMO.

1.5 SOLUBLE METHANE MONOOXYGENASE (sMMO)

Soluble methane monooxygenase is expressed by type II and X methanotrophs under copper-limited growth conditions. This enzyme serves to oxidize methane to methanol in the first step of methane utilization in these microorganisms (Equation 4).

$$CH_4 + O_2 + NADH + H^+ \longrightarrow CH_3OH + H_2O + NAD^+ \quad (4)$$

Being a soluble enzyme in comparison to pMMO, there is a larger amount of information available regarding this enzyme and its chemical mechanism. The sMMO enzyme for these biochemical studies is either obtained from *Methylosinus trichosporium* OB3b or *Methylococcus capsulatus* Bath. Although an efficient heterologous expression system for sMMO is lacking, there have been attempts made to express mutants of sMMO in the host methanotroph itself by taking advantage of the switch between sMMO and pMMO expression [60].

The sMMO enzyme is a multi-protein complex comprised of a hydroxylase protein MMOH that contains the active site of the enzyme, a regulatory protein MMOB and a reductase protein MMOR to provide the additional electrons required in the reaction (Figure 1.2A). The sMMO gene cluster consists of 6 ORF arranged in an operon (Figure 1.2B) [61]. The *mmoX*, *mmoY* and *mmoZ* genes encode the α, β and γ subunits of the sMMO hydroxylase protein, *mmoB* the regulatory protein MMOB and *mmoC* the reductase protein MMOR. There is an additional ORF *orfY*, which has been demonstrated to express a protein MMOD in conjunction with the rest of the genes on the operon. While this protein binds MMOH, its physiological role is still unclear with a proposed role suggested in the assembly of the MMOH diiron cluster [62].

A

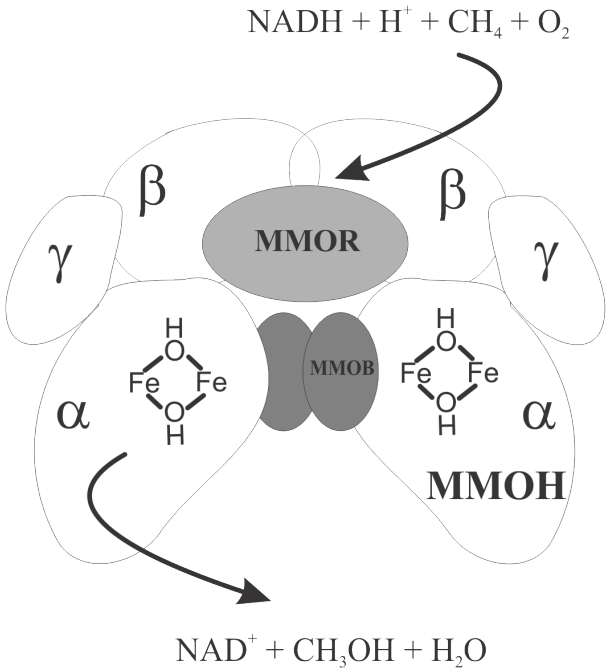

B

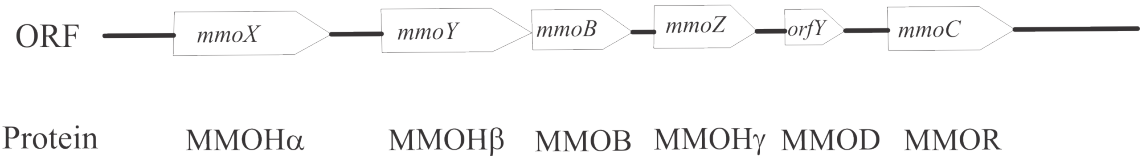

Figure 1.2 – A – The sMMO multi-protein enzyme complex. B – sMMO operon describing the order of arrangement of the sMMO genes and their respective protein products.

1.5.1 sMMO hydroxylase (MMOH)

A whole host of spectroscopic techniques including EPR, ENDOR, EXAFS, MCD/CD and Mössbauer along with X-ray crystallography have provided a detailed picture of the hydroxylase protein of sMMO and the diiron cluster at its heart. The hydroxylase protein is a predominantly helical, multi-subunit protein comprised of the α, β and γ subunits arranged in a dimeric fashion (Figure 1.3) [63, 64]. The diiron cluster is positioned between four helices in the α subunit of each protomer. A structural canyon lies at the interface between the two protomers where the regulatory MMOB protein is proposed to bind to each of the protomer units [65]. The surface of MMOH facing this groove is composed of one of the α-helices of the four-helix bundle housing the diiron cluster.

The diiron cluster is comprised of two iron atoms coordinated by two histidine and four glutamate residues from the four-helix bundle of the α subunit (Figure 1.4) [63, 64]. As the crystal structures of the hydroxylase protein from *M. trichosporium* OB3b [64] and *M. capsulatus* Bath [63, 66] show variability in the identity of the bridging ligands, the more conclusive evidence regarding their identity comes from EPR [67], Mössbauer [68] and EXAFS [69] studies. Briefly, the small value of the electronic coupling between the iron atoms compared to an oxo–bridged diiron cluster in hemerythrin and a comparison with synthetic model compounds having a similarly close Fe–Fe distance of 3.0 Å point to a bis(μ-hydroxo)(μ-carboxylato) bridging structure between the iron atoms in their oxidized state (Figure 1.4). Upon reduction to the diferrous state, the Fe-Fe distance increases to 3.3 Å and the terminal glutamate residue on one of the iron atoms undergoes a 'carboxylate shift' and replaces one of the bridging hydroxide group to bind in a bidentate fashion to one iron and monodentate to the other (Figure 1.4) [66]. The other bridging hydroxo group is also lost, thus leaving the two glutamate residues to bridge the iron atoms in different structural geometries.

The diiron cluster is located in a hydrophobic cavity (volume ~ 70 $Å^3$). This cavity is proposed to be the site where the substrate molecule is positioned adjacent to the diiron cluster during catalysis. An attempt has been made to elucidate the oxygen and substrate entry channels into this active site cavity by pressurizing oxidized MMOH crystals with an oxygen analogue xenon and substrate analogues such as bromomethane and iodomethane [70, 71]. These studies have identified a chain of hydrophobic cavities that connect the active site cavity to the bulk aqueous

solvent. A conserved Leu110 residue positioned between the active site cavity and the adjacent cavity in the chain is proposed to gate substrate entry [72]. The crystallographic studies have identified another small pore connecting the active site cavity directly to the protein surface through the four-helix bundle housing the diiron cluster. This has been proposed as the route for oxygen translocation [72]. We should add the caveat to these crystallographic studies that these are performed on MMOH in isolation and are not performed on the reactive protein complex of MMOH and MMOB. Given the crucial regulatory effect of MMOB binding (section 1.5.2 and 1.5.7), one might expect to observe large differences in the diiron cluster arrangement and entry/exit channels in such a MMOB bound MMOH protein crystal structure.

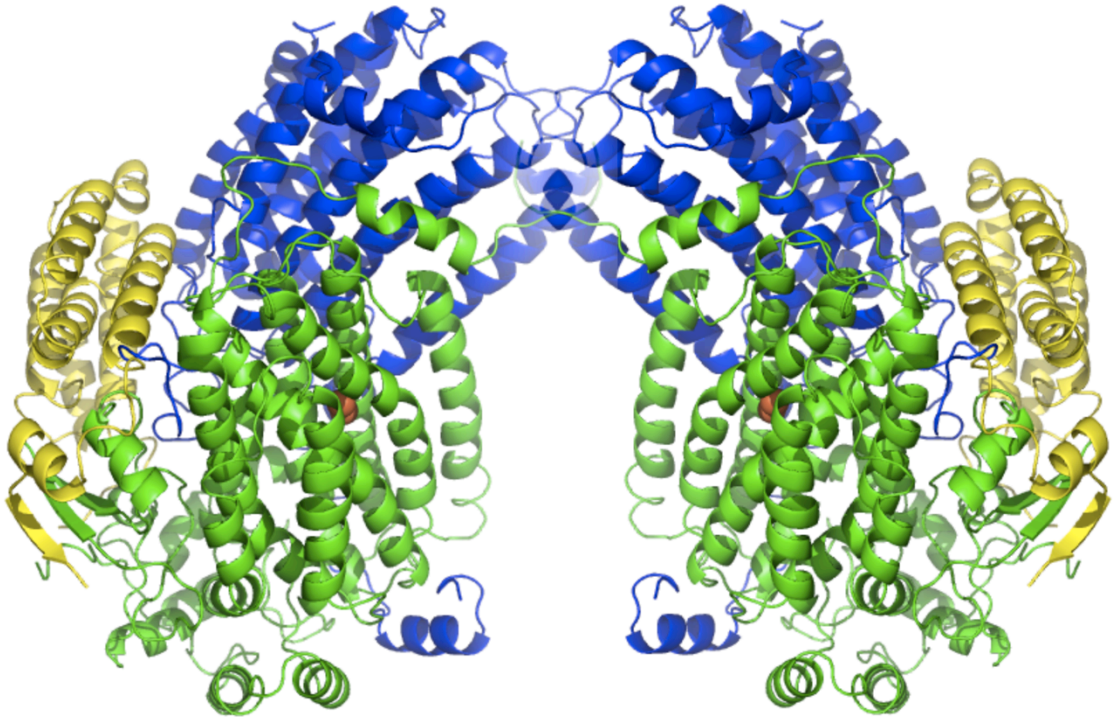

Figure 1.3 – X-ray crystal structure of the biological unit of MMOH ($\alpha_2\beta_2\gamma_2$) from *M. trichosporium* OB3b (pdb - 1MHY) [64]. The α subunit is shown in green, the β subunit in blue and the γ subunit in yellow. The iron atoms of the diiron cluster are depicted as orange spheres.

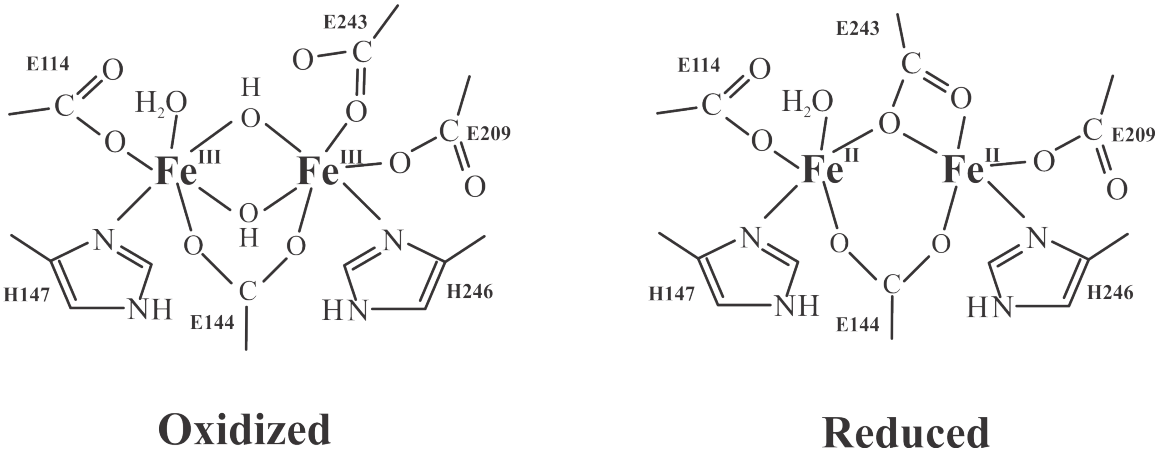

Figure 1.4 – The diiron cluster ligand-geometry in the oxidized and the reduced states of the iron atoms.

1.5.2 sMMO regulatory B component (MMOB)

MMOB is a small (15.8 kDa) accessory protein that binds to MMOH to form a catalytically active complex. The NMR structure of MMOB describes a protein with three α-helices and six anti-parallel β-strands devoid of any cofactor or metal atom (Figure 1.5) [65, 73]. The N- and C-terminal ends of MMOB are missing from the structure on account of being disordered in solution. In the absence of a crystal structure of the MMOH:MMOB complex, chemical cross-linking studies provide the next best description of MMOB binding to the α-subunit of MMOH [74]. It has been also proposed that MMOB binds in the groove formed at the interface of the symmetrical αβγ protomers of MMOH [65].

The first attempts at mapping the surface of MMOB that binds MMOH involved measuring the perturbation of the relaxation of NMR resonances of MMOB amino acid residues upon binding MMOH [65, 75]. This led to the identification of thirty amino acid residues distributed between a surface patch on the well-ordered core region and the N-terminal segment of MMOB that interact with reduced MMOH. These results also indicate that the N-terminal segment that remains structurally disordered in free MMOB assumes a degree of helical structure and interacts with MMOH in the protein complex. Measuring accessibility of site-directed spin-labels on MMOB to solvent and hydrophilic small metal chelate paramagnetic relaxation agents in the free and MMOH complex form have further refined the identity of the surface patch on MMOB [76].

X-ray crystallographic studies on a closely related bacterial multicomponent oxygenase enzyme, toluene 4-monooxygenase (T4mo), have provided us a good description of the hydroxylase and effector protein complex. The protein complex of the hydroxylase (T4moH) along with its effector protein (T4moD) was solved in both the oxidized and reduced form of the diiron cluster [77]. The close primary sequence similarity between this enzyme and sMMO, also manifested in the manner of reactivity and regulation by the effector protein, indicates that the structural observations from the T4mo crystal structures can be extended to the sMMO system. The key difference between the diferric cluster in the free hydroxylase and the effector bound hydroxylase is that one of the bridging hydroxo groups is missing in the latter structure and the iron atoms are five coordinate as a result. The active site cavity in T4moH is also modified in size upon binding T4moD to accommodate the toluene substrate. It is interesting to note that the region of T4moD

bound to T4moH, matches the region predicted in MMOB by NMR relaxation and spin labeling studies (Figure 1.6).

MMOB functions as an effector protein in the sMMO system. Such accessory proteins with regulatory roles have been observed in most of the related diiron bacterial multicomponent oxygenases [78] and in the structurally distinct cytochrome P450 oxygenase in the form of putidaredoxin [79]. The regulatory effect of MMOB on sMMO catalysis is remarkable. It enhances the steady state turnover rate of oxidation of complex substrates by about 150-fold by primarily altering the V_{max} of the reaction [74]. With substrates that can be hydroxylated at more than one position, the regioselectivity of oxidation changes in the presence of MMOB [80]. The presence of MMOB also enhances the rate constant of oxidation of the diferrous cluster by about 1000-fold, thus shifting the rate-limiting step of the catalytic cycle from diferrous oxidation to product release. This dramatically increases the accumulation of reactive intermediates in the catalytic cycle of sMMO [81]. In addition, MMOB has been implicated in coupling electron transfer from MMOR to substrate oxidation in MMOH in sMMO from *M. capsulatus* Bath [82]. These effects of MMOB on catalysis are likely achieved via either conformational change in the active site and its vicinity or by changes in the structure of the diiron cluster.

EPR and MCD/CD spectroscopic studies have revealed changes in the diiron cluster in MMOH upon binding MMOB. The EPR signal of the diiron cluster in both the mixed-valent and fully reduced states changes upon binding MMOB [74]. The MCD spectra of reduced MMOH also changes upon MMOB binding, indicating a modulation of the ligand environment of one of the iron atoms of the dinuclear cluster [83]. The midpoint reduction potential of the two irons is also lowered by 132 mV upon binding MMOB [84]. While the previous data describes localized changes at the diiron cluster of MMOH, global conformational changes in the MMOH protein structure have also been observed by X-ray scattering experiments [85]. These conformational changes might serve to form oxygen and substrate access channels to the active site in MMOH.

The regulatory role of MMOB in enhancing the oxygen reactivity of the diiron cluster has been further elucidated by MCD and density functional theory (DFT) calculations on sMMO and the related toluene-4-monooxgenase enzyme [86]. DFT calculations show that the formation of a superoxide intermediate following the binding of oxygen to one of the iron atoms of the reduced diiron cluster is an energetically unfavorable process. The formation of a peroxide intermediate

upon binding oxygen in a bridging fashion to both the iron atoms is however thermodynamically feasible. In the absence of the effector protein and despite the fact that each iron is 5-coordinate, the diiron cluster in the reduced state has an open coordination position for oxygen binding on only one of the two iron atoms. The terminal glutamate ligand on the other iron atom produces a steric block upon oxygen binding (Glu209 – Figure 1.4). DFT calculations showed that a change in the orientation of this glutamate ligand mimics the electronic perturbations of the iron atoms observed upon the binding of MMOB to MMOH. Accordingly, the regulatory role of MMOB on oxygen binding has been attributed to effecting this structural change of the glutamate residue, which subsequently allows oxygen to bind in a bridging fashion to both iron atoms and initiate the catalytic cycle.

Figure 1.5 – NMR structure of MMOB from *M. trichosporium* OB3b [73].

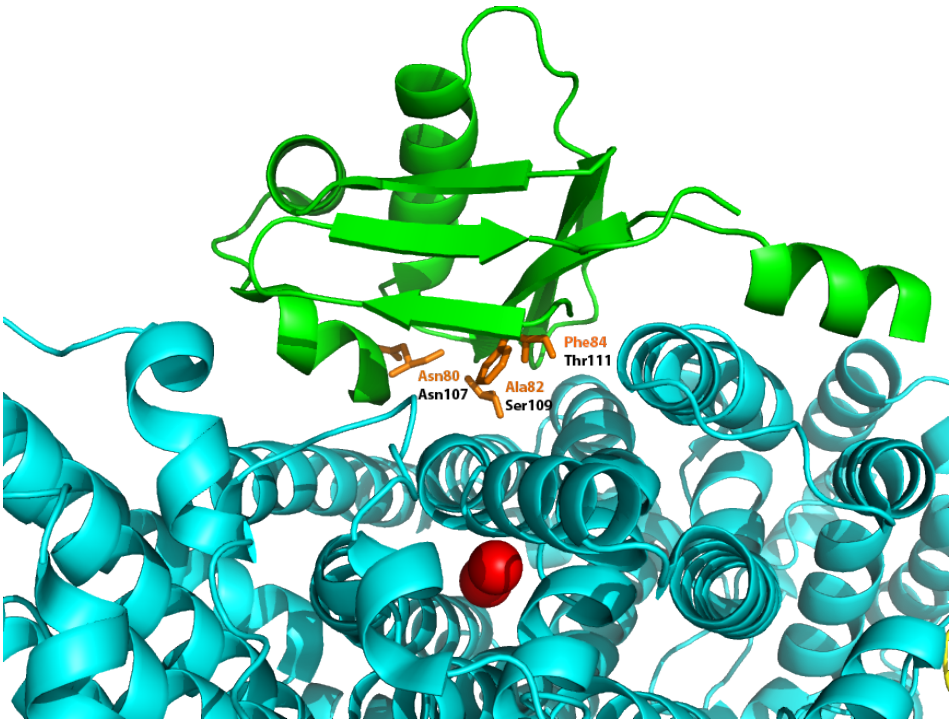

Figure 1.6 – A close-up view of the interaction surface of T4moD (green) with T4moH (cyan) (pdb code 3DHH) [77]. The diiron cluster is depicted as red spheres. The three T4moD residues (labeled in orange) depicted as sticks are homologous to the MMOB residues (labeled in black) that have been predicted to interact with MMOH based upon NMR and spin-labeling data.

1.5.3 sMMO reductase (MMOR)

The reductase protein is a 39.7 kDa protein that serves to transfer electrons from NADH to the diiron cluster in MMOH. The NMR structure of MMOR from *M. capsulatus* Bath involves two separate structure determinations of the flavin (FAD) binding domain and the ferredoxin domain constituents (Figure 1,7) [87, 88]. The FAD domain binds NADH and transfers the two electrons sequentially through the flavin moiety to the [2Fe-2S] cluster in the ferredoxin domain, which then transfers the electrons to the diiron cluster in MMOH. Measurements of the relaxation of specific amino acid NMR resonances of the ferredoxin domain protein upon forming a complex with MMOH have led to an elucidation of the protein face of this domain that binds MMOH. In the absence of a protein complex crystal structure of MMOH:MMOR, chemical cross-linking studies describe a possible binding of MMOR to the β subunit of MMOH [74].

In addition to its primary role as an electron transfer agent, MMOR was also demonstrated to play a regulatory role in the catalytic cycle of sMMO. MMOR binding to the MMOH:MMOB complex increases the midpoint reduction potential of the diiron cluster to favor a two electron reduction of the cluster [89]. It has been also observed that the formation of a MMOH:MMOB:MMOR complex reduces the rate constant of reaction of the diferrous cluster with oxygen in comparison to a MMOH:MMOB complex. As the accumulation of the substrate-reactive intermediate (**Q**) in the catalytic cycle is unchanged, it is proposed that the rate constant of a catalytic step involved in the formation of the intermediate is enhanced in such a MMOR-bound protein complex to compensate for the rate constant decrease in diferrous oxidation [89].

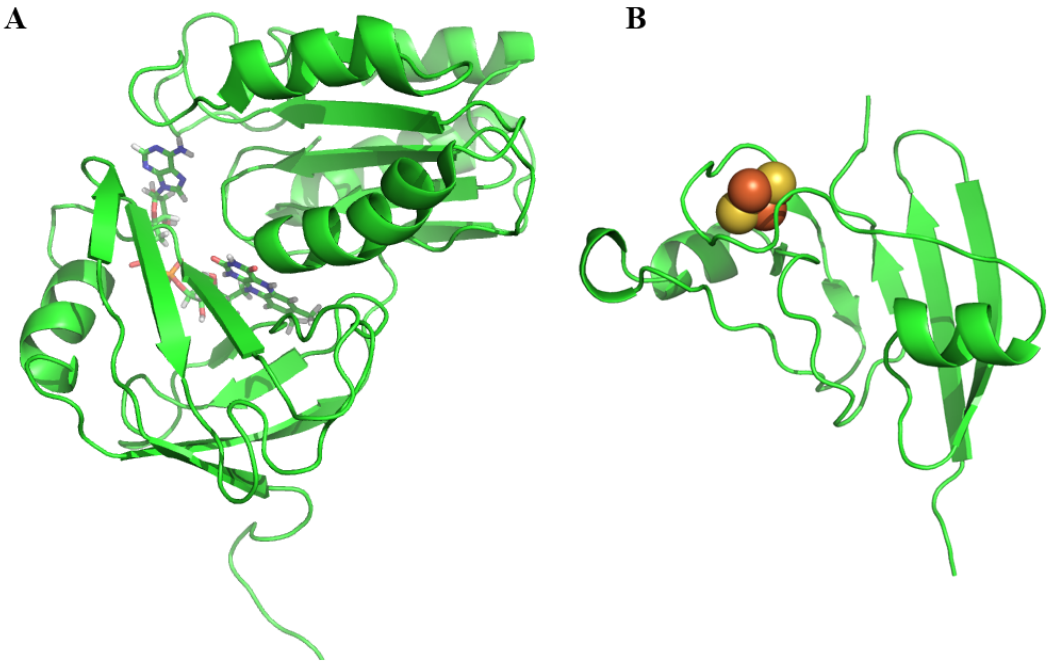

Figure 1.7 – A – The flavin/NADH binding domain (A – pdb code 1TVC) and ferrodoxin domain (B – pdb code 1JQ4) of sMMO reductase from *M. capsulatus* Bath. The FAD cofactor has been depicted in a stick model while the [2Fe-2S] cluster is depicted as spheres.

1.5.4 sMMO protein complex & turnover

The presence of three protein components in the reaction cycle brings increases the degree of complexity with regard to the stoichiometry and affinity of each component while reconstituting the enzyme system for efficient turnover. The best estimate of the binding affinity of MMOB to MMOH comes from following the change in fluorescence of a fluorescent probe (BADAN) labeled MMOB as it forms a complex with MMOH [76]. This provided a K_d for MMOB binding to oxidized MMOH ($\mathbf{H}^{ox}$) of 68 nM at pH 7.0 and a K_d of 2.2 μM for binding to reduced MMOH ($\mathbf{H}^{red}$). These binding constants are pH-dependent, which is consistent with the observation that the binding interactions between MMOB and MMOH are electrostatic in nature [76, 90]. Fluorescence quenching experiments designed to measure the binding affinity of MMOR to MMOH provided evidence for two potential binding sites on MMOH (K_{d1} = 10 nM and K_{d2} =8 μM) [74]. Two MMOR binding sites on MMOH have also been observed for the sMMO system from *M. capsulatus* (Bath) via isothermal titration calorimetry [91].

The stoichiometry of the protein components in a fully-reconstituted sMMO system were determined from steady state kinetic assays while titrating with individual proteins MMOB and MMOR [74]. The steady state activity of the sMMO system is optimal at a MMOB concentration that is stoichiometrically equivalent to the MMOH active sites. The activity steadily decreases at higher concentrations of MMOB. This behavior arises due to formation of inhibitory MMOB dimer complexes. These dimers can also form complexes with MMOR, thus sequestering the reductase from the optimal equilibrium of the protein components. The highest activity of the sMMO system with MMOR is achieved at a stoichiometry of 5 equivalents of MMOR to each equivalent of MMOH active site. Higher concentrations of MMOR decrease the activity owing to formation of MMOB:MMOR complexes which diverts MMOB from its complex with MMOH. The formation of these inhibitory complexes has been verified through chemical cross-linking studies [74].

The turnover of sMMO to yield product can be achieved in multiple combinations of the protein components. These studies have helped elucidate the functional roles of the individual proteins. The presence of MMOB is not a strict requirement for catalysis as MMOH and MMOR can form a turnover system [80], although the specific activity in the absence of MMOB is reduced by ~ 150-fold compared to the fully reconstituted system [92]. MMOH is also catalytically active in

isolation from the other protein components when provided with both oxygen and electrons in the form of hydrogen peroxide in a so-called 'peroxide shunt' pathway [93]. However, the turnover system that is optimal for the detection of reaction cycle intermediates is a single turnover system with chemically reduced MMOH and MMOB [94].

1.5.5 Intermediates in the sMMO catalytic cycle

The primary approach to elucidating the chemical mechanism of sMMO is the observation and characterization of reaction cycle intermediates. This is achieved by using transient kinetic and rapid freeze-quench techniques to observe a single turnover reaction of sMMO. The single turnover reaction is achieved by mixing chemically reduced MMOH and MMOB with oxygen in a stopped-flow instrument. The absence of MMOR and NADH ensures that there is no re-reduction of MMOH to the diferrous state, thus restricting the reaction to a single turnover. As the primary role of MMOR is to reduce the diiron cluster prior to catalysis, the MMOH:MMOB reaction is deemed to be representative of sMMO catalysis.

The single turnover cycle of MMOH initiates with the diferrous state of the diiron cluster ($\mathbf{H}^{red}$) (Figure 1.8). In the absence of characteristic optical absorption bands with large extinction coefficients, the best way to follow the decay of the diferrous state is to monitor the loss of its g = 16 parallel-mode EPR signal by freeze-quench EPR. This EPR signal arises from the S = 2 ferrous centers that are coupled ferromagnetically to yield an S = 4 ground state species [92, 95]. The rate constant of decay of this EPR signal was measured to be 22 s^{-1} at pH 7.0 and 4 °C. It was also observed that rate constant of this kinetic step did not change in the presence or absence of substrate and did not exhibit an oxygen concentration dependence [81, 94]. The absence of oxygen concentration dependence suggests the formation of an intermediate **O** from $\mathbf{H}^{red}$, where oxygen is irreversibly bound near the reduced diiron cluster in the active site. Accordingly, the rapid freeze-quench EPR studies follow the decay of intermediate **O**.

Moving further along the reaction cycle following the decay of intermediate **O**, transient kinetic optical studies describe the formation of chromophoric intermediate termed as **P**. This intermediate has a weak absorption spectrum with wavelength maxima at 700 nm (ε = 2500 M^{-1} cm^{-1}) and 420 nm (ε = 4000 M^{-1} cm^{-1}) [96-98]. A Mössbauer characterization of this intermediate indicated that the two iron atoms are in the Fe(III) state (isomer shift δ = 0.67 mm s^{-1}) [96, 99].

Accordingly, this intermediate is proposed to be a peroxide-bound diiron cluster intermediate. The formation rate constant for this intermediate is pH-dependent and is measured to be about 8 s^{-1} at pH 7.0 and 4 °C [98, 100]. The rate constant for the decay of intermediate **P** is estimated to be 2.5 s^{-1} at pH 7.0, 4 °C and is also pH-dependent [98, 100].

The obvious discrepancy between the decay rate constant of intermediate **O** (22 s^{-1}) and the formation of intermediate **P** (8 s^{-1}) indicates the presence of an intervening intermediate. The presence of this intermediate, termed as **P***, is lent further credence by the observation that while the decay of intermediate **O** is pH-independent, the formation of **P** is pH-dependent [98]. In comparison to intermediate **P**, **P*** possibly has a very weak absorption spectrum which is not very different from $\mathbf{H}^{red}$.

Intermediate **P** decays with the concomitant formation of a transient species with a broad absorption spectrum with wavelength maxima at 330 and 430 nm (ε_{430} = 7500 M^{-1} cm^{-1}) [94, 101]. The rate constant for the formation of this intermediate, designated as compound **Q**, is the same as the decay rate constant of **P** (2.5 s^{-1} at pH 7.0, 4 ^{o}C). A Mössbauer characterization of this intermediate describes both the iron atoms as being present in a high spin Fe(IV) state (δ = 0.17 mm s^{-1}) [101, 102]. The presence of substrate does not change the formation rate constant but dramatically increases the decay rate constant of compound **Q**. The decay rate constant of **Q** is linearly dependent upon substrate concentration with decay rate constants of 19000 M^{-1} s^{-1}, 9000 M^{-1} s^{-1} and 200 M^{-1} s^{-1} with methane, furan and nitrobenzene substrates respectively [94]. **Q** is the key reactive intermediate of the sMMO catalytic cycle. The absence of any effect of substrate on the steps starting from the initiation of the catalytic cycle and leading up to the formation of **Q** puts sMMO in a rare class among enzymes inasmuch as it lacks substrate regulation. This substrate regulation refers to the initiation of the catalytic cycle of a vast majority of enzymes in the presence of substrate. This substrate control acts as a check against unregulated turnover, thus preserving a high catalytic efficiency for the enzyme. The sMMO catalytic cycle is, however, capable of undergoing turnover in the complete absence of any substrate, as **Q** decays through an unknown mechanism to the resting diferric form of the enzyme ($k_{autodecay}$ = 0.05 s^{-1} at 4 ^{o}C).

The chemical mechanism proposed for the reaction of compound **Q** with methane is based primarily upon the cytochrome P450 oxygenase mechanism. Accordingly an intermediate **R** has

been proposed to form during the reaction of **Q** with substrate. As yet, **R** has not been directly observed, although diagnostic chemical probes have provided indirect evidence for it. This topic shall be discussed in greater detail further along in section 1.5.5.

The use of nitrobenzene as an alternative substrate provides an additional handle on the single turnover reaction as the primary product, *p* – nitrophenol is chromophoric. In the reaction with nitrobenzene, compound **Q** decays to form an intermediate with a maximal absorption at 325 nm and a shoulder at 395 nm. This intermediate termed as **T**, has been characterized by chemical-quench studies to be an enzyme-product complex [94]. The intermediate **T** subsequently decays as product is released from the active site with a rate constant that is identical to the steady state turnover number for nitrobenzene of 0.02 s^{-1} at 4 °C. Thus product release is the rate-limiting step for the sMMO reaction with nitrobenzene as substrate.

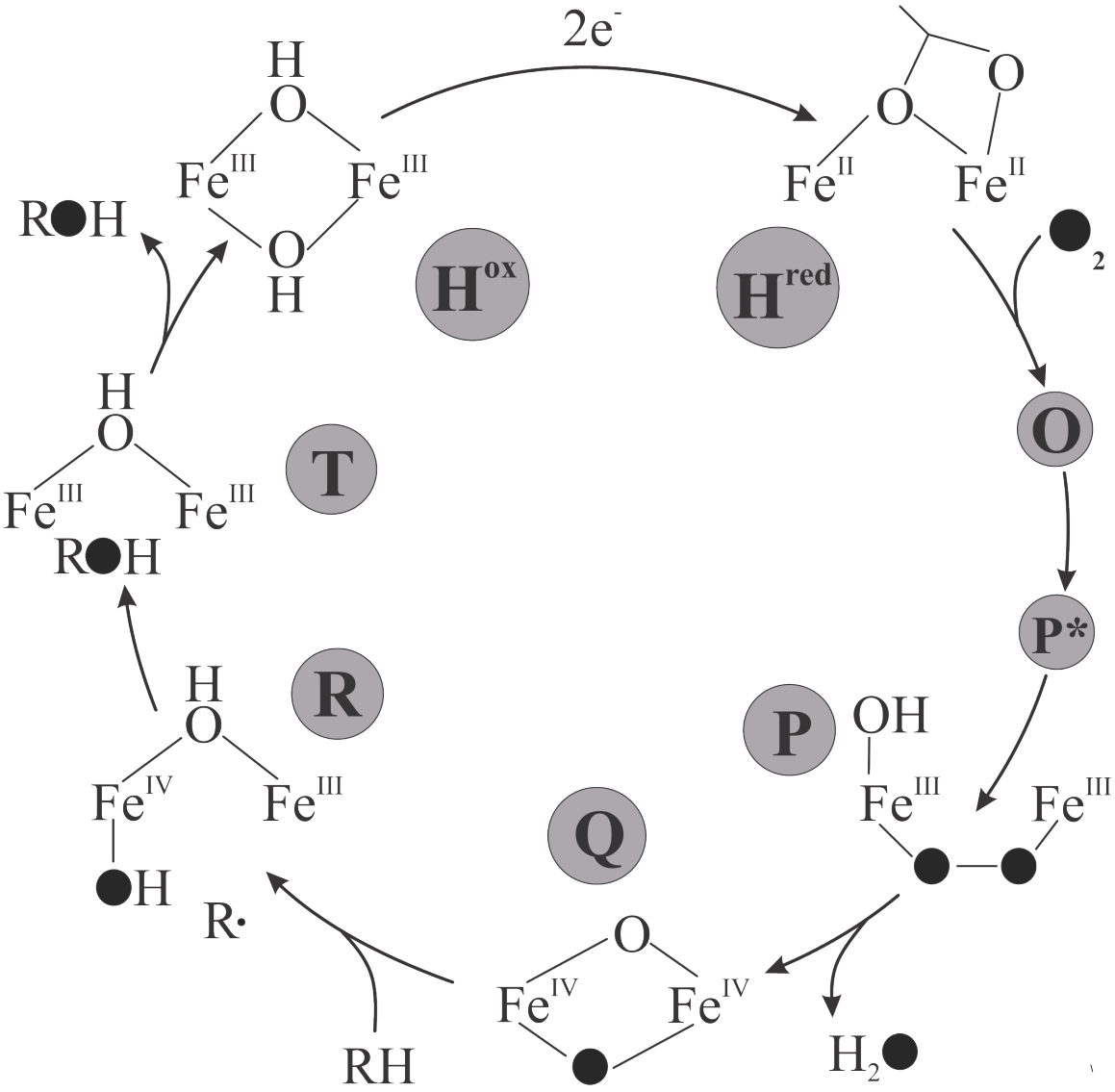

Figure 1.8 – The postulated catalytic cycle of sMMO. The intermediates along the cycle are labeled within a grey colored circle. Spectroscopic characterization has only been performed on intermediates **P**, **Q**, **T** and the starting $\mathbf{H^{red}}$ and resting $\mathbf{H^{ox}}$ states.

1.5.5.1 *Chemical nature of compound P*

The Mössbauer spectrum of intermediate **P** indicates that both the iron atoms are present in the ferric state and that their isomer shift (δ = 0.66 mm s^{-1}) and quadrupole splitting (ΔE_Q = 1.51 mm s^{-1}) are different from the resting state diferric cluster [96, 99]. Based upon the oxidation state of the iron atoms, this oxygen-bound intermediate was described as a peroxo group bound symmetrically to the iron atoms. Multiple models can be described for such a symmetrically bound peroxide moiety (Figure 1.9). A resonance Raman spectroscopic analysis would provide detailed information regarding this binding mode but such an analysis has not been performed on intermediate **P** in sMMO. Density functional calculations suggest both η^2:η^2 and μ-1,2 geometry as feasible models for the peroxo-binding mode [103-105].

The clues regarding the identity of the binding mode of the peroxide moiety in **P** comes from a comparison with peroxo intermediates in closely related carboxylate-bridged diiron monooxygenases. Peroxo intermediates with similar absorption spectra and Mössbauer parameters as **P** have been observed in Δ^9-desaturase [106], D84E & W48F/D84E variants of subunit R2 in ribonucleotide reductase [107, 108], frog M ferritin [109] and human deoxyhypusine hydroxylase (hDOHH) [110]. Crucially, the resonance Raman spectrum of all the above mentioned peroxo intermediates support the *cis*-μ-1,2 peroxide binding configuration. A similar *cis*-μ-1,2 peroxo intermediate has been observed *in-crystallo* in the sMMO related T4mo [111]. Considering the similarity of the absorption spectrum and Mössbauer parameters between the peroxo intermediates, it is reasonable to assign a μ-1,2 binding mode for the peroxo moiety in sMMO (Table 1.1).

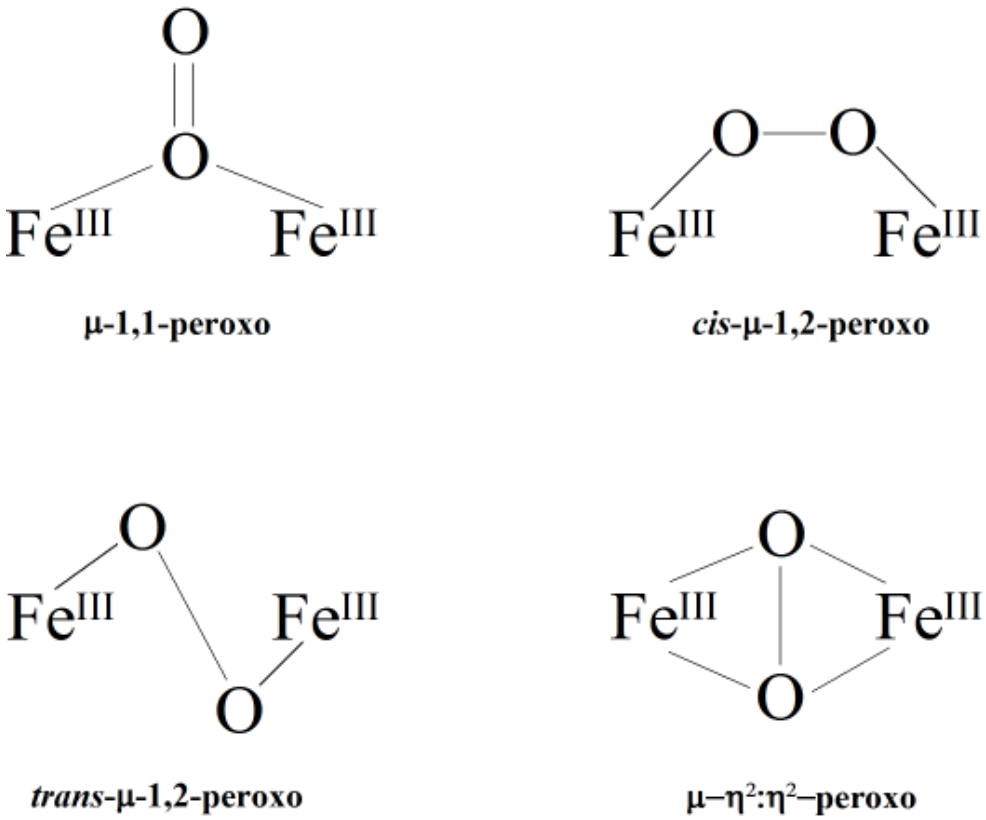

Figure 1.9 – The putative models for the symmetric peroxide-binding mode in intermediate **P**.

Species	λ_{max} (nm)	δ (mm/s)	ΔE_Q (mm/s)	Reference
sMMO – P	700	0.66	1.51	[96, 99]
D84E R2 RNR	700	0.63	1.58	[108]
Δ^9-desaturase	700	0.68,0.64	1.90, 1.06	[106, 112]
frog M ferritin	650	0.62	1.08	[109, 113, 114]
hDOHH	630	0.55, 0.58	1.16, 0.88	[110]

Table 1.1 – A comparison of the electronic absorption features and Mössbauer parameters of intermediate **P** in sMMO with peroxo intermediates in related carboxylate-bridged diiron mono-oxygenases.

1.5.5.2 *Chemical nature of compound Q*

The Mössbauer spectra of compound **Q** in sMMO from *M. trichosporium* OB3b, depicts a single quadrupole doublet with an isomer shift of 0.17 mm s^{-1} and a quadrupole splitting of 0.53 mm s^{-1} [102]. This indicates that the two iron atoms of the cluster are in a high-spin Fe(IV) oxidation state and have a similar ligand environment. This intermediate has also been trapped and characterized in sMMO from *M. capsulatus* Bath (two doublets - δ_1 = 0.21 mm s^{-1} ,ΔE_{Q1} = 0.68 mm s^{-1}; δ_2 = 0.14 mm s^{-1}, ΔE_{Q2} = 0.55 mm s^{-1}) [101, 115]. High-field Mössbauer studies show the diiron cluster as being diamagnetic indicating that the two iron centers are anti-ferromagnetically coupled [102].

A further structural elucidation of **Q** was achieved with EXAFS spectroscopy that described two characteristic features: a Fe-Fe distance of 2.46 Å and a single 1.77 Å long Fe-O bond per iron atom [99]. In addition, the pre-edge XAS data indicated that both the iron atoms are five-coordinate species with a highly distorted geometry. The Fe-O bond is too long to be a terminal Fe^{IV} =O bond as compared to porphyrin iron(IV)-oxo moieties in compound I and II of peroxidases [116]. This Fe-O bond distance is, however, similar to Fe-μ-O bonds in oxo-bridged diiron model compounds [117]. The presence of two Fe-μ-O bonds in **Q** would further shorten the Fe-Fe distance, thus distinguishing **Q** from mono-μ-oxo bridged diiron models compounds. The experimental Fe-Fe distance of 2.46 Å is, however, still shorter than a bis-μ-oxo diiron synthetic model complex [118]. This indicates that in addition to a bis-μ-oxo diamond core structure, the glutamate 144 residue which bridges the diferric and diferrous forms of the cluster is still coordinating both the iron atoms in **Q**. A closer observation of the Fe-O bonds reveals two Fe-μ-O bonds that are 1.77 Å and 2.05 Å long respectively, on each iron atom (Figure 1.10). This leads to a description of a head to tail dimer of two Fe^{IV} =O units for **Q**, an arrangement that has been proposed to stabilize this high valent iron intermediate. To date, this remains the most comprehensive description of the structure of **Q**. Vibrational structure information would help further the structural description of **Q**, but no attempts at probing these features have been yet successful.

The unique ability of compound **Q** to oxidize the strong C-H bond of methane has spurred on a multitude of theoretical calculations encompassing ab-initio quantum chemical mechanics (QM) based upon density functional theory (DFT) and mixed quantum mechanics/molecular mechanics

(QM/MM) methods to explain its structure and reactivity [119]. The structural models of **Q** proposed by these studies are depicted in Figure 1.11. In summary, these theoretical calculations match some experimental measurements of **Q** with regard to the asymmetry of the Fe^{IV} =O bonds and in some cases, the Mössbauer parameters but have not been able to describe the short Fe-Fe distance of 2.46 Å [103, 105, 120-122]. The iron atoms in these models are also both six-coordinate which does not agree with the EXAFS description of two-five coordinate iron atoms in **Q**.

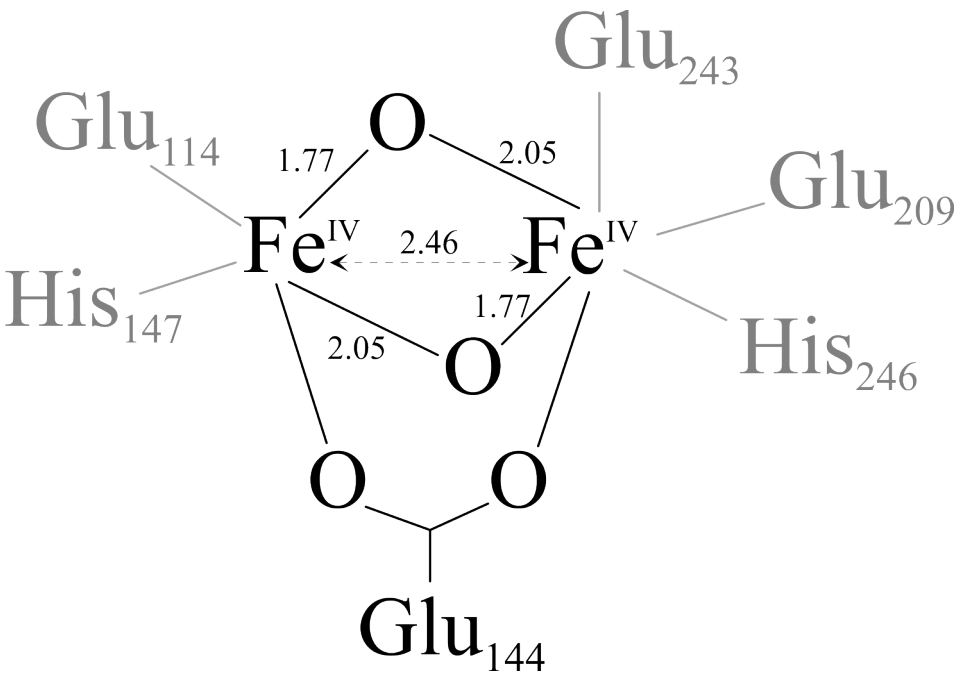

Figure 1.10 – The putative structure of the diiron cluster in **Q**. The portion of the cluster with definitive experimental information available is shaded in black. The ligands to the diiron cluster (shaded grey) are inferred to bind the iron atoms while remaining unchanged from the starting diferrous form of the cluster. The Fe-Fe distance and those for the Fe-O bonds are provided in Å.

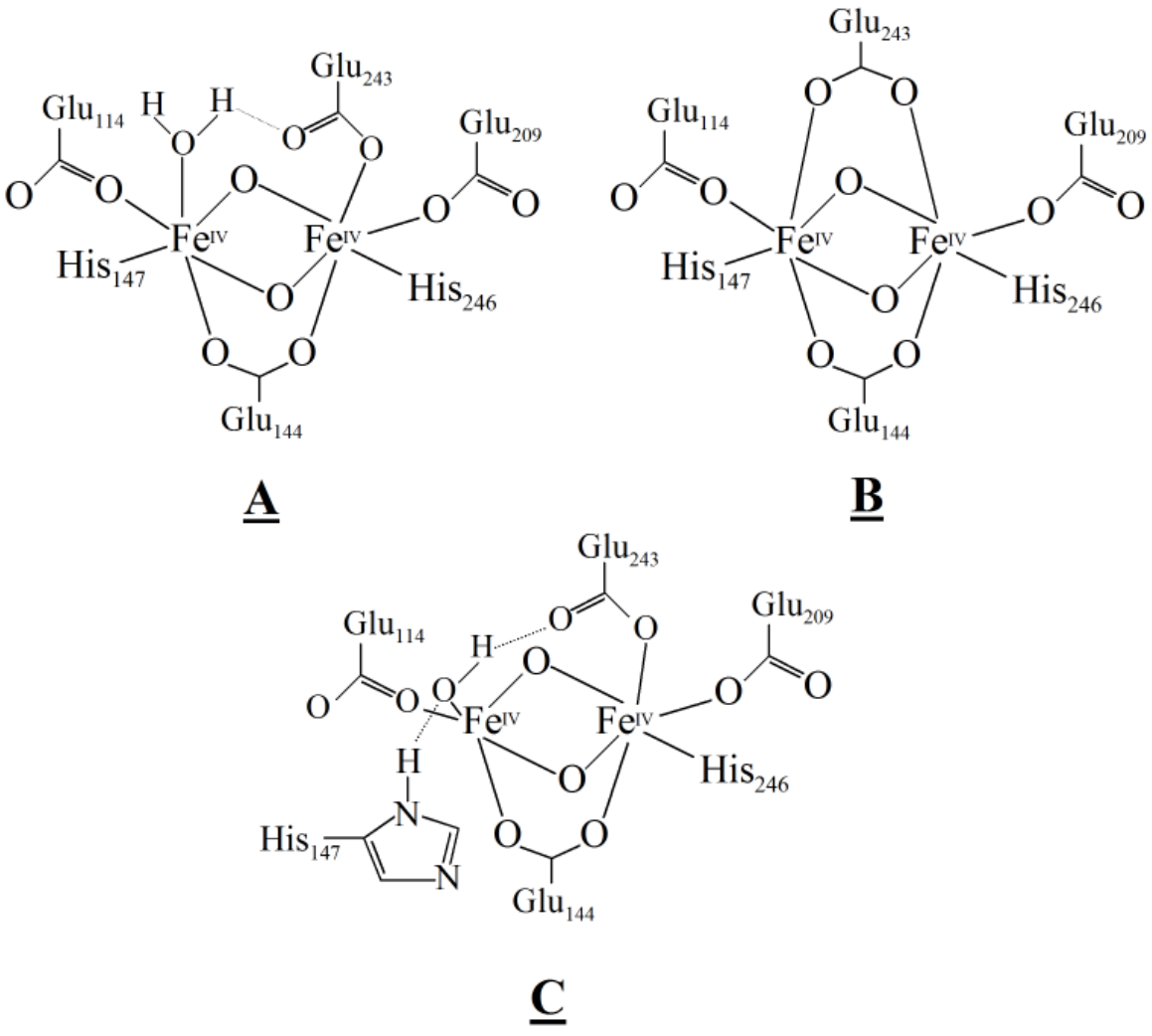

Figure 1.11 – Structural models for **Q** from DFT calculations. A – model from Friesner, Lippard and Noodleman groups [103, 120, 121], B – model from Morokuma and Siegbahn groups [105, 123], C – model from Noodleman group [120].

1.5.6 Theoretical proposals for the chemical mechanism of sMMO

The ability of sMMO to catalyze the oxidation of methane, which has the strongest known aliphatic C-H bond (BDE = 105 kcal $mole^{-1}$), is the primary driving force behind attempts to understand its catalytic mechanism. The following section describes the theoretical chemical mechanisms that have been proposed for the reaction of compound **Q** with methane.

1. Hydrogen atom abstraction and oxygen rebound – The cytochrome P450 oxygenase chemical mechanism is the archetype for this model of sMMO catalysis (Figure 1.12) [124]. In this model, one of the iron atoms of the diiron cluster in MMOH fulfills the role of the porphyrin group in heme-P450. Accordingly, compound **Q** in sMMO is formally equivalent to the reactive intermediate in P450, compound **I** (Fe(IV)-oxo, porphyrin cation radical). Following the heme-P450 mechanistic route, **Q** would abstract a hydrogen atom from the substrate to yield an Fe(III)-Fe(IV) mono-μ-oxo bridged diiron cluster with a terminal hydroxo group on the Fe(IV) and a substrate cation radical. This proposed sMMO intermediate has been termed **R** [125]. A rebound of the terminal hydroxo group on the Fe(IV)-OH onto the substrate radical to form product follows while the diiron cluster is reduced to the diferric form [126, 127]. A variation of this mechanism has also been proposed where the methyl radical formed as a result of the initial hydrogen atom abstraction, is positioned very close to the diiron cluster. This does not allow for a free motion of the methyl radical and this mechanism is thus characterized as a "bound radical" pathway [119, 128].

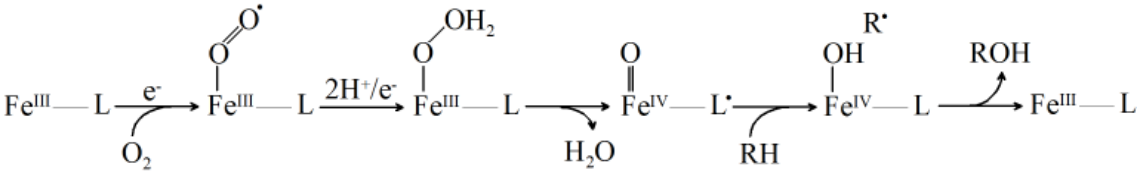

Figure 1.12 – An analogy between the hydroxylation reaction mechanisms proposed for heme-P450 and sMMO. L refers to the porphyrin group in heme-P450 or an iron atom in sMMO. While the order of addition of electrons in the first two steps would differ between sMMO and heme-P450, the proposed mechanism for sMMO attributes a similar role to the second iron atom in sMMO as the porphyrin group.

2. Non-synchronous concerted oxygen insertion – This mechanism proposes that the hydroxylation reaction proceeds through a partially concerted oxygen-insertion reaction into the substrate C-H bond. This contrasts with the formation of a discrete radical intermediate in the heme P450 model mechanism [129-131] (Figure 1.13). The non-synchronous insertion of the oxygen atom arises from differences in the vibrational frequencies of the bond-making and bond-breaking steps and allows for transient radical character on the substrate. This mechanism also mandates a side-on approach of the substrate C-H bond to the Fe-oxo moiety.

3. Diiron cluster-based concerted oxygen insertion – This mechanism proposes a role for both of the two Fe(IV)-oxo oxygen atoms in the reaction with methane, where one performs an electrophilic attack on the methane carbon while the other performs a nucleophilic attack on the hydrogen atom of the C-H bond [132, 133]. This leads to the formation of a five-coordinate substrate carbon intermediate whose subsequent rearrangement leads to the formation of product (Figure 1.13).

4. Non-radical two-step mechanism based upon the formation of an iron-carbon bond – As a methyl radical is unstable, precluding a hydrogen atom/oxygen rebound pathway, a non-radical mechanism has been suggested. Accordingly, a non-radical two-step mechanism involves the coordination of methane to one of the coordinatively unsaturated Fe(IV) atoms of **Q** [134]. This is followed by a hydrogen atom abstraction and a methyl shift that yields the product methanol bound to the iron cluster (Figure 1.13).

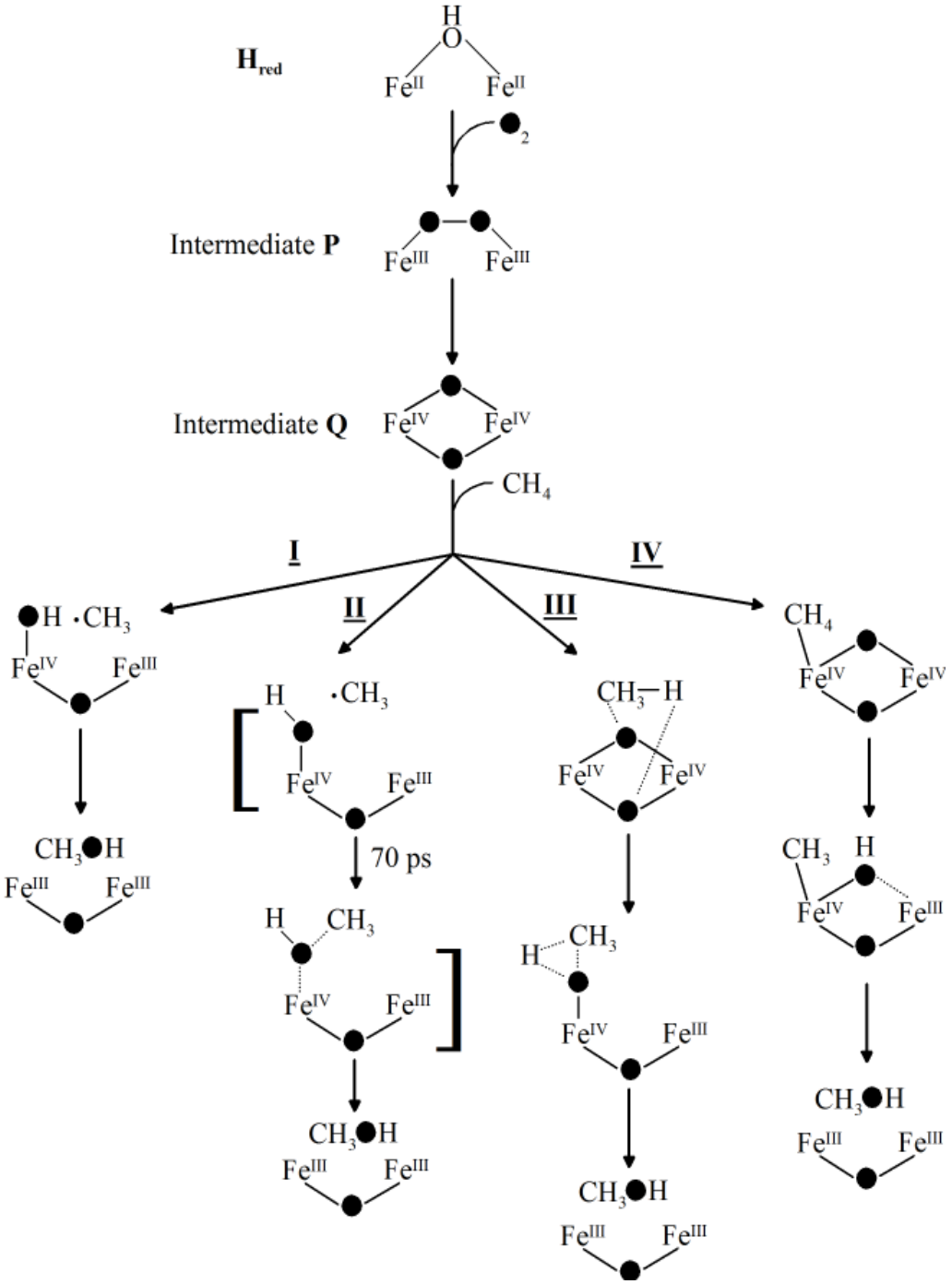

Figure 1.13 – Proposed chemical mechanisms for sMMO. I – Hydrogen atom abstraction/oxygen rebound mechanism, II – Non-synchronous concerted oxygen insertion mechanism, III - Diiron cluster-based concerted oxygen insertion mechanism and IV - Non-radical two-step mechanism based upon the formation of an iron-carbon bond.

1.5.7 Experimental elucidation of the chemical mechanism of sMMO

The proposed sMMO reaction mechanism can be divided into two classes: i.) concerted or stepwise non-radical mechanisms and ii) non-concerted radical mechanisms. Accordingly, efforts have been made to detect the transient presence of substrate radical intermediates during sMMO turnover in order to distinguish between the two above classes of mechanistic proposals. The following section describes the experimental evidence that led us to support one of these two classes of reaction mechanism.

1. Radical clock/Chiral substrate studies – The direct detection of a transient substrate radical intermediate is almost impossible considering the short lifetimes expected for such an unstable species. Thus an indirect detection approach has been employed with the use of 'radical clock' and chiral substrates. The sMMO-catalyzed oxidation of labeled chiral (*R*) and (*S*) 1-[$^{2}H_{1}$,$^{3}H_{1}$] ethane to ethanol proceeded with 35% inversion of stereochemistry [135]. The lack of retention of stereochemistry indicates that the C-H bond hydroxylation in ethane is not a concerted step and must involve a radical or cation intermediate. The absence of complete racemization during product formation indicates that the rate constant of oxygen rebound must compete with the rate constant of rotation around the ethane C-C bond. Assuming that the active site in MMOH allows a free rotation around the C-C bond, the rate constant of oxygen rebound must then be of the order of 10^{12} to 10^{13} s^{-1}. However, this rate constant is too fast for a physical motion of the OH group as it rebounds onto the substrate radical, thus indicating that hydroxylation in sMMO is subtly different from a classical two-step radical mechanism.

Radical clock compounds are strained ring (generally cyclopropane ring) compounds that isomerize to a ring-opened form upon oxidation to a radical or cation state. These rates of rearrangement have been determined for many radical clock compounds. Thus, a measurement of the relative amount of rearranged to un-rearranged product formed in the enzymatic oxidation reaction allows for a determination of the lifetime of the radical intermediate in the catalytic cycle. A large variety of radical clock compounds have been employed as substrates with sMMO from *M. trichosporium* OB3b and *M. capsulatus* Bath [129, 131, 136-141]. In summary, radical intermediate derived rearranged products have been observed with these diagnostic substrates. In addition, the formation of cation intermediate derived rearranged products was also observed. These results are indicative of a more complex picture of the sMMO hydroxylation reaction as some radical clocks fail to show rearranged products even though their rearrangement rates are

comparable with the radical clocks displaying rearranged products. This phenomenon is also manifested by the lack of correlation between the amounts of rearranged product and the rearrangement rates for the radical clocks that do display radical rearranged products. This indicates the presence of an additional variable in the form of an active site steric factor in the radical clock studies that confounds the measurement of radical lifetimes in sMMO. Radical clocks having steric bulk around the C-H bond oxidized by sMMO cannot approach the diiron cluster closely during catalysis and thus show rearrangement. In contrast, sterically unhindered radical clocks do not show rearrangement as the substrate radical is rapidly quenched by oxygen rebound from the diiron cluster that is in close proximity [139] (Figure 1.14). The role of sterics in the oxidation reaction agrees with previous experiments probing the stereochemistry of isopentane oxidation, where it was observed that the least sterically hindered carbon atom of isopentane was preferentially hydroxylated [80]. Accordingly, radical clock substrates can only be used in a qualitative sense with sMMO and cannot be used to measure the half-life of the substrate radical intermediate.

In summary, the radical clock and chiral substrates indicate the transient presence of a radical intermediate. However, the chiral ethane reaction indicates that this radical intermediate does not conform with a traditional hydrogen atom abstraction mechanism as the rate of oxygen rebound is faster than is possible for a physical motion of a hydroxyl group. The proposals for a non-synchronous concerted oxygen insertion mechanism [131], cluster-based concerted oxygen insertion mechanism [133] and the 'bound radical' variation of the hydrogen atom/oxygen rebound mechanism [128] can, however, account for these experimental observations. It is unclear how the non-radical, two-step mechanism based upon formation of an iron-carbon bond would account for these experimental observations.

The presence of cation-rearranged products was unexpected when considering a classical hydrogen atom abstraction mechanism for **Q** reaction with substrates [136, 138, 141]. There are two proposals to explain the origin of a cation substrate intermediate. The first proposal arises from the observation that the peroxo intermediate in sMMO from *M. capsulatus* Bath reacts with easily oxidized substrates like propylene and ethers [142, 143]. As such, it is proposed that intermediate **P** oxidizes radical clock substrates by transfer of an OH^+ group that is followed by loss of a water molecule to yield a cation-radical intermediate (Figure 1.15A) [138]. The second proposal is based upon the strong oxidizing ability of the [Fe(III)-Fe(IV)]-OH intermediate

formed as a result of the initial hydrogen atom abstraction by **Q**. This intermediate is formally identical to intermediate **X** in ribonucleotide reductase (RNR) in terms of the oxidation state of the iron atoms [144]. Intermediate **X** has been demonstrated to abstract an electron from a nearby tyrosine residue and generate a tyrosyl radical [145]. Based upon this chemistry of **X**, a chemical mechanism has been proposed where the one electron reduced form of **Q** in sMMO can abstract another electron from easily oxidized radical clock substrates to generate cation-substrate intermediates (Figure 1.15B)[141]. This model has been lent further credence by the observation that sMMO can catalyze desaturation chemistry. This desaturation chemistry is proposed to occur through the formation of a cation-substrate intermediate which subsequently partitions between oxygen rebound to form the alcohol and proton elimination to form the desaturated product (Figure 1.16) [146].

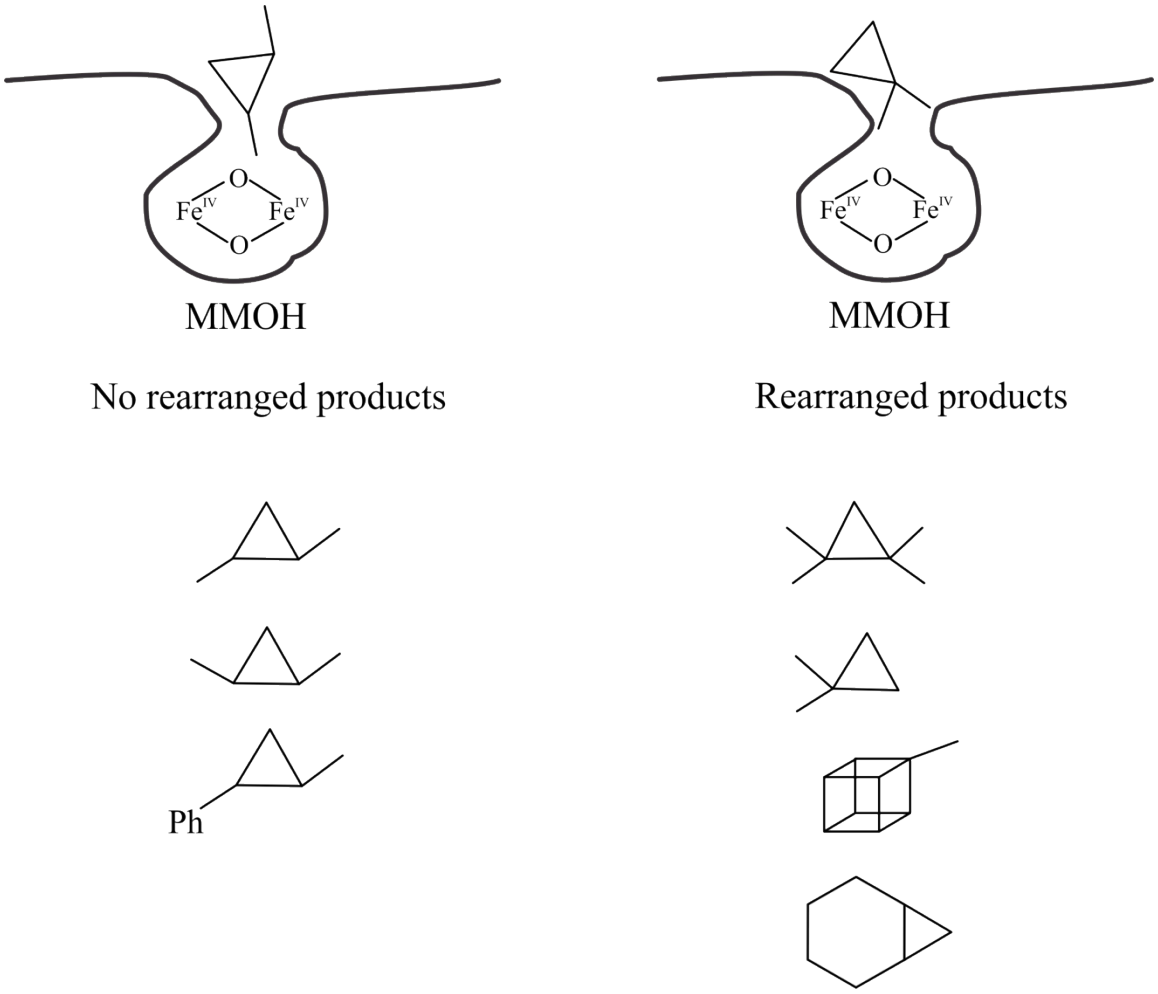

Figure 1.14 – The role of steric factors in the oxidation reaction of sMMO confounds the quantitative timing of substrate-radical lifetimes. Sterically unencumbered substrates, as for example on the left hand side of the above figure approach **Q** more closely and do not form radical rearranged products. Bulky substrates (quaternary carbon at point of oxidation) on the right hand side of the figure form radical rearranged products.

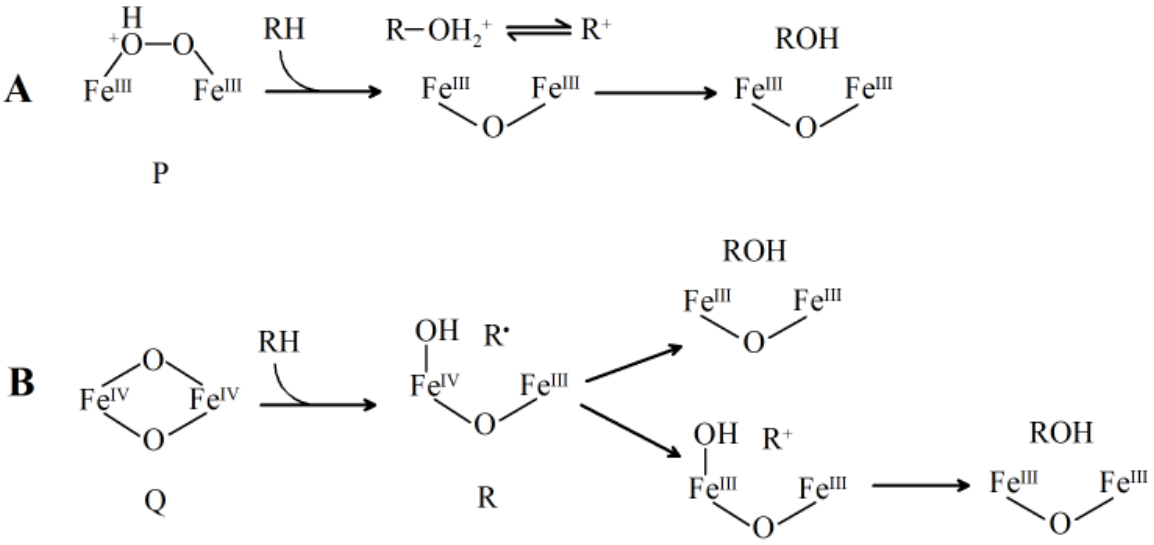

Figure 1.15 – The origin of a cation-radical intermediate can be accounted by the following mechanisms: A – reaction with intermediate **P** with radical clock, B – an abstraction of an additional electron from the substrate radical by **R**.

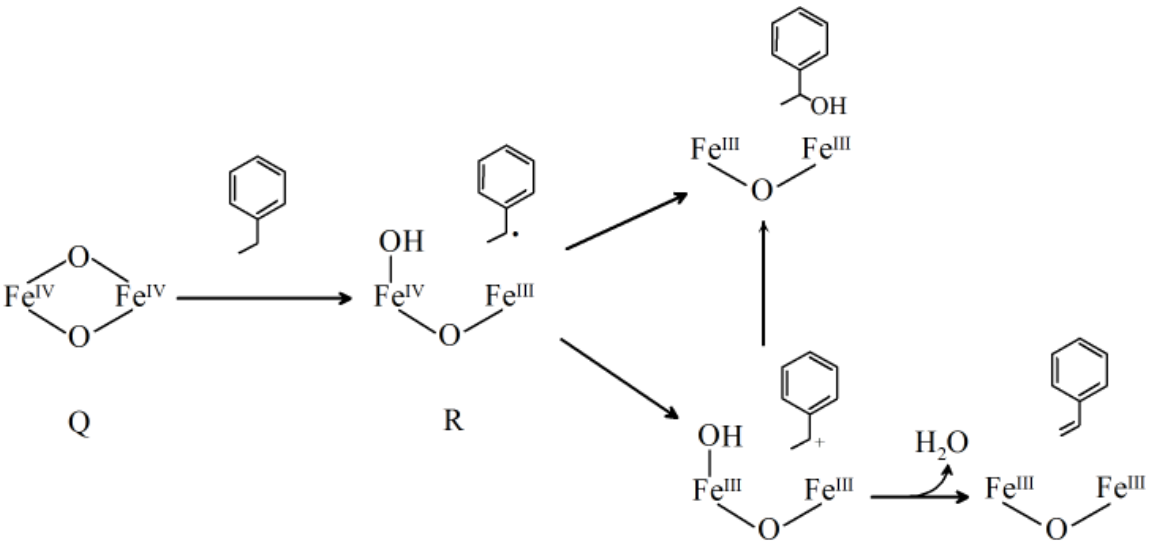

Figure 1.16 – This mechanistic scheme illustrates the desaturation reaction catalyzed by sMMO [146]. Intermediate **R** can either undergo oxygen rebound to form the alcohol product or abstract another electron from the substrate radical to yield a cation-substrate intermediate. This intermediate undergoes the loss of a proton to form the desaturated product.

2. Isotope effect studies – The intermolecular deuterium kinetic isotope effect for the reaction of **Q** with methane is observed to have an exceptionally large value of 50 [147]. A KIE of this order for the reaction of **Q** with methane unequivocally indicates that the reaction coordinate is primarily comprised of a C-H bond-breaking step. This can only be accounted by a two-step mechanism for methane hydroxylation. This result rules out the cluster-based concerted oxygen insertion mechanism for sMMO catalysis. It is not clear how the non-radical two-step mechanism based upon formation of an iron-carbon bond would account for this large KIE for methane oxidation.

The larger than classical limit values for the primary KIE indicates the presence of a hydrogen atom tunneling contribution in the C-H bond breaking reaction of methane with **Q**. A definitive proof of hydrogen tunneling requires the following evidence: i) an isotope-dependent curvature in the Arrhenius plot, ii) an Arrhenius pre-exponential factor ratio of $A_H/A_D < 1$ and $A_H/A_T << 1$, iii) a positive slope in the ln KIE versus 1/T plot that is larger than the value expected based upon the isotopic differences in zero point bond-dissociation energy [148]. Unfortunately, the comparison of ratios of deuterium and tritium kinetic isotope effects has not been made for the **Q** reaction with methane. Moreover, the reaction cannot be followed over a large enough temperature range to generate expanded Arrhenius plots owing to the low temperatures required below the freezing point of water. Then, there is a further kinetic complexity arising from the binding rate constant of methane to the active site, which has a similar magnitude to the C-H bond breaking reaction. This further limits the available temperature range over which we can follow the C-H bond breaking reaction. This issue shall be discussed in greater detail in section 1.5.7. In spite of the limitations, a plot of ln KIE versus 1/T does show a positive slope of 3.4, which is larger than an expected value of 1.25 based upon a difference in the zero point bond-dissociation energy for the isotopes [149]. This value is similar to those obtained from other enzymes demonstrated to exhibit tunneling [150] and confirms the likely role of hydrogen atom tunneling in the reaction of **Q** with methane.

The KIE for the sMMO reaction can also be determined from a measurement of the product ratio at the end of a single turnover reaction with protium and deuterium labeled methane. The intermolecular KIE obtained in such a fashion is 19.3 for a 1:1 mixture of CH_4 and CD_4, which is distinctly less than the KIE obtained from the direct observation of **Q** decay [147]. This indicates to a complex scenario for product formation in the reaction of **Q** with methane. The model for **Q**

reactivity devised to account for this observation involves a quasi-reversible hydrogen atom abstraction reaction (Figure 1.17). The methyl radical formed as a result of the hydrogen atom abstraction by **Q** can either encounter oxygen rebound to form the alcohol product or re-abstract the hydrogen atom from the diiron cluster. On account of a kinetic isotope effect also operating on the hydrogen re-abstraction step, the deuterium labeled methyl radical would preferentially undergo oxygen rebound to form product. This would reduce the product isotope enrichment that would be produced as a result of the initial hydrogen atom abstraction step and thus lower the KIE obtained through a measurement of product ratios as compared to a direct observation of **Q** decay. To satisfy this model, the resulting species of the re-abstraction of the hydrogen atom by the methyl radical, termed as **Q'**, needs to weakly absorbing at 430 nm (Figure 1.17).

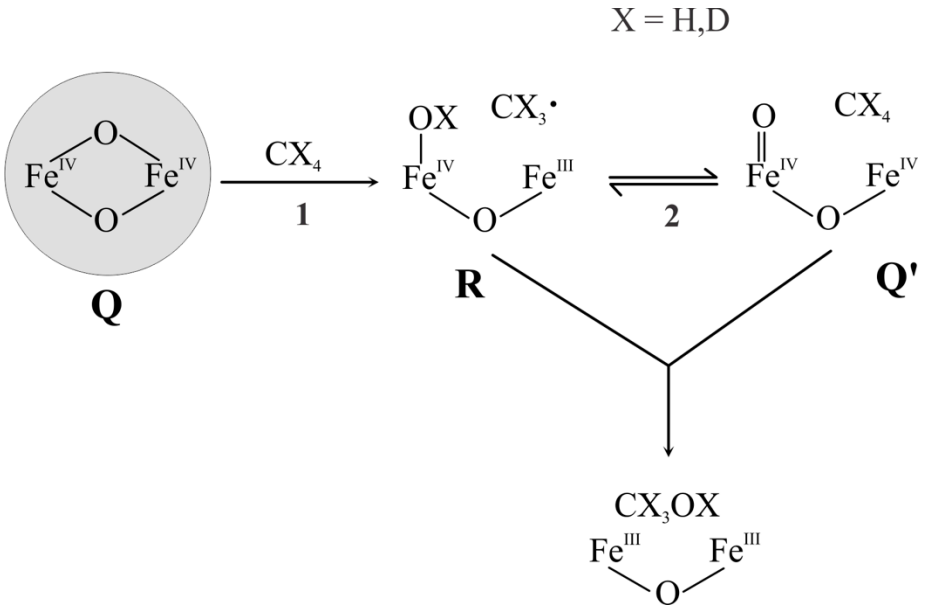

Figure 1.17 – The quasi-reversible hydrogen atom abstraction from methane (X = H, D) by **Q**. The kinetic steps 1 and 2 involve a kinetic isotope effect that together contributes to the product KIE. As **Q** (grey circle) is the only species in this scheme that absorbs at 430 nm, the KIE obtained from the loss of this absorbance involves only step 1. This accounts for the difference in the two values of KIE.

3. Spin trap studies – Spin trap compounds are chemical species built around either a nitroso or nitrone chemical group. These compounds readily react with transient radical species to form a stable nitroxide radical. An analysis of the EPR spectrum of the stable radical provides information regarding the identity of the trapped transient radical. In order to detect transient substrate radical species in sMMO, the spin trap has to be present alongside the substrate in the active site, which is quite a difficult proposition. However, the spin trap nitrosobenzene has the advantage that it is a substrate for sMMO [151]. Thus, the nitroso group that is integral to this substrate would trap the substrate radical intermediate formed during the oxidation reaction. In a steady state reaction with sMMO, nitrosobenzene does react to generate a radical species. However, the radical species detected is a neutral radical form of nitrosobenzene and is not the cation radical that would be expected to form as a result of hydrogen atom abstraction [151]. Nonetheless, the trapping of a nitrosobenzene substrate radical indicates that sMMO follows a hydrogen atom abstraction/oxygen rebound mechanism.

1.5.8 Regulation in sMMO and the role of MMOR

Regulation of the catalytic cycle is a crucial aspect of an enzyme's design. This regulation refers to the careful temporal and spatial ordering of the steps of binding reactants and the subsequent chemical reactions followed by product release. This fine control is important in order to maximize productive turnover and ensure that the correct product is made. Such regulation is made paramount in oxygenases as the reduced oxygen species generated in catalytic intermediates are very reactive and can be toxic on account of aberrant oxidation of either residues on the enzyme itself or other biomolecules in the cell. It is thus essential to tightly couple the production of these intermediates to substrate oxidation. The most common form of regulation in oxygenases involves the initiation of the catalytic cycle solely in the presence of substrate. In protocatechuate 4,5-dioxygenase and naphthalene 1,2-dioxygenase, substrate binding primes oxygen binding to the mononuclear iron atom by opening up an available coordination site [152-154]. In heme-P450 oxygenase, substrate binding in the active site changes the reduction potential of the iron center, thus permitting electron transfer from the accessory reductase protein. This reducing equivalent is essential to proceed along the catalytic cycle [79]. The circumvention of these regulatory mechanisms in the absence of substrate leads to self-hydroxylation of amino acid residues in the enzyme α-ketoglutarate-dependent taurine dioxygenase [155]. It has also been demonstrated that the heme-P450 oxygenases are a primary source of reactive oxygen species as a result of uncoupling and thus contribute to oxidative stress in eukaryotic organisms [156].

The regulation of sMMO catalysis suggests a novel and unique mechanism. This arises primarily from the observation that sMMO can undergo catalytic turnover in the absence of substrate but does not suffer from any self-hydroxylation unlike the α-ketoglutarate- dependent dioxygenases. In other words, sMMO does not employ substrate regulation. Another interesting aspect of sMMO regulation arises from the unusually broad substrate specificity of this enzyme. This begets the important question about the manner in which sMMO preferentially oxidizes methane that has the strongest C-H bond when surrounded by substrates with weaker C-H bonds in the cellular milieu. This regulation is demonstrated in sMMO in the observation that methane is a far better substrate than other compounds with weaker C-H bonds like furan and propane (second order rate constant for **Q** decay is 19000 M^{-1} s^{-1} with methane and 9000 M^{-1} s^{-1} for furan) [94].

The accessory protein MMOB is key to the regulation of sMMO. Site-directed mutagenesis studies have elucidated diverse roles for this regulatory protein. We have already discussed some aspects of its regulation of catalysis such as oxygen gating and regiospecificity of substrate oxidation previously in section 1.5.2. However, the participation of MMOB in the catalytic cycle goes further beyond the initiation of the catalytic cycle to the regulation of kinetic steps and control of substrate binding during the cycle. These regulatory roles of MMOB are described in the following sections.

1. MMOB regulation of substrate entry – The nature of substrate binding is a unique case in sMMO among all enzymes. None of the catalytic steps from the initiation of the single turnover reaction up to the formation of the reactive intermediate **Q** show substrate concentration dependence. The decay rate constant of **Q** is, however, dependent upon substrate concentration and this dependence is linear for all substrates tested [94]. This behavior requires **Q** decay to be a bimolecular reaction that must include the kinetic step of substrate binding to the enzyme active site. The substrate-mediated **Q** decay was probed in greater detail with Arrhenius plots at varying methane concentrations showing a non-linear behavior with a distinct breakpoint [97]. The Arrhenius plots are, however, linear for all other substrates including fully deuterated methane. The non-linear Arrhenius plots indicate the presence of two chemical steps in the decay of **Q** with substrates. The absence of any substrate-binding step prior to **Q** formation led to the hypothesis that one of the two steps in **Q** decay involves substrate binding to the active site while the other involves the actual C-H bond breaking step (Figure 1.18A). The curious absence of a KIE in the **Q** decay reaction with ethane and other substrates indicates that the substrate-binding reaction is rate limiting for all substrates larger in size than methane. The C-H bond breaking reaction is thus masked for all substrates except methane, precluding measurement of the rate constant of C-H bond cleavage. This explains why methane displays a higher rate constant for **Q** decay than other substrates with weaker C-H bonds. The break in the Arrhenius plot for methane is accounted for by a shift in the rate-limiting step from C-H bond breaking to methane binding as the temperature decreases. In the case of deuterated methane, the C-H bond breaking reaction is rate limiting in the available temperature range over which **Q** decay can be measured, thus yielding a linear Arrhenius plot. The linear Arrhenius plots for all substrates excluding methane arises from the substrate-binding step that is rate limiting over the available temperature range.

Further details regarding the substrate-binding step were obtained through the use of mutants of the regulatory MMOB protein. The N107G/S109A/S110A/T111A and subset mutants N107A/S110A and S109A/T111A of MMOB were designed based upon the interaction surface mapping of MMOB through NMR (Figure 1.6) [65, 73]. An analysis of the kinetic cycle in the presence of these variant MMOB proteins showed the following perturbations – i.) a substantial increase in the rate constant of reaction of **Q** with large substrates like nitrobenzene and furan, ii) an acceleration in the release of products from the active site that increases the turnover number for large substrates, and iii) a decrease in the rate constant for **Q** reaction with methane [157, 158]. The enhancement of **Q** reactivity and product release with large substrates in the presence of the MMOB mutants led to the description of a "molecular sieve" model for sMMO. The binding interface between MMOB and MMOH likely includes a channel through which substrates enter the active site. The size of the entrance into this channel is optimal for small molecules like methane. The MMOH:MMOB complex thus enforces a size selection on substrate entry and allows for the preferential reactivity of **Q** with methane (Figure 1.18B). A mutagenesis of the interfacial amino acid residues on MMOB to counterparts with smaller side-chains increases the size of this entrance to the substrate channel thus manifesting an enhancement in the binding rate constant of larger substrates (Figure 1.6).

This "molecular sieve" model is substantiated through the use of ethane as a substrate. In contrast to the absence of a KIE with wild type MMOB, the use of the N107G/S109A/S110A/T111A MMOB mutant displays a KIE of 2.0 when measuring **Q** decay in the presence of ethane [159]. This is expected according to the "molecular sieve" model, where the MMOB mutant opens up the substrate entry channel, thus increasing the binding rate constant for large substrates such as ethane. The shift in the rate-limiting step from substrate binding to C-H bond cleavage accordingly allows for the observation of a KIE with ethane. The Arrhenius plot also shows a non-linear behavior with the mutant MMOB and ethane, similar to what is observed with wild-type MMOB and methane [149].

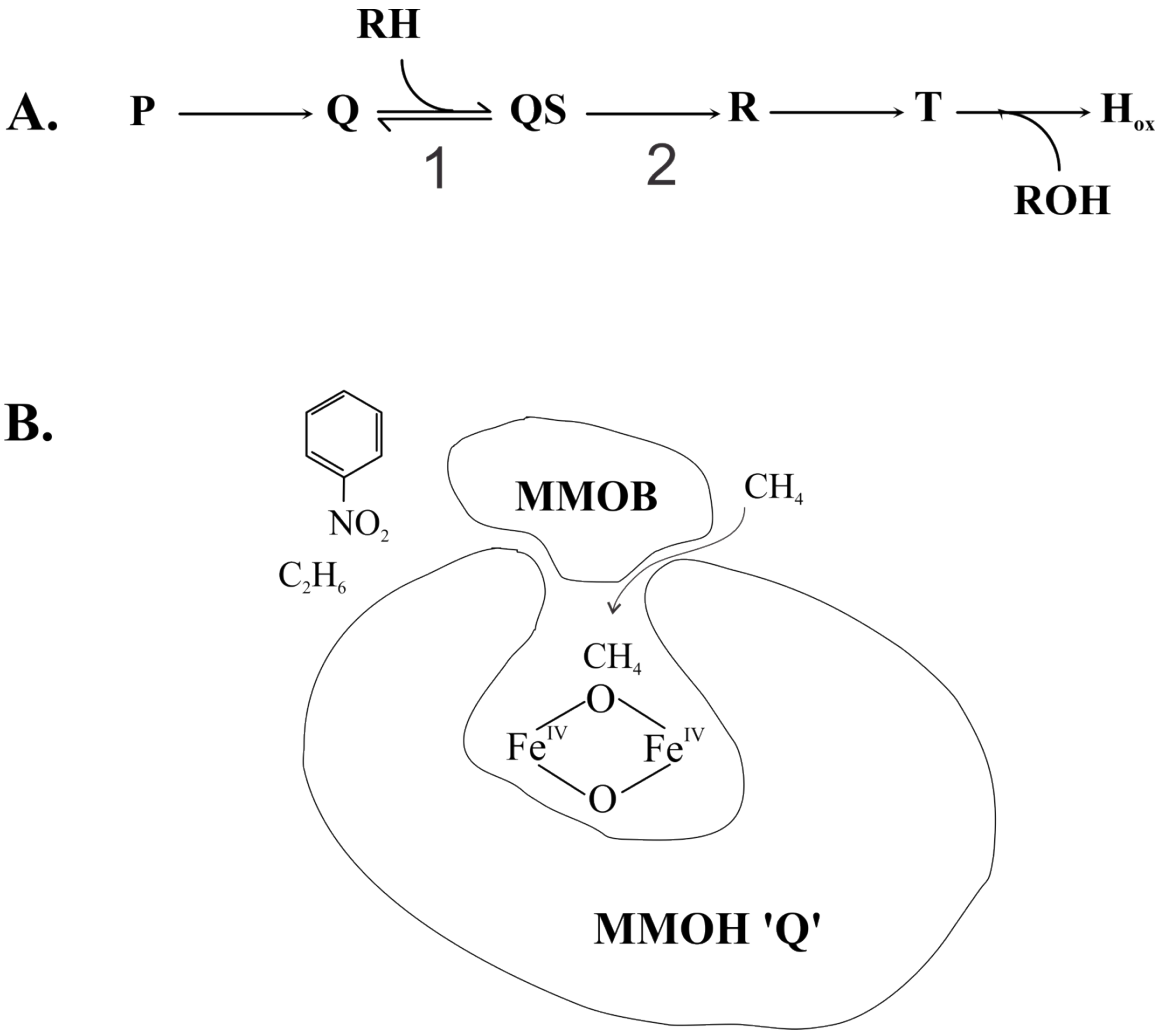

Figure 1.18 – A – The two-step **Q** decay mechanism for sMMO. The first step (1) involves substrate binding to the active site while the second step (2) is the C-H bond-breaking step leading to the formation of intermediate **R**. B – MMOB enforces a size-selective entrance to the active site that is suitable for small substrates like methane.

2. MMOB regulation of tunneling – It has been demonstrated that the hydrogen atom abstraction from methane by **Q** occurs through a quantum mechanical tunneling process [149]. This is evident in the large KIE in the kinetic step of **Q** decay with methane. The core N107G/S109A/S110A/T111A mutant of MMOB displays diametrically opposite effects on **Q** decay with large substrates (furan, nitrobenzene) and native methane. The second order rate constant for **Q** decay with methane decreases in the presence of this mutant MMOB. A further exploration of this adverse effect on methane hydroxylation revealed a lower value for KIE at 6.0 [159]. The decrease in KIE from 50.0 (tunneling range) to 6.0 (classical range) indicates that the tunneling nature of the hydrogen atom transfer reaction has been lost in the presence of the MMOB mutant. The primary requirement for hydrogen atom tunneling is a close donor-acceptor distance that provides an optimal overlap of the molecular wave function orbitals of the donor and acceptor molecules [160]. Accordingly, the protein complex of MMOH and MMOB possesses an active site geometry that enforces such an optimal positioning of the methane substrate with respect to **Q**. A mutation on MMOB changes the active site geometry leading to a modulation of the reaction coordinate and a loss of the tunneling contribution to the hydrogen atom transfer process. In summary, the regulatory MMOB protein enforces a preferential reactivity of **Q** towards methane by not only restricting the entry of larger substrates into the active site but also by careful positioning the methane substrate near **Q**, such that the hydrogen atom abstraction reaction can obtain the kinetic advantage of tunneling.

3. MMOB regulation through the N-terminal region – The N-terminal region of MMOB is important for sMMO catalysis as a deletion mutant abolishes steady state activity [161]. Among the substitution mutants, the H5A and the H33A mutants display a large decrease in the rate constant of formation of compound **Q** [157]. The H33A mutant displays the largest decrease and the transient kinetic studies show almost no accumulation of intermediate **P**. Accordingly, it has been reasoned that the H33A MMOB mutant decreases the rate constant of formation of **P** from **P***. The most plausible explanation for the decrease in rate constant is that the histidine residues on the N-terminal region of MMOB control proton transfer originating from bulk solvent to the active site. Thus, a loss of function substitution mutation adversely affects the pH dependent kinetic steps of **P** and **Q** formation.

4. MMOB regulation through the C-terminal region – The C-terminal region of MMOB is also implicated in the regulation of kinetic steps in the single turnover catalytic cycle. Deletion

mutants of this region decrease the rate constant of formation of intermediate **P** as well as lower the steady-state turnover number [162]. Moreover, these mutants result in a large uncoupling of the reaction owing to a loss of peroxide from, possibly, intermediate **P***. Thus the regulatory role of MMOB extends to ensuring a properly coupled turnover system to maximize product turnover and preventing the generation of toxic reactive oxygen species.

1.6 BIOMIMETIC OXYGEN CHEMISTRY

The ability of metalloenzymes to catalyze the oxidation of hydrocarbons under mild conditions with great stereo and regio-selectivity has spurred attempts to design synthetic catalysts to mimic the oxidative chemistry. These synthetic catalysts would be invaluable in catalyzing industrial chemical transformations on a large variety of compounds with tuned regioselectivity and stereospecificity. The mild conditions of the synthetic chemical reaction would spur "green chemistry" where environmentally friendly reagents replace hazardous chemical conditions, expensive metal-based oxidants and energy intensive processes. In addition, the synthetic chemical models provide a valuable information feedback towards understanding metalloenzyme mechanism. This is achieved primarily by providing a large library of chemical models and their respective spectroscopic fingerprints, based on which the physical and electronic structure of trapped enzyme intermediates can be refined.

The primary aim behind the design of synthetic biomimetic catalysts of sMMO has been the utilization of methane as an energy source. The natural reserves of methane both as a constituent in natural gas and in methane gas hydrates are immense and are comparable with the rapidly dwindling oil reserves [163, 164]. However, methane has been underutilized as an energy source on account of a lack of transportation facilities from foreign oilfields to centers of consumption. Liquefaction of methane for transport is very expensive. One current means to utilize methane is through an indirect production of 'synthesis gas' that involves a high temperature, high pressure mixture of carbon monoxide (produced from CH_4) and hydrogen [164]. The synthesis gas is used as an intermediate in the industrial production of hydrogen, ammonia and synthetic liquid fuel through the Fisher-Tropsch process. As a partial oxidation product of methane, methanol can also be used as an energy source. And in contrast to methane, methanol has the additional advantage of cost-effective transportation and an ability to be used as a fuel for internal combustion engines [165]. Thus an indirect utilization of methane through a controlled oxidation to methanol could be a more efficient and cost-effective process.

The literature on synthetic diiron model compounds is quite rich. The primary benefit of these models to the biochemical inquiry of sMMO is the provision of spectroscopic fingerprints for a variety of synthetic models. A comparison of the experimental spectroscopic measurements on sMMO intermediates with these models refines the description of the sMMO intermediates. The

diiron synthetic model compounds can be classified into two categories: i) carboxylate-rich ligand sets that provide a high-spin iron center, which is a better mimic of MMOH, ii.) nitrogen-rich ligand sets that enforce a low-spin state on the iron atoms. The nitrogen-rich MMOH model complexes have, however, been more successful in trapping activated oxygen species that mimic the proposed intermediates in sMMO.

There are two reported model compound examples of a diiron superoxo intermediate. The first one is observed in a carboxylate-rich ligand set diiron model upon a reaction of the diferrous model with oxygen [166]. Mössbauer and XAS spectroscopies have characterized it as a superoxo intermediate although a definitive Resonance Raman characterization of an oxygen-sensitive band was not obtained. The other diiron superoxo model compound was trapped in a nitrogen-rich ligand set environment and characterized by Resonance Raman spectroscopy [167]. This intermediate was additionally observed to convert to a hydroperoxo diiron species. Although the presence of a superoxo intermediate in the sMMO catalytic cycle has not yet been confirmed, the identity of the **P*** intermediate in sMMO has not been probed sufficiently to rule out a possible superoxo-bound diiron structure.

The peroxo species is the most frequently prepared intermediate in the synthetic diiron model compounds [168-170]. The peroxo binding mode to the iron atoms is a cis-μ-1,2 geometry. These peroxo intermediates approximate closely the 700 nm absorption band and the isomer shift of the iron atoms in intermediate **P** [170].

The formation of high valent iron model compound intermediates as mimics of **Q** has been a difficult task. The closest attempts have been made in the nitrogen-rich ligand set model compounds, as the electron-rich ligands are able to stabilize the high valent iron atoms. The synthetic model that approximates the structure of **Q** the closest, is the bis-μ-oxo diiron(IV) intermediate of the starting $[Fe_2(\mu\text{-}O)_2L_2]$ complex (L = tris(3,5-dimethyl-4-methoxypyridyl-2-methyamine)) **1** (Figure 1.19) [171]. The Mössbauer spectrum of this intermediate indicates that both the iron atoms are in their low-spin +4 oxidation state. This prevents a direct comparison of the Mössbauer parameters with **Q** on account of the difference in spin state. The presence of a resonance Raman band at 674 cm^{-1} is indicative of a bis-μ-oxo diamond core structure [172].

Although this model compound has an optical absorption feature similar to **Q**, the Fe-Fe distance at 2.73 Å is larger than the 2.5 Å distance measured in **Q** [99].

An interesting observation is made upon a comparison of the reactivity of the above **Q** mimic and a low-spin mononuclear Fe(IV)=O synthetic model towards hydrogen atom abstraction reactions [171]. The closed core [$Fe_2(\mu\text{-}O)_2$] model proved to be 100-fold less reactive than the mononuclear counterpart despite having a larger reduction potential. Further light was shed on this unexpected observation with the generation of two high valent diiron synthetic models. These are a low-spin, open-core [OH-Fe^{IV}-O-Fe^{IV}=O] model **2** and a high-spin, open-core [OH-Fe^{III}-O-Fe^{IV}=O] model **3** (Figure 1.19) [173, 174]. A comparison of the hydrogen atom abstraction reactivity between **1** and **2** showed that **2** was a 100-fold more reactive than **1**. Considering the similarities in the oxidation state and spin state of the iron atoms, the higher reactivity of **2** was reasoned to arise from the presence of the terminal oxoiron moiety. A bridging oxo group is thus less reactive than a terminal oxo group towards hydrogen atom abstraction. The comparison of reactivity between **2** and **3** showed that **3** was a 1000-fold more reactive than **2**. The high-spin state of the iron atoms was reasoned to account for the higher reactivity of **3**. The greater reactivity of the high-spin state of iron atoms is corroborated by theoretical density functional calculations [175, 176]. Considering that the iron atoms in **Q** already have a high-spin state, the interesting implication from these model compound studies for sMMO is the possibility for the closed diiron core of **Q** opening up to provide terminal Fe=O groups. This open-core isomer form of **Q** would then be the truly reactive intermediate in the sMMO catalytic cycle.

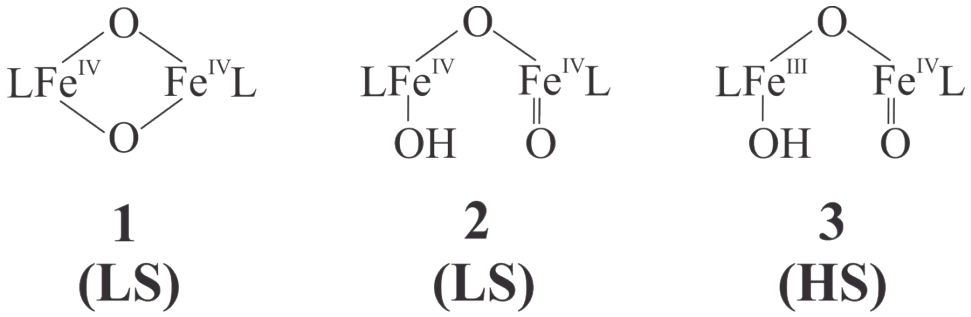

L = tris((4-methoxy-3,5-dimethylpyridin-2-yl)methyl)amine

Figure 1.19 – The open and closed core diiron synthetic model compounds. The spin states of the iron atoms differ between these model compounds (LS = low spin, HS = high spin).

1.7 SCOPE OF THE PRESENT WORK

Research on sMMO in the last two decades has elucidated significant aspects of the chemical mechanism of this enzyme. A structural description is now available for the individual protein components of the multi-protein complex and the diiron active site. Insight has also been obtained into the catalytic cycle of sMMO with the isolation and characterization of two intermediates. A notable discovery has been that of compound **Q**, which is the presumed reactive intermediate in the catalytic cycle. The regulation of the catalytic cycle, conferred through the protein complex of MMOH and MMOB, has provided a significant contribution to diiron oxygenase research. In spite of these advances, there remain key questions about the catalytic cycle of sMMO that preclude a complete understanding of its catalysis:

- How does the diiron cluster bind and activate oxygen, which leads to the formation of the peroxo intermediate **P**? The characterization of compound **P***, which lies between **O** and **P** in the catalytic cycle, would be crucial towards understanding oxygen activation in diiron oxygenases.
- What is the electronic and geometric structure of compound **P** in sMMO? A comparison of **P** with other peroxo intermediates observed in related diiron enzymes, with consideration of the second sphere residues, is crucial towards explaining the exclusive observation of compound **Q** in sMMO. This is pertinent, considering that recently reported catalytic models suggests that the peroxo intermediate is the reactive species in T4mo and TOMO [177, 178].
- Does the conversion from **P** to **Q** involve a heterolytic or homolytic cleavage of the O-O bond of oxygen?
- What is the electronic and geometric structure of compound **Q** in sMMO, based upon experimental data of the Fe-O vibrational bonds obtained through either NRVS or resonance Raman spectroscopy?
- What is the identity of the proposed intermediate **QS** based upon the two-step **Q** reactivity model?
- What is the structure of the active site in the catalytically relevant MMOH:MMOB protein complex, *in crystallo*?
- How is the electron transfer from MMOR regulated, such that the diferric resting state of MMOH is reduced exclusively where the highly oxidized compound **Q** state is not?

The research conducted under the ambit of this doctoral thesis, has attempted to answer some of the aforementioned questions regarding sMMO catalysis. Some of these attempts have been successful in expanding our understanding of the chemical mechanism of sMMO and is described in detail in the following chapters.

Chapter 2 explores the causes for lowered and variable activity in MMOH protein preparations. A detailed study of this phenomena addresses a long-standing issue in the sMMO research field, which manifests itself in a lower than expected yield of catalytic intermediates during single turnover reactions. The variability in the fraction of active MMOH enzyme in the protein purifications appears to originate during expression in *M. trichosporium* OB3b. A partial remedy has been described that led to a significant improvement in the fractional amount of active enzyme. Although MMOH specific activity has not yet been restored to its maximal reported value, this chapter provides important information that should be utilized in future attempts to enhance the activity of MMOH.

Chapter 3 encompasses experimental data describing the isolation of compound **P*** in the catalytic cycle of sMMO. While the existence of **P*** has been previously implied by kinetic models incorporating the pH dependence of catalytic steps, the use of the H33A MMOB mutant and excess substrate to quench **Q** has allowed optical observation of the formation and decay of this intermediate. Mössbauer spectroscopy has further characterized **P*** to be a diferrous species. **P*** is distinct from compound **O** and $\mathbf{H}^{\mathbf{red}}$, inasmuch as it lacks a $g = 16$ integer spin EPR signal. A detailed characterization of **P*** will prove invaluable towards completely elucidating the manner of oxygen activation in diiron oxygenases.

Chapter 4 describes the resonance Raman spectrum of compound **Q**. More detailed vibrational structure information on **Q** has been sorely lacking since its initial discovery in 1993. This chapter builds upon promising preliminary data obtained by Dr. Jeremy Nesheim in collaboration with Dr. Gerald T. Babcock at Michigan State University (MSU). In continuation of the collaboration, presently with Dr. Proshlyakov at MSU, the resonance Raman spectrum for **Q** has been obtained using a time-resolved resonance Raman technique.

Chapter 5 includes very interesting preliminary information on another sMMO catalytic intermediate termed as **Q'**, which follows **Q** in the catalytic cycle. The hitherto undiscovered intermediate possesses a distinct electronic absorption spectrum from **Q**. More importantly, **Q'** is catalytically competent and reacts with substrates with a similar rate constant as has been previously attributed to **Q**. The kinetic data suggests that **Q'** might be the actual reactive intermediate in sMMO. Preliminary information from resonance Raman studies also supports the presence of an intermediate following **Q** in the reaction cycle of sMMO. The confirmation of **Q'** as the true reactive intermediate in sMMO would have a profound impact on the diiron oxygenase research field.

CHAPTER 2

An investigation into the less than expected yield of Q from the single turnover reaction of MMOH

2.1 INTRODUCTION

The key to elucidating the chemical mechanism of methane oxidation performed by sMMO lies in the detailed electronic and structural characterization of compound **Q**. Mössbauer and X-ray absorption spectroscopy have together contributed to our current description of **Q** as a bis-μ-oxo-$Fe(IV)_2$ species [99, 102]. However, there still remain some significant questions regarding the following characteristics of **Q**: i) the coordination geometry of the iron atoms, ii) the origin of the oxygen atoms of the bridging-oxo moieties which may derive from either molecular oxygen or a combination of molecular oxygen and a solvent water molecule, and iii) the degree of asymmetric binding of the bridging-oxo groups in the diamond core structure of **Q**. These questions can be addressed by additional spectroscopic techniques like Resonance Raman, Magnetic Circular Dichroism (MCD) and Nuclear Resonance Vibrational Spectroscopy (NRVS). Furthermore, there has been a wealth of spectroscopic information obtained from more recent and improved synthetic model compound mimics of **Q** [171, 173, 174, 179]. Since these model compounds provide a library of spectroscopic fingerprints, a comparison with **Q** would be essential towards a complete and detailed electronic and structural characterization.

The catalytic cycle of sMMO is unique because it can be initiated in the absence of substrates. The kinetic steps prior to the formation of **Q** do not depend upon substrate while the decay rate constant of **Q** shows an apparently linear dependence on substrate concentration [94]. In the absence of substrate, the kinetic rate contants for formation and auto-decay of **Q** predict an accumulation of **Q** to almost 90 % of the enzyme active sites at its t_{max} in the single turnover reaction (Figure 2.1). Accordingly, **Q** is theoretically a readily accessible intermediate to trap by a freeze-quench method. However, repeated attempts at detailed Mössbauer studies of **Q** in the last decade have been unsuccessful on account of very low accumulation of the intermediate. A similar trend of low **Q** accumulation has been observed in the stopped flow single turnover optical studies. The **Q** yield (maximum **Q** concentration at t_{max}) is obtained by a measurement of the observed **Q** accumulation based upon its extinction coefficient (ε_{430} = 7500 M^{-1} cm^{-1}) and normalizing it by the expected amount of intermediate that would accumulate under the experimental conditions and the previously measured kinetic rates of formation and decay. Since the initial observation and characterization of this intermediate [94], the **Q** yields have been decreasing in succeeding transient kinetic studies (Table 2.1). This problem of low **Q** yields has also been observed in the sMMO enzyme purified from *M. capsulatus* (Bath) [100] (Table 2.1).

Lower than theoretically predicted accumulation of **Q** appears to correlate with the specific activity of the hydroxylase protein (MMOH). MMOH protein samples displaying low **Q** accumulation consistently report a low specific activity in comparison to protein samples with the highest reported activity values [92]. The specific activity of MMOH has been observed to be especially variable between the multiple reported purifications of this protein from *M. trichosporium* OB3b [81, 92, 180-182] and *M. capsulatus* Bath [100, 115, 142, 183]. This is indicative of a long-standing problem in the sMMO research field that is manifested in the low amount of accumulation of intermediates in the catalytic cycle and has possibly stymied the complete characterization of compound **Q**.

As a part of this thesis research, we have been able to dissect this problem and attribute it to two causes. The primary factor is the *M. trichosporium* OB3b cell growth conditions. The secondary cause is the existing protein purification protocol for MMOH, which, in addition to lowering the specific activity, also results in an altered optical absorption spectrum of the protein. Modifications to the growth conditions of *M. trichosporium* OB3b and MMOH purification have led to a two-fold increase in the specific activity of MMOH and **Q** yields, although an optimal solution to the primary cause has not yet been devised.

Q Maximal Accumulation (%)	Reference
MMOH (*M. trichosporium* OB3b)	
90	[94]
68	[81]
42	[157]
19	[158]
20	[162]
MMOH (*M. capsulatus* Bath)	
48	[143]
42	[142]
32	[100]

Table 2.1 – The percent yield of **Q** has been calculated on the basis of the observed absorbance change at the λ_{max} (430 nm for *M. trichosporium* OB3b and 420 nm for *M. capsulatus* Bath) with normalization to the expected amount of **Q** based upon the protein concentration and rate constants of **Q** formation and decay.

2.2 MATERIALS & METHODS

Chemicals - All common reagents and chemicals were of the highest grade available and were obtained from Sigma. The chromatography resins were obtained from GE Healthcare. Water is deionized and purified further by passage through a Millipore SuperQ system.

Bacterial growth - MMOH was obtained from *M. trichosporium* OB3b, which was grown according to a previously published protocol [184]. MMOB was obtained from a recombinant expression system in *E. coli* as previously described [157]. A recombinant expression system in the BL21(DE3) strain of *E. coli* has also been developed for MMOR by Dr. John Broadwater. The *mmoC* gene encoding MMOR was PCR amplified from pDVC202 [185] and ligated into a pET29 plasmid using the restriction enzymes NdeI and HindIII. *E. coli* BL21(DE3) cells transformed with this plasmid were cultured in LB media containing 50 μg/ml kanamycin at 37 °C. The MMOR protein expression was induced with 0.3 mM IPTG when the OD at 600 nm reached 0.7 - 0.9. The growth was continued for 3.5 hours at 37 °C following which the cells were harvested and pelleted by centrifugation at 9000 × g for 10 minutes.

sMMO protein purifications - Hydroxylase – The MMOH purification protocol is based upon the original purification scheme [184] with the key improvements being an anaerobic process and an altered second chromatographic step. Anaerobic conditions were achieved through a nitrogen purging assembly consisting of a bottle-top screw cap lid with a purging line for nitrogen equipped with a sparger and a liquid outlet line for withdrawing buffer. The buffers containing $Fe(NH_4)_2SO_4.6H_2O$ and cysteine as a stabilizer for the active site iron were left to age for 3 hours at 4 °C, at which point, the purple color of the buffers had disappeared. This was followed by nitrogen purging for at least an hour before use and continuing into the time of utilization of the buffer in the purification. The three 200 ml volumes of buffer that were added to the cells to make up the cell free extract contained 100 μM $Fe(NH_4)_2SO_4.6H_20$ and 1.4 mM cysteine, in contrast to the rest of the buffers which contained 200 μM $Fe(NH_4)_2SO_4$ and 2.0 mM cysteine. These three volumes of buffer were also not subjected to nitrogen purging. All chromatography columns were equilibrated with nitrogen-purged anaerobic buffers before equilibration with the iron-cysteine containing anaerobic buffers. The steps of cell sonication and centrifugation to obtain the cell free extract were performed as in the original purification scheme. The cell free extract was then allowed to batch bind to the fast flow DEAE Sepharose (Sigma DFF-100) resin for 25 minutes at

4 °C. The protein-bound resin was poured back into the column and washed with one column volume of equilibration buffer at a linear flow rate of 22 cm/hr. The methane monooxygenase components were eluted according to the original protocol at a linear flow rate of 10 cm/hr. The eluent fractions containing MMOH were collected in argon purged sealed glass vials in order to maintain anaerobic conditions. The pooled fractions were subsequently concentrated by ultrafiltration. The subsequent steps of the new purification scheme differed completely from the original scheme. The concentrated DEAE pool was desalted through a Sephadex G-25 column (3 × 22 cm) that was developed under anaerobic conditions with 25 mM MOPS, pH 6.8 and collected in argon-purged sealed glass vials. The next purification step replaced the size-exclusion chromatography step, as in the original scheme, with a high-resolution ion-exchange chromatography step. An additional oxygen-scrubbing step was performed on the second ion-exchange column with the passage of 20 ml of 5.0 mM sodium hydrosulfite solution under anaerobic conditions. The desalted protein pool was applied to this high-resolution Q Sepharose (Sigma Q1754) column (3 × 12 cm) equilibrated with 25 mM MOPS, pH 6.8 under anaerobic conditions. The protein-bound column was subsequently washed with 50 ml of equilibration buffer. MMOH was eluted with a 900 ml gradient from 0 to 0.08 M NaCl in the same buffer at a linear flow rate of 23 cm/hr. The MMOH protein elutes at a NaCl concentration of 0.035 M and was collected in argon-purged sealed glass vials. The hydroxylase fractions were assayed with the nitrobenzene steady state assay method [158], pooled and concentrated via ultrafiltration. Glycerol was added to a final concentration of 5% (v/v) to the MMOH protein pool. The concentrated protein was frozen in liquid N_2 and stored at -80 °C.

sMMO Component B – The purification of recombinantly expressed MMOB and its mutants was performed as previously described [162]. A minor change was implemented during the screening of eluent fractions for MMOB. The eluent fractions of MMOB were pooled on the basis of the ratio of absorbance at 280 nm and 290 nm. Ratios with a value > 1.45 indicate the presence of a population of MMOB that have truncated N and C – terminal ends (confirmed by SDS gels and ESI-MS – Molecular weight = 10123 Da). This non-native population of MMOB has a higher ratio of absorbance than fully intact MMOB (A_{280}/A_{290} = 1.43) and elutes as a shoulder at the front end of the native MMOB protein peak.

sMMO Reductase – The purification of recombinantly expressed MMOR was accomplished through an anaerobic refolding method from inclusion bodies, developed by Dr. John

Broadwater. The cell pellet (10 g) was resuspended in 50 mM HEPES buffer, pH 8.0 followed by sonication to break open the cells. The cell lysate was incubated with DNAse I (0.2 mg/g cells) for 15 minutes at 4 °C. Triton-X100 and NaCl were subsequently added to a final concentration of 1% (v/v) and 0.5 M respectively. After incubation for 20 minutes at 4 °C, the solution was centrifuged at 40000 × *g* for 30 minutes. The pellet containing the inclusion bodies was resuspended in 50 mM HEPES buffer, pH 8.0 and spun down again by centrifugation in order to remove the excess detergent. The pellet was then resuspended in 15 ml of 50 mM HEPES buffer, pH 8.0, 8.0 M urea. This suspension was stirred for 30 minutes at room temperature to ensure complete solubilization of the protein. Any insoluble material was removed by centrifugation at 40000 × *g* for 15 minutes. DTT (0.1 M) and FAD (8 mg) were added to the supernatant. This mixture was made anaerobic in a sealed Wheaton bottle through gentle vacuum/argon cycles while chilled on ice. 100 μl aliquots of the following anaerobic solutions were added to the unfolded protein solution: i) 200 mM $Fe(NH_4)_2(SO_4)_2$, ii) 200 mM $FeCl_3$, iii) 200 mM Na_2S. The unfolded protein solution was incubated with the iron and sulfur reagents for 15 minutes on ice. This solution was then added in an anaerobic fashion, dropwise, to 180 ml of cold, anaerobic 50 mM HEPES buffer, pH 8.0 in order to refold the MMOR protein. This solution was subsequently loaded on a DEAE Sepharose (Sigma DFF100) column (12 × 2.5 cm) equilibrated with 25 mM MOPS, pH 7.0, 5.0 mM sodium thioglycolate. The column was washed with 3 column volumes of equilibration buffer containing 0.1 M NaCl. The MMOR protein was eluted with a 500 ml gradient from 0.1 M NaCl to 0.5 M NaCl in the equilibration buffer at a linear flow rate of 8 cm/hr. The fractions containing MMOR were pooled on the basis of its characteristic absorption spectra [92] and the ratio of absorbance at 458 nm and 340 nm (between 1.3 and 1.6). The A_{458}/A_{340} ratio was used to distinguish between the completely reconstituted MMOR ([2Fe-2S]/FAD) and MMOR reconstituted with only the FAD cofactor. The protein pool was concentrated and loaded onto an Ultrogel AcA-54 column (40 x 2.5 cm) equilibrated in 25 mM MOPS, pH 7.0, 5 mM sodium thioglycolate. MMOR was eluted off the column with the same equilibration buffer at a flow rate of 5 cm/hr. The fractions containing MMOR were again pooled on the basis of its absorption spectra and A_{458}/A_{340} ratio. The protein was concentrated along with glycerol as a cryo-protectant (5% v/v). It was frozen and stored at -80 °C.

Enzyme activity assay - Gas chromatographic and polarographic assays of sMMO activity were performed as previously reported [184]. Experiments probing the MMOH:MMOB protein

complex formation utilized nitrobenzene as a substrate while measuring the formation of the colored *p*-nitrophenol product [158] at 404 nm. Protein concentration was measured by using the following extinction coefficients for the sMMO protein components – MMOH (ε_{280} = 539 mM^{-1} cm^{-1}), MMOB (ε_{280} = 20.8 mM^{-1} cm^{-1}) & MMOR (ε_{458} = 18.6 mM^{-1} cm^{-1}) [92, 184].

Transient kinetics experiments - Pre-steady state transient kinetic experiments were performed on an Applied Photophysics stopped flow instrument (SX.18MV with a SX Pro-Data upgrade). MMOH was made anaerobic under a constant stream of argon gas, following which it was transferred into a Coy anaerobic glove bag for further manipulations. It was chemically reduced with an excess of methyl viologen (mediator) (1X) and sodium hydrosulfite (10X) for 20 minutes at room temperature while stirring. The reductant system was then separated from MMOH by passage through a Sephadex G-25 PD-10 column (GE Healthcare). This desalting column was pre-equilibrated with 50 mM MOPS buffer at the desired pH containing 200 μM $Fe(NH_4)_2SO_4.6H_2O$ and 2 mM cysteine (aged at 4 °C until the purple color had dissipated). The reduced MMOH was loaded into one of the drive syringes on the stopped flow instrument via a gas-tight syringe (Hamilton). The second drive syringe contained a stoichiometric amount of MMOB (1:1 to MMOH active sites) in oxygen-saturated buffer (saturated at the temperature utilized in the experiment). Single turnover experiments with substrates required the addition of the substrate to the MMOB and oxygen-saturated buffer containing drive syringe. The single wavelength transient kinetic data were analyzed with the Pro-Data Viewer software (Applied Photophysics). The simulation of a single turnover MMOH reaction time course was performed using the program KSIM (Dr. Neil C. Millar (Kings College, London)).

Freeze-quench EPR/Mössbauer experiments - The reduced MMOH protein was prepared in a similar manner as described for transient kinetic experiments. The MMOB protein was added to MMOH in the appropriate stoichiometry (1:1 MMOB:MMOH active sites) under anaerobic conditions. This protein complex was loaded into one of the rapid freeze quench (RFQ) syringes in the anaerobic glove bag. The other RFQ syringe contained oxygen-saturated buffer. The RFQ syringes were loaded on an Update Instrument model 1019 RFQ apparatus. A low-temperature bath circulator (Neslab LT-50) maintained the reactants at a temperature of 4 °C. The RFQ samples were made by freezing the reaction mixture (1:1 mixing of the reactants from both RFQ syringes) at defined time points using calibrated aging hoses on our custom designed freeze-

quench apparatus [186]. Briefly, the freeze-quench device includes two liquid nitrogen chilled, counter-rotating aluminum cylinders. The aged solutions freeze when shot onto the top of the cylinders. The counter-rotating cylinders crush the frozen material into a powder that collects below in a liquid nitrogen filled cup. The frozen powder was then packed into either EPR tubes or RFQ Mössbauer cups. EPR spectra were recorded using a Bruker Elexsys E-500 spectrometer. EPR data were analyzed using the Spincount software from Dr. Hendrich (Carnegie Mellon University, Pittsburgh). The Mössbauer data were collected and then analyzed by Katlyn Meier in Dr. Eckard Münck's laboratory (Carnegie Mellon University, Pittsburgh).

Mass-spectrometry – The mass-spectrometric characterization of MMOH and MMOB was obtained at the Center for Mass Spectrometry and Proteomics facility at the University of Minnesota.

MMOB affinity column purification of MMOH – The Ala62Cys (A62C) mutant of MMOB was used to prepare an MMOB affinity column. A62C MMOB in a working concentration range of 250 – 500 μM was treated with a 10-fold excess of Tris(2-carboxyethyl)phosphine hydrochloride (TCEP) at 4 °C for 1 hour. It was subsequently separated from TCEP by passage through a Sephadex G-25 PD-10 desalting column. This desalting step was also used to exchange the protein buffer to 25 mM Tris pH 7.5. The MMOB protein was then allowed to bind to the activated thiol-linked Sepharose 4B (GE Healthcare) resin at 4 °C for 14 hours with stirring. The suspension was subsequently poured into a column (1 X 6 cm) and the unbound protein washed off with 25 mM MOPS buffer pH 7.0. The amount of unbound MMOB protein in the wash and flow-through was measured and a comparison with the starting amount of MMOB provided a quantitative value for the amount of resin linked MMOB protein. The MMOB charged resin was then resuspended in anaerobic equilibration buffer (25 mM MOPS, pH 7.0, 0.1 mM $Fe(NH_4)_2SO_4$, 1.0 mM cysteine). A 12-fold excess (over resin-bound MMOB) of MMOH protein active sites was added to the MMOB affinity resin in an anaerobic fashion and the batch binding process was allowed to continue for 1.5 hours at 4 °C. This suspension of MMOB affinity resin was packed into a column (1 X 6 cm) and washed with anaerobic buffer (25 mM MOPS, pH 7.0, 0.1 mM $Fe(NH_4)_2SO_4$, 1.0 mM cysteine). The bound MMOH protein was eluted off the column in a stepwise manner with elution buffer (25 mM MOPS, pH 7.0, 0.1 mM $Fe(NH_4)_2SO_4$, 1.0 mM cysteine, 0.6 M NaCl). The protein containing eluent fractions were pooled and concentrated.

2.3 RESULTS

2.3.1 Characterization of low specific activity hydroxylase protein

Steady-state and single-turnover activity of MMOH - The specific activity values for MMOH has varied between 180 – 650 nmoles/min/mg with furan and between 250 – 900 nmoles/min/mg with propylene for the multiple preparations performed for this enzyme in the course of this thesis research. In comparison to the highest reported specific activity values of 1200 nmoles/min/mg with furan and 1700 nmoles/min/mg with propylene [184], these MMOH protein samples display a fraction of its maximum activity (17 – 60 %). The large variation in the specific activity of MMOH preparations has been previously observed in the hydroxylase purified from both *M. trichosporium* OB3b [68, 81, 139, 181] and *M. capsulatus* Bath [100, 115, 142, 183].

In contrast to steady-state activity, pre-steady state transient kinetic studies can follow a single turnover catalytic cycle of sMMO. The single turnover cycle is a simpler system within which the low specific activity of MMOH can be investigated, as this reaction utilizes a protein complex of MMOH and MMOB in the absence of MMOR. We are primarily interested in the accumulation of compound **Q** in the single turnover reaction of MMOH. Based upon the known rates of formation and decay of this intermediate, a simulation of the catalytic cycle predicts an accumulation of **Q** to almost 90 % of MMOH active sites at 4 °C and the absence of substrate (Figure 2.1). However, MMOH protein with a specific activity of 226 nmoles/min/mg (MMOH_226SpA) and 470 nmoles/min/mg (MMOH_470SpA) with furan, consistently display an accumulation of **Q** to only 17 % and 37 % of active sites, respectively (Figure 2.2). This estimation is based upon the measured extinction coefficient of **Q** at 430 nm (ε = 7500 M^{-1} cm^{-1}) [94]. It is important to note that this extinction coefficient was measured from a single turnover reaction of MMOH having the highest reported specific activity. The accumulation of **Q** with these MMOH protein samples is lower than seen in previously reported optical measurements [81, 94]. Some potential causes of low **Q** accumulation are: i) incomplete chemical reduction of MMOH, ii) presence of excess reduced sodium dithionite that quenches **Q** during the reaction, and iii) presence of substrate. These first two concerns have been addressed and discounted by a new chemical reduction protocol for MMOH, which ensures a complete reduction of MMOH by using excess sodium dithionite and stoichiometric methyl viologen for a duration of 20 minutes at room temperature. These small molecule chemical reductants are then separated from reduced MMOH by passage through a desalting column under anaerobic conditions in an anaerobic glove

bag. The presence of substrate in the single turnover reaction is easily diagnosed by following the decay rate constant of **Q**, which accelerates in its presence. This rate constant of decay is similar to the autodecay of **Q** in the absence of substrates for the MMOH preparations showing low **Q** accumulation [94]. Thus, the cause of the low yield of **Q** must originate within the purified protein rather than the reduction scheme or experimental conditions of the single turnover reactions.

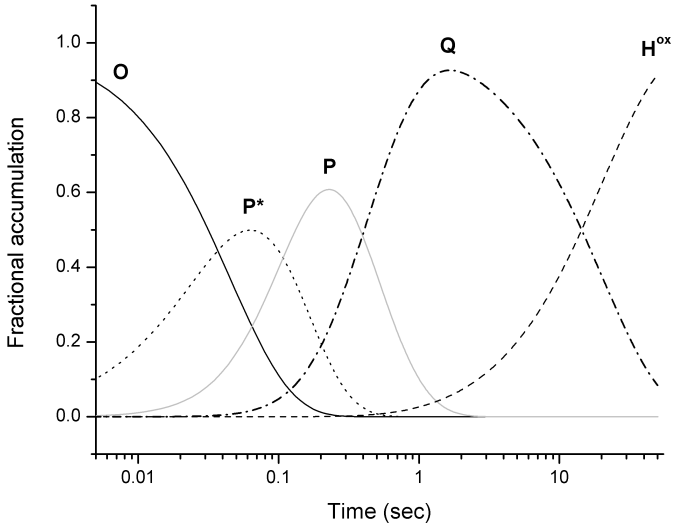

Figure 2.1 – Time course of a single turnover reaction of sMMO depicting the accumulation of intermediates in the catalytic cycle. The kinetic model for the single turnover reaction is **O → P* → P → Q → H^{ox}** where $k_1 = 26\ s^{-1}$, $k_2 = 11\ s^{-1}$, $k_3 = 2.7\ s^{-1}$, $k_4 = 0.05\ s^{-1}$ at 4 °C and pH 7.0 [97]**.**

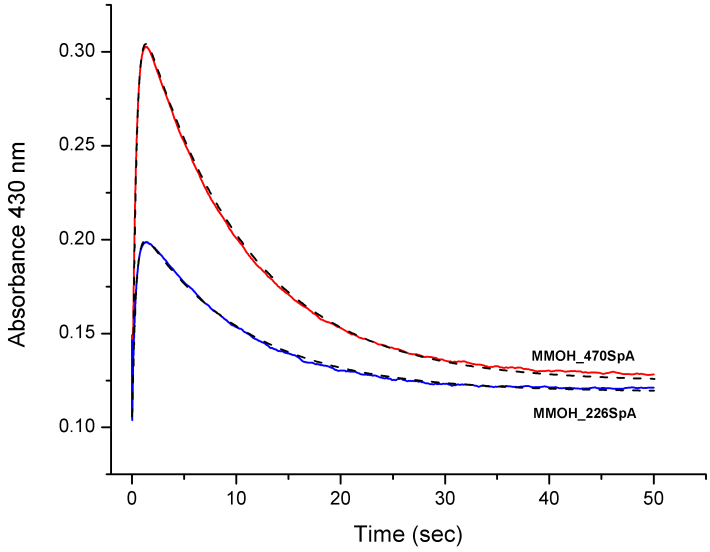

Figure 2.2 – Time course of a single turnover reaction followed at 430 nm with two MMOH protein batches MMOH_470SpA (red trace) and MMOH_226SpA (blue trace). A simulation (black trace) is performed on both of the kinetic data based upon the model described in Figure 2.1, the extinction coefficients of the intermediates in the catalytic cycle and the amount of enzyme used. The simulation has been normalized by a factor of 0.17 for MMOH_226SpA and 0.37 for MMOH_470SpA in order to match the experimental data. These values of 0.17 and 0.37 thus represent the fractional turnover in the respective catalytic cycles of the two MMOH protein batches.

Single turnover reaction of sMMO observed through Mössbauer spectroscopy – The optical observation of a low yield of **Q** is corroborated by Mössbauer studies of the single turnover reaction of MMOH in the presence of MMOB. An RFQ Mössbauer sample prepared at a time point close to the t_{max} for **Q** accumulation indicates that only 18 % of the total enzyme active site iron is associated with compound **Q** (site 1; δ = 0.17 mm/s; ΔE_Q = 0.53 mm/s) (Figure 2.3A). The majority of the remaining active site iron atoms are present in the diferrous state (72 %). A small population of active site iron is present in a diferric state that was not reduced by the chemical reduction scheme employed (site 2 & 3, total 20 %). The Mössbauer parameters for this diferric population are, however, quite different from the resting diferric state of the enzyme observed with more active enzyme (δ = 0.50 mm/s; ΔE_Q = 0.87 mm/s) and hence presumably arises from a non-native population of MMOH [102]. The diferrous active site population is still present in almost 26 % of enzyme active sites at a later time point of 8 seconds (Figure 2.3B). This observation for a long-lived diferrous population is at odds with the simulation for the single turnover reaction, which indicates that the diferrous state of the enzyme should completely decay by 120 milliseconds (Figure 2.1). The Mössbauer sample for the endpoint of the single turnover reaction (10 min) describes two populations of diferric active sites (Figure 2.3C). The native diferric population is associated with 38 % of the total active site iron (site 1) while the other non-native population accounts for the remaining amount (site 2 & 3). The fraction of native diferric enzyme population correlates quite closely with the expected amount of reactive enzyme based upon the specific activity of MMOH used in this experiment (430 nmoles/min/mg with furan). This specific activity is 36 % of the maximal specific activity observed for MMOH (1200 nmoles/min/mg with furan). It is important to mention that the amount of oxygen available for the RFQ single turnover reaction (850 μM) was in excess of the enzyme active sites (740 μM). In summary, the Mössbauer studies provide the following conclusions: i) the low **Q** yields arise because only a small fraction of the enzyme active sites turn over with previously observed kinetic rates, and ii) the non-native fraction of the enzyme is characterized by a slow oxidation of the diferrous cluster.

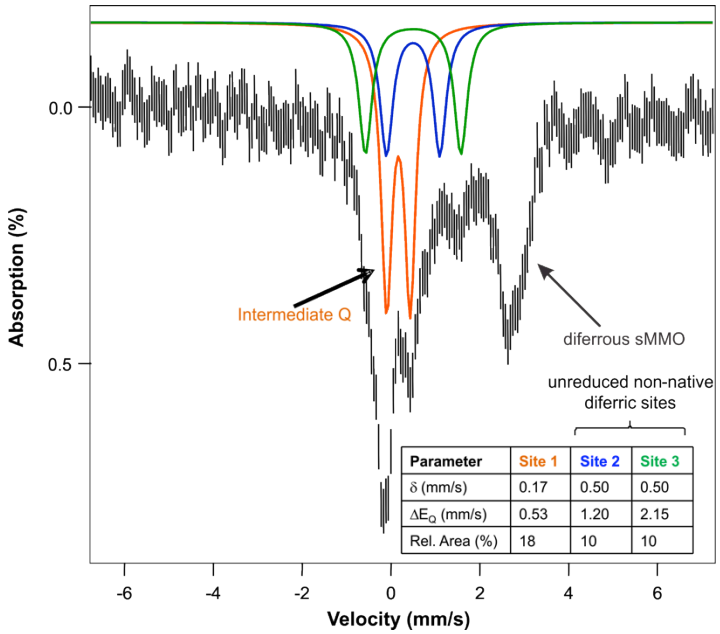

Figure 2.3A – Mössbauer spectrum and fits of a single turnover reaction of MMOH trapped at 1 sec (4 °C, pH 7.0). The spectrum is comprised of 18 % **Q** (site 1), two non-native diferric active sites (sites 2 & 3, total 20 %) and 68 % diferrous active sites.

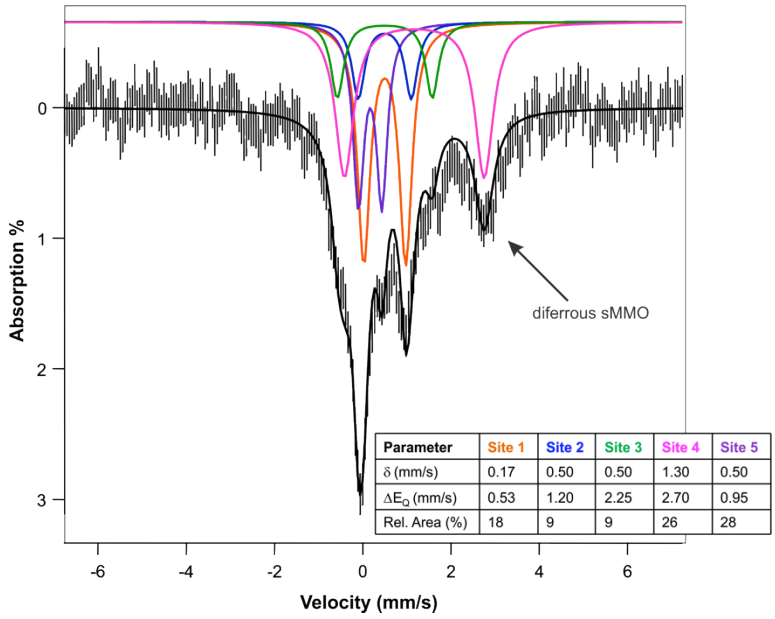

Figure 2.3B – Mössbauer spectrum and fits of a single turnover reaction of MMOH trapped at 8 sec (4 °C, pH 7.0). Sites 1 – 3 are as Figure 2.3A. Site 4 is associated with diferrous active sites while site 5 is associated with the resting diferric state of sMMO.

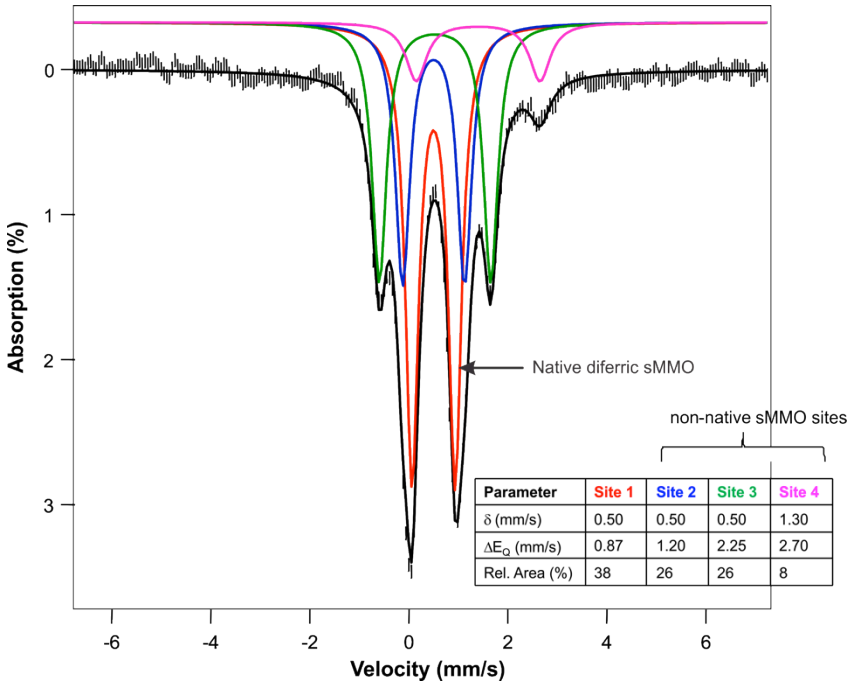

Figure 2.3C – Mössbauer spectrum and fits of a single turnover reaction of MMOH trapped at 600 sec at 4 °C, pH 7.0 (endpoint of reaction). Site 1 is associated with the native resting diferric form of the enzyme. Sites 2 and 3 arise from a non-native diferric form on the enzyme while site 4 is associated with a residual amount of active sites in the diferrous state.

Observation of the slow oxidation of a diferrous MMOH cluster population through EPR spectroscopy – The oxidation of diferrous MMOH in the presence of MMOB can be tracked by measuring the decay of compound **O** through the loss of its characteristic integer-spin $g = 16$ EPR signal [81, 94, 95]. The EPR spectrum of an MMOH single turnover reaction sample frozen at 8 seconds (pH 7.0, 4 °C) indicates that a substantial amount of the enzyme population is present in the diferrous state (Figure 2.4). A comparison of the $g = 16$ EPR signal intensity (double-integration of the area covered by the resonance signal) between the starting point of the reaction $\mathbf{H}^{red}$ ($t = 0$ seconds) and the later time-point, suggests that almost 31% of the diferrous clusters remain at $t = 8$ seconds. As the simulation for a single-turnover reaction indicates that the oxidation of the diferrous enzyme active sites is complete by 120 milliseconds (Figure 2.1), the presence of diferrous cluster at 8 seconds must arise from the non-native population of MMOH indicated by the Mössbauer studies.

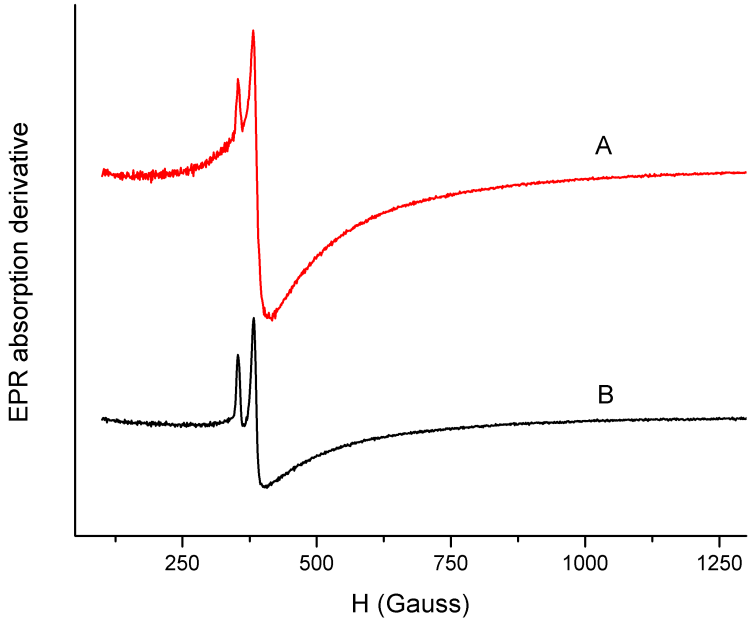

Figure 2.4 – Parallel mode X-Band EPR spectra of the single turnover reaction of MMOH in the starting fully reduced state $t = 0$ seconds (A) and a time point of $t = 8$ seconds (B) at pH 7.0, 4 °C. Almost 31 % of the diferrous cluster ($g = 16$) is still present at 8 seconds in the single turnover reaction. Instrument conditions: modulation amplitude = 4 Gauss, microwave power = 4 milliwatts, temperature = 2.1 K, microwave frequency = 9.405 GHz.

Formation of the MMOH:MMOB complex with hydroxylase protein batches with varying specific activity – The formation of the MMOH:MMOB protein complex is critical to the reaction cycle of sMMO as this complex enhances the rate constant of oxygen binding to the diiron cluster by about 1000-fold over the reduced MMOH protein in isolation [81]. The observation of the presence of a significant population of diferrous active sites oxidizing at a much slower rate constant than the native population suggests an impaired protein complex formation between MMOH and MMOB. Accordingly, the sMMO protein complex formation has been investigated further by titrating MMOB with two batches of MMOH protein with varied specific activity values. The two MMOH protein batches used are MMOH_226SpA (226 nmoles/min/mg with furan) and MMOH_470SpA (470 nmoles/min/mg with furan). We observe the turnover number of nitrobenzene to maximize at approximately a stoichiometry of 0.33:1 (MMOB : MMOH active sites) and 0.5:1 in the MMOB titration plot with MMOH_226SpA and MMOH_470SpA, respectively (Figure 2.5). This observation is in contrast to the maximum turnover number being achieved at a stoichiometry of 1:1 with MMOH protein with the highest recorded specific activity (1200 nmoles/min/mg with furan) [74]. The values for the stoichiometric ratio at which maximal turnover is achieved for the MMOH protein batches also correlate closely with their specific activity values measured as a percentage fraction of the highest reported activity (19 % for MMOH_226SpA and 39 % for MMOH_470SpA). This value also correlates with the **Q** yields observed with these MMOH protein batches in their respective single turnover reactions (Figure 2.2) (Table 2.2). This result implies that the low specific activity of MMOH and the low **Q** yields arise from an inability of a fraction of the protein to form a reactive MMOH:MMOB complex. As this unreactive, non-native population of MMOH does not bind MMOB in a productive fashion, the diferrous clusters might oxidize at a much slower rate constant than the native, reactive population. The presence of long-lived active site diferrous clusters as observed by EPR and Mössbauer spectroscopies provide supporting evidence for this hypothesis (Figure 2.3 & 2.4).

	Ratio MMOB:MMOB at maximal turnover	% of highest reported specific activity	% Q maximal accumulation [(a)]
MMOH_226SpA	0.33:1	19	17
MMOH_470SpA	0.5:1	39	37

(a) – optical determination

Table 2.2 – A positive correlation is observed between the maximal **Q** yields and the specific activity of the MMOH protein batches.

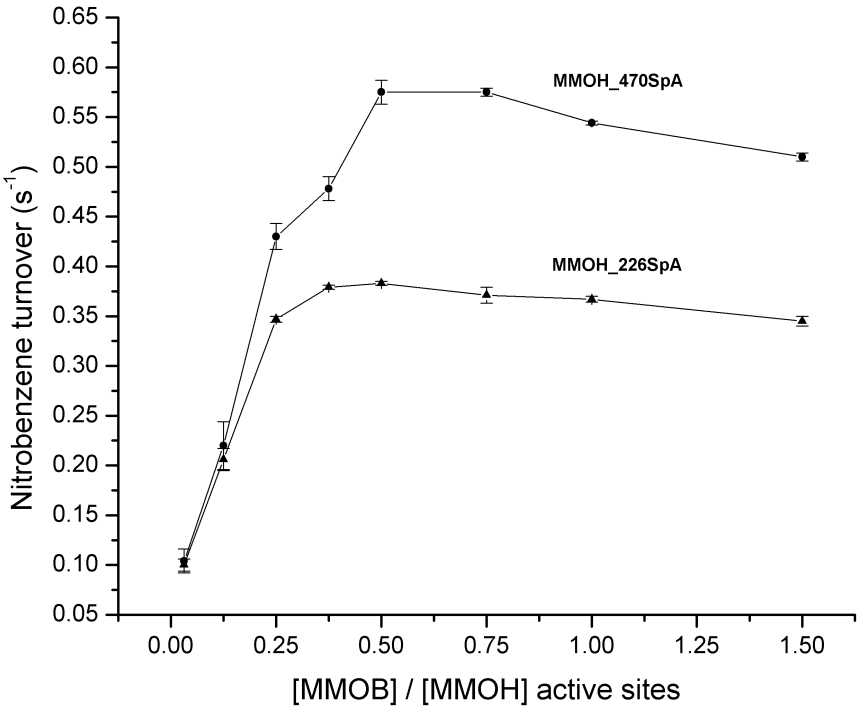

Figure 2.5 – Titration of MMOB with 2 batches of MMOH protein having different specific activity values; MMOH_470SpA = 470 nmoles/min/mg, MMOH_226SpA = 226 nmoles/min/mg. The turnover number for nitrobenzene oxidation maximizes around a MMOB:MMOH ratio of 0.33:1 and 0.5:1 for the two batches of MMOH protein.

2.3.2 Mass-spectrometric characterization of MMOB and MMOH

The MMOB protein is subjected to mass spectrometric characterization to determine whether an altered MMOB causes the MMOH:MMOB complex not to form productively. Electrospray ionization-time of flight (ESI-TOF) mass spectrometric measurements indicate a uniform population of MMOB with a molecular mass identical to the predicted value based upon the genetic sequence of 14751 Da (Figure 2.6). Indeed, the sMMO specific activity values do not alter with MMOB protein batches. Moreover, the origin of component B, either from native source (*M. trichosporium* OB3b) or heterologous expression (*E. coli*), does not change the yield of **Q** obtained in the single turnover reaction. These results strongly suggest that the low **Q** yields do not arise from an altered population of MMOB.

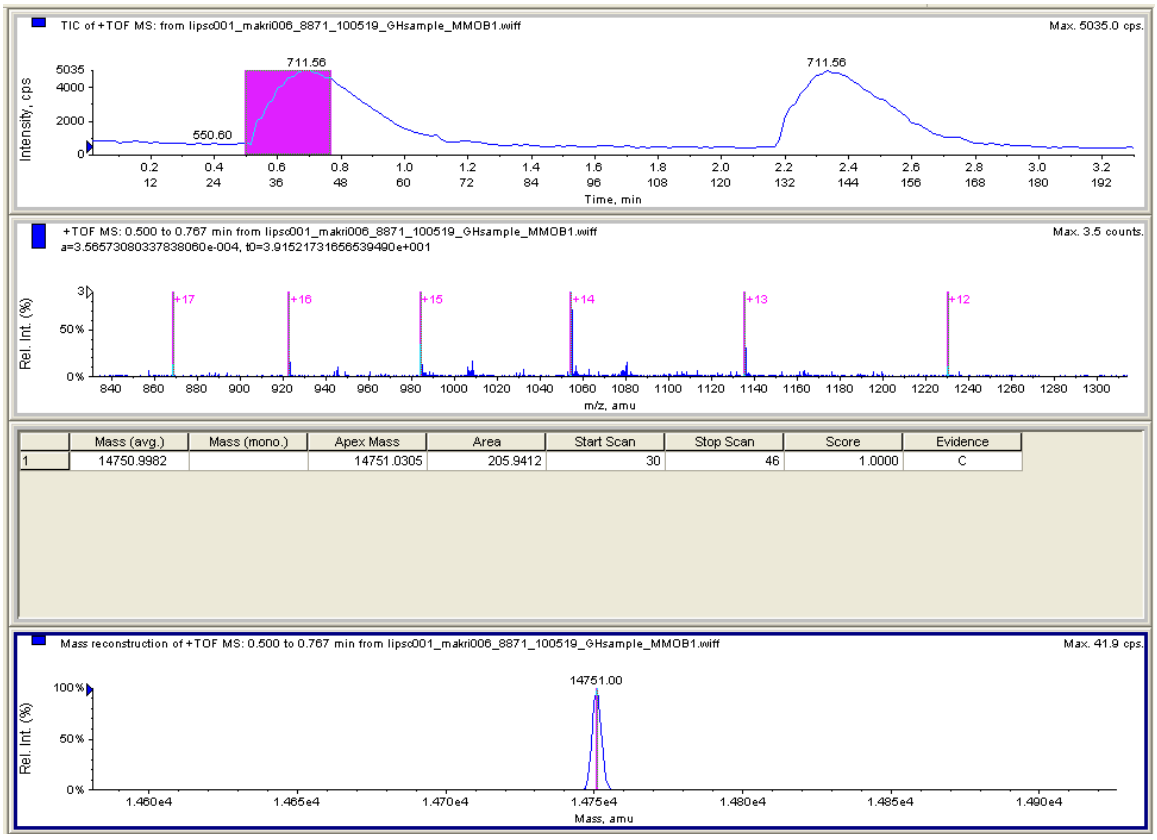

Figure 2.6 – ESI-TOF mass spectrometric characterization of MMOB. A uniform population of MMOB protein is observed with a molecular mass of 14751 Daltons.

The MMOH protein was also subjected to an ESI-TOF mass-spectrometric characterization in order to obtain evidence for post-translational modifications (Figure 2.7). The α-subunit of MMOH is observed to possess a molecular mass identical to its predicted value of 59823 Da based upon the genetic sequence [185]. The observation of a mass fragment corresponding to the β-subunit is hampered by either a low ionization or poor flight of the subunit in the instrument (low area for this mass fragment). A mass fragment with an average mass of 19281 Da is observed which is close to the expected molecular mass of 19195 Da for the γ-subunit of MMOH [185]. The extra molecular weight of 86 Da does not match any common single amino acid post-translational modification. However a significant caveat to this mass characterization is that there is a discrepancy between the molecular masses predicted by the crystal structure and the genetic sequence. This is on account of 41 sequence variations between the genetic sequence and the observed amino acid sequence in the crystal structure. Accordingly, the calculated molecular masses of the α, β and γ subunits from the crystal structure are, respectively, 59850.3 Da, 44981.14 Da and 19197.1 Da [64]. In addition, the ESI-TOF method utilized is not sensitive enough to resolve between multiple protein subunit populations present in a heterogeneous MMOH protein. Together, these two caveats have limited the interpretation of the aforementioned mass-spectrometric data of MMOH. A separation of the individual MMOH protein subunits would decrease the complexity of the protein sample and may prove more amenable to mass-spectrometric characterization of multiple populations.

	Mass (avg.)	Mass (mono.)	Apex Mass	Area	Start Scan	Stop Scan	Score	Evidence
1	19281.2877		19281.2963	497.0259	47	59	1.0000	C
2	59823.9034		59825.0521	304.6768	47	59	1.0000	C
3	38561.5766		38562.0413	36.7735	47	59	1.0000	C

Figure 2.7 – ESI-TOF mass spectrometric characterization of MMOH. Three protein mass fragments are observed for the entire MMOH protein complex. The average mass and area for each individual mass fragment is indicated in the figure by red boxes.

2.3.3 An improved MMOH purification scheme

Deleterious effects of fresh Fe(II)-cysteine containing buffers – The established purification protocol [184] for MMOH utilizes 0.2 mM $Fe(NH_4)_2(SO_4)_2$ and 2.0 mM L-cysteine in all buffers, added immediately prior to use. The Fe(II)-cysteine complex acts as a stabilizing agent for MMOH activity by preventing the loss of iron from the enzyme active site [92]. However, the use of freshly added Fe(II)-cysteine complex compared to an aged complex (vide infra) consistently leads to a loss of MMOH activity and imparts a brown coloration to the protein (Figure 2.8 inset).

The freshly dissolved Fe(II) and cysteine salt forms a purple colored solution that slowly dissipates over time (Figure 2.8). A chance observation while purging such a solution with nitrogen indicates that the purple color arises from a Fe(II)-cysteine-oxygen complex. This observation is corroborated by published literature depicting the formation of such a chemical species [187-189]. This complex has been demonstrated to form reactive hydroxyl radicals while catalyzing the oxidation of cysteine to cystine with oxygen acting as the electron acceptor [188]. Indeed, 5,5'-dithiobis-(2-nitrobenzoic acid) (DTNB) estimation of thiol groups and polarographic measurement of dissolved oxygen indicates that the aged Fe(II)-cysteine containing buffer (after the purple color dissipates completely) has lost titratable thiol groups and oxygen in a stoichiometric ratio of 2:1. Considering the reactive nature of hydroxyl radicals, a semi-anaerobic purification scheme is devised for MMOH. The Fe(II)-cysteine containing buffer is incubated at 4 °C until the purple color disappears. The subsequent nitrogen purging of the buffers and collection of MMOH protein fractions in argon-purged sealed vials ensures that the purple Fe(II)-cysteine-oxygen complex does not reform and the complex Fe(II) does not oxidize to Fe(III). The latter oxidation process has also been demonstrated to form reactive oxygen free radicals that may adversely affect MMOH activity [190]. The metal ion catalyzed oxidation of proteins has been documented in the literature [191]. This modification to the MMOH purification protocol abolishes the loss of enzyme activity during purification and prevents the brown coloration being imparted to MMOH (Table 2.3) (Figure 2.8 inset). In combination with the modifications made to the *M. trichosporium* OB3b growth conditions (vide infra), this purification protocol enables a consistent production of MMOH with specific activity values between 450 – 500 nmoles/min/mg with furan.

Modification of the protein chromatography steps – The following activity-enhancing improvements have been made to the MMOH purification protocol: i) batch-binding of the cell free extract (CFE) to the DEAE resin in the first chromatographic step in lieu of binding to a pre-packed column, ii) a high-resolution Q Sepharose ion-exchange chromatographic step in place of the size-exclusion chromatographic step. The batch binding method prevents the pH increase observed previously to be associated with the elution of the MMOH protein [157]. This is achieved by presumably diluting the local concentration of proteins bound to the resin as the pH increase is possibly due to the co-elution with MMOH of a protein with a high isoelectric point. The second chromatographic step has been replaced by a high-resolution ion-exchange chromatographic step, as the size-exclusion chromatography did not significantly increase hydroxylase purity. Crucially, this change results in a drastic reduction in the fluorescence background of the purified MMOH protein. This has been integral for the success of the Resonance Raman studies with MMOH that has been described in a later chapter. The purification in terms of fold purification and yield of enzyme activity is similar to that previously described for MMOH with the highest specific activity [92]. This is evidence that the low specific activity of MMOH either originates *in vivo* or occurs immediately upon breaking the cell.

MMOB affinity column purification of MMOH – The putative difference in the affinity of the active and inactive populations of MMOH towards MMOB (Figure 2.5) has been exploited in order to design a MMOB affinity column to purify the active MMOH fraction. The A62C MMOB protein is chosen for the MMOB affinity purification as this residue is proposed to lie on the MMOB surface facing away from the region that binds MMOH [76]. Accordingly, a disulfide cross-linking of MMOB to the resin at this position would not perturb MMOH:MMOB complex formation. The MMOH protein does bind to this affinity column and is eluted off with buffer possessing a high ionic strength [192]. The MMOH protein eluted off this column does possess a higher specific activity than the starting material (*cf.* 83 nmoles/min/mg versus 207 nmoles/min/mg with propylene as substrate). However, this activity is substantially less than the highest reported specific activity value of 1700 nmoles/min/mg with propylene.

Step	Volume (ml)	Total protein (mg)	Specific activity[1] (mU/mg)	Total activity (mU)	Yield (%)	Purification (-fold)
Cell-free extract	390	7886	70	552020	100	1.0
DEAE-Sepharose CL-6B	208	1781	240	427440	77	3.4
Q-Sepharose HR	186	789	510	402390	73	7.3

1. A unit is defined as the amount of methane monooxygenase hydroxylase protein required, in the presence of optimal concentrations of the other sMMO protein components and saturating concentrations of NADH and furan, to catalyze the production of 1 μmol of furan per minute at 25 °C in 25 mM MOPS buffer, pH 7.5, equilibrated with air.

Table 2.3 – Purification table for MMOH**.**

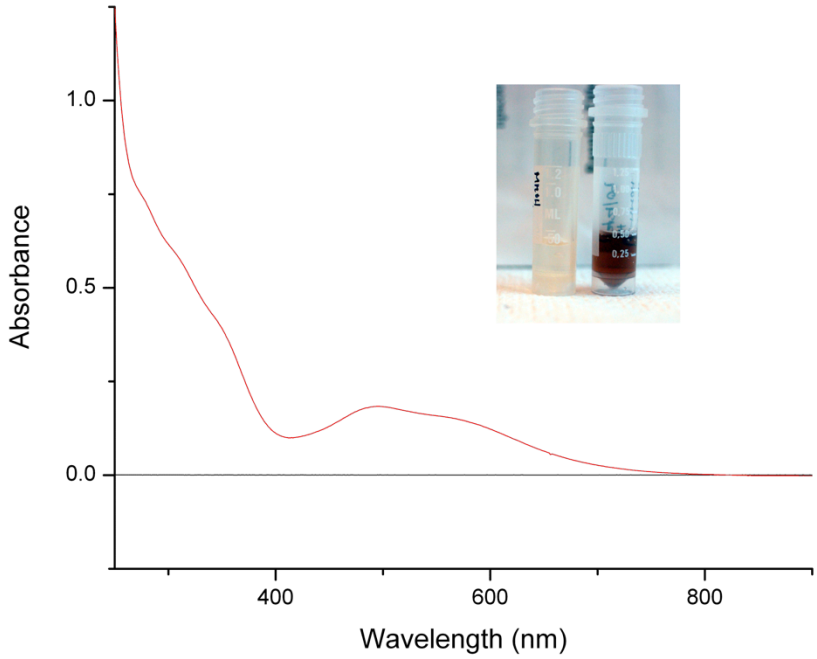

Figure 2.8 – Absorption spectrum of the purple Fe(II)-cysteine complex immediately after addition to cold buffer (25 mM MOPS, pH 7.0). The purple color arises from the putative formation of an Fe(II)-cysteine-O_2 complex. Inset – The MMOH protein sample (right hand side) develops a brown coloration when purified with buffers with the Fe(II)-cysteine complex added immediately before use, which the semi-anaerobic purification prevents (left hand side).

2.3.4 Variation in the specific activity of MMOH is growth dependent

The specific activity of MMOH sourced from cells grown under a range of fermentation conditions has varied from 300 to 700 nmoles/min/mg with furan as a substrate. This variation in specific activity is observed after the incorporation of the improvements to the MMOH purification scheme. However, there are no apparent differences in the growth characteristics between the fermentor runs affording the high and low specific activity MMOH batches. Multiple modifications to the fermentor growth parameters have been tried out to coax higher activity out of the purified MMOH protein. These have been further described in Table 2.4. The only growth parameter that has an effect on the expression level and specific activity of MMOH is the methane flux through the fermentor at a set optical density of the bacterial culture. At an optical density of about 12 - 15 at 540 nm, a methane flux of 0.05 – 0.1 L/min through the 10 liter fermentor vessel restricts the growth rate of the culture. While this enhances the expression level of MMOH, the specific activity of the purified protein is consistently around 300 nmoles/min/mg with furan. A much higher methane flux of 1.0 – 1.5 L/min enhances the growth rate of the culture while decreasing the expression level of MMOH. However, the specific activity of MMOH purified from cells grown under these conditions is still low at 250 nmoles/min/mg with furan. The optimal methane flux seems to be around 0.3 L/min. While this still restricts the growth rate of the culture, the specific activity of MMOH is around 500 – 700 nmoles/min/mg. Further modulation of the methane flux does not provide higher specific activity preparations of MMOH. The introduction of the 500 ml starter cultures at low optical densities (<1.2 at 540 nm) into the fermentor and the maintenance of a low dissolved oxygen level between 5 – 8 % seem to be most effective towards obtaining a higher specific activity of MMOH.

Extensive attempts have also been made to grow *M. trichosporium* OB3b cells from old -80 °C freezer stock of cells. These cells are fermentor harvests from a period during which the purified MMOH protein displayed a high specific activity (1995) [81]. However, these cell stocks were contaminated with non-methanotrophic, heterotrophic bacterial contaminants, which are very commonly associated with methanotrophs [193]. A pure culture of *M. trichosporium* OB3b is obtained by plating serial dilutions of a NMS media liquid suspension of the frozen cell stock onto NMS media plates, such that single colonies are obtained from the plated cells [184]. The colonies arising from a pure culture of *M. trichosporium* OB3b are rounded in shape with a defined edge and are opalescent in color. The bacterial colonies that appear opaque with irregular colony edge morphology are mixed cultures and test positively for the heterotrophic contaminants

as they show growth on Luria Bertani media plates. However, the pure cultures of *M. trichosporium* OB3b resurrected from old freezer stocks did not provide MMOH protein with any higher specific activity that the current laboratory OB3b strain.

	Growth parameter	Rationale	Effect
1.	Methane flux	Varied between 0.05 – 1.5 L/min	optimal flow rate is 0.3 L/min at OD_{540} of 12 – 15
2.	Dissolved oxygen level	Varied between 2 – 35 %	optimal level is between 5 – 8 %
3.	Ultra High purity methane gas (99.97 %)	To check for the presence of acetylene (irreversibly inactivates sMMO [194]) in the usual methane delivery system comprising of methane gas (chemically pure grade) equipped with a hydrocarbon trap.	No effect on activity
4.	Pure grade medical air	To check for the presence of acetylene in the house air line.	No effect on activity
5.	Trace metal solution containing nickel and a larger concentration of molybdenum	This is based upon a different recipe for the trace metals solution used to make the NMS media [195].	No effect on activity
6.	Citrate salt in NMS media (0.015 mM)	citrate ions have been shown to have a beneficial effect on *M. trichosporium* OB3b growth [196].	No effect on activity
7.	NMS media pH varied between 6.8 – 7.6	Original attempts at growing *M. trichosporium* OB3b used a home built fermentor with poor pH control - variation in specific activity could have arisen from a difference in pH of the NMS media.	No effect on activity

Continued from previous page…

	Growth parameter	Rationale	Effect
8.	Copper variation 0.1 μM – 1 μM	The sMMO enzyme from *Methylocystis* sp strain WI 14 has been shown to be inactivated by Cu(II) ions [197].	No effect on activity
9.	Different optical densities of the culture - OD_{540} varied between 8 – 24	High optical densities of the culture may limit nutrients and could affect the specific activity of sMMO.	No effect on activity
10.	Introduction of the starter culture into the fermentor at low ($OD_{540} < 1$) and high ($OD_{540} > 4$) optical density	High optical densities in the 500 ml starter cultures severely limit methane in the shake flasks, which can affect the specific activity of sMMO in the culture.	Lower OD's are beneficial.

Table 2.4 – The modifications to the *M. trichosporium* OB3b growth conditions have been listed in this table. Each modification is individually tested on a fermentation growth cycle. The effect of the growth variable is observed by measuring the specific activity of MMOH purified from the fermentation cell harvest. The purification of MMOH incorporated the beneficial modifications mentioned in the previous section.

2.4 DISCUSSION

The steady-state activity of sMMO is dependent upon the formation of a multi-protein complex between MMOH, MMOB and MMOR, which makes it difficult to tease apart the origin of the low specific activity. The single turnover reaction of sMMO requiring only MMOH and MMOB produces a much lower than expected yield of intermediates. Mössbauer and EPR spectroscopic studies of this single turnover reaction suggest that the low yield of intermediates might arise from the presence of two populations of sMMO that undergo turnover at different kinetic rates, one of which corresponds to previous observations and compares well with the highest specific activity preparation of MMOH [94]. The single turnover reaction also suggests that the origin of low specific activity of hydroxylase lies with either MMOH or MMOB. The presence of heterogeneity in the diferrous form of sMMO has been previously observed and discussed in the sMMO enzyme from *M. capsulatus* Bath [115]. Mössbauer studies of the single turnover reaction indicated the presence of two populations of the diferrous enzyme that react with oxygen at different kinetic rates. It appears thus that the low yield of intermediates in the sMMO catalytic cycle arising from a heterogeneous population is an issue common to this enzyme.

The MMOH:MMOB titration data reveal that maximal turnover of the nitrobenzene substrate occurs with only a 20 - 45 % fraction (native) of the total number of MMOH:MMOB complex molecules. The remaining unreactive protein complexes (non-native) may account for the seemingly large population of diferrous enzyme that oxidizes at a much slower rate constant (Figure 2.3 & 2.4). Since the formation of a MMOH:MMOB protein complex enhances the rate constant of oxygen binding to the diferrous cluster by almost 1000-fold over reduced MMOH in isolation [81], potentially a significant fraction of MMOH cannot form a productive protein complex with MMOB and hence oxidizes at a slower rate constant than previously observed (Figure 2.3 & 2.4) [94]. This oxidation of the diferrous cluster becomes the rate-limiting step in the catalytic cycle for this non-native population of MMOH, thus leading to a loss of accumulation of compound **Q**.

The specific activity values and **Q** yields show a dependence upon the growth and purification of MMOH. The uniform population of unmodified MMOB and the absence of a specific activity variation with MMOB purification batches suggests that the impaired MMOH:MMOB protein complex does not originate in MMOB. The low **Q** yields thus arise from an altered population of

hydroxylase that is present along with a native population of MMOH. Fluctuations in the respective amounts of these two populations in the purified protein batch leads to the varying enzyme specific activities.

Impaired binding between a non-native hydroxylase molecule and MMOB might originate from post-translational modification of amino acid residues on the MMOH surface that interacts with MMOB. This hypothesis is primarily based upon the observation that the genome of *M. trichosporium* OB3b contains only a single copy of the MMOH gene [198]. As such, this argues against a genetic mutation in MMOH from the *M. trichosporium* OB3b strain being currently used, since such a mutation would create a uniform population of modified MMOH. Moreover, single amino acid mutations of MMOB located on the MMOH binding interface, adversely affect the binding constant [157]. The MMOH:MMOB titration data also suggest that the native, highly-reactive fraction of MMOH has a greater affinity for MMOB than the non-native population. Attempts at the MMOB affinity column purification of MMOH suggest that this difference in affinity is not substantial enough to fully separate these two populations of MMOH from each other. This putative post-translational modification of MMOH might either occur *in-vivo* during cell growth or during purification.

The aforementioned heterogeneity of the MMOH protein population has been observed previously [199, 200]. In these reports, the heterogeneity was observed in the form of two populations of the diiron cluster in the diferric state. The Mössbauer spectrum of diferric MMOH in complex with MMOB indicated the presence of two distinct iron clusters with different parameters distributed in a 80 % : 20 % ratio among the hydroxylase active sites [200]. The EXAFS data also described two populations present at a ratio of 60 % : 40 %. The two types of clusters have a Fe-Fe distance of 3.0 Å and 3.4 Å respectively [199]. This data was interpreted through comparison to synthetic model compounds to suggest that the cluster with the shorter Fe-Fe distance had a bis(μ-hydroxo)(μ-carboxylato) bridge while the other had a (μ-hydroxo)(μ-carboxylato) bridge. The level of specific activity of the MMOH protein used in this study relative to the maximum reported activity (58 %; cf. 700 nmoles/min/mg to 1200 nmole/min/mg with furan) suggests that the active form of MMOH correlates closely with the fractional amount of the diiron cluster with the shorter Fe-Fe distance. The binding of MMOB to MMOH results in significant structural and electronic rearrangement of the diiron cluster, as observed by changes in

the EPR and MCD spectrum of the mixed-valent and diferrous cluster respectively [74, 83]. The mid-point reduction potential of the iron atoms is also reduced by 132 mV upon complex formation with MMOB [84]. Thus, the heterogeneity of the bridging ligand structure suggests a mixed population of MMOH:MMOB protein complex molecules, of which only one species is a native and productive complex.

The putative post-translational modification of MMOH resulting in an unreactive population might arise either *in-vivo* during growth of *M. trichosporium* OB3b or during purification. There is a significant loss of MMOH activity and a brown color imparted to the protein in the aerobic purification protocol using Fe(II)-cysteine added immediately before use. This loss of activity possibly arises from the formation of reactive free radical intermediates in the purification buffer during the oxidation of cysteine to cystine by the Fe(II)-cysteine complex. These reactive oxygen species can oxidize and thus modify susceptible amino acid residues on the MMOH surface. These modifications would adversely affect MMOH activity by interfering with the formation of the reactive MMOH:MMOB complex, if present on the MMOH surface that binds MMOB. The brown coloration might indeed be arising from the formation of quinolic compounds derived from oxidized amino acid residues like tyrosine [201]. The semi-anaerobic modification to the MMOH purification protocol minimizes the exposure of MMOH to the reactive free radical species while still preserving the stabilizing role of the Fe(II)-cysteine complex.

While these modifications have eliminated the loss of hydroxylase activity during purification (Table 2.3), the specific activity value of MMOH purified in this study still falls short of the maximal value. This indicates that the low specific activity of MMOH might arise *in-vivo,* and thus there may be an uncontrolled aspect of the growth conditions of *M. trichosporium* OB3b. Accordingly, multiple controllable growth parameters have been individually modified to test for their effect on MMOH activity. The methane flux through the fermentor does alter the expression level and specific activity of MMOH. The conditions of either severe methane limitation or excess methane adversely affect the specific activity of the hydroxylase component. This physiological effect might be an effect of metabolic feedback inhibition as sMMO is the first enzyme on the pathway involved in carbon assimilation. Such a post-translational feedback inhibition mechanism has been demonstrated to occur in the closely related butane monooxygenase enzyme from *Pseudomonas butanovora* [202].

The modulation of multiple variables in both the growth of *M. trichosporium* OB3b and the purification of the hydroxylase protein has successfully increased the specific activity of MMOH by two-fold (580 nmoles/min/mg compared to 220 nmoles/min/mg with furan). However, since this activity is less than the maximal reported value, it suggests the presence of an unidentified growth-dependent variable or variables that could be explored in future studies. In comparison to the activity of MMOH protein used previously in the literature (Table 2.1), the hydroxylase used in these studies provides an excellent starting enzyme to use for the isolation and characterization of sMMO catalytic intermediates. The specific activity and **Q** yields from the protein batches used in this study are comparable to those used in seminal papers in the sMMO field [147, 181]. More importantly, the comparison of the specific activity of MMOH and **Q** yields provides information regarding the amount of non-native population of sMMO that manifests as a slowly oxidizing diferrous site in the single turnover reaction. Accordingly, experiments can now be designed with additional control samples and where spectroscopic data are interpreted more accurately. This key finding enables a more efficient and definitive study of the sMMO catalytic cycle some aspects of which are reported in this thesis.

CHAPTER 3

Kinetic trapping and characterization of intermediate P* from soluble methane monooxygenase

3.1 INTRODUCTION

The soluble form of methane monooxygenase (sMMO) found in many methanotrophs catalyzes the oxidation of methane to methanol as part of the metabolic pathway that allows these microorganisms to use methane as the sole carbon and energy source [43]. This demanding reaction (methane bond dissociation energy equals 105 kcal $mole^{-1}$) [44] is catalyzed only by sMMO and particulate MMO (and to a lesser extent, pMMO-like ammonia monooxygenase in ammonia autotrophic bacteria) [51, 203, 204]. sMMO is an enzyme system comprised of three protein components: i) a hydroxylase (MMOH) containing a diiron metal cluster in the active site, ii) a [2Fe-2S] cluster and FAD containing reductase (MMOR) that mediates electron transfer between NADH and the diiron cluster, and iii) a regulatory protein MMOB that is devoid of any cofactors [92]. The unique reactivity of sMMO has spurred research into its chemical mechanism and led to extensive efforts to mimic the chemistry using synthetic model compounds [23, 78, 205]. We have studied the mechanism of sMMO using the enzyme from the Type II methanotroph *Methylosinus trichosporium* OB3b (*M. t.* OB3b), while others have used the enzyme from the Type X methanotroph *Methylococcus capsulatus* Bath (*M. c.* Bath) with similar results [78, 119].

Single turnover transient kinetic studies have been used to map the reaction cycle intermediates as shown in Scheme 3.1 [78, 97, 100, 119]. The resting diferric MMOH ($\mathbf{H^{ox}}$) can be reduced by two electrons from either MMOR or chemical reductants to form diferrous MMOH ($\mathbf{H^{red}}$) [92]. This form of the enzyme reacts with O_2 to form intermediate **O** which has oxygen bound to the enzyme, but perhaps not to the diiron cluster [81, 94]. Intermediate **O** decays to form intermediate **P**, which exhibits a weak optical band at 700 nm and Mössbauer parameters diagnostic of a diferric cluster with a peroxo moiety bound to the iron atoms [98, 99, 115]. The precise nature of the cluster in **P** is unknown, but comparison with model complexes and peroxo intermediates in related diiron enzymes suggests that it is a μ-1,2-peroxo dinuclear Fe^{III} complex [205]. Intermediate **P** decays to form intermediate **Q**, which has been shown by Mössbauer and X-ray absorption studies to contain a unique bis-μ-oxo Fe^{IV}_2 diamond core cluster [94, 99, 102]. **Q** exhibits a relatively intense optical spectrum with maxima at 330 and 430 nm (ε_{430} = 7500 M^{-1} cm^{-1}). This spectrum has allowed extensive studies of the mechanism of the reaction with methane and adventitious substrates [94, 97, 115, 141, 143, 147, 149]. It is likely the reaction

occurs by hydrogen atom abstraction with a substantial tunneling component to form intermediate **R** [119 , 135, 147, 149, 157, 159]. In contrast to intermediates **O**, **P**, and **Q**, intermediate **R** does not live long enough to be directly observed, but it is postulated to occur based on racemization during chiral ^{1}H, ^{2}H, ^{3}H-ethane oxygenation and computational studies showing that a substrate radical is transiently formed [103, 126, 127, 135]. Rebound of the cluster-bound hydroxyl group onto the substrate radical would yield the product complex, termed **T**, which dissociates to complete the cycle [94].

Our transient kinetic studies of the **O** to **P** conversion have indicated the presence of an intervening intermediate termed **P*** [98]. Two experimental observations led to this mechanistic proposal. The first evidence is that the rate constant of formation of **P** (10 s^{-1} at 4 °C, pH 7.0) is slower than the rate constant for the decay of **O** (26 s^{-1} at 4 °C, pH 7.0), indicating that there must be an intermediate in between. The second line of evidence arises from the observation that the decay rate constant of **O** is pH independent, in contrast to the pH dependent rate constant for the formation of **P,** showing that the reactions cannot be the same. To date, transient kinetic single turnover studies on MMOH from *M. t.* OB3b have failed to reveal any spectral features that can be attributed to **P***. However, the fact that the $g = 16$ signal of diferrous cluster disappears as **P*** is formed was interpreted to indicate that either one or both cluster irons are oxidized due to formation of a metal-ligated superoxo or peroxo complex [98].

Recent studies using the *M. c.* Bath enzyme provide kinetic evidence for the presence of an intermediate before H_{peroxo} (equivalent to **P**) in the MMOH catalytic cycle [100]. A global fitting of the kinetic time traces at 420 nm and 720 nm of a single turnover reaction of reduced *M. c.* Bath MMOH with O_2 in the presence of methane is consistent with an intermediate with an electronic absorption spectrum similar to that of H_{peroxo}, which is known to have an $Fe^{III}Fe^{III}$ cluster. Accordingly, it was reasoned that the intermediate (also named P*) and H_{peroxo} both have $Fe^{III}Fe^{III}$ clusters in nearly identical electronic environments.

One particularly relevant aspect of the MMOH reaction cycle for the present study is the dramatic effect of MMOB on the rate of catalysis [157, 158]. The rate constant for the conversion of intermediate **O** to **P** in the *M. t.* OB3b enzyme system is accelerated 1000 fold by the presence of MMOB [81]. For adventitious substrates, the regiospecificity of hydroxylation is sometimes different depending on the presence or absence of MMOB, and spectroscopic studies indicate that

the diiron cluster environment of MMOH is altered in the MMOH-MMOB complex [80, 95, 206]. The residues that form the interface between MMOH and MMOB have been identified by spectroscopic studies [75, 76]. A set of MMOB variants made by introducing site-specific mutations at these residues has been shown to alter the rate constants for interconversion between MMOH reaction cycle intermediates [157, 158]. One of the variants, MMOB His33 to Ala (H33A), specifically decreases the rate constant for interconversion of intermediate **O** to **P**, potentially allowing this reaction to be studied in detail.

Here, we use MMOB H33A to decrease the rate constant of formation of **P** by about 30 fold without a significant decrease in the rate constant for **O** decay, resulting in substantial increase in the accumulation of **P***. This permits the observation of the electronic absorption and Mössbauer spectra of **P***. It is shown that **P*** has a different structure than previously proposed, suggesting a new approach to formation of the peroxo complex in diiron cluster containing oxygenases.

Scheme 1

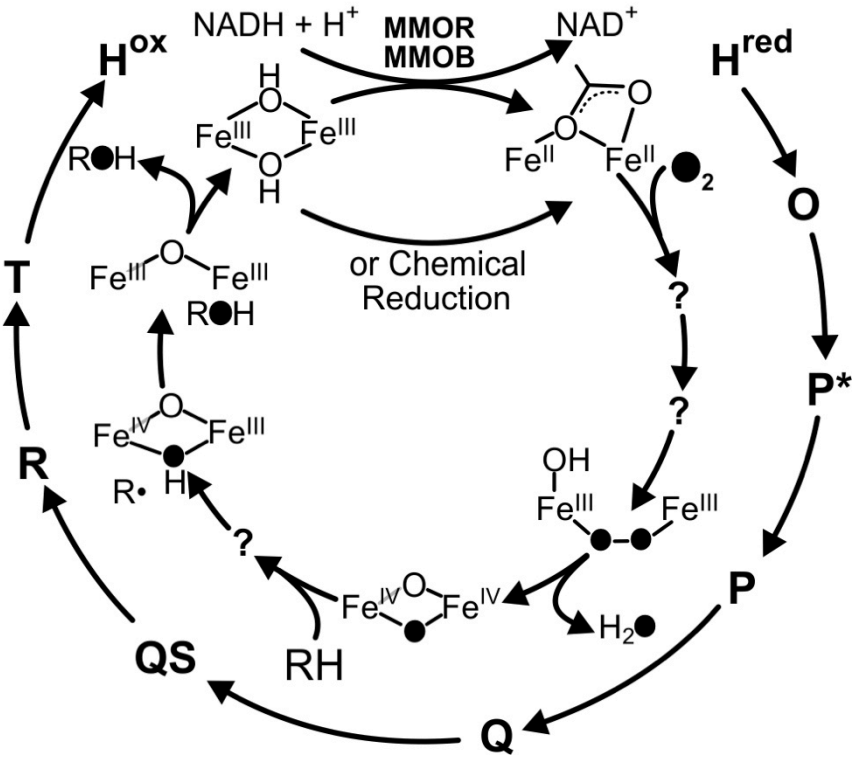

Scheme 3.1 – Reaction cycle intermediate of sMMO.

3.2 MATERIALS AND METHODS

Chemicals – 3-(N-morpholino)-propanesulfonic acid, glycerol, ferrous ammonium sulfate, cysteine, urea, furan, sodium hydrosulfite and methyl viologen were purchased from Sigma-Aldrich.

Biological Materials – MMOH was purified from *M. trichosporium* OB3b with the following modifications to the published protocol [184]. All purification buffers contained 0.2 mM ferrous ammonium sulfate and 2.0 mM cysteine as a stabilizer for the active site iron of MMOH. These were added to the cold buffers at least 3 h before use and nitrogen purged for 1 h before and during use. The chromatography columns were also equilibrated with nitrogen-purged buffers before loading the iron/cysteine stabilizer containing buffers. The second high-resolution ion-exchange chromatography column was additionally scrubbed free of oxygen with 20 ml of 5.0 mM sodium hydrosulfite solution. The *M. t.* OB3b cell free extract was applied to the initial DEAE ion-exchange column in a batch-binding manner. The protein fractions containing MMOH were subsequently collected in sealed argon-purged glass vials. The MMOH containing protein fractions were pooled and concentrated. This concentrated eluent pool was desalted through a Sephadex G-25 column (22 × 2.8 cm) equilibrated in 25 mM MOPS, pH 6.8. The desalted protein pool was subsequently applied to a high-resolution Q-Sepharose column (12 × 2.8 cm) equilibrated in 25 mM MOPS, pH 6.8. MMOH is eluted with a 900 ml gradient from 0 M to 0.08 M NaCl in the same buffer at a linear flow rate of 23 cm/h. The MMOH containing protein fractions were collected in argon-purged sealed glass vials, pooled and concentrated via ultrafiltration. Glycerol was added to a final concentration of 5% (v/v) to the protein pool. Recombinantly expressed H33A MMOB mutant was purified according to the protocol previously described [162].

Site-directed mutagenesis of MMOB – The QuikChange kit from Stratagene was used to construct the site-directed mutants of MMOB. DNA sequencing at the BioMedical Genomics Center at the University of Minnesota have subsequently confirmed these mutations. The oligonucleotides used to construct these mutants are as follows –

H33T – (5’-GAACCAGGTCGTCACCGAGTCCAACGC-3’ and
5’-GCGTTGGACTCGGTGACGACCTGGTTC-3’)

H33G – (5'-GAACCAGGTCGTCGGCGAGTCCAACGC-3' and
5'-GCGTTGGACTCGCCGACGACCTGGTTC-3')
H33F – (5'-GAGAACCAGGTCGTCTTTGAGTCCAACGCCGTG-3' and
5'-CACGGCGTTGGACTCAAAGACGACCTGGTTCTC-3')
H33E – (5'-GAGGAGAACCAGGTCGTCGAAGAGTCCAACGCCGTGGTTC-3' and
5'-GAACCACGGCGTTGGACTCTTCGACGACCTGGTTCTCCTC-3')

Transient Kinetic Experiments – Transient kinetic single turnover experiments were performed on an Applied Photophysics stopped-flow instrument (Model SX.18MV with SX Pro-Data upgrade). The sample preparation for MMOH involved making MMOH anaerobic under argon at 4 °C followed by a transfer into an anaerobic glove bag (Coy). The protein was reduced with a stoichiometric excess of sodium hydrosulfite and methyl viologen at room temperature for 20 minutes. The chemical reductants were separated from MMOH by passage through a Sephadex G-25 PD-10 desalting column (GE Healthcare) equilibrated in 100 mM MOPS buffer at the chosen pH point containing 0.2 mM ferrous ammonium sulfate and 2.0 mM cysteine. The iron/cysteine-containing buffer was incubated for 1.5 h at 4 °C (until purple color dissipates) before being made anaerobic. The reduced protein was loaded into one of the drive syringes on the stopped flow instrument using a Hamilton gas-tight syringe. The other drive syringe was loaded with a stoichiometric equivalent amount of H33A MMOB in oxygen-saturated buffer. If an sMMO substrate was utilized in the single turnover experiment, it is also added to this drive syringe. The single-wavelength kinetic data was analyzed with the Pro-Data Viewer software from Applied Photophysics. Singular value decomposition of spectro-kinetic multiple-wavelength data was performed using the Pro-Kineticist global analysis software (Applied Photophysics). The protein concentration of MMOH used in the transient kinetic experiments has been described in terms of reactive MMOH active sites. This description arises from the presence of two populations of MMOH active sites: i.) a native population that undergoes turnover with previously observed kinetic rate constants and forms catalytic intermediates, [94] ii) a non-native fraction that undergoes oxidation on a slower time scale and does not accumulate catalytic intermediates during turnover. The presence of two populations of MMOH with only one population displaying intermediates in the single turnover catalytic cycle, is also observed in MMOH from *M. c.* Bath [100]. The reactive population of MMOH active sites comprises of 40 % of the total MMOH active sites in the MMOH protein used in the experiments described in this study. The specific activity of the MMOH is 510 nmoles/min/mg with furan.

Rapid Freeze-Quench (RFQ) Mössbauer/EPR Experiments – For the preparation of rapid freeze-quench Mössbauer and EPR samples, MMOH was reduced with a stoichiometric amount of sodium hydrosulfite in the presence of methyl viologen (10 % of the MMOH active site concentration). A stoichiometric amount (per active site) of H33A MMOB was then added to reduced MMOH under anaerobic conditions and the mixture loaded in an RFQ syringe. The RFQ syringe was loaded on an Update Instrument Model 1019 RFQ apparatus. A low-temperature bath circulator (Neslab LT-50) maintained the reactants in the RFQ assembly at a temperature of 4 °C. The RFQ samples were produced by mixing the reduced MMOH enzyme with oxygen-saturated buffer and freezing the reaction at specified time points on counter-rotating aluminum wheels at liquid nitrogen temperature [186]. The frozen sample was then packed in RFQ Mössbauer cups or EPR tubes under liquid nitrogen.

3.3 RESULTS

3.3.1 Single turnover reaction using H33A MMOB in the absence of substrate slows the P* to P conversion

The photodiode-array traces for the single-turnover reaction of $\mathbf{H}^{\mathbf{red}}$ in the presence of H33A MMOB but no substrate are shown in Figure 3.1. The formation and decay of intermediate **Q** are easily seen in the 400 – 450 nm region, but there is no evidence of the spectrum of intermediate **P**, normally seen in the 700 nm region [97, 100, 157]. Extraction of the rate constants for the reaction by multiple exponential fitting of the time course shown in Figure 3.1, *inset* indicates that the apparent formation rate constant of **Q** at 4 °C is decreased from 2.7 s^{-1} observed with wild-type MMOB to 0.38 s^{-1}, similar to our previous findings [157]. When considered together, these results mean that the use of H33A greatly slows formation of **Q** by slowing a step prior to the **P** to **Q** conversion.

The slow step in the **O** to **P** sequence can be determined by monitoring the disappearance of intermediate **O** using rapid freeze quench techniques and EPR spectroscopy. As shown in Figure 3.2, the decay of the g = 16 EPR signal of **O** is nearly unchanged when using H33A MMOB in place of WT MMOB (k = 28 s^{-1} and 26 s^{-1}, respectively). Together the kinetic data show that it is the **P*** to **P** step which is greatly slowed by the mutation.

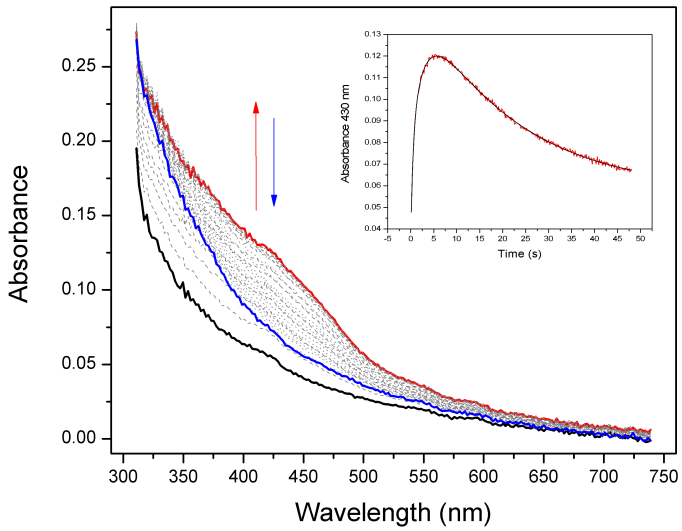

Figure 3.1 – Photo-diode array spectra of a single-turnover reaction of MMOH with H33A MMOB (12 μM reactive MMOH active sites) in the absence of substrate, pH 7.0, 4 °C. The diferrous form of the enzyme $\mathbf{H}^{red}$ (black trace) oxidizes to form **Q** (red trace). **Q** subsequently decays to the resting diferric state $\mathbf{H}^{ox}$ of the enzyme (blue trace). There is no optical evidence for the formation any other intermediate apart from **Q** in this reaction. Inset: Kinetic time course at 430 nm (red) extracted from the diode array data. The 2-exponential fit (black) shows that **Q** forms with a rate constant of 0.38 s^{-1}.

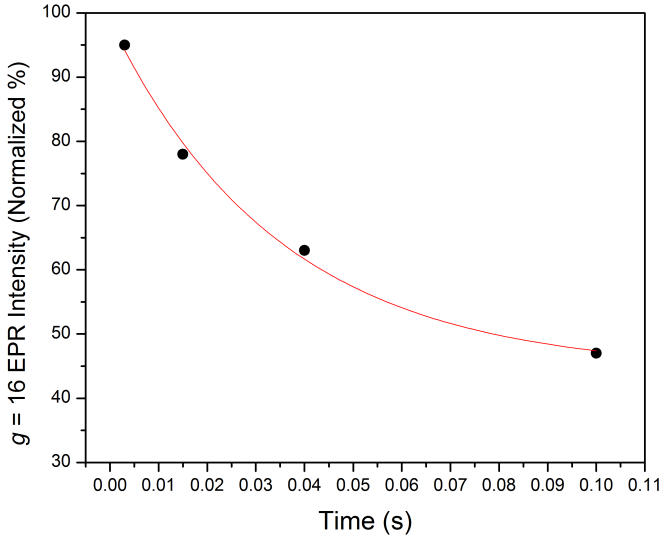

Figure 3.2 – Decay of the g = 16 integer-spin signal of compound **O** with H33A MMOB at pH 7.0, 4 °C. A single exponential fit to the data yields a rate constant of 28 s^{-1}. EPR measurement conditions: T = 2.0 K, microwave power = 0.5 mW, microwave frequency = 9.405 GHz. The residual g =16 EPR intensity (~ 50%) at 0.1 s arises from the unreactive fraction of reduced MMOH that reacts very slowly with oxygen.

3.3.2 Single turnover reaction using H33A MMOB in the presence of a substrate facilitates direct detection of P*

The broad electronic absorption spectrum of **Q** with large extinction coefficients (Figure 3.1) masks the spectra of other intermediates with weaker optical absorbance. In order to circumvent this problem, we have utilized furan as a substrate to rapidly react with **Q**, and therefore quench its optical spectrum [97]. Since this substrate does not change the rate constants of the catalytic cycle prior to the decay of **Q,** the accumulation of intermediates preceding **Q** should not be altered [94, 97]. We have also used methane instead of furan to quench **Q** with no change in the results. However, since methane is a gas, it limits the amount of O_2 that can be dissolved into the buffer, thereby restricting the concentration range available for the kinetic experiments.

A search for the optical features of **P*** using the commonly employed diode array detector as in Figure 3.1 proved unsuccessful. This is due to the relative insensitivity of the diode array detector. As an alternative, a spectra-kinetic data accumulation method was used to observe the single turnover reaction of MMOH with H33A MMOB and furan. In this technique, a series of single wavelength time courses are monitored at 15 nm intervals between 325 nm and 685 nm. These traces are then used to reconstruct the electronic absorption spectra of **O**, $\mathbf{H^{ox}}$ and the intervening intermediates in the catalytic cycle. While this requires much more enzyme than a single diode-array measurement, the input light intensity is greatly attenuated, and much finer temporal resolution is obtained due to the shorter integration time. This leads to much higher signal to noise ratios. Moreover, the higher dynamic range of the photomultiplier detector allows the 300-380 nm region to be accurately monitored at the protein concentrations used in the experiment. The latter was critical for the characterization of **P***.

In the single turnover reaction of $\mathbf{H^{red}}$ with H33A MMOB and furan, we can observe the rapid formation of an intermediate species with a t_{max} of 0.25 seconds, which subsequently decays over 10 seconds to the resting diferric form of the enzyme, $\mathbf{H^{ox}}$ (Figure 3.3). While the formation of this transient intermediate can be observed across the whole wavelength region scanned, the decay can be only seen at long wavelengths between 535 nm and 685 nm. The absence of this decay phase at shorter wavelengths occurs because the formation of diferric $\mathbf{H^{ox}}$ has the same rate constant as the decay of the intermediate. $\mathbf{H^{ox}}$ possesses an electronic absorption band with a large extinction coefficient in the near-UV region (Figure 3.1), which masks the decay of the intermediate.

In order to obtain accurate rate constants and estimates for the relative accumulations of the intermediates, a global analysis was performed using a data set accumulated over a range of wavelengths. This technique utilizes the entire data set and adds the additional constraint of accommodating the kinetic model at multiple wavelengths. The global fitting analysis of the spectra-kinetic data supports the following kinetic model for the single turnover reaction: **O** → **P*** → **P** → $\mathbf{H^{ox}}$. The rate constants determined for the steps in the reaction are: $k_1 = 21.9 \pm 0.5$ s^{-1}, $k_2 = 0.33 \pm 0.03$ s^{-1}, $k_3 = 1.76 \pm 0.05$ s^{-1}. The result of this fit is shown as an overlay of the time course at 625 nm in Figure 3.3. The formation rate constant of 21.9 s^{-1} for the first intermediate is similar to the decay rate constant of compound **O**, as measured by following the decay of its characteristic integer spin $g = 16$ EPR signal (Figure 3.2) [81]. The decay rate constant for this intermediate (0.33 s^{-1}) is also similar to the formation rate constant of 0.38 s^{-1} for **Q** (in actuality **P)** in the single turnover monitored by diode array (Figure 3.1) [157]. This confirms the identity of the observed intermediate as compound **P***. It also implies that the observation of the single turnover reaction starts with compound **O**. The formation of **O** is not observed here as it likely occurs in the dead time of the stopped flow instrument and has spectral properties indistinguishable from those of $\mathbf{H^{red}}$.

The global fit allows estimation of the time dependent accumulation of each intermediate as shown in Figure 3.4. **P*** is predicted to accumulate to approximately 90 % of the total active site concentration after 250 ms. Later, a small accumulation of intermediate **P** is also predicted as **P*** decays. The observed decay rate constant of **P** (1.7 s^{-1}) is slightly smaller than is observed in a single-turnover reaction in the presence of wild type MMOB (2.7 s^{-1}) [157]. This is not unexpected because the functionally related MMOB H5A variant has been shown to decrease this rate constant to 1.71 s^{-1} [157]. The global fit to the MMOH reaction does not require the accumulation of compound **Q** between the decay of **P** and the formation of $\mathbf{H^{ox}}$. This is expected because the presence of 6 mM furan will completely quench **Q** ($k_{form} = 1.7$ s^{-1}, $k_{decay} \sim 72$ s^{-1} as calculated from the second order rate constant of **Q** decay with furan) [94, 157]. Compound **P*** is a catalytically competent intermediate because its rate constant for decay exceeds the turnover number for furan as a substrate at 4 °C ($k_{cat} = 0.12$ s^{-1}) [94, 157].

3.3.3 Electronic absorption spectrum of P*

Multicomponent analysis of the data shown in Figure 3.3 allows the electronic absorption spectrum of **P*** to be approximated (Figure 3.5). It has a maximal absorption in the near-UV region (ε_{325} = 12000 M^{-1} cm^{-1}) which is very similar to that observed for $\mathbf{H}^{red}$ (ε_{325} = 11100 M^{-1} cm^{-1}). In fact, the entire electronic absorption spectrum of **P*** is remarkably similar to those of $\mathbf{H}^{red}$ and **O**, suggesting that they are similar species (Table 3.1).

Intermediate species	$\Delta\varepsilon_{325}$ (M^{-1} cm^{-1})	$\Delta\varepsilon_{430}$ (M^{-1} cm^{-1})	$\Delta\varepsilon_{700}$ (M^{-1} cm^{-1})
P*	900	-	-
P	5160	1800	1900
Q	12300	8400	1700

Table 3.1 – The difference extinction coefficients for the MMOH intermediates has been obtained after subtracting the electronic absorption background of $\mathbf{H}^{red}$. These values pertain to the case in which all the diiron clusters in fully occupied MMOH react with oxygen with the native rate constant to form compound **Q**.

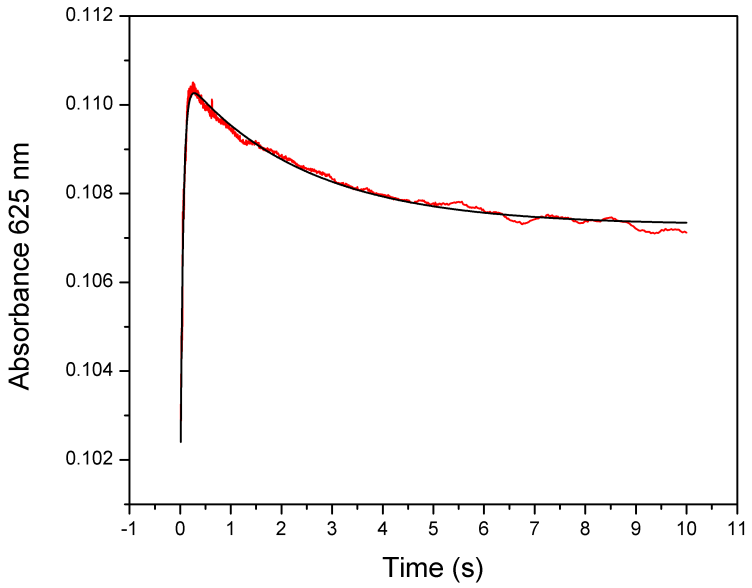

Figure 3.3 – Single wavelength kinetic trace at 625 nm for the single turnover reaction of MMOH with H33A MMOB (83 μM reactive MMOH active sites) and 6 mM furan at pH 7.0 and 4 °C, indicates the rapid formation and decay of a transient species. The fit to the kinetic data (black trace) is obtained from a global fit to the multiple wavelength data (325 nm - 685 nm).

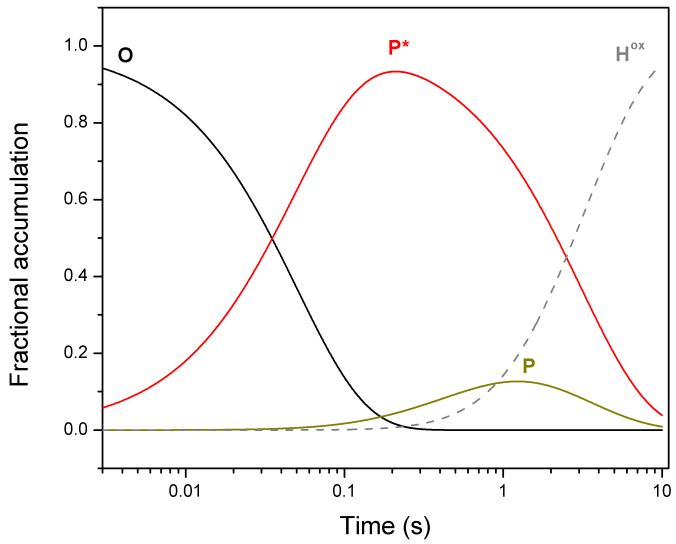

Figure 3.4 – Global fitting analysis to the spectra-kinetic data of single turnover of MMOH in the presence of H33A MMOB and furan indicates the temporal accumulation of intermediate **P*** to almost 90 % of the enzyme active sites. Compound **P** is also observed to accumulate to a marginal level of 10 % demonstrating the ability of the global fitting analysis to identify minor species.

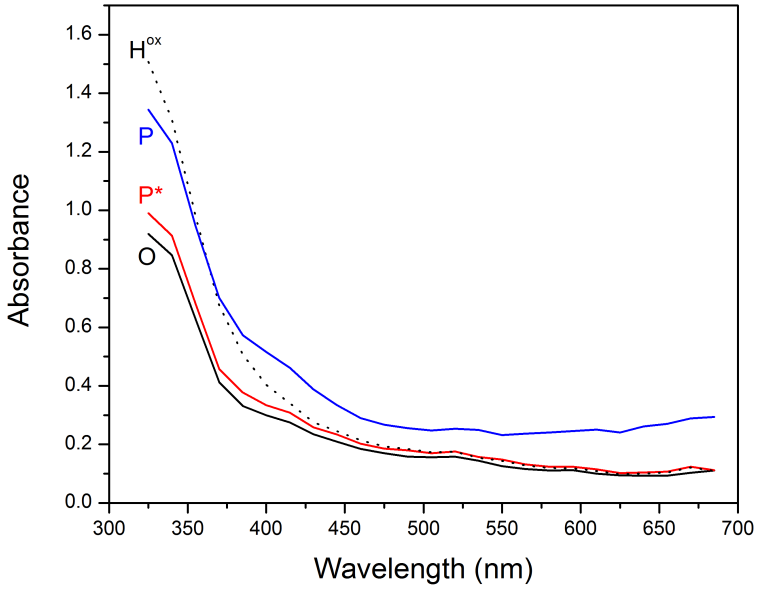

Figure 3.5 – The pure component spectrum of compound **P*** as obtained by global fitting of spectra-kinetic data compared to those of compound **O**/**H**^{red} and **H**^{ox}. The pure component spectrum of **P** (from a MMOH reaction with WT-MMOB) has been overlaid for a comparison with **P***.

3.3.4 pH dependence of P* formation and decay steps

The pH dependence of the kinetic steps of formation and decay of compound **P*** has been studied in order to draw a comparison with the observation of pH dependence of **O** decay and **P** formation when using wild type MMOB [98]. The results clearly indicate that the formation of **P*** is pH independent while its decay is a proton dependent step (Figure 3.6). Based on the similarity with the pH dependence of the kinetic steps observed when using wild type MMOB, this data strongly corroborates the **O** → **P*** → **P** → $\mathbf{H^{ox}}$ kinetic model based on electronic absorption spectroscopy.

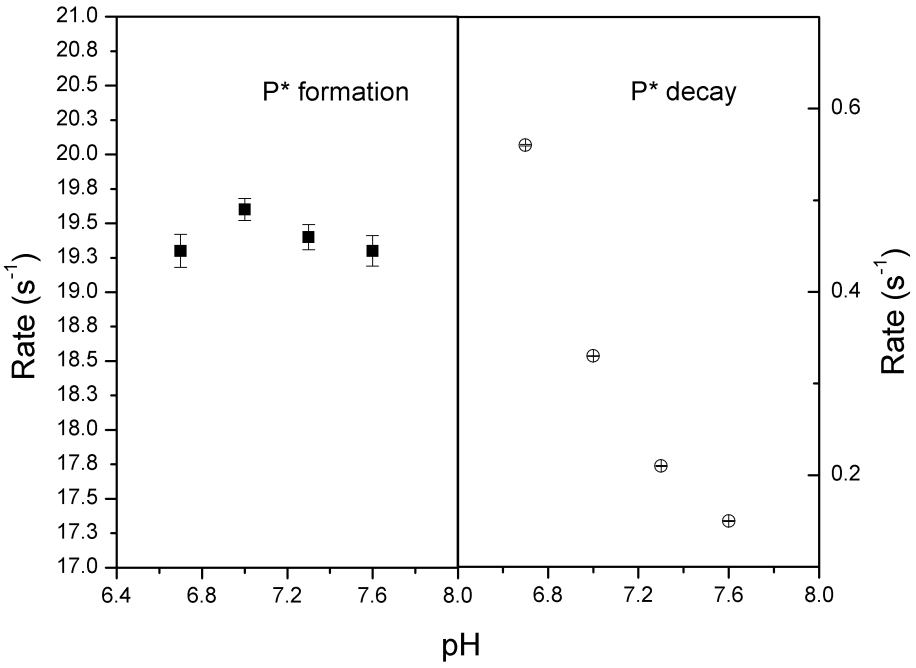

Figure 3.6 – pH dependence profile of the kinetic steps of **P*** formation and decay. The rate constants are obtained from a global fit of $\mathbf{H^{red}}$ single turnover reaction with H33A MMOB in the presence of furan at each pH point.

3.3.5 Mössbauer characterization of compound P*

The electronic properties of **P*** were probed using Mössbauer spectroscopy of samples from the reaction time course made using ^{57}Fe enriched $\mathbf{H}^{red}$ and H33A MMOB in the absence of a substrate. Samples were rapid freeze quenched at 312.5 ms and 3 s after mixing with O_2 where **P*** and **Q**, respectively, are near maximum levels. Analyses of the Mössbauer spectra were complicated by the presence of a large fraction of unreactive diferrous MMOH that is always encountered for MMOH from both *M. t.* OB3b and *M. c.* Bath [99, 115]. The starting $\mathbf{H}^{red}$ sample shown in Figure 3.7A reveals a mixture of two exchange-coupled diferrous cluster types. These cluster types have been previously described, and are known to appear in varying ratios [68, 181]. Very little change in this spectrum is observed for the sample of Figure 3.7B frozen at the time when **P*** should account for 90 % of the fraction of the sample that reacts rapidly with O_2 (~36 %). The spectrum of Figure 3.7C shows that approximately 18 % of the sample, or about 50% of the reactive fraction has converted to compound **Q**. This is the expected fraction based on rate constants for intermediate conversion determined in the solution kinetic study described above as shown in Figure 3.8. Consequently, it is likely that the sample of Figure 3.7B contains the expected fraction of **P***. This being the case, **P*** has a diferrous cluster quite distinct from that of the diferric peroxo intermediate **P**.

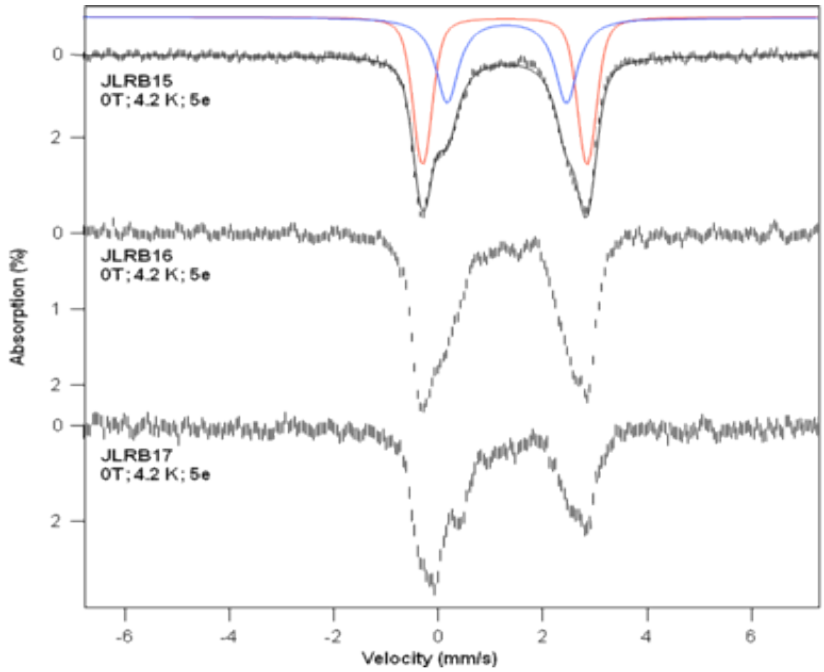

Figure 3.7 – RFQ Mössbauer spectra from the time course of the reaction of $\mathbf{H}^{red}$ in the presence of stoichiometric H33A MMOB with a saturated solution of O_2.

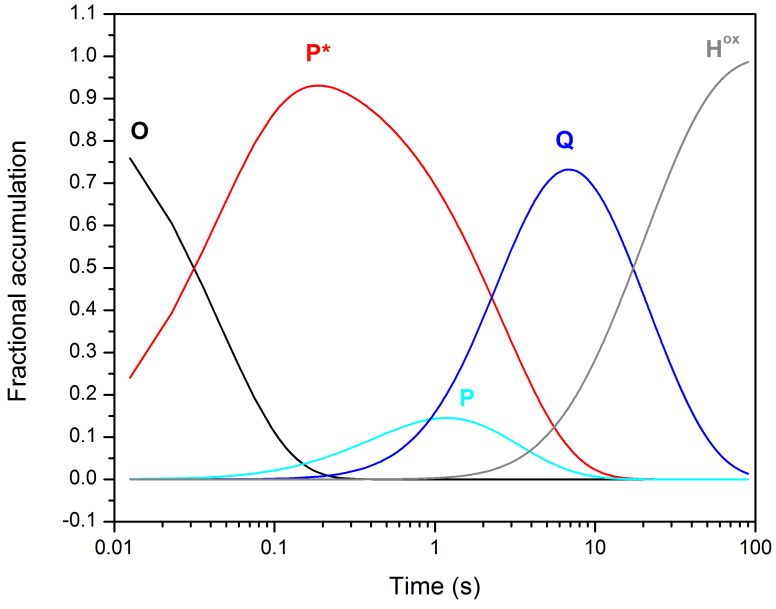

Figure 3.8 – Speciation plot for the single turnover reaction of MMOH with H33A MMOB used to make the Mössbauer samples for **P*** (312.5 ms) and a later time point for **Q** (3 s). The speciation plot accounts for the reactive MMOH population (36 % of total active sites). The unreactive fraction of MMOH is present in the diferrous state at these time points.

3.3.6 Transient kinetics of P* accumulation with other H33 MMOB mutants

In order to discern the role of the H33A MMOB mutation in the decrease in the rate constant of **P*** decay, a range of H33 site-directed MMOB mutants has been created. Each of the H33 MMOB mutants significantly decreases the rate constant of **P*** decay from that observed with wild type MMOB, in a manner similar to H33A MMOB (Table 3.2).

MMOB species	Rate constant of P* decay (s^{-1})
WT-MMOB	10 ± 0.5
H33A	0.33 ± 0.03
H33G	0.34 ± 0.05
H33F	0.43 ± 0.03
H33T	0.50 ± 0.07
H33E	0.18 ± 0.07

Table 3.2 – Variation of the rate constant of **P*** decay with H33 MMOB mutants. The rate constant of **P*** decay is obtained from a global fit of single wavelength data at 330 nm, 430 nm, 550 nm and 700 nm of a single turnover reaction of MMOH with the H33 MMOB mutants at pH 7.0, 4 °C in the absence of substrate. The rate constant of **P*** decay is similar to the apparent formation rate of **Q**.

3.4 DISCUSSION

The combined use of H33A MMOB to provide a constriction in the flow of the reaction cycle, inclusion of substrate to eliminate the strong background chromophore from compound **Q**, and the use of the spectra kinetic data collection method has allowed the observation of the transient intermediate **P*** in the single turnover reaction of MMOH. Our early transient kinetic studies strongly suggested that a reaction cycle intermediate occurs after **O** and before **P**, and that it should accumulate to observable levels (maximum ~45 %) [81, 98, 157]. Nevertheless, direct detection has proven difficult. The current results show that this was the case because intermediates $\mathbf{H}^{red}$, **O** and **P*** have very similar optical spectra and also because the kinetics of intermediate interconversion dictate that a high background from the more strongly absorbing **P** and **Q** is always present when wild type MMOB is utilized in the reaction. Based on the observation that the decay of **O** results in the loss of the g = 16 EPR signal characteristic of the diferrous cluster, we originally proposed that **P*** would contain one or two Fe^{III} ions in some sort of oxygen-bound cluster [81, 94, 98]. This now appears not to be the case, suggesting that the critical step in the preparation of the cluster to bind and activate O_2 occurs by a novel mechanism. This aspect of the MMOH reaction cycle is discussed here.

3.4.1 The diferrous nature of P* is not consistent with a superoxo or peroxo cluster

The Mössbauer spectrum of **P*** shows that the diiron cluster is diferrous in nature (Figure 3.7). Thus, **P*** can be neither an $Fe^{II}Fe^{III}$-superoxo intermediate nor an $Fe^{III}Fe^{III}$-peroxo intermediate distinct from **P**. Considering that the spectroscopic characterization of **P** indicates that it is a $Fe^{III}Fe^{III}$-peroxo intermediate of some sort, [99, 115] the current spectroscopic and kinetic data suggest that the diiron cluster in MMOH proceeds directly from a diferrous state in **P*** to a bridged peroxo-bound diferric state in **P** without an intervening $Fe^{II}Fe^{III}$ intermediate detectable on the millisecond time scale. This experimental conclusion matches the prediction from density functional theory studies, which indicate that the binding of oxygen to one of the two iron atoms to form a $Fe^{II}Fe^{III}$-superoxo intermediate is thermodynamically unfavorable [86, 207]. These observations may mean that O_2 is bound in the active site in **P*** but does not bind the cluster iron atoms, as we have proposed for intermediate **O** [98]. However, O_2 must be present for **P*** to form and its optical spectrum is subtly different from those of $\mathbf{H}^{red}$ and **O**. One possibility is that O_2 binds weakly to the cluster, displacing the solvent water molecule that has been shown to bridge the iron atoms in the crystal structure of diferrous MMOH from the nearly identical MMOH from

M. c. Bath [208]. However, VTVH MCD and CD studies indicate that the iron atoms of the diferrous cluster are both 5-coordinate indicating that the additional solvent ligand of the crystal structure is likely to be weakly bound [86, 209]. If the conversion of **O** to **P*** involves displacement of this solvent and subsequent O_2 binding to the cluster, then O_2 must bind with little electron transfer from the cluster iron atoms. While there is no precedent for this in O_2 reactions with diiron clusters, we have recently shown that a weak Fe^{II}-O_2 complex can form in the active site of a mononuclear Fe^{II} dioxygenase when an active site mutation prevents efficient electron transfer to the oxygen [210]. Computational studies for both nonheme and heme systems have shown that O_2 binding to Fe^{II} is comparatively weak, a useful property in systems where modulation of O_2 affinity is important [211-214]. Transfer of electron density from the Fe^{II} to the O_2 is often far from complete, and it is strongly dependent on factors such as the state of hydrogen bonding or charge interactions in the active site, as well as the nature of the ligand trans to the metal bound O_2 [5, 215]. In the current case, replacing solvent with weakly bound O_2 in the coordination sphere (Scheme 3.2, a or b pathway) would be consistent with the minor increase in the intensity of the optical spectrum of **P*** compared with that of **O**.

3.4.2 Origin of the loss of the g = 16 EPR signal in P*

The loss of the g = 16 EPR signal as **O** converts to **P*** provides an important clue to the structure of the diferrous **P*** intermediate. If the loss of this signal is not due to cluster oxidation, then it must be due to a change in the electronic nature of the exchange coupling between the iron atoms. The g = 16 EPR signal from the diferrous cluster in $\mathbf{H}^{\mathbf{red}}$ and **O** arises from a $\Delta m_i = 0$ transition of an inverted zero-field split S = 4 multiplet (D_1, $D_2 < 0$) formed as a result of a ferromagnetic coupling between the two S = 2 high-spin Fe^{II} atoms [68, 95, 209]. The exchange coupling constant (J) between the iron atoms is small (J = 0.3 – 0.5 cm^{-1}) [209]. A similar ferromagnetic coupling of the diiron site in toluene-4-monooxygenase (T4mo) leads to an integer-spin g = 16 signal [86, 216]. In contrast, the diferrous clusters of related carboxylate-bridged diiron enzymes such as ribonucleotide reductase (RNR) and stearoyl-acyl carrier protein bound Δ^9-desaturase are weakly anti-ferromagnetically coupled (J = -0.5 cm^{-1} and -1.0 cm^{-1}, respectively with unequal ZFS values; $D_1 < 0$, $D_2 > 0$), leading to an EPR-silent S = 0 spin state [217, 218]. This difference in the sign of the exchange coupling constant between MMOH/T4mo and RNR/Δ^9-desaturase has been attributed to the altered binding of a bridging carboxylate residue to the diiron cluster in the reduced state [219].

Glu243 is bound in a μ-1,1 fashion to the diferrous diiron cluster in $\mathbf{H^{red}}$ (and presumably **O**) as is the homologous Glu231 residue in T4mo [66, 77]. In comparison, the homologous carboxylate residue in RNR (Glu238) and Δ^9-desaturase (Glu229) bind the diiron cluster in a μ-1,3 fashion [220, 221]. This is in accord with calculations that suggest that a μ-1,1 bridging carboxylate mediates ferromagnetic coupling whereas a μ-1,3 bridging mode leads to a anti-ferromagnetic coupling between the two iron atoms [219]. Crystal structures of $\mathbf{H^{ox}}$ from *M. t.* OB3b as well as $\mathbf{H^{ox}}$ and $\mathbf{H^{red}}$ from *M. c.* Bath MMOH show that Glu243 is the most mobile residue among the ligands coordinating the diiron cluster [63, 64, 208]. In the resting antiferromagnetically coupled $\mathbf{H^{ox}}$ state, Glu243 is bound solely to Fe2 in a monodentate fashion. It then shifts to the bridging μ-1,1 binding mode (and shifts to bidentate binding to Fe2) upon reduction of $\mathbf{H^{ox}}$ to $\mathbf{H^{red}}$. Another shift in Glu243 during the **O** to **P*** transition might lead to antiferromagnetic coupling and loss of the integer-spin g =16 signal. Compound **P** is diamagnetic due to anti-ferromagnetic coupling between the iron atoms [101]. As such, it is plausible that the change from ferromagnetic coupling in **O** to antiferromagnetic coupling in **P** might occur in the conversion from **O** to **P***.

One possible shift in Glu243 would move it back to the position it occupies in $\mathbf{H^{ox}}$, namely monodentate binding to Fe2. However, this would result in only one carboxylate bridge and one weak solvent or O_2 bridge between the two Fe^{II} atoms, leading to a less well organized cluster. This would be likely to decrease the intensity of the optical spectrum, in contrast to the increased intensity that is observed. We do note that this orientation for Glu243 would be compatible with intermediate **P** because the homologous Glu231 in the structurally characterized peroxo intermediate of T4mo assumes a similar position [111]. While it seems likely that the peroxo intermediate of T4mo goes on to form a **Q**-like species, it has never been observed. This suggests that the forces that stabilize the intermediates, if not the intermediates themselves, differ. Two perhaps more feasible changes in the orientation of Glu243 in MMOH that would result in a new μ-1,3 bridging carboxylate, and thus might lead to antiferromagnetic coupling, are illustrated in Scheme 3.2. In pathway (a), the bond from the bridging oxygen of Glu243 to Fe2 is broken. This change requires the least structural rearrangement. In pathway (b), Glu243 displaces the axial solvent on Fe1, shifting it to an equatorial position.

Three facts are known about intermediates **P** and/or **Q** that must be reconciled in considering the models shown in Scheme 3.2 and other models proposed from DFT studies [103, 105, 120-122, 126, 127]. First, the two iron atoms are in very similar electronic environments in **P** and in **Q** [99, 102, 115]. Second, pH studies reported here and in previous studies of both *M. t.* and *M. c.* MMOH single turnover kinetics show that the **O** to **P*** transition does not require a proton transfer, whereas both the **P*** to **P** and **P** to **Q** transitions are pH dependent [98, 100]. A proton inventory study suggests that each of the pH dependent steps involve a single proton hop, although one essential and one nonessential proton translocation are predicted based on fitting the pH dependency for the **P** to **Q** transition in *M. c.* MMOH [98, 100 , 115]. Third, the Mössbauer spectrum of **P** exhibits an isomer shift of about 0.66 mm/s which is similar to that observed for deprotonated peroxo ligands [21, 222-224]. This suggests that a proton is transferred to some moiety other than the bridging peroxo group as **P** is formed. It is also relevant to note here that metal centers in enzymes tend to maintain a constant net local charge, and this appears to be a net charge of zero for the structurally characterized states of MMOH [225-227]. For this to be true in the case of **P** formation, the proton transfer must occur between groups bound to the diiron cluster. Charge balance at each iron requires that the donor and acceptor groups be associated with the same iron atom. Finally, the diamond core structure for **Q**, which is consistent with both experimental and computational studies, requires that the equatorial bridging oxygen from either solvent or Glu243 on the face opposite the peroxo moiety of **P** be displaced as **Q** forms [99, 103, 105, 120-122, 126, 127].

Scheme 2

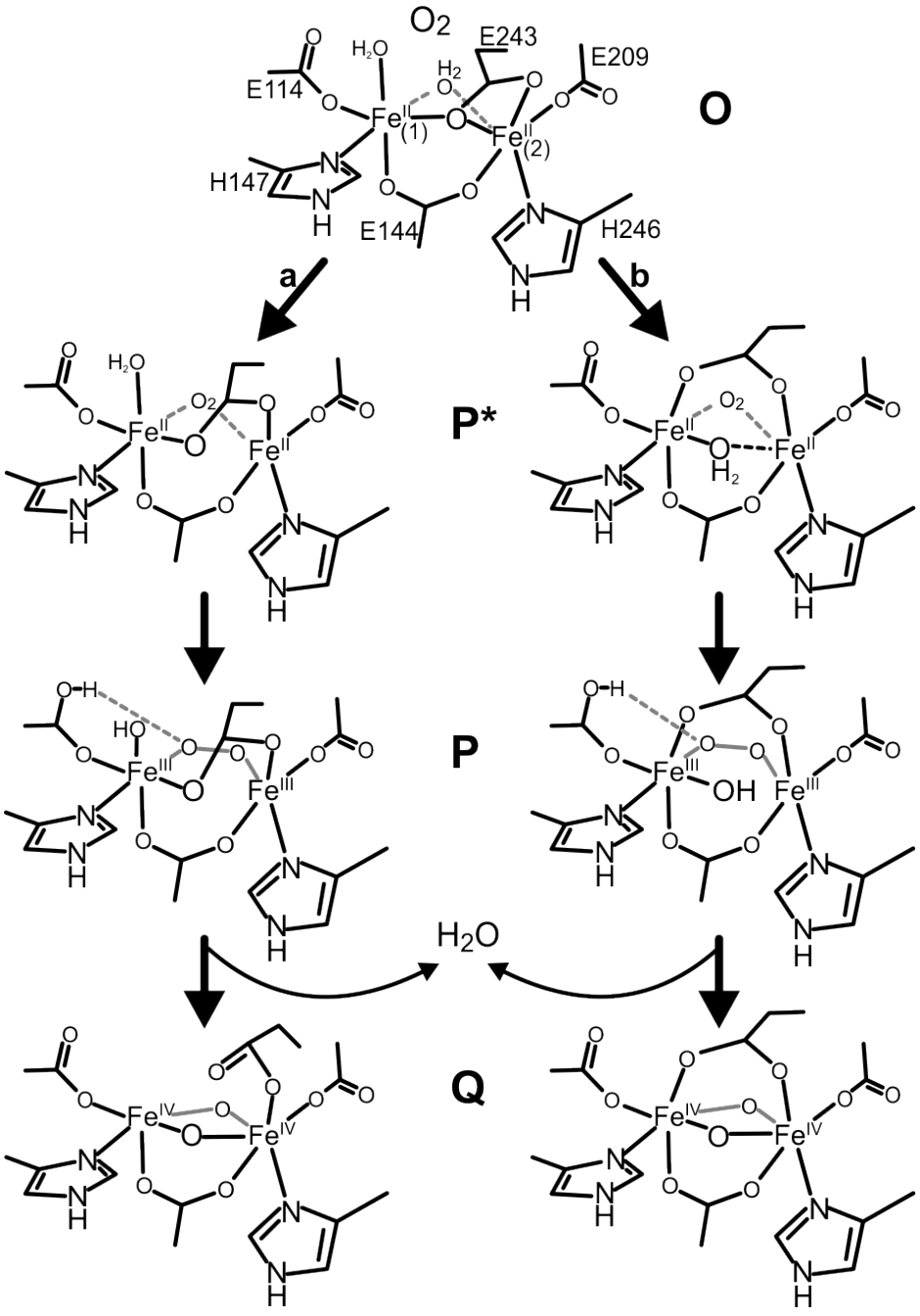

Scheme 3.2 – Proposed structures of MMOH single turnover cycle intermediates.

All of the intermediates shown in Scheme 3.2 maintain a neutral net charge. Glu114 is proposed to play the same role in each pathway by accepting a proton from Fe1-bound solvent and eventually donating it to the peroxo moiety to promote O-O bond cleavage [98]. This maintains the local charge on Fe1 and satisfies the required one hop proton transfer process. The protonation of the carboxylate residue and its hydrogen bonding interaction with the bridging peroxide moeity is supported by information obtained from synthetic diiron model compound mimics of **P** and DFT studies of oxygen activation in RNR [228, 229]. Pathway (a) has the advantage that it requires the minimum structural reorganization to form **P*** and **P**. However, during the **Q** formation step, the net charge on each individual iron atom and their coordination numbers become different. This would be likely to evoke distinguishable Mössbauer spectra for the two iron atoms, which is contrary to what is observed for **Q** from *M. t.* OB3b. The coordination number disparity can be addressed by retaining the solvent shown as being released, on Fe1. Indeed, some DFT computations show that this solvent is retained and becomes hydrogen bonded to Glu243 [103, 120, 121]. Pathway (b), requires signficantly more structural reorganization to form **P*** than pathway (a), but once it is formed, no further rearrangement of Glu243 or solvent is required to form **Q**. Furthermore, the iron atoms possess a net charge that remains balanced throughout as well as identical coordination enviroments. One unusual property for **Q** is the exceptionally short Fe-Fe distance, nominally 2.5 Å [99]. DFT computations predict slightly longer distances, but both the symmetry of the iron sites and the Fe-Fe distance are mimicked most effectively by formation of the second carboxylate bridge by Glu243 in addition to the oxygen diamond core structure as shown in pathway (b) [105, 122].

While the explanation for the loss of the $g = 16$ signal as **P*** forms attributed to a change from ferromagnetic to antiferromagnetic coupling is reasonable based on numerous precedents from other diiron cluster containing enzymes and models, there are other possible origins for this change. These include a signficant increase in zero field splitting or loss of the inverted zero field splitting seen in $\mathbf{H}^{red}$ or **O**. A better understanding of the nature of the exchange-coupling system of **P*** would be useful in assigning its structure. This system can, in principle, be elucidated by high-field Mössbauer studies. However, the presence of a large background from unreactive diferrous active sites has not allowed us to achieve the required resolution to date.

3.4.3 Comparison with intermediate P* from *M. capsulatus* Bath

An intermediate occuring before H_{peroxo} in the *M. capsulatus* Bath MMOH single turnover cycle (*M. c*. **P***) has been observed that differs from the **P*** reported here in its oxidation state [100]. An $Fe^{III}Fe^{III}$ oxidation state assignment in the case of *M. c*. **P*** was based on the observation of an electronic absorption spectrum similar to that of H_{peroxo} that was obtained by a global fit of the single turnover absorption data at two diagnostic wavelengths in the presence of wild type MMOB and methane. While the presence of a substrate in both studies quenches the large absorption background arising from **Q**, the H33A MMOB mutant used in the current report provides the additional advantages of increasing the yield of **P*** and reducing the background absorption from **P**. Both studies are hampered by the presence of a large fraction of unreactive $\mathbf{H^{red}}$. In our case, the oxidation state of the intermediate was directly determined using Mössbauer spectroscopy, making it clear that there is no $Fe^{III}Fe^{III}$ species present at the time when **P*** maximizes. The kinetics of intermediate interconversion also differ significantly. The **P*** formation rate constants at 4 °C and pH 7.0 are 26 s^{-1} and 6.7 s^{-1}, for the *M. t.* and *M. c.* enzymes in the presence of MMOB, respectively. Similarly, the **P** formation rate constants are reported to be 9 s^{-1} and 0.75 s^{-1} using wild type MMOB for *M. t.* and *M. c.* enzymes, respectively. The alignment of the **P*** formation rate constant in the *M. c.* MMOH and that of **P** in the *M. t.* system, raises the possibility that the **P*** observed in the former enzyme is, in fact, another form of **P** accounting for its similar optical spectrum. Thus far, we have not observed evidence for this species in the *M. t.* system.

3.4.4 H33 MMOB mutants may cause a structural change in the MMOH active site

In order to probe the manner of decrease in the rate constant of conversion between **P*** and **P** in the MMOH catalytic cycle with H33A, a variety of other site-directed H33 MMOB mutants were created. The rate constant for this catalytic step with both polar and non-polar amino acid variants remains slow compared to the MMOH reaction with wild type MMOB (Table 3.2) demonstrating that a histidine residue is essential at this position. The histidine residue is unique in possessing a pK_a close to pH 7.0 and its proton donating ability may not be substituted by the H33E MMOB mutant, thus maintaining the possibility that the decrease in the rate constant is due to an impaired proton donation in the proton dependent step. However, such a proton donation through a solvent chain starting at H33 on the MMOH surface and terminating at the diiron cluster would be at odds with the linear proton-inventory plot for this catalytic step that indicates a single proton hop [98]. Thus, it is likely that the mutation at the H33 position impairs the ability of MMOB to effect

a structural change at the diiron site of MMOH, thereby causing a decrease in the rate constant of **P*** conversion to **P**.

3.4.5 Conclusion

In summary, this study has elucidated the electronic absorption and Mössbauer spectra of intermediate **P*** in the single turnover cycle of *M. t.* MMOH. The results indicate that **P*** is a diferrous intermediate which lacks an integer-spin $g = 16$ EPR signal. Two possible structures of **P*** have been proposed where a carboxylate shift of the Glu243 residue in the conversion from **O** to **P*** establishes the changes in geometry and spin state required by the diiron cluster in order to bind O_2 and form the peroxo intermediate **P**. These proposed structural changes would also anticipate and facilitate the cleavage of the O-O bond by establishing an appropriately placed proton donor. Finally, they would allow formation of the diamond core structure of intermediate **Q** with minimal structural rearrangement. The association of O_2 with the diferrous cluster is proposed to occur stepwise following an effectively irreversible binding in the hydrophobic enzyme active site. A subsequent and relatively slow displacement of solvent from the metal center and formation of a weak Fe^{II}-oxygen complex would overcome the most difficult steps in metal-O_2 complex formation and facilitate formation of the strong peroxo complex needed for O-O bond cleavage in the next step. Steps similar to this occur in other non-heme iron enzymes, and may reflect the rather weak affinity of O_2 for the metal in nonheme Fe^{II} containing enzymes in the absence of stabilizing interactions [210].

CHAPTER 4

Time resolved resonance Raman characterization of compound Q

4.1 INTRODUCTION

The oxygen-mediated oxidation of methane to methanol by soluble methane monooxygenase (sMMO) is a remarkable feat of enzymatic catalysis, as methane possesses the largest C-H bond dissociation energy among aliphatic hydrocarbons (105 kcal $mole^{-1}$) [44]. This is emphasized by the considerably higher temperatures (>1100 K) required for the catalytic oxy-methane reforming reaction integral to the industrial conversion of methane to synthesis gas [230]. The ability of sMMO to oxidize methane at standard temperature and pressure arises from the formation of the methane reactive intermediate; compound **Q**, which forms in the hydroxylase component (MMOH) during the catalytic cycle [94, 115].

The key to deciphering the chemical mechanism of hydroxylation of methane by sMMO lies in the characterization of the electronic and structural nature of compound **Q**. The electronic absorption spectrum of **Q** shows electronic transitions at 330 nm and 430 nm with large extinction coefficients (ε_{430} = 7500 M^{-1} cm^{-1}) [94, 115]. Mössbauer spectroscopy indicates that the two iron atoms of the diiron cluster in **Q** (Fe1 and Fe2) are present in a high-spin Fe(IV) oxidation state with very similar environments (δ = 0.17 mm/sec; ΔE_Q = 0.53 mm/sec) [102]. The high-field Mössbauer spectrum of **Q** also suggests that the iron atoms are coupled anti-ferromagnetically. This diamagnetic nature of the diiron cluster does not allow direct characterization of **Q** by techniques such as EPR and MCD. However, an EXAFS study of **Q** has provided key structural information about the arrangement of the iron and oxygen atoms in the high-valent intermediate. The characteristic features include a short Fe-Fe distance of 2.46 Å and two Fe-O bonds per iron atom at 1.77 and 2.05 Å, respectively [99]. The shorter Fe-O bond is too long to be described as a terminal Fe(IV)-oxo group, as observed in the porphyrin iron(IV)-oxo moieties in compound I and II of peroxidases [116]. However, this distance compares well to those of the Fe-μ-O bridges in oxo-bridged diiron model compounds [117]. The observation of an additional longer Fe-O bond for each iron led to the proposal of an asymmetric bis-μ-oxo "diamond core" for the diiron cluster in **Q** (Figure 4.1). This can be envisioned as a head to tail dimer of two Fe^{IV}=O units to form the diamond core [99]. The bridging glutamate 144 residue in the diferrous state of the cluster is understood to also coordinate the iron atoms, as a tri-bridged diiron cluster would help to account for the unusually short Fe-Fe distance. Indeed, this distance

may be further shortened by the Fe2 ligand Glu243 contributing either a second bridging carboxylate or a hydrogen bond to a solvent bound to Fe1.

A more detailed electronic and structural characterization of **Q** can be made using resonance Raman (rRaman) spectroscopy. Information regarding the Fe-O bond vibration frequency would provide answers to many questions about **Q** such as the degree of asymmetric binding of the oxygen atoms to the iron atoms. It would also be important in testing the bridging bis-μ-oxo model for the Fe-O bonds. The use of isotopic oxygen in both oxygen gas and solvent water could help identify the source of the both the Fe(IV)-O oxygen atoms in **Q**, which would give insight into whether the O–O bond cleavage in the conversion from compound **P** to **Q** is heterolytic or homolytic. The use of deuterated solvent could also provide information regarding the protonation states of the Fe-O moieties. Finally, the combination of structural data from EXAFS and rRaman studies would be invaluable towards validating structural models for **Q** based upon density functional calculations.

Compound **Q** should be amenable to rRaman studies on account of its broad electronic absorption spectrum with large extinction coefficients. However, repeated attempts at obtaining a rRaman spectrum of frozen samples of **Q** by several laboratories over the past two decades have not been successful. This may arise in part from scattering due to multiple reflections by frozen samples which increases the background signal due to stray light that passes through wavelength filters [231]. This background signal from frozen samples may obscure the rRaman signal from **Q**. Furthermore, the opaque nature of polycrystalline samples complicates the optimization of signal collection at a favorable geometry. The inability to obtain a rRaman spectrum may also arise from the photolabile nature of **Q**. This intermediate has been demonstrated to be photolabile in MMOH from *M. capsulatus* Bath [143]. In sMMO from *M. trichosporium* OB3b, the use of white light from the lamp in the photodiode array setup causes the decay rate of **Q** to increase 3 fold over the rate constant measured with monochromatic light at 430 nm. There is precedent for such a photodecomposition of high-valent iron intermediates in the laser beam with compound I of horseradish peroxidase [232]. Thus, although scattering and other problems typically encountered when using frozen samples may have complicated the measurement of a rRaman spectrum of **Q**, the large flux of photons from the laser beam may also have accelerated its decay.

Many of the problems encountered in measuring rRaman spectra of frozen samples can be overcome by employing a continuous flow Time Resolved Resonance Raman (TRRR) technique. The combined advantages of a liquid sample and reduced photodecomposition owning to a low residence time for the intermediate in the laser probe might allow for the observation of the rRaman signal for compound **Q**. Indeed, preliminary TRRR experiments on **Q** by Drs. Jeremy Nesheim and Sang Kyu Lee in our laboratory in collaboration with Dr. Gerald T. Babcock and Dr. Denis Proshlyakov at Michigan State University had indicated the presence of a rRaman signal [233]. We have continued this work successfully in collaboration with Dr. Proshlyakov and Eric Bergeron at Michigan State University. We report here the first unambiguous rRaman signal from compound **Q** in the single turnover reaction cycle of MMOH. This is also the first reported observation of a rRaman signal from a high-valent diiron(IV,IV) enzyme intermediate

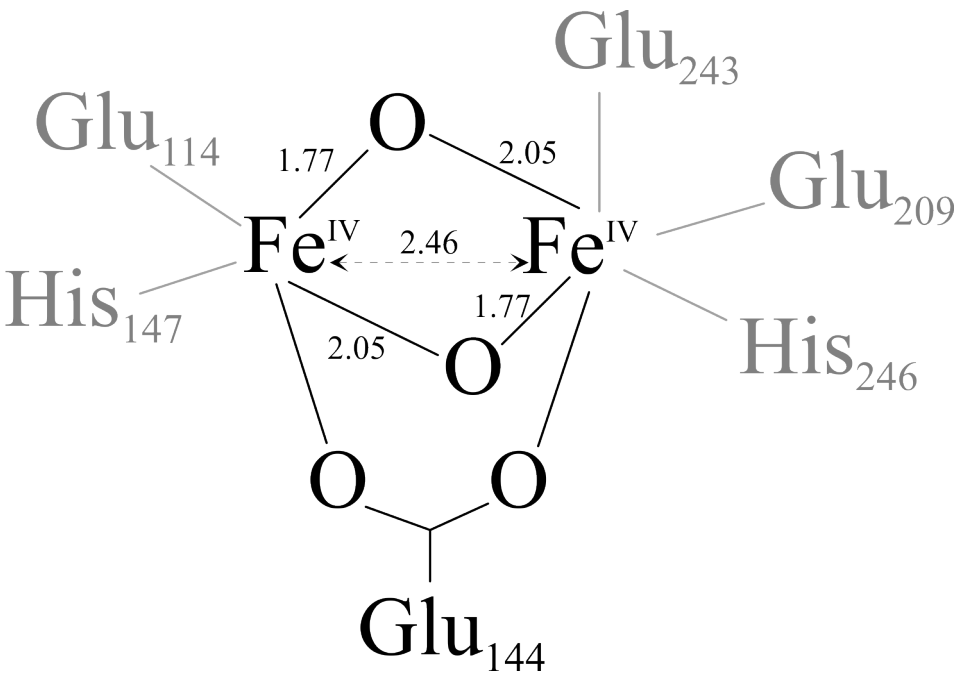

Figure 4.1 – The putative structure of the diiron cluster in **Q**. The portion of the cluster with definitive experimental information available is shaded in black. The ligands to the diiron cluster (shaded grey) are inferred to bind the iron atoms while remaining unchanged from the starting diferrous form of the cluster. The Fe-Fe distance and those for the Fe-O bonds are provided in Å.

4.2 MATERIALS & METHODS

Chemicals - All chemicals used were of the highest grade available and were purchased from Sigma Aldrich. The PD-10 desalting columns were obtained from GE Healthcare. $^{18}O_2$ was obtained from ICON. The asymmetrically labeled oxygen isotope (^{16}O-^{18}O) was synthesized by Dr. E. H. Appelman from Argonne National Laboratory. The synthesis of this oxygen isotope has been described in detail in the supplementary text for the following reference [234]. D_2O was obtained from Cambridge Isotope Laboratories.

Biological materials - MMOH was purified from *M. trichosporium* OB3b according to a protocol described in chapter 1 of this thesis. MMOB was purified from a heterologous expression system in *E. coli* according to a purification protocol described previously [162] and amended slightly according to a description in chapter 1 of this thesis. The nature of the TRRR experiment requires a large amount of the MMOH protein, estimated to be about 15 g for the experimental results presented here.

Sample preparation - Anaerobic solutions of MMOH in 50 mM MOPS, pH 7.0, 5% glycerol and MMOB in 50 mM MOPS, pH 7.0 were prepared by exchanging the headspace gas with argon while stirring on ice for 1 hour. The chemical reduction of MMOH was conducted inside an anaerobic glove bag (MBRAUN) by the addition of methyl viologen (200 μM) and sodium hydrosulfite (4 mM) while stirring for 15 minutes at room temperature. MMOH was subsequently separated from the small molecule reducing agents by passage through a Sephadex G-25 PD-10 desalting column equilibrated in 75 mM MOPS, pH 7.0, 5% glycerol, 0.1% Triton X-100, 200 μM $Fe(NH_4)_2SO_4$ and 2.0 mM L-cysteine. The iron/cysteine-containing buffer was incubated for 1.5 hours on ice (until the purple color dissipated) before being made anaerobic. The glycerol stabilizes the diferrous enzyme while Triton X-100 prevents protein aggregation inside the flow cuvette under laser excitation. A calculated amount of anaerobic MMOB was added to reduced MMOH to obtain a 1:1 MMOH active sites to MMOB ratio and a working protein concentration of 480 μM MMOH active sites before mixing with oxygen. The protein was loaded into a 2.5 ml Hamilton gas-tight syringe and transferred to the secondary glove bag (Plas-Labs) where it was installed on the enzyme syringe infusion pump (Harvard Apparatus). The reduced MMOH protein is not very stable at room temperature and in order to reduce protein precipitation, the

running enzyme syringe is continuously chilled to 4 °C using a Peltier cooling block mounted atop the syringe (Figure 4.3). In the experiments with deuterated solvents, the MMOH protein was exchanged on the PD-10 desalting column into buffer (75 mM MOPS, pD 7.2, 5% glycerol, 0.1% Triton X-100, 200 μM $Fe(NH_4)_2SO_4$ and 2.0 mM L-cysteine) prepared in D_2O. The MMOB protein was not exchanged into D_2O buffer and hence a small dilution of isotopic label occurs. The isotopic enrichment of deuterated samples is estimated at >90%. Triton X-100 and glycerol do not act as substrates for MMOH as observed in the single turnover reaction of the enzyme in the presence of either glycerol or Triton X-100 in the stopped-flow instrument.

Time resolved rRaman - While the core instrument setup for the TRRR experiment is described in detail in the supplementary text of the following reference [234], a brief overview of the experiment shall be provided here since it underwent significant revision to enable experiments described herein.

The TRRR experiment relies on the continuous flow and mixing of reduced MMOH and oxygen saturated buffer. Subsequent to mixing in a volumetric ratio of 1:1, the enzyme solution flows through a quartz flow cuvette (25 mm long, internal cross section 0.20 × 1.0 mm) where it is probed approximately 5 mm from the mixer outlet (dead volume ~ 2 μl). The time resolved aspect of the TRRR experiment is achieved by varying the flow rates of the sample solutions driven by computer controlled high-pressure syringe pumps (Harvard Apparatus). Flow rates varying between 40 μl/min – 10 μl/min result in aging times of 1.5 – 6.0 s for the dead volume of 2 μl. The flow cuvette is mounted on a translation stage outfitted with an actuator drive (model ZST25, Thorlabs, Inc) and driven by a motion control board (KFLOP, DynoMotion) (Figure 4.4). This actuator maintains a constant back and forth motion of the flow cuvette over a distance between 0.4 – 0.8 mm at a speed of 0.2 – 0.4 mm/sec. This limits the residence time of the slow-moving protein solution along the walls of the flow cuvette in the laser beam and prevents precipitation of the protein. Significant buildup of aggregated protein at the illuminated spot of the wall has been observed in the stationary cuvette.

The temperature of the incoming MMOH solution and oxygenated buffer, flow cuvette and the mixer body is maintained at 4 °C by a stream of cold nitrogen running within insulation jackets enclosing incoming reactant solution lines (Figure 4.4). The temperature is controlled by re-

heating the nitrogen stream from a dry-ice/ethanol bath with a 25W temperature controller (Model 34, Cryocon). In addition, the temperature of the core mixing chamber is further controlled by attached miniature Peltier cells. The syringe pump housing the enzyme syringe is operated from within an anaerobic glove bag to ensure that the MMOH enzyme remains reduced during the entire duration of the experiment, which can run up to 5 hours for a reaction aging time of 6 s (Figure 4.2). All wetted surfaces in the TRRR setup are comprised of PEEK (polyether ether ketone), quartz and glass in order to minimize protein precipitation.

The oxygen-saturated buffer was prepared by addition of 1 ml of oxygen gas with a gastight syringe to 6 ml of argon-sparged anaerobic buffer at room temperature (75 mM MOPS pH 7.0, 5% glycerol) contained in a 10 ml gastight syringe (Figure 4.2). The injection was made with a blunt-end needle through a rubber septa seal on an Upchurch T-valve connected to the 10 ml gas-tight syringe. The contents of the syringe to be used for preparation of oxygen saturated buffer were maintained at atmospheric pressure as the 1 ml of oxygen gas displaces an equal volume of anaerobic buffer. The buffer solution was considered to be saturated with oxygen after active stirring with a magnetic stir bar for 20 minutes. Oxygen saturated buffers were transferred into 2.5 ml gastight running syringes that were mounted on individual syringe pumps. During operation of the TRRR experiment, the oxygen-saturated buffers are automatically switched from one isotope to the other using computer-controlled actuated HPLC valves (Upchurch & Rheodyne). A short pulse of higher flow of new oxygen-saturated buffer (200 μl/min) is delivered following every switch to purge the previous isotope from the lines. rRaman scattering data were collected in 2 – 3 pairs of oxygen isotope runs in the course of a single TRRR experiment. This randomizes the non-isotopic variations in the rRaman scattering data.

rRaman scattering from MMOH reaction intermediates was excited with a 351.0 nm argon laser line (Coherent, model 100). This wavelength was chosen to elicit a resonance enhancement of the rRaman signal from compound **Q**, as the electronic absorption band with the largest extinction coefficient lies in the near-UV region of the absorption spectrum (ε_{350} = 20000 M^{-1} cm^{-1}). The laser power was modulated between 15 mW and 60 mW at the sample point during power dependence studies. (6700 photons absorbed per molecule of **Q** at a flow rate of 10 μl/min and 60 mW power). The laser beam samples a small volume in the middle of the flow cuvette (0.08 mm diameter × 0.8 mm tall) in order to exclude rRaman scattering from slow-moving MMOH protein

close to the walls of the cuvette. Owing to laminar flow, the velocity of the protein solution decreases from the center up to the wall of the cuvette, thus altering the aging time for the MMOH reaction unequally across the cross-section of the cuvette. The central 0.08 mm wide region of the a 0.20 mm wide cuvette encompasses protein solution moving at velocities close to the intended flow rate.

Acetone was used as a vibrational standard in the flow cuvette for calibration of the rRaman shifts. The acetone was subsequently cleaned out of the TRRR cuvette and tubing by exhaustive purging with anaerobic buffer. A buffer/glycerol rRaman vibrational band in the spectra of MMOH samples was used as an internal standard to normalize the intensity of isotope-difference vibrational signal across multiple experimental runs. The rRaman scattering data from a single TRRR experiment were averaged for each oxygen isotope. A $^{16}O/^{18}O$ difference spectrum was obtained from the rRaman scattering data to observe oxygen isotope sensitive modes that show up as a derivative line shape. Further details of the spectral analysis are described in the supplementary text of the following reference [234].

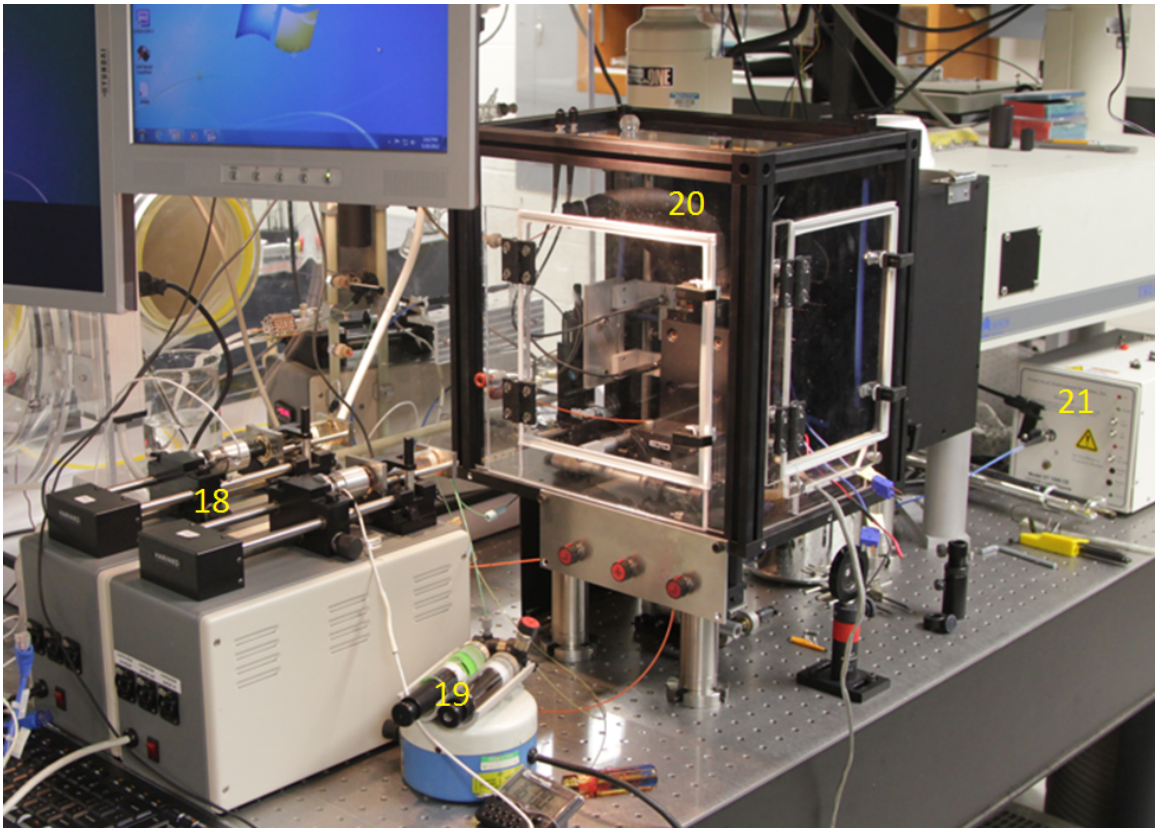

Figure 4.2 – The TRRR setup is shown here with its key elements described by numbers: 18 – high-pressure infusion syringe pumps for oxygen-saturated buffer; 19 – A pair of oxygen saturation syringes where anaerobic buffer is exchanged individually with the two oxygen isotopes $^{16}O_2$ and $^{18}O_2$; 20 – Nitrogen purged cage containing the reaction chamber; 21 – optical fiber equipped UV-visible light source. The secondary glove box housing the syringe pump for reduced enzyme can be seen on the left hand side of the cage.

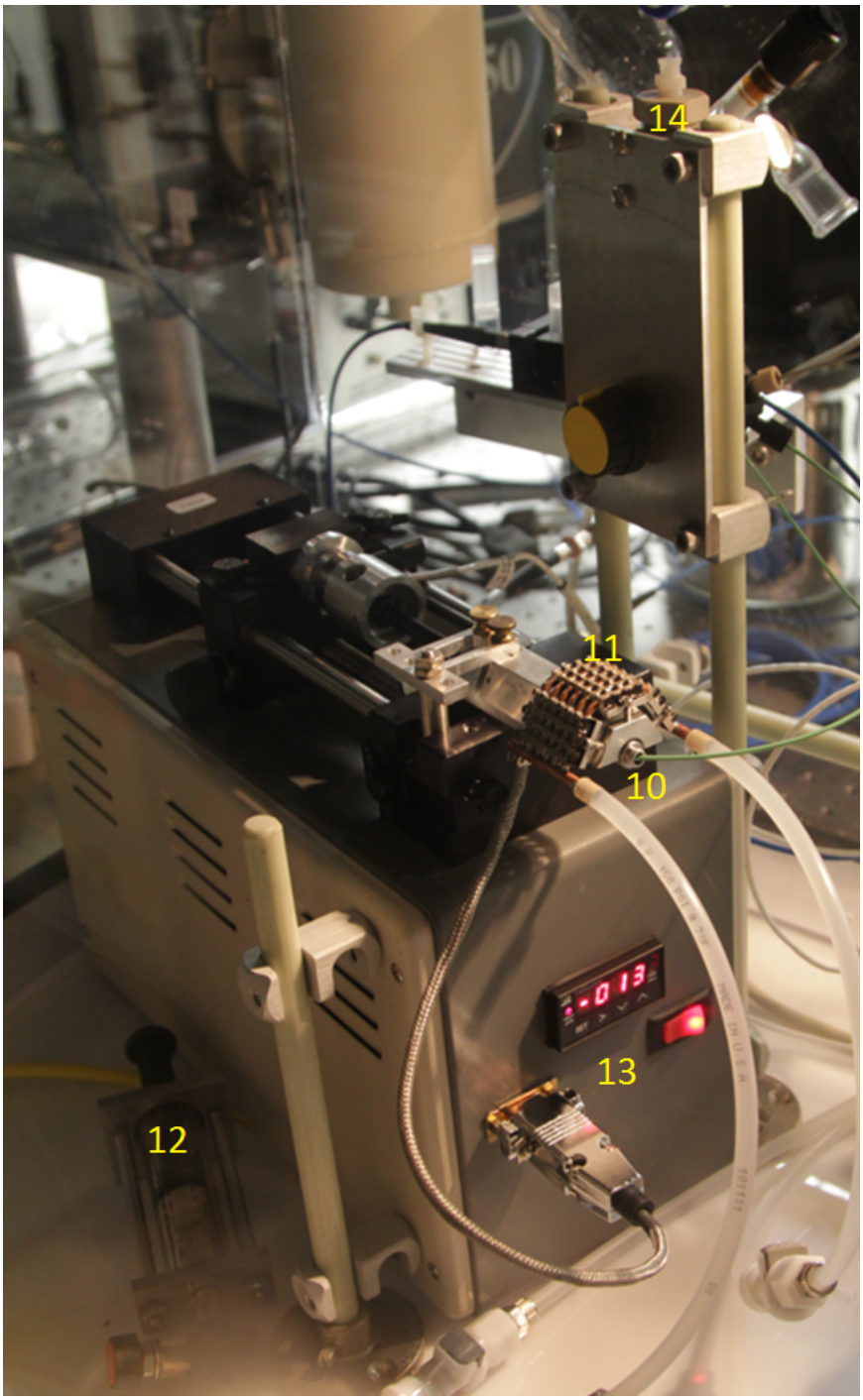

Figure 4.3 – A close-up view of the high-pressure syringe pump with mounted enzyme syringe: 10 – The tip of a 2.5 ml gastight syringe containing the reduced enzyme that is connected to the reaction chamber in the cage by HPLC tubing; 11 – Thermoelectric Peltier cooling cell that maintains the enzyme at a set point of 4 °C; 13 – temperature controller and temperature readout of the Peltier cooling cell.

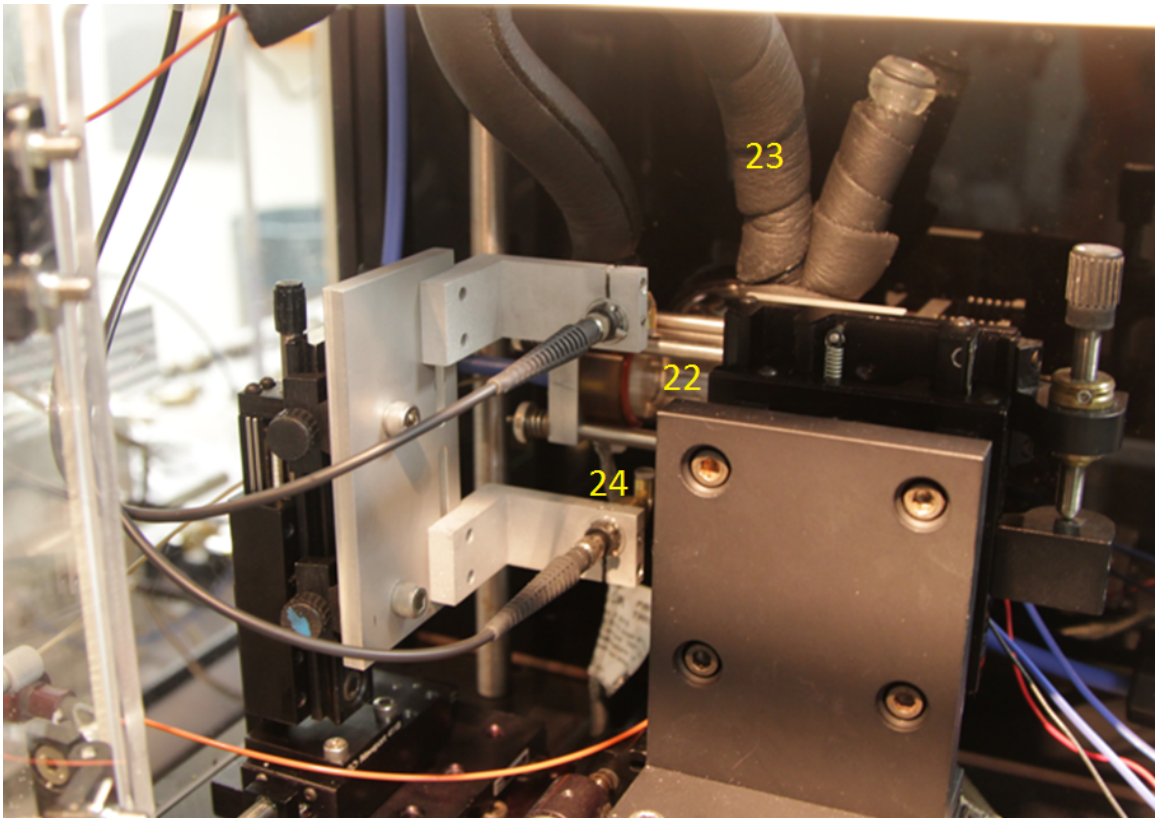

Figure 4.4 – A close-up view of the TRRR reaction chamber: 22 – rRaman flow cuvette. The rRaman scattering collection lens can be seen behind it; 23 – Incoming enzyme line encased in a jacket purged with a cold nitrogen stream; 24 – In-situ optical probe with fiber-optic cables.

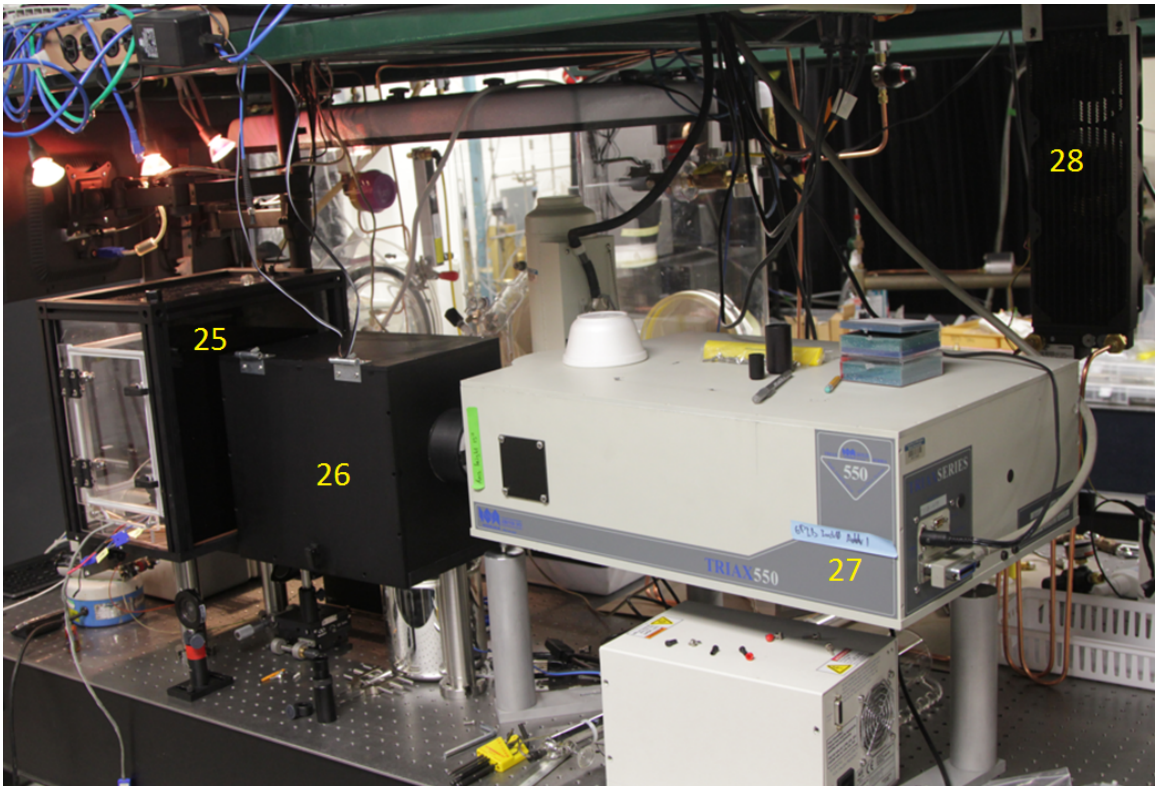

Figure 4.5 – A view of the rRaman detector: 25 – Cage containing the TRRR reaction chamber; 26 – Optics box for collection of rRaman scattering; 27 – rRaman spectrometer; 28 – Heat-exchanger for thermoelectric Peltier cooling device inside secondary glove box.

4.3 RESULTS

4.3.1 Electronic absorption measurement of compound Q in the TRRR setup

Considering the variety of organic hydrophobic compounds that can serve as substrates for MMOH, it is important to show that compound **Q** does, in fact form in the flow cell of the TRRR instrument. A substrate contamination of the flow tubing and connections of the TRRR setup is possible and can quench compound **Q**, thus precluding its rRaman measurement. An optical fiber equipped spectrophotometer was used to measure the electronic absorption spectra of the MMOH reaction within the flow cell under the experimental conditions used in the TRRR experiment. The electronic absorption spectrum observed in the flow cell at a delay of 2 s after initiation of the MMOH/MMOB turnover is depicted in Figure 4.6. This spectrum is a difference of the electronic absorption spectrum of the reaction in the presence and absence of oxygen and shows absorption bands at 330 nm and 430 nm. A comparison with the pure component difference spectrum of **Q** obtained from a stopped-flow instrument indicates that **Q** is accumulating within the TRRR flow cuvette (Figure 4.6). The observed yield of **Q** is similar to that expected based upon the amount of enzyme utilized. A laser excitation wavelength of 351 nm was chosen for the rRaman experiment as it lies close to the maximal wavelength of electronic absorption of **Q** while minimizing excitation of potential traces of porphyrin contaminants.

4.3.2 rRaman spectrum of compound Q

The absolute rRaman spectrum of the MMOH/MMOB reaction is described in Figure 4.7. A comparison of the $^{16}O_2$ and $^{18}O_2$ spectra of the enzyme reaction with the anaerobic buffer spectra indicates that the dominant features observed arise from Raman vibrational modes of the buffer used in the experiment and these mask the weak rRaman features from **Q**. Thus, despite this interference preventing the direct observation of the absolute rRaman spectrum of **Q**, a subtraction operation can be performed on these absolute spectra. Provided the rRaman data for **Q** are obtained with $^{16}O_2$ and $^{18}O_2$ under identical experimental conditions, the subtraction operation removes all the Raman modes that do not involve motion of labeled oxygen atom(s) associated with the chromophore. The transient rRaman spectrum of the MMOH/MMOB reaction at a delay time of 1.5 seconds and an excitation wavelength of 351 nm is depicted in Figure 4.8 in the form of a difference spectrum. The primary feature is an oxygen sensitive vibration at 690 cm^{-1} with $^{16}O_2$ that shifts to 655 cm^{-1} with $^{18}O_2$. Another vibrational mode is observed at 560 cm^{-1} in

$^{16}O_2$ buffer with an isotopic $^{16}O_2/^{18}O_2$ shift of 32 cm^{-1}. These rRaman signals are not observed in a negative control experiment performed in the absence of MMOH (Figure 4.7).

As compound **Q** has been shown to be photolabile, the laser power dependence of the two rRaman vibrations was examined so that the optimum conditions for collecting rRaman scattering from **Q** could be achieved. The two vibrational features do not show any change in intensity with increasing laser power from 15 mW to 60 mW while normalizing for internal standard (vide supra methods), thus indicating that the enzymatic species responsible for these two rRaman modes is not sensitive to the excitation laser power under present conditions (data not shown).

The temporal dependence of the isotope difference rRaman modes is shown in Figure 4.9. The mode at 690/655 cm^{-1} shows a different temporal behavior than the vibration at 560/528 cm^{-1}. This suggests that these vibrations arise from distinct species. Although the rRaman data are insufficient to clearly indicate the temporal character of the 560/528 cm^{-1} vibration, the 690/655 cm^{-1} mode appears to decay rapidly over 10 seconds at 4 °C. A global analysis modeling of the rRaman data would provide a quantitative measure of the decay, but this is still a work in progress presently. This global analysis would also probe the line shape of the vibrational features to investigate the possibility of another vibration superimposed with currently observed modes.

4.3.3 Effect of solvent deuteration on the rRaman signal

The rRaman spectrum of the MMOH/MMOB reaction in deuterated solvent suggests that the 690/655 cm^{-1} vibration mode does undergo a small upshift (2.5 cm^{-1}) in its vibrational frequency (Figure 4.10). However, this upshift only occurs with the vibration mode in $^{18}O_2$ buffer as the vibrational frequency at 690 cm^{-1} ($^{16}O_2$) shows little change. A small upshift is also observed for the vibration mode at 560/528 cm^{-1} in D_2O.

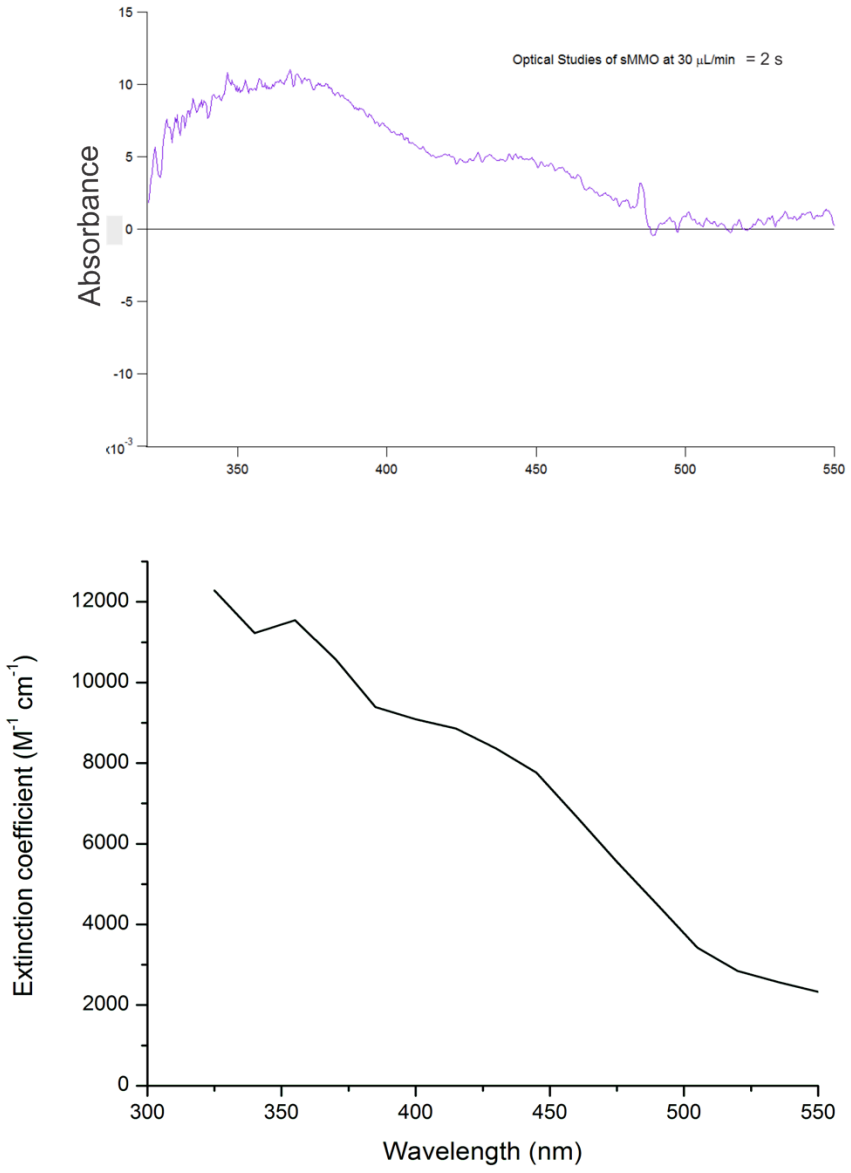

Figure 4.6 – Top panel: The electronic absorption spectrum of the MMOH reaction in the TRRR flow cuvette at 2 s, 4 °C, pH 7.0 is shown after subtracting the absorption spectrum of differous MMOH (collected under identical conditions after mixing with anaerobic buffer). Bottom panel: A difference electronic absorption spectrum for compound **Q** (**Q** – $\mathbf{H}^{red}$).

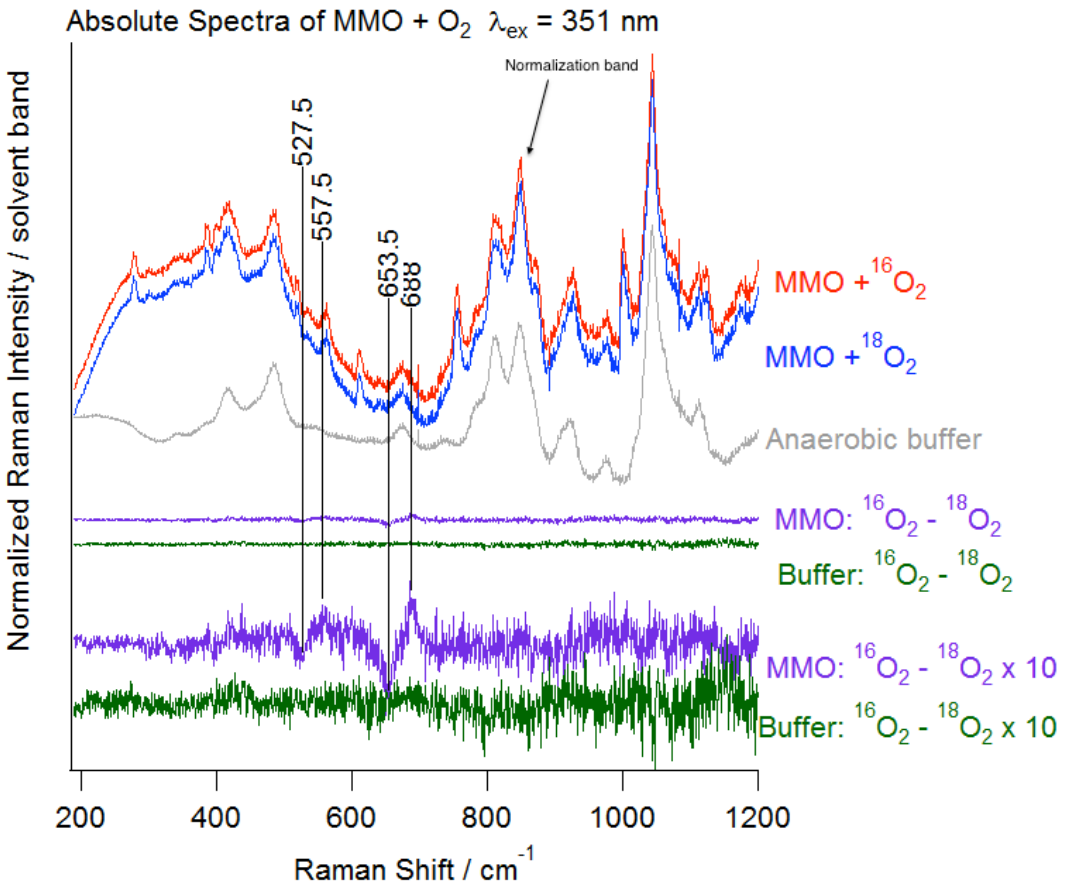

Figure 4.7 – The absolute rRaman spectra of the MMOH/MMOB reaction with $^{16}O_2$ buffer (red trace) and $^{18}O_2$ buffer (blue trace) at a delay time of 1.5 seconds and an excitation wavelength of 351 nm. A polynomial function has been used to correct for the fluorescence background. The absolute rRaman spectrum of the buffer solution is depicted in the grey trace. The purple trace (MMO: $^{16}O_2 - ^{18}O_2$) is the difference of the MMOH reaction absolute spectra obtained with the oxygen isotopes. This difference spectrum has been magnified (purple trace MMO: $^{16}O_2 - ^{18}O_2$ x 10) to show rRaman vibration modes. The rRaman difference spectrum of the negative control (absence of enzyme) has been shown in the green traces (Buffer: $^{16}O_2 - ^{18}O_2$). The intensity of the labeled vibrational band is used to normalize observed rRaman signals.

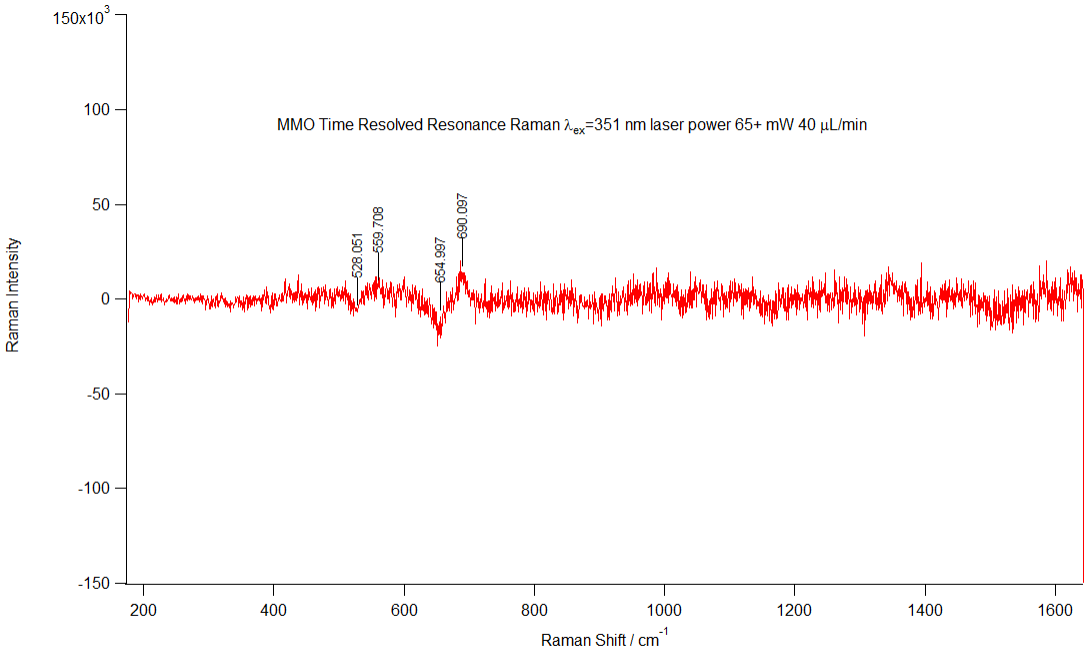

Figure 4.8 – The time-resolved difference rRaman spectra of the MMOH/MMOB reaction, 1.5 seconds after the initiation of the single turnover reaction at 4 °C. The two rRaman vibrational modes observed appear as a derivative line shape and are indicated in the figure.

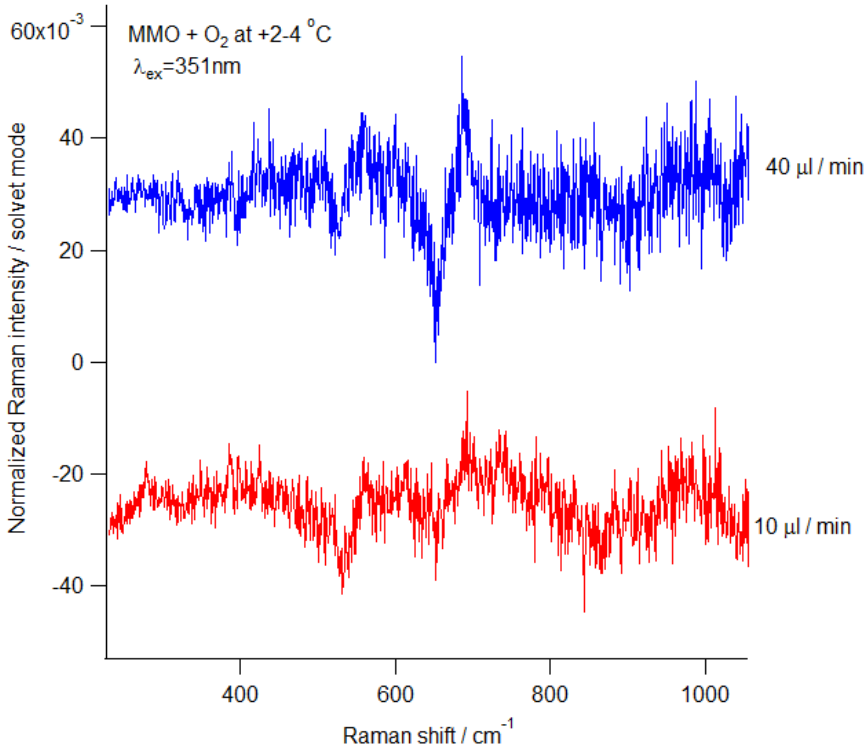

Figure 4.9 – Temporal profile of the rRaman vibrational modes from the MMOH/MMOB reaction. The 690/655 cm^{-1} mode seems to decay rapidly over 6 seconds, which indicates that the 690/655 cm^{-1} and 560/528 cm^{-1} vibrational modes arise from different enzymatic intermediates.

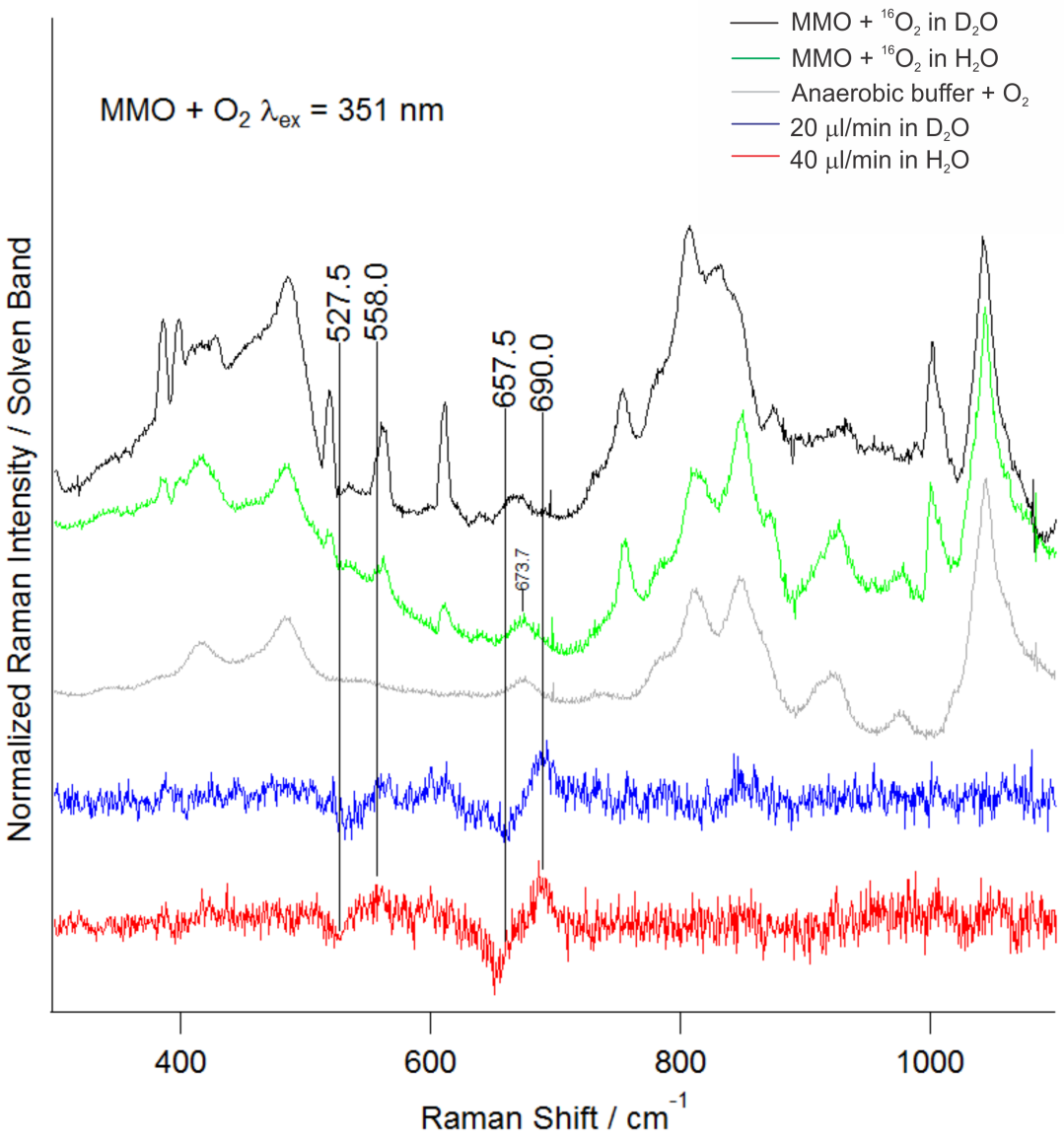

Figure 4.10 – Time-resolved rRaman spectra of the MMOH single turnover reaction (difference and absolute spectra) at 1.5 seconds in H_2O buffer (difference spectra –red trace) and at 3.0 seconds in D_2O buffer (difference spectra - blue trace).

4.4 DISCUSSION

It is shown here that time-resolved rRaman spectroscopy allows the detection of two transient vibrational modes associated with oxygen atoms derived from molecular oxygen in reaction cycle intermediates of MMOH. These vibrational bands are observed at a delay time for the enzymatic reaction where compound **Q** is known to accumulate (Figure 4.6). Furthermore, a temporal difference in the decay of these vibrational bands allows assignment of one band to **Q** and suggests that the second band belongs to a new species beyond **Q**. The assignment of these vibrational bands and their significance to sMMO catalysis is discussed here.

4.4.1 Choice of excitation wavelength

The assignment of the vibrational bands to specific intermediates is facilitated by the selection of excitation wavelength. In the current case, the choice of 351 nm for detection of **Q** is justified primarily by the large extinction coefficient for electronic absorption of **Q** in the near-UV region (Figure 4.6). Moreover, density functional calculations of the electronic absorption spectrum of high valent intermediate X in RNR suggest that the near-UV range absorption bands arise from oxo → Fe(IV) charge transfer transitions [235]. This is also supported by the observation that the largest resonance enhancement of the Fe-μ-oxo bond occurs in the near-UV region in the rRaman enhancement profiles of synthetic diiron model compounds and hemerythrin [236].

4.4.2 Assignment of the 690/655 cm^{-1} band

The approximate time dependent behavior of the 690/655 cm^{-1} vibration matches the half-life of compound **Q** according to the kinetic model developed from extensive past studies and expanded in Chapter 5. The assignment of this band can be made based on studies of synthetic diiron model compounds designed to mimic **Q** that incorporate a bis-μ-oxo diamond core structure. These feature a characteristic oxygen atom sensitive bond vibration between 650 and 690 cm^{-1} [171, 172, 237] with an oxygen isotopic shift of about 30 cm^{-1} (Table 4.1). In fact, this signature vibration is also observed in dicopper and dimanganese synthetic model compounds with a diamond core structure [172, 237]. This vibration is assigned to a tetraatomic vibration of the entire bis-μ-oxo bridged diiron core. The crucial experimental evidence for the assignment of the nature of this bond vibration has been provided by the measurement of the rRaman spectrum of the diiron model where the oxo-bridge oxygen atoms incorporate both ^{16}O and ^{18}O isotopomers

[$Fe_2(\mu\text{-}^{16}O^{18}O)$] [172]. The bond vibration for such a 'mixed-label' diiron model shows an intermediate band to the bond vibrations obtained with both oxo-bridges having either a ^{16}O or ^{18}O label. If the bond vibration between 650 – 690 cm^{-1} instead arose from a triatomic Fe-O-Fe stretch, a mixture of the Fe-^{16}O-Fe and Fe-^{18}O-Fe frequencies would be expected with an intensity depending upon the fractional amount of the individual isotopic labels in the oxo-bridges. An equivalent experiment with MMOH shall be performed in the future.

The upshift of the 690/655 cm^{-1} vibration mode upon deuteration seems to suggest an association of the diamond core cluster with an exchangeable hydrogen atom. However, the asymmetric nature of the shift indicates that it may not originate directly from association with a structural hydrogen within the chromophore, but from secondary interactions such as a Fermi-resonance with a protein/solvent vibrational band that shifts to a frequency region close to 655 cm^{-1} upon deuteration. A fit of the observed difference rRaman spectra to a symmetric difference of two Gaussian bands is required before any firm estimation can be made of the shifts upon deuteration. This would help us distinguish between a shift arising from either Fermi-resonance or association with a hydrogen atom.

4.4.3 Fe-O-Fe bond angle

Normal coordinate analysis of the diamond core synthetic model compounds indicates that the 650 – 690 cm^{-1} bond vibration is associated with an asymmetric 'pairwise' stretching mode of the $Fe_2(\mu\text{-}O_2)$ cluster [172]. This vibration mode is more intense and prominent in diiron clusters possessing an asymmetry between the two iron atoms, which usually arises from a less than perfect symmetry of the coordinating ligand environment. The analysis of the rRaman spectra of a large breadth of mono-μ-oxo Fe-O-Fe and bis-μ-oxo $Fe_2(\mu\text{-}O_2)$ model compounds suggest that the bond vibrations of the triatomic and tetraatomic clusters are closely related. As a result, information regarding the Fe-O-Fe bond angle in the diamond core cluster can be obtained from a plot of Fe-O-Fe bond angles versus ν_{sym} and ν_{asym} bond vibrations of mono-μ-oxo diiron model compounds [172, 236]. This plot indicates that there is a linear correlation between the ν_{sym} and ν_{asym} bond vibrations of mono-μ-oxo iron oxygen bonds and the Fe-O-Fe bond angle. The extrapolated values for the bond angles in diamond core mimics match well with those obtained from a more direct observation with EXAFS (Table 4.1) [237].

Although we cannot yet definitively ascertain the chemical structure in **Q** that gives rise to 690/655 cm^{-1} bond vibration in the absence of the pending mixed-oxygen labeling experiment, the precedent from diiron synthetic mimics of **Q** suggests that it is likely to arise from a tetraatomic vibration of the diamond core cluster. Although structural and spectroscopic studies of the MMOH cluster structure show that the ligand environments of the irons are similar, they are not identical [64]. Consequently, the prominent bond vibration associated with this cluster in **Q** would probably arise from an asymmetric mode. Based upon the plot of Fe-O-Fe bond angles versus ν_{sym} and ν_{asym} bond vibrations of mono-μ-oxo diiron model compounds, a ν_{asym} bond vibration with a frequency of 690 cm^{-1} with $^{16}O_2$ would suggest a Fe-O-Fe bond angle of approximately 95°. The EXAFS characterization of **Q** provides Fe-Fe and two Fe-O bond distances of 2.46 Å, 1.77 Å and 2.05 Å respectively [99]. These bond distances suggest an Fe-O-Fe bond angle of 82° that is close to the extrapolated value of 95°. Thus, the rRaman spectrum of **Q** at first glance, seems to corroborate the diamond core model obtained from EXAFS spectroscopy.

4.4.4 Origin of the 560/528 cm^{-1} vibration mode

A comparison of a more detailed temporal profile of the 560/528 cm^{-1} vibration mode with other intermediates in the MMOH catalytic cycle would be required to ascertain the identity of the enzymatic species responsible for this mode. The small upshift of this vibrational mode in deuterated solvent suggests that oxygen atom associated with this vibration is bound to a hydrogen atom that is also involved in a hydrogen bond interaction (vide infra). However, until the characterization of the time-dependent behavior of this vibrational mode is complete, we can only speculate about its nature based upon vibrational fingerprints provided by other proteins and synthetic model compounds (Table 4.2). The rRaman spectra of diferric clusters with μ-oxo bridges possess a vibration mode between 450 – 520 cm^{-1} that originates from a symmetric Fe-μ-O-Fe stretch [236]. Diferric MMOH is a μ-hydroxo bridged species [67-69]. The only rRaman information available for a μ-hydroxo bridged diiron cluster is from synthetic model compounds, which also describe the presence of a vibrational mode around 500 cm^{-1} (Table 4.2). The isotopic $^{16}O_2/^{18}O_2$ shift of the vibrational mode at 560 cm^{-1} found for MMOH is, however, much larger than those for the μ-oxo and μ-hydroxo bridged diiron clusters (*cf.* 32 cm^{-1} and an average of 16 cm^{-1}). Monoiron and diiron centers coordinated by a terminal hydroxo moiety describe a vibrational mode around 510 - 580 cm^{-1} that has an isotopic shift of a similar magnitude to the

560 cm^{-1} mode in MMOH (Table 4.2). Some of these vibrational modes respond to deuteration with an expected downshift. An upshift of the vibrational frequency is also observed and is believed to arise from a hydrogen-bonded hydroxo moiety on the metal center. The deuterium substitution reduces the strength of the hydrogen bond, which in effect weakens the Fe-OH stretch [238].

4.4.5 Ongoing studies

Future work on the TRRR characterization of **Q** includes the use of the mixed-oxygen isotopomer in combination with $^{16}O_2$ and $^{18}O_2$. This mixed-labeling experiment would help in elucidating the nature of the **Q** bond vibration observed with a vibrational frequency of 690 cm^{-1} with $^{16}O_2$. Based upon the precedent of diamond core synthetic model compounds, the observation of a single vibration mode centered in between 690 cm^{-1} and 655 cm^{-1} with mixed-oxygen isotopomer will support a tetratomic vibration model for **Q** (vide supra). Such a tetraatomic vibration for **Q** would unequivocally validate the diamond core model. This experiment will also provide critical information regarding the origin of the oxygen atoms in **Q**. The mechanism of O-O bond cleavage in the conversion from **P** to **Q** is an important and unanswered question in the MMOH catalytic cycle. A heterolytic versus a homolytic mechanism of breaking the O-O bond can be distinguished by probing the origin of the two oxygen atoms in the μ-oxo bonds of **Q**. The presence of a solvent water molecule derived oxygen atom in the diamond core cluster has been predicted to support a heterolytic mechanism for O-O bond cleavage [98] (Figure 4.11). If the 690/655 cm^{-1} vibration mode arises from a tetraatomic vibration, then the magnitude of the isotopic shift between $^{16}O_2$ and $^{18}O_2$ (35 cm^{-1}) shows that both the oxygen atoms in **Q** originate from molecular oxygen. This is based upon a comparison with the rRaman data from diamond core synthetic model compounds in Table 4.1 (both cluster oxygen atoms uniformly labeled – $\Delta(^{18}O)_2$ = -31 cm^{-1}; mixed-label cluster atoms – $\Delta(^{18}O)(^{16}O)$ = -22 cm^{-1}) [172].

It is also imperative to demonstrate the catalytic competence of the two transient species observed in the rRaman experiment. Thus, methane shall be used as a substrate to quench **Q** and probe whether the two observed rRaman modes (690/655 cm^{-1}; 560/528 cm^{-1}) disappear rapidly. This would reinforce our conclusion that these two rRaman signals arise from a substrate reactive intermediate. The measurement of the rRaman spectrum of the MMOH reaction in the presence of deuterated methane would also be an interesting experiment as the two-step **Q** decay model

predicts that accumulation of compound **QS** in lieu of **Q** in this reaction [97]. Another future experiment is the measurement of the temporal behavior of the 560/528 cm^{-1} bond vibration for comparison with the kinetic behavior of the newly discovered **Q'** intermediate in the MMOH catalytic cycle (vide infra Chapter 5).

4.4.6 Conclusion

In summary, the rRaman spectrum of intermediate **Q** has been reported here. The vibrational mode correlates well with those found for diamond core bis-μ-oxo bridged dinuclear iron clusters in synthetic model complexes, suggesting that this is the overall structure of the cluster in **Q**. The experiments conducted thus far establish the method and conditions required to conduct additional kinetic, mixed-isotope, and substrate-quenching experiments that will allow the detailed mechanism of formation and structure of **Q** to be established. Additionally, the bond vibration of another labeled oxygen atom associated intermediate distinct from **Q** has been observed in the MMOH reaction. This unexpected enzyme-derived species may correlate with an intermediate following **Q** in the reaction cycle that has been observed in parallel transient kinetic investigations. Further studies of the temporal behavior of this vibrational mode in the presence or absence of substrate for comparison with the results of the solution transient kinetic studies will provide a definitive assignment of the origin of this spectral feature.

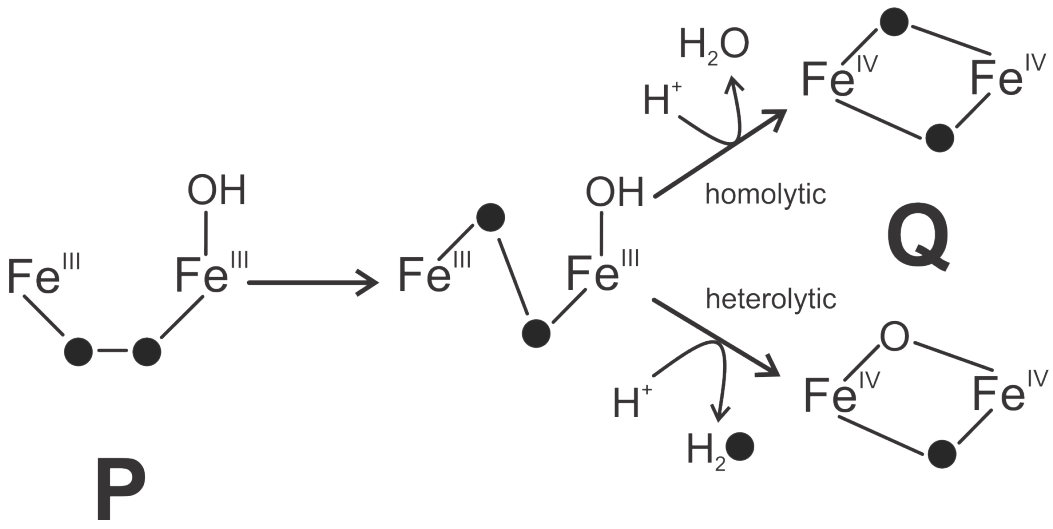

Figure 4.11 – Predicted outcome of either a heterolytic or homolytic cleavage of the O-O bond in the conversion from **P** to **Q** [98, 173]. The conversion between **P** and **Q** is depicted in this scheme to occur through a transient *trans*-μ-1,2-peroxo intermediate that may arise from a rearrangement of the predicted *cis*-μ-1,2-peroxo intermediate **P**.

Compound	Diiron core	Fe-μ-O-Fe angle	ν_{asym} (cm^{-1})	Fe-Fe distance (Å)	Reference
$[Fe_2\text{-}(\mu\text{-}O)_2(6\text{-}Me_3\text{-}TPA)_2]^{2+}$	$Fe^{III}{}_2(\mu\text{-}O)_2$	92.5°	692(-30)	2.716	[172, 239]
$[Fe_2\text{-}(\mu\text{-}O)_2(5\text{-}Me_3\text{-}TPA)_2]^{3+}$	$Fe^{III}Fe^{IV}(\mu\text{-}O)_2$	106°	666.2(-31.2)	2.89	[172]
$[Fe_2\text{-}(\mu\text{-}O)_2(3,5\text{-}Me\text{-}4\text{-}Methoxy\text{-}TPA)_2]^{4+}$	$Fe^{IV}{}_2(\mu\text{-}O)_2$	101°	674(-30)	2.73	[171]

Table 4.1 – A representation of the quantitative values for Fe-Fe distance, Fe-μ-O-Fe angle and ν_{asym} vibration frequencies for asymmetric synthetic model compounds containing a bis-μ-oxo diamond core cluster similar to **Q**. The oxygen isotopic shift is described in parentheses.

Species	ν(Fe-O) (cm^{-1})	$\Delta^{18}O$ (cm^{-1})	$\Delta^{2}H$ (cm^{-1})	Reference
hydroxo-bridged diiron cluster ν(Fe-OH-Fe)				
$[Fe_2\text{-}(\mu\text{-}O)(\mu\text{-}OH)(4,6\text{-}Me_6\text{-}TPA)_2]^{3+}$	497	-13	-3	[239]
$[Fe_2\text{-}(\mu\text{-}O)(\mu\text{-}OH)(BPEEN)_2]^{3+}$	504	-16	-4	[239]
oxo-bridged diiron cluster ν_{sym}(Fe-O-Fe)				
RNR	493	-14	+3	[240]
Δ^9-desaturase	519	-18	0	[241]
CmlA	481	-17	0	[242]
$[Fe_2\text{-}(\mu\text{-}O)Cl_6]^{2-}$	458	-18	-	[236]
$[Fe_2\text{-}(\mu\text{-}O)(TPA)_2(OBz)]^{3+}$	497	-17	-	[236]
monoiron & diiron centers with terminal hydroxo moiety ν(Fe-OH)				
TauD (Fe^{III})	578	-23	0	[234]
Hydroxomet-Hr	565	-27	-5	[243]
HRP (Fe^{III})	503	-19	+6	[238]
CPO CpdII (Fe^{IV})	565	-22	-13	[244]
$[Fe(tnpa)\text{-}(OH)(RCO_2)]^{+}$	574	-20	0	[245]

Table 4.2 – A tabulation of diiron and monoiron synthetic model compounds and proteins that possess an iron-oxygen vibration mode between 500 - 600 cm^{-1}. The oxygen isotopic shift of the vibration mode is depicted within parentheses. The magnitude and direction of the shift with deuteration is also mentioned when available.

CHAPTER 5

Kinetic characterization of a novel intermediate Q' in the sMMO catalytic cycle

5.1. INTRODUCTION

The oxidation of the strong C-H bond (BDE = 105 kcal $mole^{-1}$ [44]) of methane by sMMO and pMMO is a very difficult reaction to catalyze. Accordingly, the enzyme derived oxidant species that reacts with the substrate is potent. While the identity of the oxidant in pMMO remains a mystery, the oxidant in sMMO has been demonstrated to be a bis-μ-oxo diiron(IV,IV) intermediate termed as compound **Q**, which is formed in the hydroxylase component (MMOH) [94, 99, 101]. Among other similarly potent enzyme-derived oxidants, the Fe^{IV}=O porphyrin cation radical intermediate compound I in cytochrome P450 is the most studied [246]. This intermediate has the same formal oxidation state as **Q** and can oxidize strong C-H bonds such as that in camphor (BDE = 98 kcal $mole^{-1}$), but it has only recently been trapped for study [20, 247]. Although compound I does not naturally oxidize methane, *in vitro* reactions utilizing terminal oxidants such as iodosobenzene and chemical tuning of the spin state of the heme iron with perfluoro carboxylic acid additives do suggest that this intermediate is also capable of oxidizing methane to methanol [248, 249]. The structural contrast between **Q** and P450 compound I makes the full characterization of **Q** structure and reactivity valuable research objectives in the study of oxygen activation chemistry.

In the MMOH catalytic cycle, none of the kinetic steps leading up to the formation of compound **Q** display any substrate concentration dependence. The rate of decay of **Q,** however, shows a linear dependence upon methane concentration up to the limit of methane solubility in aqueous buffer [94]. This strongly suggests that compound **Q** is the oxidant in the MMOH catalytic cycle. However, an Arrhenius plot for the **Q** decay reaction with methane shows a distinct break, suggesting the presence of two or more steps. Even more surprisingly, the Arrhenius plot for the **Q** decay reaction is linear with either deuterated methane [97] or alternative larger substrates with weaker C-H bonds. The **Q** decay reaction also displays a deuterium KIE of ~ 50 with methane while there is no KIE observed with all other substrates. Moreover, the second order rate constant of **Q** decay does not linearly correlate with the C-H bond strength of the substrate. A two-step model for **Q** decay has been proposed to account for these observations, where the first step involves substrate binding to the active site while the second step involves the actual C-H bond breaking and hydroxylation reaction [97]. The MMOH structure severely restricts the access of large molecules into the active site, thus making the first step rate limiting for all substrates with a

larger molecular size than methane. However, once the access is gained, **Q** rapidly cleaves the weak C-H bonds of these substrates. In comparison, a small molecule such as methane enters the active site swiftly, whereupon, its strong C-H bond makes the bond-breaking reaction rate-limiting, thus displaying a KIE. This model has been validated by the design of a MMOB mutant that opens up the substrate access channel, thus enhancing the rate of substrate binding to **Q** with ethane and, in effect, unmasks the KIE for this alternative substrate [159]. The implication of this model is that there exists an intermediate in between compound **Q** and **R** in the catalytic cycle, which has a substrate molecule bound in the active site and still retains the 430 nm absorbance characteristic of **Q**. Such a proposed intermediate has been designated as compound **QS** [97].

It has recently been demonstrated in the sMMO enzyme from *M. capsulatus* Bath that compound **Q** decays to form another intermediate termed as **Q*** in the catalytic cycle [100]. Global fitting of transient kinetic electronic absorption data indicates the presence of this intermediate, which has an electronic absorption band at 420 nm and a shoulder at 455 nm. However as **Q*** was observed to not react with substrates, it is proposed that this intermediate forms along the auto-decay path of **Q** that occurs in the absence of substrate. Accordingly **Q*** cannot be the **QS** intermediate proposed in the two-step **Q** decay model.

In this study, a detailed analysis of the transient kinetic electronic absorption time course of **Q** decay in the presence and absence of substrates has been conducted. A new intermediate is detected in the MMOH catalytic cycle that evolves from compound **Q** and is spectroscopically distinct from **Q***. The kinetic properties of the new intermediate suggest that it is formed rapidly as substrates bind to **Q** resulting in **Q'S**. This complex then appears to be the reactive form of **Q**. This investigation offers insight into the design of nature's most potent oxidant and the manner in which its reactivity can be regulated within an enzyme environment.

5.2. MATERIALS AND METHODS

Chemicals - 3-(N-morpholino)-propanesulfonic acid, glycerol, ferrous ammonium sulfate, cysteine and methyl viologen were purchased from Sigma –Aldrich. Methane gas was purchased from Matheson Tri-Gas. Fully deuterated methane was purchased from Cambridge Isotope Laboratories.

Biological materials - MMOH was purified from *M. trichosporium* OB3b according to protocols for cell growth and protein purification described in Chapter 2 of this thesis (Materials and Methods). MMOB was purified from a heterologous expression in *E. coli* as described previously (vide supra Chapter 2-Materials and Methods).

Transient kinetic techniques - The protocol for reduction of MMOH for transient kinetic studies has been described previously (vide supra Chapter 2 – Materials and Methods). Transient kinetic pre-steady state electronic absorption experiments were performed on an Applied Photophysics stopped flow instrument (SX.18MV with a SX Pro-Data upgrade). The reduced MMOH protein was loaded into one of the stopped flow drive syringes through a Hamilton gas-tight syringe. The other drive syringe contained a stoichiometric equivalent of MMOB (to MMOH active sites) in oxygen-saturated buffer at the chosen pH point. If substrate was required for the single turnover experiment, it was added to the contents of this drive syringe. In the sequential-mix transient kinetic experiments, the MMOH reaction was initiated with the first push of the drive syringes by mixing reduced MMOH with MMOB and dissolved oxygen in buffer. After a chosen delay time, the second push of the drive syringes mixes in substrate and this solution flows into the optical cell, where the subsequent reaction was monitored. A spectra-kinetic data accumulation method was also used to monitor the single turnover reaction. In this method, a series of single wavelength time courses are monitored at 10 nm intervals between 310 nm and 450 nm. These traces were then used to reconstruct the electronic absorption spectra of **O**, $\mathbf{H^{ox}}$ and the intervening intermediates in the catalytic cycle. The single-wavelength kinetic data were analyzed with the Pro-Data Viewer software from Applied Photophysics. Singular value decomposition of spectra-kinetic multiple-wavelength and photodiode array data was performed using the Pro-Kineticist global analysis software (Applied Photophysics).

The protein concentration of MMOH used in the transient kinetic experiments has been described in terms of reactive MMOH active sites. This description arises from the presence of two

populations of MMOH active sites (vide supra Chapter 2) – i) a native population that undergoes turnover with previously observed kinetic rates and forms catalytic intermediates, ii) a non-native fraction that undergoes oxidation on a slower time scale and does not accumulate catalytic intermediates during turnover. The reactive population of MMOH active sites comprises of 40 % of the total active sites in the MMOH protein used in the experiments described in this study. The methane and deuterated methane substrate solutions were prepared by evacuating buffer solutions in sealed vials and filling in the headspace with the desired gas. The concentration of dissolved methane in the gas-saturated solution is 1.5 mM at 25 °C (Merck Index).

5.3. RESULTS

5.3.1 Single turnover reaction of MMOH in the absence of substrate

The single turnover reaction of MMOH in the absence of substrates displays the accumulation of compound **P** and **Q** as has been described previously (Figure 5.1) [94]. During the 7 seconds following the maximal formation of **Q** at 1.5 s (pH 7.0, 4 °C), the conversion of compound **Q** to a previously unobserved transient species possessing a broad electronic absorption spectrum is observed. This new intermediate, designated as compound **Q'**, subsequently decays to the resting diferric state ($\mathbf{H^{ox}}$) of the enzyme. The presence of an additional transient intermediate following compound **Q** is borne out clearly by the single wavelength traces at the wavelength maxima of 330 nm and 430 nm (Figure 5.2). The electronic absorption at 330 nm reaches a maximum and then plateaus for several seconds whereas that at 430 nm decreases. This occurs because the extinction coefficients for **Q** and **Q'** are different at 330 and 430 nm.

Compound **Q'** is particularly photo-labile as the use of white light in the photo-diode array setup for collecting full scans of the electronic absorption spectra leads to a minimal accumulation of **Q'** (Figure 5.3). The decay rate constant for the electronic absorption at 430 nm arising from **Q** is also increased 3 fold from 0.05 s^{-1} to 0.15 s^{-1} at 4 °C, pH 7.0 by the strong illumination. This photo-sensitivity necessitates the use of a spectra-kinetic approach where time-dependent electronic absorption spectra are compiled from series of single wavelength time courses taken in rapid succession using the relatively weak light from a monochromator .

A global fitting of the multiple wavelength spectra-kinetic data (wavelength range expanded from 300 nm to 725 nm for the fit) provides a solution of three intervening intermediates between the starting diferrous enzyme ($\mathbf{H^{red}}$) and the resting oxidized form ($\mathbf{H^{ox}}$) of the enzyme (Figure 5.4). Compound **P** is the first intermediate observed to accumulate in the catalytic cycle, which subsequently evolves to form compound **Q**. Compound **Q** then decays to form compound **Q'**, which has a similarly broad electronic absorption spectrum with large extinction coefficients. The extinction coefficients for **Q** and **Q'** are different at 330 nm and 430 nm, such that compound **Q'** has a much less pronounced shoulder at 430 nm than **Q**. The kinetic rates for these steps in the catalytic cycle are: i.) $k_{P^*\text{-}P} = 10.34 \pm 0.51\ s^{-1}$; ii) $k_{\mathbf{P\text{-}Q}} = 2.70 \pm 0.15\ s^{-1}$; iii) $k_{\mathbf{Q\text{-}Q'}} = 0.22 \pm 0.03\ s^{-1}$; iv) $k_{\mathbf{Q'\text{-}H}^{ox}} = 0.06 \pm 0.01\ s^{-1}$. Although the reaction initiates from diferrous enzyme ($\mathbf{H^{red}}$), the

first two intermediates **O** and **P*** do not possess electronic absorption spectra that are significantly distinct from $\mathbf{H}^{red}$ to be detected under the conditions used. Accordingly, there is a small lag phase at the beginning of the kinetic time courses arising from the weakly absorbing intermediates **O** and **P*** that has not been fit by the global fitting analysis. The global fit thus starts with the formation of compound **P** from **P***. A numerical simulation of the single turnover reaction of MMOH in the absence of substrate and incorporating the known rate constants of **P*** formation and decay is shown in Figure 5.5 [98]. As a result of the simultaneous decay of **Q** and formation of **Q'**, the electronic absorption at 330 nm does not undergo much change between 1 – 10 s despite the higher extinction coefficient of **Q'** at 330 nm.

5.3.2 Single turnover reaction of MMOH in the presence of substrate

The large deuterium isotope effect of CD_4 as a substrate allows pseudo-first order conditions in substrate to be established without accelerating **Q** decay to the point where the intermediates oxidizing the substrate are unobservable. The spectra-kinetic data for the reaction in the presence of CD_4 display the normal accumulation of **P** followed by the formation of an intermediate with optical features similar to those of **Q** (or **Q'**). However, there is no subsequent conversion of this species as occurs in the absence of substrate. This **Q**- (or **Q'**-) like intermediate subsequently decays to the diferric form of the enzyme ($\mathbf{H}^{ox}$) with formation of deuterated methanol. When this reaction is followed at single wavelengths, it is found that the time for maximal formation of the **Q**- (or **Q'**-) intermediate is similar, but not identical, at 330 nm and 430 nm (Figure 5.6).

The global fitting analysis for the single-turnover reaction of MMOH in the presence of CD_4 provides a solution where only two intermediates are observed to accumulate (Figure 5.7). The first species is **P**, followed by a **Q**- (or **Q'**-) like species. A comparison between the pure component spectrum of the latter intermediate with those of **Q** and **Q'** indicates that the spectra for the **Q**-like species in the presence of substrate is distinct from both (Figure 5.8). It might arise from an admixture of **Q** and **Q'** or it might be another new species, for example **QS** or **Q'S**. The subtle difference in the t_{max} for the kinetic traces at 330 nm and 430 nm suggests the presence of more than one **Q**/**Q'** like species, which seems to support a scenario for an admixture of **Q** and **Q'** with an altered accumulation ratio than in the absence of substrate. The apparent kinetic rate constants for these steps in the catalytic cycle at 4 °C and pH 7.0 are i.) $k_{\mathbf{P^*\text{-}P}} = 11.0 \pm 0.4\ s^{-1}$; ii) $k_{\mathbf{P\text{-}Q/Q'}} = 2.40 \pm 0.1\ s^{-1}$; iii) $k_{\mathbf{Q/Q'\text{-}H}^{ox}} = 0.20 \pm 0.02\ s^{-1}$. The rate constant of the last step in this

reaction is a pseudo first order constant that is dependent upon CD_4 concentration as the reaction is bimolecular .

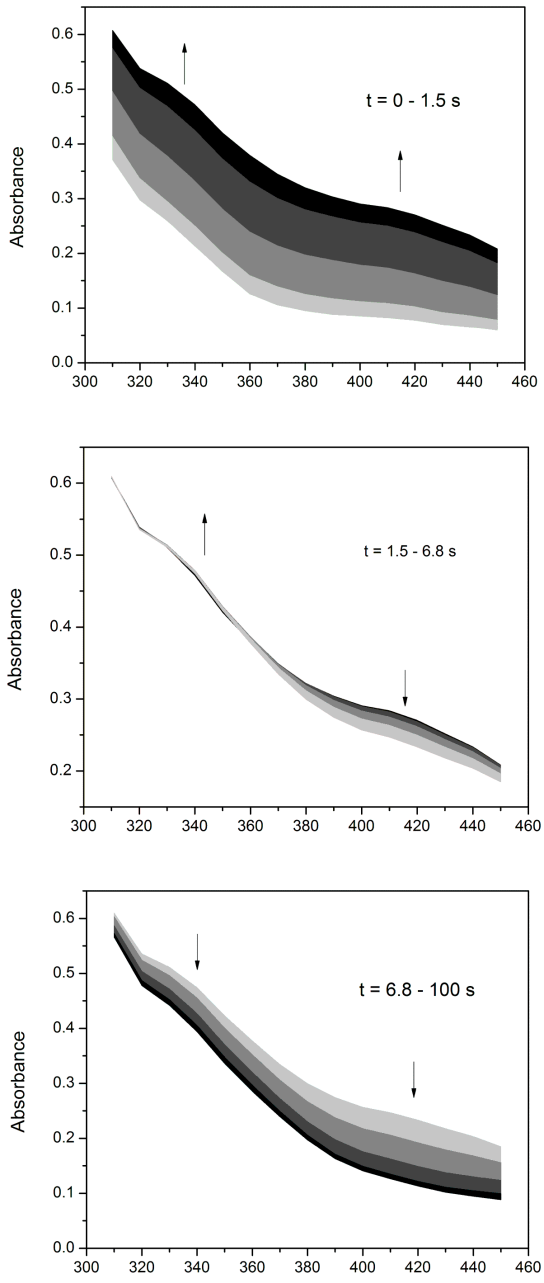

Figure 5.1 – The electronic absorption spectra of a single turnover reaction of MMOH (18 μM reactive active sites) in the absence of substrate at pH 7.0 and 4 °C is shown divided into three time regions: 0 – 1.5 s - formation of compounds **P** and **Q**; 1.5 – 6.8 s –conversion of **Q** to new intermediate **Q'** - absorption between 370 - 450 nm decreases while the absorption between 320 - 350 nm increases marginally; 6.8 – 100 s – decay of **Q'** to diferric enzyme ($\mathbf{H^{ox}}$). The formation and decay of **P** cannot be clearly observed here, as data were not collected at its defining electronic absorption band at 700 nm**.**

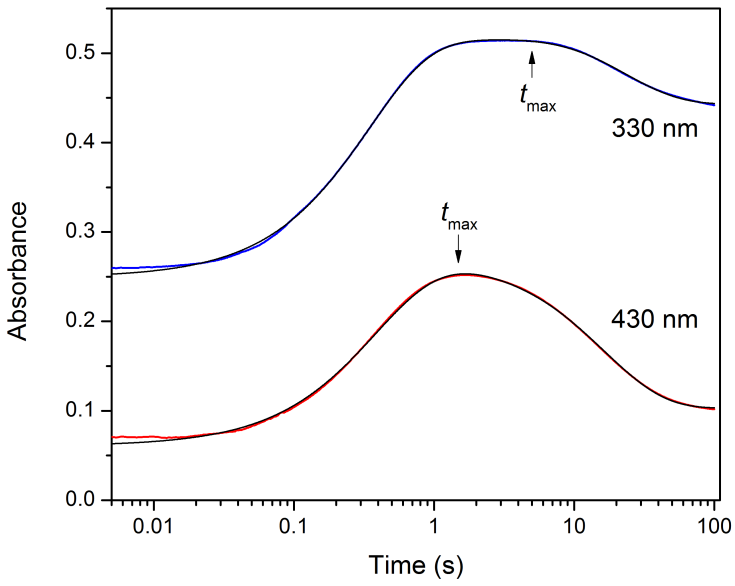

Figure 5.2 – Kinetic traces at 330 nm (blue) and 430 nm (red) along with the respective fits from the global fitting analysis (black) are depicted for the single turnover reaction of MMOH in the absence of substrate at pH 7.0, 4 °C. The different t_{max} values for the traces indicates the formation of **Q'** (max at 7 s) following **Q** (max at 1.5 s).

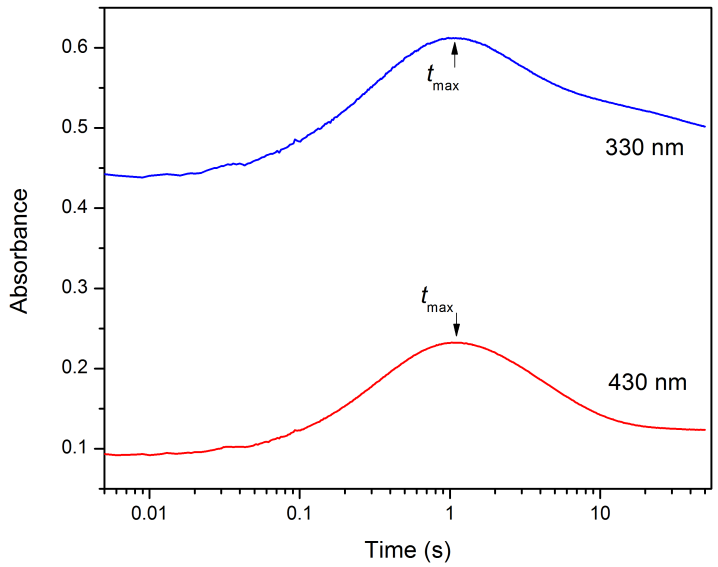

Figure 5.3 – The intense white light illumination in the photodiode array setup abolishes the accumulation of **Q'** as observed in the similar t_{max} for the kinetic traces at 330 nm and 430 nm (compare with Figure 5.2).

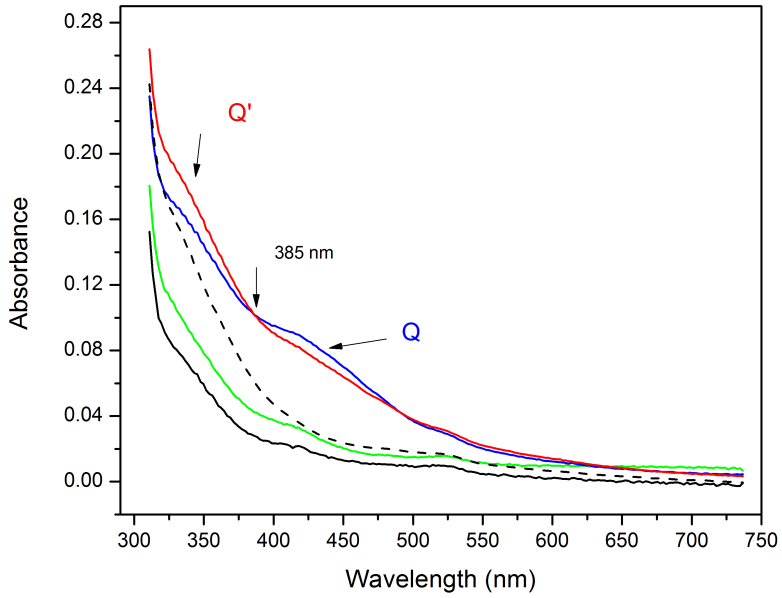

Figure 5.4 – Pure component spectra of the starting $\mathbf{H}^{red}$ (black trace), **P** (green trace), **Q** (blue trace), **Q'** (red trace) and $\mathbf{H}^{ox}$ (black dashed trace) obtained from a global fitting of the single turnover reaction (8 μM reactive active sites) in the absence of substrate at pH 7.0, 4 °C.

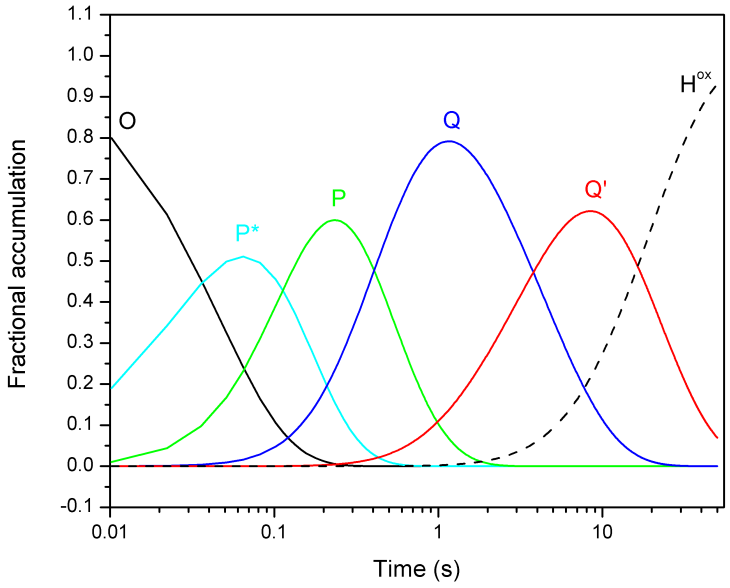

Figure 5.5 – Speciation plot for the single turnover reaction of MMOH in the absence of substrate. The kinetic model for the single turnover reaction is **O** → **P*** → **P** → **Q** → **Q'** → $\mathbf{H}^{ox}$ where $k_1 = 26\ s^{-1}$, $k_2 = 10.4\ s^{-1}$, $k_3 = 2.7\ s^{-1}$, $k_4 = 0.23\ s^{-1}$, $k_4 = 0.05\ s^{-1}$ at 4 °C and pH 7.0.

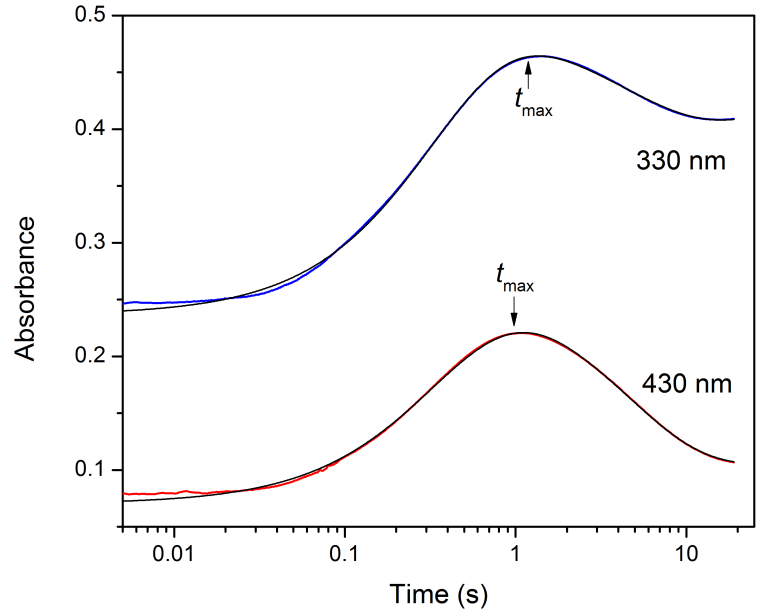

Figure 5.6 - Kinetic traces at 330 nm (blue) and 430 nm (red) along with the respective fits from the global fitting analysis (black) are depicted for the single turnover reaction of MMOH (18 μM reactive active sites) in the presence of CD_4 (0.7 mM) at pH 7.0, 4 °C.

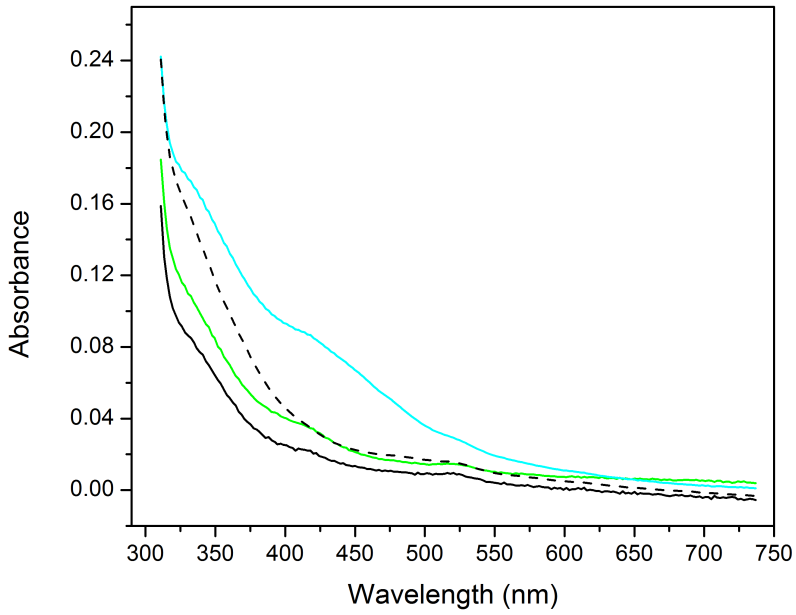

Figure 5.7 - Pure component spectra of the starting $\mathbf{H}^{red}$ (black trace), **P** (green trace), **Q**- (or **Q'**-) (cyan trace) and $\mathbf{H}^{ox}$ (black dashed trace) obtained from a global fitting of the single turnover reaction (8 μM reactive active sites) in the presence of CD_4 (0.7 mM) at pH 7.0, 4 °C.

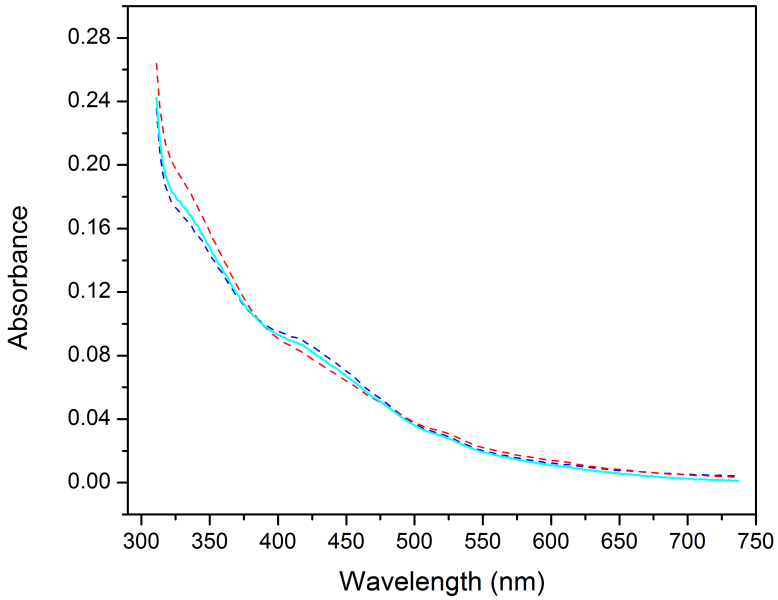

Figure 5.8 – A comparison of the electronic absorption spectra of the **Q**- (or **Q'**-) like intermediate (cyan trace) formed in the presence of CD_4 with the pure component spectra of **Q** (blue dashed trace) and **Q'** (red dashed trace) obtained in the absence of substrate.

5.3.3 Reactivity of compound Q' towards substrates

A sequential-mix stopped flow experiment has been devised to explore the reactivity of **Q'** with substrates. The first push (pre-mix) initiates the single turnover cycle of MMOH in the absence of substrate. After a delay time chosen as the time of maximal formation of compound **Q'**, the second push (flush) mixes in substrate and moves the reaction into the optical cell. An accelerated loss of absorbance at 430 nm is observed with the use of either CH_4 or CD_4 (Figure 5.8). The rate constants for decay with these substrates are the same as those previously reported for single mix experiments with no aging time [94, 147]. In other words, **Q'** appears to react with substrates with the same rate constant that we previously have attributed to the **Q** reaction with substrates.

Since both **Q** and **Q'** absorb at 430 nm, it is possible that the observed decay in the presence of substrates originates from the residual **Q** at the time of the second mix. This would account for the similar decay rate constants seen in the single and sequential mix experiments. Accordingly, it is important to know the relative magnitudes of absorbance change arising from each intermediate after the chosen aging time. A numerical simulation of the time course for the MMOH reaction using the kinetic rates obtained from the global fitting analysis in the absence of substrate indicates that **Q** accumulates to 80% at 1 second and declines to a 10% accumulation at 8 seconds (Figure 5.5). Based upon the concentration of MMOH active sites used in the sequential-mix experiment, the decay of this 10% residual **Q** should cause an absorbance change of only 0.02 at 430 nm, which is far less than observed (Figure 5.9). Thus, the majority of the absorbance change observed at 430 nm is attributed to the decay of **Q'** upon its reaction with substrate. This demonstrates that **Q'** can bind substrates and is consistent with it being a substrate reactive intermediate.

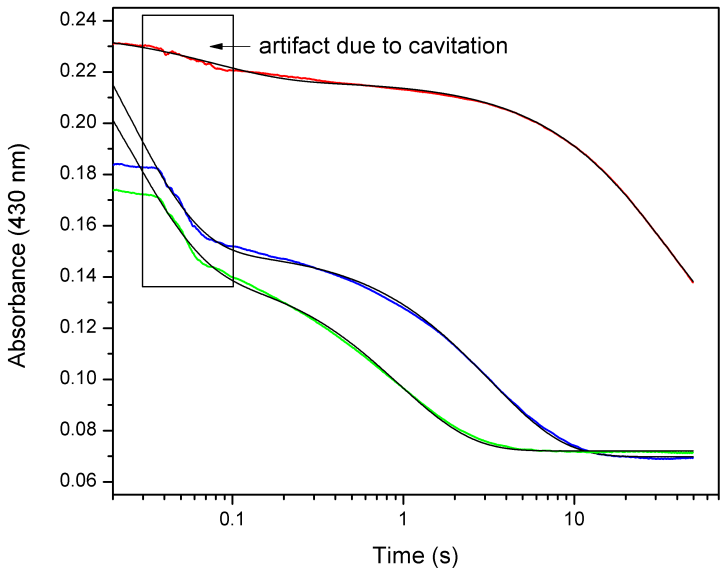

Figure 5.9– Kinetic traces at 430 nm describe the reaction of substrate with the MMOH single turnover reaction after an aging time of 8 s. Red trace – absence of substrate; Blue trace – presence of 0.5 mM CD_4; Green trace – presence of 0.05 mM CH_4; Black traces – fits to the kinetic traces: absence of substrate – k_1 = 12.2 s^{-1}, k_2 = 0.03 s^{-1}; presence of 0.5 mM CD_4 – k_1 = 41.8 s^{-1}, k_2 = 0.31 s^{-1}; presence of 0.05 mM CH_4 – k_1 = 40 s^{-1}, k_2 = 1.07 s^{-1}. The first phase in each fit arises from the artifact caused due to cavitation.

5.3.4 pH dependence of the Q to Q' conversion step

The pH dependence of the kinetic step of conversion of **Q** to **Q'** has been measured. The rate constant for this step decreases between pH 6.85 and pH 7.0 (Figure 5.10). This rate constant, however, cannot be followed over a wider pH range as the protein precipitates below a pH of 6.7. At a pH value higher than 7.1, the kinetic phase associated with the **Q** to **Q'** conversion cannot be observed. This most likely arises because the rate constant for the formation of **Q'** is slower than or comparable to the rate of decay of **Q'** (0.06 s^{-1}), leading to a minimal accumulation of compound **Q'**. In spite of the narrow pH range tested, the significant decrease in the rate constant between pH 6.85 and pH 7.0 suggests that this kinetic step is a proton dependent process.

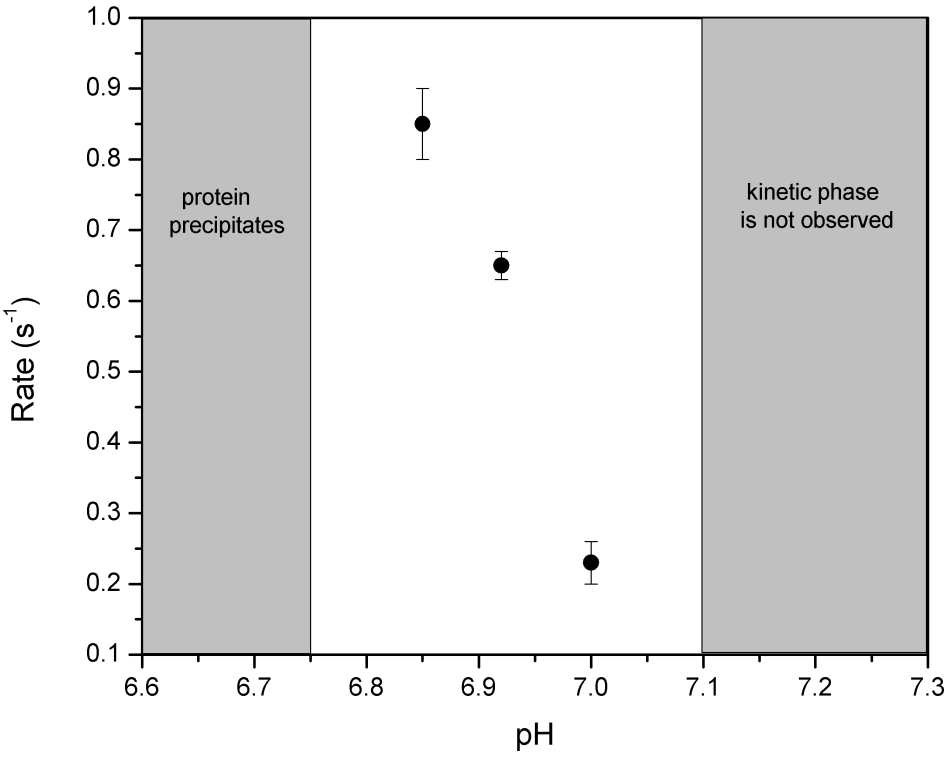

Figure 5.10 – pH dependence profile of the kinetic step of conversion of **Q** to **Q'** at 4 °C.

5.4. DISCUSSION

It has been demonstrated in this study that during the spontaneous decay of compound **Q** in the absence of substrate, a new species with an electronic absorption spectrum similar to **Q** is formed. This new intermediate, compound **Q'**, exhibits the auto-decay rate constant previously associated with **Q,** suggesting that it is in the decay pathway. It has been also shown that, in sequential-mix single turnover reactions, **Q'** appears to react with substrates with the rate constant previously attributed to the **Q** reaction. This raises questions such as whether **Q'** is formed and reacts with substrates in the normal reaction cycle of MMOH and if so, whether it, rather than **Q,** is the primary reactive species. These questions as well as the possible structure of compound **Q'** are addressed here.

5.4.1 Resolution of Q' from Q

In previous investigations of the time course of MMOH single turnover reaction in the absence of substrate monitored at 430 nm and pH 7.6, it was noted that the best fit to the kinetic data was obtained using a summed 3-exponential expression [94, 115]. However, the amplitude of the additional phase was small and the quality of the data did not justify the proposal of an additional step apart from **Q** formation and **Q** decay. In the current study, improvements in the transient kinetic equipment, the removal of near-UV absorbing material remaining from the chemical reduction process, monitoring the reaction at 330 nm, and the use of lower pH, all contribute to the observation of **Q'**. The current study demonstrates that the use of pH 7.6 buffer as in our previous studies would have led to little accumulation of **Q'** as it is not formed fast enough to accumulate (Figure 5.10). Also, monitoring the reaction at 430 nm in our earlier studies made it difficult to resolve the loss of **Q** due to decay to $\mathbf{H}^{ox}$ from loss due to formation of **Q'**, as **Q'** possesses a smaller extinction coefficient at 430 nm than **Q**.

5.4.2 MMOH single turnover reaction in the presence of substrate

The single turnover catalytic cycle in the presence of substrate exhibits an intermediate with a spectrum that is similar to those of both **Q** and **Q'**. In fact, its spectrum appears to lie in between those of **Q** and **Q'** at all wavelengths. The global fitting analysis would be compatible with either of the following solutions: a) a single intermediate accumulates that might, for example, be **QS** or **Q'S,** or b) formation of both **Q** and **Q'** (or **QS** and **Q'S**) on a similar time scale so that the spectrum of the intermediate is an admixture of the **Q** and **Q'** spectra. The latter scenario requires

that **Q'** be formed much faster than in the absence of substrate because very little **Q'** would be present at the t_{max} for the observed intermediate if this were not the case. It is known from previous studies that increasing the substrate concentration increases the rate of **Q** decay, presumably by progressively saturating the **QS** (or **Q'S**) complex [97, 149]. Two schemes that would account for these observations are shown below.

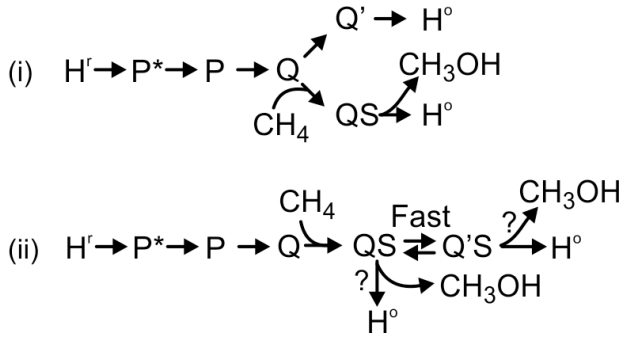

The model depicted in Scheme (i) proposes that **Q'** intermediate succeeds **Q** along the auto-decay pathway but not on the pathway that leads to substrate hydroxylation. The enhanced rate of **Q** decay in the presence of substrate would mean that there would be almost no formation of compound **Q'**. This scheme is similar to that proposed to explain the absence of intermediate Q* during the reaction of the MMOH enzyme from *M. capsulatus* (Bath) [100] except that here the reaction is proposed to include formation of **QS,** in accord with our previous studies [97]. In this case, the slightly altered electronic absorption spectrum observed in the presence of substrate would be due to **QS** alone. In Scheme (ii), substrate binding in the active site modulates the structure of the resulting **QS** intermediate to rapidly and perhaps reversibly convert to **Q'S**. The altered spectrum in this case would result from either **Q'S** or an admixture of spectra from the **QS** and **Q'S** species. The key question in this case is whether **QS**, **Q'S**, or both of these intermediates are the reactive species.

The sequential mix stopped flow experiment directly tests the ability of **Q'** to bind substrates and allows us to observe if the reaction to form product then occurs. The results indicate that compound **Q'** does indeed interact with substrates, resulting in decay of the species and product formation. Importantly, this decay reaction exhibits the same rate constants as we have previously attributed to **Q** decay in the presence of substrates. This supports the notion that **Q'S** is the reactive species that can transfer oxygen to the substrate. However, it remains possible that

the presence of substrate in Scheme (ii) accelerates both the forward and reverse **Q** to **Q'** reactions, allowing formation of **QS** as the reactive species. This would require that the reverse reaction to reform **QS** proceed at a rate much greater than **Q'S** decay. The need for regulation of the exceptional reactivity of the key intermediate in the MMOH cycle argues in favor of **Q'S** being the true reactive species as discussed below.

5.4.3 Identity of compound Q'

The broad and intense electronic absorption spectrum of **Q'** suggests that the iron atoms in the diiron cluster still retain their high valent oxidation state from compound **Q**. The apparent reactivity of **Q'** towards hydrocarbons also supports this hypothesis. A conclusive assessment of the oxidation state can be made with Mössbauer spectroscopy, which will be addressed in future studies. The proton dependent conversion of **Q** to **Q'** suggests that the structure of the diiron cluster is different in these two intermediates. We can speculate that the enhancement in the rate of this conversion between **Q** and **Q'** by the presence of substrate in the active site might occur due to a facilitation of this step of proton donation owing to the steric presence of substrate in vicinity of the diiron cluster.

Further clues to the nature of compound **Q'** can be obtained from diiron synthetic model compounds. In addition to a closed diamond core mimic of **Q** [171], a series of open core diiron models have been prepared recently [173, 174]. A comparison of the reactivity towards hydrogen atom abstraction between **1**, **2** and **3** (Figure 5.11) indicates that **2** is about a 100-fold more reactive than **1** while **3** is a 1000-fold more reactive than **2** [174]. The quintet-spin state ($S = 2$) of iron atoms in **3** is responsible for the enhanced reactivity over the triplet-spin state ($S = 1$) iron atoms in **2**. This experimental observation is corroborated by density functional theory calculations [250, 251]. Considering the similarities in the oxidation state and the low spin triplet state of the iron atoms, the higher reactivity of **2** was reasoned to arise from the presence of the terminal oxo-iron moiety. A bridging oxo group is thus much less reactive than a terminal oxo moiety towards hydrogen atom abstraction. This conclusion is underscored by the observation that **1** is a 100-fold less reactive than a quintet-spin mononuclear Fe(IV)=O model compound despite having a higher reduction potential. Monoiron nonheme oxygenases utilizing high valent iron(IV) oxygen intermediates to catalyze oxidative C-H bond cleavage such as α-ketoglutarate and pterin dependent dioxygenases, also employ a terminal oxo-iron(IV) moiety as the reactive

intermediate [20, 252, 253]. The high valent iron atom in these enzymes such as TauD and phenylalanine hydroxylase is high spin (S = 2) [252, 254]. Thus, one model for compound **Q'** is an open core form of compound **Q** with a terminal oxo-iron (IV) group. It is likely that the high spin state of the iron atoms (S = 2 in **Q**) would not be altered in the conversion from the closed core to open core structure on account of the weak ligand field of the carboxylate bridged diiron cluster. This hypothesis is also supported by information from synthetic diiron model compounds where the opening up of the diamond core structure leads to change from S = 1 to S = 2 iron atoms [174]. Thus, if the iron atoms in **Q'** retain the high spin nature along with acquiring a terminal Fe(IV)=O moiety, then an exceptionally powerful reagent will be formed (Figure 5.12).

There is further supporting evidence from synthetic model compounds and density functional theory calculations for an open core high valent iron(IV) structure for **Q'**. Although the lack of a high spin diamond core model compound hampers the comparison of the electronic absorption properties of the high spin closed and open core diiron structures, the low spin open core counterpart has a smaller extinction coefficient between 400 nm and 600 nm than the closed diamond core model compound [173]. This matches the smaller extinction coefficient for **Q'** than **Q** in the analogous wavelength range. DFT calculations of the electronic transitions of high valent intermediate X in RNR have assigned the electronic absorption bands into two groups [235]. The first group encompassing electronic transitions beyond 400 nm arises from ligand field d – d transitions on the iron atom. The second group comprises electronic transitions in the wavelength region between 300 nm and 400 nm that arise from oxo → Fe(IV) charge transfer bands. Computational studies evaluating a mono-μ-oxo, a μ-oxo/μ-hydroxo and a bis-μ-oxo structure for intermediate X predict an increase in the energy of the d – d Fe(IV) transitions to shorter wavelengths in moving from a bis-μ-oxo to mono-μ-oxo structure [235]. Furthermore, it is plausible that the oxo → Fe(IV) charge transitions would also shift to higher energies and become more intense upon the strengthening of the iron – oxo bond in the conversion from a bridged oxo moiety to a terminal oxo species. The predicted changes match the differences in the electronic absorption spectrum of compound **Q** and **Q'** (Figure 5.4), thus supporting a putative open core structure for **Q'** (Figure 5.12).

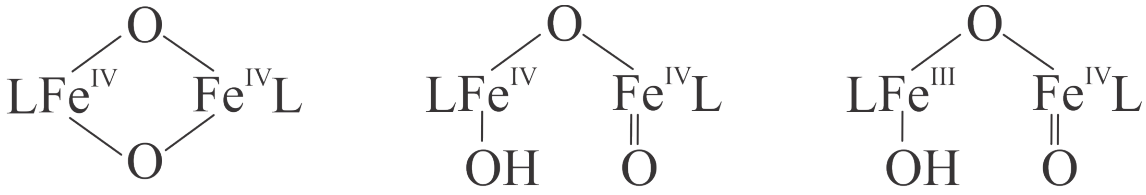

1 (LS) **2** (LS) **3** (HS)

L = tris((4-methoxy-3,5-dimethylpyridin-2-yl)methyl)amine

Figure 5.11 – Synthetic model compounds that contain either a closed diamond core or an open core diiron cluster. Both the iron atoms of the cluster are in the low-spin state (LS) in contrast to the high spin iron atoms (HS) of **Q**.

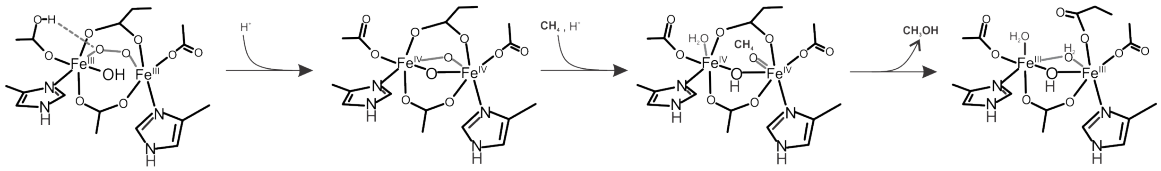

Figure 5.12 – Proposed structures for some of the diiron cluster intermediates in the sMMO catalytic cycle. **P** – μ-1,2-peroxo diiron(III) species[205], **Q** – bis-μ-oxo diiron(IV) species [99], **Q'** – open core diiron(IV) species and $\mathbf{H^{ox}}$ – resting state μ-hydroxo diiron(III) species [67-69].

5.4.4 Regulation of the formation of high valent oxygen intermediates

The formation of high-valent oxygen intermediates is strictly regulated in the oxygenase family of enzymes to prevent adventitious reactions. A common means of regulation involves the initiation of the formation of reactive species solely in the presence of substrate, as observed in cytochrome P450, α-ketoglutarate dependent dioxygenases, and Rieske dioxygenases [79, 154, 255]. A similar type of substrate regulation was demonstrated in the synthetic diiron model compounds described above (Figure 5.11), where water or alcohol substrates can activate the diiron cluster towards C-H bond oxidation by coordinating the iron atoms and converting the closed diamond core cluster to an open core form with a terminal oxo-iron moiety [256]. The circumvention of this regulatory mechanism by the omission of substrate from the catalytic cycle primarily leads to a very slow oxidation of the reduced iron center through inefficient oxygen activation and occasionally leads to self-hydroxylation on the protein backbone in some α-ketoglutarate dependent dioxygenases [155]. The mode of regulation in MMOH turnover differs in that it does not require substrate to be present to form the reactive intermediate **Q**. Indeed, it can slowly complete many reaction cycles in the absence of substrate without undergoing damaging self hydroxylation [94]. When substrate is present, the rate of oxygen activation is unchanged while the latter half of the reaction cycle in which **Q** can attack the substrate C-H bond is greatly accelerated. A comparison of the active site pocket in the reduced form of MMOH and RNR reveals that there are no aromatic amino acid side-chain residues in vicinity of the diiron cluster in MMOH unlike Phe208 and Tyr122 in RNR that undergo self hydroxylation [208, 257, 258]. Although this arrangement of the active site pocket in MMOH prevents self hydroxylation reactions, it is possible that the enzyme forms the readily observed and relatively stable **Q** intermediate in a state that has decreased reactivity, in order to allow time for substrate to bind. This is necessary because the enzyme must select methane from other more readily oxidized adventitious substrates that cannot be metabolized by methanotrophs. We believe that it does this by using a methane-sized selective "pore", so that the substrate binding process is very slow compared with the substrate binding rates of other enzymes [97, 149]. The requirement for a stable form of the high valent intermediate is emphasized by the observation that the substrate binds to MMOH only when intermediate **Q** is formed in the catalytic cycle [94, 97]. Once methane is bound, it is possible that the conversion to the more reactive **Q'** is triggered, leading to rapid substrate hydroxylation as depicted in Scheme (ii) above. The trigger for this conversion also occurs in the absence of substrate but is much slower in comparison. Such a

substrate-mediated conversion of the high valent intermediate from a stable (**Q**) to a more reactive form (**Q'**) would represent a novel and elegant means of regulation in oxygenase chemistry.

5.4.5 Comparison of Q' and Q*

It has been demonstrated in the single turnover reaction of the MMOH enzyme from *M. capsulatus* Bath that an intermediate **Q*** is formed after compound **Q** [100]. The electronic absorption spectrum of **Q*** however differs from **Q'** in having electronic transitions centered at 420 nm and 455 nm instead of 330 nm and 430 nm observed for **Q'**. The electronic absorption spectrum of **Q*** also has a smaller extinction coefficient for absorbance than **Q** beyond 490 nm, which is unlike **Q'** (Figure 5.4). The most compelling evidence that **Q'** and **Q*** are different species is based upon the observation that **Q*** is unreactive towards methane. As such, this enzyme intermediate is believed to lay along the autodecay pathway for **Q** in the absence of substrate.

5.4.6 Future studies

The future experiments will attempt to probe the structural and electronic identity of compound **Q'** through Mössbauer, EXAFS and rRaman spectroscopy. These spectroscopic tools will also be utilized to investigate the identity of the high-valent **Q**/**Q'** like intermediate formed in the presence of substrate. Further transient kinetic experiments with substrates other than CD_4 and MMOB mutants such as the DBL2 MMOB [149] are also required to answer the following questions regarding the new kinetic model: i) Is the **Q** to **Q'** conversion a reversible step in the presence of substrate? ii) How does the model of the two-step **Q** decay model fit in the light of discovery of compound **Q'**?

REFERENCES

1. Sessions, A.L., D.M. Doughty, P.V. Welander, R.E. Summons, and D.K. Newman, *The continuing puzzle of the great oxidation event.* Current biology : CB, 2009. **19**(14): p. R567-74.
2. Raymond, J. and D. Segre, *The effect of oxygen on biochemical networks and the evolution of complex life.* Science, 2006. **311**(5768): p. 1764-7.
3. Falkowski, P.G., *Evolution. Tracing oxygen's imprint on earth's metabolic evolution.* Science, 2006. **311**(5768): p. 1724-5.
4. Metz, M. and E.I. Solomon, *Dioxygen binding to deoxyhemocyanin: electronic structure and mechanism of the spin-forbidden two-electron reduction of O_2.* J. Am. Chem. Soc., 2001. **123**(21): p. 4938-50.
5. Jensen, K.P. and U. Ryde, *How O_2 binds to heme: reasons for rapid binding and spin inversion.* J. Biol. Chem., 2004. **279**(15): p. 14561-9.
6. Wood, P.M., *The potential diagram for oxygen at pH 7.* The Biochemical journal, 1988. **253**(1): p. 287-9.
7. Mayer, J.M., *Understanding hydrogen atom transfer: from bond strengths to Marcus theory.* Acc. Chem. Res., 2011. **44**(1): p. 36-46.
8. Borovik, A.S., *Role of metal-oxo complexes in the cleavage of C-H bonds.* Chemical Society Reviews, 2011. **40**(4): p. 1870-4.
9. Springer, B.A., S.G. Sligar, J.S. Olson, and G.N. Phillips, *Mechanisms of ligand recognition in myoglobin.* Chem. Rev. , 1994. **94**: p. 699-714.
10. Feig, A.L. and S.J. Lippard, *Reactions of non-heme iron(II) centers with dioxygen in biology and chemistry.* Chem. Rev. , 1994. **94**: p. 759-805.
11. Solomon, E.I., F. Tuczek, D.E. Root, and C.A. Brown, *Spectroscopy of binuclear dioxygen complexes.* Chem. Rev. , 1994. **94**(3): p. 827-56.
12. Das, T.K., M. Couture, Y. Ouellet, M. Guertin, and D.L. Rousseau, *Simultaneous observation of the O---O and Fe---O2 stretching modes in oxyhemoglobins.* Proc. Nat. Acad. Sci. USA, 2001. **98**(2): p. 479-84.
13. Xing, G., Y. Diao, L.M. Hoffart, E.W. Barr, K.S. Prabhu, R.J. Arner, C.C. Reddy, C. Krebs, and J.M. Bollinger, Jr., *Evidence for C-H cleavage by an iron-superoxide complex in the glycol cleavage reaction catalyzed by myo-inositol oxygenase.* Proc. Nat. Acad. Sci. USA, 2006. **103**(16): p. 6130-5.
14. Roach, P.L., I.J. Clifton, C.M. Hensgens, N. Shibata, C.J. Schofield, J. Hajdu, and J.E. Baldwin, *Structure of isopenicillin N synthase complexed with substrate and the mechanism of penicillin formation.* Nature, 1997. **387**(6635): p. 827-30.
15. Klinman, J.P., *The copper-enzyme family of dopamine beta-monooxygenase and peptidylglycine alpha-hydroxylating monooxygenase: resolving the chemical pathway for substrate hydroxylation.* J. Biol. Chem., 2006. **281**(6): p. 3013-6.
16. Granata, A., E. Monzani, L. Bubacco, and L. Casella, *Mechanistic insight into the activity of tyrosinase from variable-temperature studies in an aqueous/organic solvent.* Chemistry-a European Journal, 2006. **12**(9): p. 2504-2514.
17. Davydov, R.M., T. Yoshida, M. Ikeda-Saito, and B.M. Hoffman, *Hydroperoxy-heme oxygenase generated by cryoreduction catalyzes the formation of alpha-meso-hydroxyheme as detected by EPR and ENDOR.* J. Am. Chem. Soc., 1999. **121**(45): p. 10656-10657.
18. Eswaramoorthy, S., J.B. Bonanno, S.K. Burley, and S. Swaminathan, *Mechanism of action of a flavin-containing monooxygenase.* Proc. Nat. Acad. Sci. USA, 2006. **103**(26): p. 9832-7.

19. Price, J., C., E. Barr, W., L. Hoffart, M., C. Krebs, and J.M. Bollinger, Jr., *Kinetic dissection of the catalytic mechanism of taurine:alpha-ketoglutarate dioxygenase (TauD) from Escherichia coli.* Biochemistry, 2005. **44**(22): p. 8138-47.
20. Rittle, J. and M.T. Green, *Cytochrome P450 compound I: capture, characterization, and C-H bond activation kinetics.* Science, 2010. **330**(6006): p. 933-7.
21. Neibergall, M.B., A. Stubna, Y. Mekmouche, E. Münck, and J.D. Lipscomb, *Hydrogen peroxide dependent cis-dihydroxylation of benzoate by fully oxidized benzoate 1,2-dioxygenase.* Biochemistry, 2007. **46**: p. 8004-8016.
22. Nordlund, P. and P. Reichard, *Ribonucleotide reductases.* Annual Review of Biochemistry, 2006. **75**: p. 681-706.
23. Lipscomb, J.D., *Catalysis and regulation in the soluble methane monooxygenase system: Applications of isotopes and isotope effects*, in *Isotope Effects in Chemistry and Biology*, A. Kohen and H.-H. Limbach, Editors. 2006, CRC Press: Boca Raton, FL. p. 931-953.
24. Dubois, J.L. and J.P. Klinman, *Mechanism of post-translational quinone formation in copper amine oxidases and its relationship to the catalytic turnover.* Archives of Biochemistry and Biophysics, 2005. **433**(1): p. 255-65.
25. Rogers, M.S. and D.M. Dooley, *Copper-tyrosyl radical enzymes.* Curr. Opin. Chem. Biol. , 2003. **7**(2): p. 189-96.
26. Solomon, E.I., P. Chen, M. Metz, S.-K. Lee, and A.E. Palmer, *Oxygen binding, activation, and reduction to water by copper proteins.* Angew. Chem. Int. Edit., 2001. **40**(24): p. 4570-4590.
27. Yoshikawa, S., K. Muramoto, and K. Shinzawa-Itoh, *Proton-pumping mechanism of cytochrome C oxidase.* Annual review of biophysics, 2011. **40**: p. 205-23.
28. Pau, M.Y., J.D. Lipscomb, and E.I. Solomon, *Substrate activation for O_2 reactions by oxidized metal centers in biology.* Proc. Nat. Acad. Sci. USA, 2007. **104**(47): p. 18355-62.
29. Solomon, E.I., J. Zhou, F. Neese, and E.G. Pavel, *New insights from spectroscopy into the structure/function relationships of lipoxygenases.* Chem. Biol., 1997. **4**(11): p. 795-808.
30. Frankenberg, C., J.F. Meirink, M. van Weele, U. Platt, and T. Wagner, *Assessing methane emissions from global space-borne observations.* Science, 2005. **308**(5724): p. 1010-4.
31. Dlugokencky, E.J., L. Bruhwiler, J.W.C. White, L.K. Emmons, P.C. Novelli, S.A. Montzka, K.A. Masarie, P.M. Lang, A.M. Crotwell, J.B. Miller, and L.V. Gatti, *Observational constraints on recent increases in the atmospheric CH_4 burden.* Geophysical Research Letters, 2009. **36**.
32. Foustoukos, D.I. and W.E. Seyfried, *Hydrocarbons in hydrothermal vent fluids: The role of chromium-bearing catalysts.* Science, 2004. **304**(5673): p. 1002-1005.
33. Zeikus, J.G., *The biology of methanogenic bacteria.* Bacteriological reviews, 1977. **41**(2): p. 514-41.
34. *Inventory of U.S. Greenhouse Gas Emissions and Sinks: 1990–2010*, 2012, U.S. Environmental Protection Agency.
35. Shakhova, N., I. Semiletov, A. Salyuk, V. Yusupov, D. Kosmach, and O. Gustafsson, *Extensive methane venting to the atmosphere from sediments of the east siberian arctic shelf.* Science, 2010. **327**(5970): p. 1246-1250.
36. Krey, V., J.G. Canadell, N. Nakicenovic, Y. Abe, H. Andruleit, D. Archer, A. Grubler, N.T.M. Hamilton, A. Johnson, V. Kostov, J.F. Lamarque, N. Langhorne, E.G. Nisbet, B. O'Neill, K. Riahi, M. Riedel, W.H. Wang, and V. Yakushev, *Gas hydrates: entrance to a methane age or climate threat?* Environmental Research Letters, 2009. **4**(3).

37. Li, S., J. Matthews, and A. Sinha, *Atmospheric hydroxyl radical production from electronically excited NO_2 and H_2O.* Science, 2008. **319**(5870): p. 1657-60.
38. Manning, M.R., D.C. Lowe, R.C. Moss, G.E. Bodeker, and W. Allan, *Short-term variations in the oxidizing power of the atmosphere.* Nature, 2005. **436**(7053): p. 1001-4.
39. Holmes, A.J., P. Roslev, I.R. McDonald, N. Iversen, K. Henriksen, and J.C. Murrell, *Characterization of methanotrophic bacterial populations in soils showing atmospheric methane uptake.* Applied and Environmental Microbiology, 1999. **65**(8): p. 3312-8.
40. Knittel, K. and A. Boetius, *Anaerobic oxidation of methane: progress with an unknown process.* Annual Review of Microbiology, 2009. **63**: p. 311-34.
41. Raghoebarsing, A.A., A. Pol, K.T. van de Pas-Schoonen, A.J. Smolders, K.F. Ettwig, W.I. Rijpstra, S. Schouten, J.S. Damste, H.J. Op den Camp, M.S. Jetten, and M. Strous, *A microbial consortium couples anaerobic methane oxidation to denitrification.* Nature, 2006. **440**(7086): p. 918-21.
42. Kruger, M., A. Meyerdierks, F.O. Glockner, R. Amann, F. Widdel, M. Kube, R. Reinhardt, J. Kahnt, R. Bocher, R.K. Thauer, and S. Shima, *A conspicuous nickel protein in microbial mats that oxidize methane anaerobically.* Nature, 2003. **426**(6968): p. 878-81.
43. Hanson, R.S. and T.E. Hanson, *Methanotrophic bacteria.* Microbiological Reviews, 1996. **60**(2): p. 439-47.
44. Ruscic, B., M. Litorja, and R.L. Asher, *Ionization energy of methylene revisited: Improved values for the enthalpy of formation of CH_2 and the bond dissociation energy of CH_3 via simultaneous solution of the local thermochemical network.* J. Phys. Chem. A, 1999. **103**(43): p. 8625-8633.
45. Fox, B.G., J.G. Borneman, L.P. Wackett, and J.D. Lipscomb, *Haloalkene oxidation by the soluble methane monooxygenase from Methylosinus trichosporium OB3b: mechanistic and environmental implications.* Biochemistry, 1990. **29**(27): p. 6419-6427.
46. Green, J. and H. Dalton, *Substrate specificity of soluble methane monooxygenase. Mechanistic implications.* J. Biol. Chem., 1989. **264**(30): p. 17698-17703.
47. Sullivan, J.P., D. Dickinson, and H.A. Chase, *Methanotrophs, Methylosinus trichosporium OB3b, sMMO, and their application to bioremediation.* Crit. Rev. Microbiol., 1998. **24**(4): p. 335-73.
48. Enzien, M.V., F. Picardal, T.C. Hazen, R.G. Arnold, and C.B. Fliermans, *Reductive dechlorination of trichloroethylene and tetrachloroethylene under aerobic conditions in a sediment column.* Applied and Environmental Microbiology, 1994. **60**(6): p. 2200-4.
49. Brusseau, G.A., H.C. Tsien, R.S. Hanson, and L.P. Wackett, *Optimization of trichloroethylene oxidation by methanotrophs and the use of a colorimetric assay to detect soluble methane monooxygenase activity.* Biodegradation, 1990. **1**(1): p. 19-29.
50. Lee, S.-W., D.R. Keeney, D.-H. Lim, A.A. Dispirito, and J.D. Semrau, *Mixed pollutant degradation by Methylosinus trichosporium OB3b expressing either soluble or particulate methane monooxygenase: Can the tortoise beat the hare?* Applied and Environmental Microbiology, 2006. **72**(12): p. 7503-7509.
51. Hyman, M.R., I.B. Murton, and D.J. Arp, *Interaction of ammonia monooxygenase from Nitrosomonas europaea with alkanes, alkenes, and alkynes.* Applied and Environmental Microbiology, 1988. **54**(12): p. 3187-90.
52. Nguyen, H.H., A.K. Shiemke, S.J. Jacobs, B.J. Hales, M.E. Lidstrom, and S.I. Chan, *The nature of the copper ions in the membranes containing the particulate methane monooxygenase from Methylococcus capsulatus (Bath).* J. Biol. Chem., 1994. **269**(21): p. 14995-15005.

53. Lieberman, R.L. and A.C. Rosenzweig, *Crystal structure of a membrane-bound metalloenzyme that catalyzes the biological oxidation of methane.* Nature 2005. **434**(7030): p. 177-182.
54. Lieberman, R.L., K.C. Kondapalli, D.B. Shrestha, A.S. Hakemian, S.M. Smith, J. Telser, J. Kuzelka, R. Gupta, A.S. Borovik, S.J. Lippard, B.M. Hoffman, A.C. Rosenzweig, and T.L. Stemmler, *Characterization of the particulate methane monooxygenase metal centers in multiple redox states by X-ray absorption spectroscopy.* Inorg. Chem., 2006. **45**(20): p. 8372-8381.
55. Chan, S.I. and S.S. Yu, *Controlled oxidation of hydrocarbons by the membrane-bound methane monooxygenase: the case for a tricopper cluster.* Acc. Chem. Res., 2008. **41**(8): p. 969-79.
56. Martinho, M., D.W. Choi, A.A. Dispirito, W.E. Antholine, J.D. Semrau, and E. Münck, *Mössbauer studies of the membrane-associated methane monooxygenase from Methylococcus capsulatus bath: evidence for a diiron center.* J. Am. Chem. Soc., 2007. **129**(51): p. 15783-5.
57. Hakemian, A.S. and A.C. Rosenzweig, *The biochemistry of methane oxidation.* Annual Review of Biochemistry, 2007. **76**(1).
58. Balasubramanian, R., S.M. Smith, S. Rawat, L.A. Yatsunyk, T.L. Stemmler, and A.C. Rosenzweig, *Oxidation of methane by a biological dicopper centre.* Nature, 2010. **465**(7294): p. 115-9.
59. Woertink, J.S., P.J. Smeets, M.H. Groothaert, M.A. Vance, B.F. Sels, R.A. Schoonheydt, and E.I. Solomon, *A $[Cu_2O]^{2+}$ core in Cu-ZSM-5, the active site in the oxidation of methane to methanol.* Proc. Nat. Acad. Sci. USA, 2009. **106**(45): p. 18908-13.
60. Smith, T.J., S.E. Slade, N.P. Burton, J.C. Murrell, and H. Dalton, *Improved system for protein engineering of the hydroxylase component of soluble methane monooxygenase.* Applied and Environmental Microbiology, 2002. **68**(11): p. 5265-5273.
61. Murrell, J.C., *Molecular genetics of methane oxidation.* Biodegradation, 1994. **5**(3-4): p. 145-59.
62. Merkx, M. and S.J. Lippard, *Why orfY? Characterization of MMOD, a long overlooked component of the soluble methane monooxygenase from Methylococcus capsulatus (Bath).* J. Biol. Chem., 2002. **277**(8): p. 5858-5865.
63. Rosenzweig, A.C., C.A. Frederick, S.J. Lippard, and P. Nordlund, *Crystal structure of a bacterial non-haem iron hydroxylase that catalyses the biological oxidation of methane.* Nature, 1993. **366**(6455): p. 537-543.
64. Elango, N., R. Radhakrishnan, W.A. Froland, B.J. Wallar, C.A. Earhart, J.D. Lipscomb, and D.H. Ohlendorf, *Crystal structure of the hydroxylase component of methane monooxygenase from Methylosinus trichosporium OB3b.* Protein Science, 1997. **6**(3): p. 556-568.
65. Walters, K.J., G.T. Gassner, S.J. Lippard, and G. Wagner, *Structure of the soluble methane monooxygenase regulatory protein B.* Proc. Nat. Acad. Sci. USA, 1999. **96**(14): p. 7877-7882.
66. Rosenzweig, A.C., P. Nordlund, P.M. Takahara, C.A. Frederick, and S.J. Lippard, *Geometry of the soluble methane monooxygenase catalytic diiron center in two oxidation states.* Chemistry & Biology, 1995. **2**(6): p. 409-418.
67. Thomann, H., M. Bernardo, J.M. McCormick, S. Pulver, K.K. Andersson, J.D. Lipscomb, and E.I. Solomon, *Pulsed EPR studies of mixed valence [Fe(II)Fe(III)] forms of hemerythrin and methane monooxygenase: Evidence for a hydroxide bridge.* J. Am. Chem. Soc., 1993. **115**: p. 8881-8882.

68. Fox, B.G., M.P. Hendrich, K.K. Surerus, K.K. Andersson, W.A. Froland, J.D. Lipscomb, and E. Münck, *Mössbauer, EPR, and ENDOR studies of the hydroxylase and reductase components of methane monooxygenase from Methylosinus trichosporium OB3b.* J. Am. Chem. Soc., 1993. **115**: p. 3688-3701.
69. Shu, L., Y. Liu, J.D. Lipscomb, and L. Que, Jr., *EXAFS studies of the methane monooxygenase hydroxylase component from Methylosinus trichosporium OB3b.* J. Biol. Inorg. Chem., 1996. **1**: p. 297-304.
70. Whittington, D.A., A.C. Rosenzweig, C.A. Frederick, and S.J. Lippard, *Xenon and halogenated alkanes track putative substrate binding cavities in the soluble methane monooxygenase hydroxylase.* Biochemistry, 2001. **40**(12): p. 3476-3482.
71. Sazinsky, M.H. and S.J. Lippard, *Product bound structures of the soluble methane monooxygenase hydroxylase from Methylococcus capsulatus (Bath): Protein motion in the α-subunit.* J. Am. Chem. Soc., 2005. **127**(16): p. 5814-5825.
72. Murray, L.J. and S.J. Lippard, *Substrate trafficking and dioxygen activation in bacterial multicomponent monooxygenases.* Acc. Chem. Res., 2007. **40**(7): p. 466-474.
73. Chang, S.L., B.J. Wallar, J.D. Lipscomb, and K.H. Mayo, *Solution structure of component B from methane monooxygenase derived through heteronuclear NMR and molecular modeling.* Biochemistry, 1999. **38**(18): p. 5799-812.
74. Fox, B.G., Y. Liu, J.E. Dege, and J.D. Lipscomb, *Complex formation between the protein components of methane monooxygenase from Methylosinus trichosporium OB3b. Identification of sites of component interaction.* J. Biol. Chem., 1991. **266**(1): p. 540-550.
75. Chang, S.L., B.J. Wallar, J.D. Lipscomb, and K.H. Mayo, *Residues in Methylosinus trichosporium OB3b methane monooxygenase component B involved in molecular interactions with reduced- and oxidized-hydroxylase component: a role for the N-terminus.* Biochemistry, 2001. **40**(32): p. 9539-51.
76. Zhang, J., B.J. Wallar, C.V. Popescu, D.B. Renner, D.D. Thomas, and J.D. Lipscomb, *Methane monooxygenase hydroxylase and B component interactions.* Biochemistry, 2006. **45**(9): p. 2913-2926.
77. Bailey, L.J., J.G. McCoy, G.N. Phillips, Jr., and B.G. Fox, *Structural consequences of effector protein complex formation in a diiron hydroxylase.* Proc. Nat. Acad. Sci. USA, 2008. **105**(49): p. 19194-8.
78. Wallar, B.J. and J.D. Lipscomb, *Dioxygen activation by enzymes containing binuclear non-heme iron clusters.* Chem. Rev. , 1996. **96**(7): p. 2625-2657.
79. Lipscomb, J.D., S.G. Sligar, M.J. Namtvedt, and I.C. Gunsalus, *Autooxidation and hydroxylation reactions of oxygenated cytochrome P-450cam.* J. Biol. Chem., 1976. **251**(4): p. 1116-24.
80. Froland, W.A., K.K. Andersson, S.-K. Lee, Y. Liu, and J.D. Lipscomb, *Methane monooxygenase component B and reductase alter the regioselectivity of the hydroxylase component-catalyzed reactions. A novel role for protein-protein interactions in an oxygenase mechanism.* J. Biol. Chem., 1992. **267**(25): p. 17588-17597.
81. Liu, Y., J.C. Nesheim, S.-K. Lee, and J.D. Lipscomb, *Gating effects of component B on oxygen activation by the methane monooxygenase hydroxylase component.* J. Biol. Chem., 1995. **270**(42): p. 24662-24665.
82. Green, J. and H. Dalton, *Protein B of soluble methane monooxygenase from Methylococcus capsulatus (Bath). A novel regulatory protein of enzyme activity.* J. Biol. Chem., 1985. **260**(29): p. 15795-15801.
83. Pulver, S., W.A. Froland, B.G. Fox, J.D. Lipscomb, and E.I. Solomon, *Spectroscopic studies of the coupled binuclear non-heme iron active site in the fully reduced*

hydroxylase component of methane monooxygenase: comparison to deoxy and deoxy-azide hemerythrin. [Erratum to document cited in CA120:3498]. J. Am. Chem. Soc., 1994. **116**(10): p. 4529.

84. Paulsen, K.E., Y. Liu, B.G. Fox, J.D. Lipscomb, E. Münck, and M.T. Stankovich, *Oxidation-reduction potentials of the methane monooxygenase hydroxylase component from Methylosinus trichosporium OB3b.* Biochemistry, 1994. **33**(3): p. 713-722.
85. Gallagher, S.C., A.J. Callaghan, J. Zhao, H. Dalton, and J. Trewhella, *Global conformational changes control the reactivity of methane monooxygenase.* Biochemistry, 1999. **38**(21): p. 6752-60.
86. Schwartz, J.K., P.-p. Wei, K.H. Mitchell, B.G. Fox, and E.I. Solomon, *Geometric and electronic structure studies of the binuclear nonheme ferrous active site of toluene-4-monooxygenase: Parallels with methane monooxygenase and insight into the role of the effector proteins in O_2 activation.* J. Am. Chem. Soc., 2008. **130**(22): p. 7098-7109.
87. Chatwood, L.L., J. Mueller, J.D. Gross, G. Wagner, and S.J. Lippard, *NMR structure of the flavin domain from soluble methane monooxygenase reductase from Methylococcus capsulatus (Bath).* Biochemistry, 2004. **43**(38): p. 11983-11991.
88. Muller, J., A. Lugovskoy, A., G. Wagner, and S. Lippard, J., *NMR structure of the [2Fe-2S] ferredoxin domain from soluble methane monooxygenase reductase and interaction with its hydroxylase.* Biochemistry, 2002. **41**(1): p. 42-51.
89. Liu, Y., J.C. Nesheim, K.E. Paulsen, M.T. Stankovich, and J.D. Lipscomb, *Roles of the methane monooxygenase reductase component in the regulation of catalysis.* Biochemistry, 1997. **36**(17): p. 5223-5233.
90. Balendra, S., C. Lesieur, J. Smith Thomas, and H. Dalton, *Positively charged amino acids are essential for electron transfer and protein-protein interactions in the soluble methane monooxygenase complex from Methylococcus capsulatus (Bath).* Biochemistry, 2002. **41**(8): p. 2571-9.
91. Blazyk, J., L., G. Gassner, T., and S. Lippard, J., *Intermolecular electron-transfer reactions in soluble methane monooxygenase: a role for hysteresis in protein function.* J. Am. Chem. Soc., 2005. **127**(49): p. 17364-76.
92. Fox, B.G., W.A. Froland, J.E. Dege, and J.D. Lipscomb, *Methane monooxygenase from Methylosinus trichosporium OB3b. Purification and properties of a three-component system with high specific activity from a type II methanotroph.* J. Biol. Chem., 1989. **264**(17): p. 10023-10033.
93. Andersson, K.K., W.A. Froland, S.-K. Lee, and J.D. Lipscomb, *Dioxygen independent oxygenation of hydrocarbons by methane monooxygenase hydroxylase component.* New Journal of Chemistry, 1991. **15**: p. 411-415.
94. Lee, S.-K., J.C. Nesheim, and J.D. Lipscomb, *Transient intermediates of the methane monooxygenase catalytic cycle.* J. Biol. Chem., 1993. **268**(29): p. 21569-21577.
95. Hendrich, M.P., E. Münck, B.G. Fox, and J.D. Lipscomb, *Integer-spin EPR studies of the fully reduced methane monooxygenase hydroxylase component.* J. Am. Chem. Soc., 1990. **112**: p. 5861-5865.
96. Liu, K.E., A.M. Valentine, D. Qiu, D.E. Edmondson, E.H. Appelman, T.G. Spiro, and S.J. Lippard, *Characterization of a diiron(III) peroxo intermediate in the reaction cycle of methane monooxygenase hydroxylase from Methylococcus capsulatus (Bath).* J. Am. Chem. Soc., 1995. **117**: p. 4997-4998.
97. Brazeau, B.J. and J.D. Lipscomb, *Kinetics and activation thermodynamics of methane monooxygenase compound Q formation and reaction with substrates.* Biochemistry, 2000. **39**(44): p. 13503-13515.

98. Lee, S.-K. and J.D. Lipscomb, *Oxygen activation catalyzed by methane monooxygenase hydroxylase component: proton delivery during the O-O bond cleavage steps.* Biochemistry, 1999. **38**(14): p. 4423-32.
99. Shu, L., J.C. Nesheim, K. Kauffmann, E. Münck, J.D. Lipscomb, and L. Que, Jr., *An $Fe(IV)_2O_2$ diamond core structure for the key intermediate Q of methane monooxygenase.* Science, 1997. **275**(5299): p. 515-518.
100. Tinberg, C.E. and S.J. Lippard, *Revisiting the mechanism of dioxygen activation in soluble methane monooxygenase from M. capsulatus (Bath): Evidence for a multi-step, proton-dependent reaction pathway.* Biochemistry, 2009. **48**(51): p. 12145-12158.
101. Liu, K.E., D. Wang, B.H. Huynh, D.E. Edmondson, A. Salifoglou, and S.J. Lippard, *Spectroscopic detection of intermediates in the reaction of dioxygen with the reduced methane monooxygenase hydroxylase from Methylococcus capsulatus (Bath).* J. Am. Chem. Soc., 1994. **116**: p. 7465-7466.
102. Lee, S.K., B.G. Fox, W.A. Froland, J.D. Lipscomb, and E. Münck, *A transient intermediate of the methane monooxygenase catalytic cycle containing an Fe(IV)Fe(IV) cluster.* J. Am. Chem. Soc., 1993. **115**(14): p. 6450-6451.
103. Gherman, B.F., M.-H. Baik, S.J. Lippard, and R.A. Friesner, *Dioxygen activation in methane monooxygenase: a theoretical study.* J. Am. Chem. Soc., 2004. **126**(9): p. 2978-2990.
104. Han, W.G. and L. Noodleman, *Structural model studies for the peroxo intermediate P and the reaction pathway from P-->Q of methane monooxygenase using broken-symmetry density functional calculations.* Inorg. Chem., 2008. **47**(8): p. 2975-86.
105. Siegbahn, P.E.M., *O-O bond cleavage and alkane hydroxylation in methane monooxygenase.* J. Biol. Inorg. Chem., 2001. **6**(1): p. 27-45.
106. Broadwater, J.A., J. Ai, T.M. Loehr, J. Sanders-Loehr, and B.G. Fox, *Peroxodiferric intermediate of stearoyl-acyl carrier protein delta 9 desaturase: oxidase reactivity during single turnover and implications for the mechanism of desaturation.* Biochemistry, 1998. **37**(42): p. 14664-71.
107. Skulan, A., J., T. Brunold, C., J. Baldwin, L. Saleh, J.M. Bollinger, Jr., and E. Solomon, I., *Nature of the peroxo intermediate of the W48F/D84E ribonucleotide reductase variant: implications for O_2 activation by binuclear non-heme iron enzymes.* J. Am. Chem. Soc., 2004. **126**(28): p. 8842-55.
108. Moenne-Loccoz, P., J. Baldwin, B.A. Ley, T.M. Loehr, and J.M. Bollinger, Jr., *O_2 activation by non-heme diiron proteins: identification of a symmetric μ-1,2-peroxide in a mutant of ribonucleotide reductase.* Biochemistry, 1998. **37**(42): p. 14659-63.
109. Moenne-Loccoz, P., C. Krebs, K. Herlihy, D.E. Edmondson, E.C. Theil, B.H. Huynh, and T. Loehr, *The ferroxidase reaction of ferritin reveals a diferric μ-1,2 bridging peroxide intermediate in common with other O_2-activating non-heme diiron proteins.* Biochemistry, 1999. **38**: p. 5290-5295.
110. Vu, V.V., J.P. Emerson, M. Martinho, Y.S. Kim, E. Münck, M.H. Park, and L. Que, Jr., *Human deoxyhypusine hydroxylase, an enzyme involved in regulating cell growth, activates O_2 with a nonheme diiron center.* Proc. Nat. Acad. Sci. USA, 2009. **106**(35): p. 14814-14819, S14814/1-S14814/12.
111. Bailey, L.J. and B.G. Fox, *Crystallographic and catalytic studies of the peroxide-shunt reaction in a diiron hydroxylase.* Biochemistry, 2009. **48**(38): p. 8932-9.
112. Broadwater, J.A., C. Achim, E. Muenck, and B.G. Fox, *Mössbauer studies of the formation and reactivity of a quasi-stable peroxo intermediate of stearoyl-acyl carrier protein Δ9-desaturase.* Biochemistry, 1999. **38**(38): p. 12197-12204.

113. Krebs, C., J.M. Bollinger, Jr., C. Theil Elizabeth, and H. Huynh Boi, *Exchange coupling constant J of peroxodiferric reaction intermediates determined by Mossbauer spectroscopy.* J. Biol. Inorg. Chem., 2002. **7**(7-8): p. 863-9.
114. Pereira, A.S., W. Small, C. Krebs, P. Tavares, D.E. Edmondson, E.C. Theil, and B.H. Huynh, *Direct spectroscopic and kinetic evidence for the involvement of a peroxodiferric intermediate during the ferroxidase reaction in fast ferritin mineralization.* Biochemistry, 1998. **37**: p. 9871-9876.
115. Liu, K.E., A.M. Valentine, D.L. Wang, B.H. Huynh, D.E. Edmondson, A. Salifoglou, and S.J. Lippard, *Kinetic and spectroscopic characterization of intermediates and component interactions in reactions of methane monooxygenase from Methylococcus capsulatus (Bath).* J. Am. Chem. Soc., 1995. **117**(41): p. 10174-10185.
116. Penner-Hahn, J.E., K. Smith Eble, T.J. McMurry, M. Renner, A.L. Balch, J.T. Groves, J.H. Dawson, and K.O. Hodgson, *Structural characterization of horseradish peroxidase using EXAFS spectroscopy. Evidence for Fe = O ligation in compounds I and II.* J. Am. Chem. Soc., 1986. **108**(24): p. 7819-25.
117. Kurtz, D.M., Jr., *Oxo- and hydroxo-bridged diiron complexes: A chemical perspective on a biological unit.* Chem. Rev. , 1990. **90**: p. 585-606.
118. Zang, Y., Y. Dong, K. Kauffmann, E. Münck, and L. Que, Jr., *The first bis(μ-oxo)diiron(III) complex. Structure and magnetic propeties of $[Fe_2(\mu\text{-}O)_2(6TLA)_2](ClO_4)_2$.* J. Am. Chem. Soc., 1995. **117**: p. 1169-1170.
119. Baik, M.-H., M. Newcomb, R.A. Friesner, and S.J. Lippard, *Mechanistic studies on the hydroxylation of methane by methane monooxygenase.* Chem. Rev. , 2003. **103**(6): p. 2385-2419.
120. Han, W.G. and L. Noodleman, *Structural model studies for the high-valent intermediate Q of methane monooxygenase from broken-symmetry density functional calculations.* Inorganica Chimica Acta, 2008. **361**(4): p. 973-986.
121. Rinaldo, D., D.M. Philipp, S.J. Lippard, and R.A. Friesner, *Intermediates in dioxygen activation by methane monooxygenase: A QM/MM study.* J. Am. Chem. Soc., 2007. **129**(11): p. 3135-3147.
122. Torrent, M., G. Musaev Djamaladdin, H. Basch, and K. Morokuma, *Computational studies of reaction mechanisms of methane monooxygenase and ribonucleotide reductase.* Journal of Computational Chemistry, 2002. **23**(1): p. 59-76.
123. Torrent, M., D.G. Musaev, H. Basch, and K. Morokuma, *Computational studies of reaction mechanisms of methane monooxygenase and ribonucleotide reductase.* Journal of Computational Chemistry, 2002. **23**(1): p. 59-76.
124. Ortiz de Montellano, P.R., *Cytochrome P-450*, ed. P.R. Ortiz de Montellano1985, New York: Plenum Press.
125. Lipscomb, J.D., *Biochemistry of the soluble methane monooxygenase.* Ann. Rev. Microbiol., 1994. **48**: p. 371-399.
126. Basch, H., D.G. Musaev, K. Mogi, and K. Morokima, *Theoretical studies on the mechanism of the methane -> methanol conversion reaction catalyzed by methane monooxygenase (MMO): The O-side vs N-side mechanisms.* J. Phys. Chem. A, 2001. **105**: p. 3615-3622.
127. Siegbahn, P.E.M., R.H. Crabtree, and P. Nordlund, *Mechanism of methane monooxygenase - a structural and quantum chemical perspective.* J. Biol. Inorg. Chem., 1998. **3**(3): p. 314-317.
128. Dunietz, B.D., M.D. Beachy, Y. Cao, D.A. Whittington, S.J. Lippard, and R.A. Friesner, *Large scale ab initio quantum chemical calculation of the intermediates in the soluble*

methane monooxygenase catalytic cycle. J. Am. Chem. Soc., 2000. **122**(12): p. 2828-2839.
129. Liu, K.E., C.C. Johnson, M. Newcomb, and S.J. Lippard, *Radical clock substrate probes and kinetic isotope effect studies of the hydroxylation of hydrocarbons by methane monooxygenase.* J. Am. Chem. Soc., 1993. **115**: p. 939-947.
130. Newcomb, M., M.-H.L. Tadic-Biadatti, D.L. Chestney, E.S. Roberts, and P.F. Hollenberg, *A nonsynchronous concerted mechanism for cytochrome P-450 catalyzed hydroxylation.* J. Am. Chem. Soc., 1995. **117**: p. 12085-12091.
131. Choi, S.-Y., P.E. Eaton, P.F. Hollenberg, K.E. Liu, S.J. Lippard, M. Newcomb, D.A. Putt, S.P. Upadhyaya, and Y. Xiong, *Regiochemical variations in reactions of metylcubane with tert-butoxyl radical, cytochrome P-450 enzymes, and a methane monooxygenase system.* J. Am. Chem. Soc., 1996. **118**: p. 6547-6555.
132. Shteinman, A.A., *Does the non-heme monooxygenase sMMO share a unified oxidation mechanism with the heme monooxygenase cytochrome P-450?* J. Biol. Inorg. Chem., 1998. **3**(3): p. 325-330.
133. Shestakov, A.F. and A.E. Shilov, *Five-coordinate carbon hydroxylation mechanism.* J. Mol. Catal. A:, 1996. **105**: p. 1-7.
134. Yoshizawa, K., *Nonradical mechanism for methane hydroxylation by iron-oxo complexes.* Acc. Chem. Res., 2006. **39**(6): p. 375-82.
135. Priestley, N.D., H.G. Floss, W.A. Froland, J.D. Lipscomb, P.G. Williams, and H. Morimoto, *Cryptic stereospecificity of methane monooxygenase.* J. Am. Chem. Soc., 1992. **114**: p. 7561-7562.
136. Ruzicka, F., D.S. Huang, M.I. Donnelly, and P.A. Frey, *Methane monooxygenase catalyzed oxygenation of 1,1-dimethylcyclopropane. Evidence for radical and carbocationic intermediates.* Biochemistry, 1990. **29**(7): p. 1696-1700.
137. Valentine, A.M., M.-H. LeTadic-Biadatti, P.H. Toy, M. Newcomb, and S.J. Lippard, *Oxidation of ultrafast radical clock substrate probes by the soluble methane monooxygenase from Methylococcus capsulatus (Bath).* J. Biol. Chem., 1999. **274**(16): p. 10771-10776.
138. Choi, S.-Y., P.E. Eaton, D.A. Kopp, S.J. Lippard, M. Newcomb, and R. Shen, *Cationic species can be produced in soluble methane monooxygenase-catalyzed hydroxylation reactions; Radical intermediates are not formed.* J. Am. Chem. Soc., 1999. **121**(51): p. 12198-12199.
139. Jin, Y. and J.D. Lipscomb, *Probing the mechanism of C-H activation: oxidation of methylcubane by soluble methane monooxygenase from Methylosinus trichosporium OB3b.* Biochemistry, 1999. **38**(19): p. 6178-86.
140. Jin, Y. and J.D. Lipscomb, *Mechanistic insights into C-H activation from radical clock chemistry: Oxidation of substituted methylcyclopropanes catalyzed by soluble methane monooxygenase from Methylosinus trichosporium OB3b.* Biochim. Biophys. Acta., 2000. **1543**: p. 47-59.
141. Brazeau, B.J., R.N. Austin, C. Tarr, J.T. Groves, and J.D. Lipscomb, *Intermediate Q from soluble methane monooxygenase hydroxylates the mechanistic substrate probe norcarane: Evidence for a stepwise reaction.* J. Am. Chem. Soc., 2001. **123**(48): p. 11831-11837.
142. Beauvais, L.G. and S.J. Lippard, *Reactions of the peroxo intermediate of soluble methane monooxygenase hydroxylase with ethers.* J. Am. Chem. Soc., 2005. **127**(20): p. 7370-7378.

143. Valentine, A.M., S.S. Stahl, and S.J. Lippard, *Mechanistic studies of the reaction of reduced methane monooxygenase hydroxylase with dioxygen and substrates.* J. Am. Chem. Soc., 1999. **121**(16): p. 3876-3887.
144. Sturgeon, B.E., D. Burdi, S. Chen, B.-H. Huynh, D.E. Edmondson, J. Stubbe, and B.M. Hoffman, *Reconsideration of **X**, the diiron intermediate formed during cofactor assembly in E. coli ribonucleotide reductase.* J. Am. Chem. Soc., 1996. **118**: p. 7551-7557.
145. Stubbe, J. and P. Riggs-Gelasco, *Harnessing free radicals: formation and function of the tyrosyl radical in ribonucleotide reductase.* Trends in Biochemical Sciences, 1998. **23**(11): p. 438-443.
146. Jin, Y. and J.D. Lipscomb, *Desaturation reactions catalyzed by soluble methane monooxygenase.* J. Biol. Inorg. Chem., 2001. **6**(7): p. 717-725.
147. Nesheim, J.C. and J.D. Lipscomb, *Large isotope effects in methane oxidation catalyzed by methane monooxygenase: evidence for C-H bond cleavage in a reaction cycle intermediate.* Biochemistry, 1996. **35**(31): p. 10240-10247.
148. Klinman, J.P., *The role of tunneling in enzyme catalysis of C-H activation.* Biochim. Biophys. Acta, Bioenerg., 2006. **1757**(8): p. 981-987.
149. Zheng, H. and J.D. Lipscomb, *Regulation of methane monooxygenase catalysis based on size exclusion and quantum tunneling.* Biochemistry, 2006. **45**(6): p. 1685-1692.
150. Siebrand, W. and Z. Smedarchina, *Mechanism of CH-bond cleavage catalyzed by enzymes*, in *Isotope Effects in Chemistry and Biology*, A. Kohen and H.-H. Limbach, Editors. 2006, Taylor & Francis: Boca Raton, FL. p. 725-741.
151. Liu, A., Y. Jin, J. Zhang, B.J. Brazeau, and J.D. Lipscomb, *Substrate radical intermediates in soluble methane monooxygenase.* Biochem. Biophys. Res. Comm., 2005. **338**(1): p. 254-261.
152. Arciero, D.M. and J.D. Lipscomb, *Binding of ^{17}O-labeled substrate and inhibitors to protocatechuate 4,5-dioxygenase-nitrosyl complex. Evidence for direct substrate binding to the active site Fe^{2+} of extradiol dioxygenases.* J. Biol. Chem., 1986. **261**(5): p. 2170-2178.
153. Ryle, M.J., R. Padmakumar, and R.P. Hausinger, *Stopped-flow kinetic analysis of Escherichia coli taurine/alpha-ketoglutarate dioxygenase: interactions with alpha-ketoglutarate, taurine, and oxygen.* Biochemistry, 1999. **38**(46): p. 15278-86.
154. Wolfe, M.D., J.V. Parales, D.T. Gibson, and J.D. Lipscomb, *Single turnover chemistry and regulation of O_2 activation by the oxygenase component of naphthalene 1,2-dioxygenase.* J. Biol. Chem., 2001. **276**(3): p. 1945-53.
155. Koehntop, K.D., S. Marimanikkuppam, M.J. Ryle, R.P. Hausinger, and L. Que, Jr., *Self-hydroxylation of taurine/α-ketoglutarate dioxygenase: evidence for more than one oxygen activation mechanism.* J. Biol. Inorg. Chem., 2006. **11**(1): p. 63-72.
156. Gorsky, L.D., D.R. Koop, and M.J. Coon, *On the stoichiometry of the oxidase and monooxygenase reactions catalyzed by liver microsomal cytochrome P-450. Products of oxygen reduction.* J. Biol. Chem., 1984. **259**(11): p. 6812-7.
157. Wallar, B.J. and J.D. Lipscomb, *Methane monooxygenase component B mutants alter the kinetics of steps throughout the catalytic cycle.* Biochemistry, 2001. **40**(7): p. 2220-2233.
158. Brazeau, B.J. and J.D. Lipscomb, *Key amino acid residues in the regulation of soluble methane monooxygenase catalysis by component B.* Biochemistry, 2003. **42**(19): p. 5618-5631.
159. Brazeau, B.J., B.J. Wallar, and J.D. Lipscomb, *Unmasking of deuterium kinetic isotope effects on the methane monooxygenase compound Q reaction by site-directed mutagenesis of component B.* J. Am. Chem. Soc., 2001. **123**(42): p. 10421-2.

160. Nagel, Z.D. and J.P. Klinman, *Tunneling and dynamics in enzymatic hydride transfer.* Chem. Rev., 2006. **106**(8): p. 3095-3118.
161. Brandstetter, H., D.A. Whittington, S.J. Lippard, and C.A. Frederick, *Mutational and structural analyses of the regulatory protein B of soluble methane monooxygenase from Methylococcus capsulatus (Bath).* Chem. Biol., 1999. **6**(7): p. 441-449.
162. Zhang, J. and J.D. Lipscomb, *Role of the C-terminal region of the B component of Methylosinus trichosporium OB3b methane monooxygenase in the regulation of oxygen activation.* Biochemistry, 2006. **45**: p. 1459-1469.
163. Boswell, R., *Is gas hydrate energy within reach?* Science, 2009. **325**(5943): p. 957-958.
164. Lunsford, J.H., *Catalytic conversion of methane to more useful chemicals and fuels: a challenge for the 21st century.* Catalysis Today, 2000. **63**(2-4): p. 165-174.
165. Olah, G.A., A. Goeppert, and G.K.S. Prakash, *Beyond oil and gas: The methanol economy*2009: Wiley-VCH.
166. Zhao, M., B. Helms, E. Slonkina, S. Friedle, D. Lee, J. DuBois, B. Hedman, K.O. Hodgson, J.M.J. Frechet, and S.J. Lippard, *Iron complexes of dendrimer-appended carboxylates for activating dioxygen and oxidizing hydrocarbons.* J. Am. Chem. Soc., 2008. **130**(13): p. 4352-4363.
167. Shan, X. and L. Que, Jr., *Intermediates in the oxygenation of a nonheme diiron(II) complex, including the first evidence for a bound superoxo species.* Proc. Nat. Acad. Sci. USA, 2005. **102**(15): p. 5340-5345.
168. Chavez, F., A., R. Ho, Y. N., M. Pink, V. Young, G., Jr., S. Kryatov, V., E. Rybak-Akimova, V., H. Andres, E. Munck, L. Que, Jr., and W. Tolman, B., *Unusual peroxo intermediates in the reaction of dioxygen with carboxylate-bridged diiron(II,II) paddlewheel complexes.* Angew. Chem. Int. Edit., 2002. **41**(1): p. 149-52.
169. Ookubo, T., H. Sugimoto, T. Nagayama, H. Masuda, T. Sato, K. Tanaka, Y. Maeda, H. Okawa, Y. Hayashi, A. Uehara, and M. Suzuki, *cis-μ-1,2-peroxo diiron complex: Structure and reversible oxygenation.* J. Am. Chem. Soc., 1996. **118**: p. 701-702.
170. Tshuva, E.Y. and S.J. Lippard, *Synthetic models for non-heme carboxylate-bridged diiron metalloproteins: strategies and tactics.* Chem. Rev. , 2004. **104**(2): p. 987-1011.
171. Xue, G., D. Wang, R. De Hont, A.T. Fiedler, X. Shan, E. Münck, and L. Que, Jr., *A synthetic precedent for the [Fe^{IV}_2(μ-O)$_2$] diamond core proposed for methane monooxygenase intermediate Q.* Proc. Nat. Acad. Sci. USA, 2007. **104**(52): p. 20713-20718.
172. Wilkinson, E.C., Y.H. Dong, Y. Zang, H. Fujii, R. Fraczkiewicz, G. Fraczkiewicz, R.S. Czernuszewicz, and L. Que, *Raman signature of the Fe_2O_2 "diamond" core.* J. Am. Chem. Soc., 1998. **120**(5): p. 955-962.
173. Xue, G., A.T. Fiedler, M. Martinho, E. Münck, and L. Que, Jr., *Insights into the P-to-Q conversion in the catalytic cycle of methane monooxygenase from a synthetic model system.* Proc. Nat. Acad. Sci. USA, 2008. **105**(52): p. 20615-20620.
174. Xue, G., R. De Hont, E. Münck, and L. Que, Jr., *Million-fold activation of the [Fe_2(μ-O)$_2$] diamond core for C-H bond cleavage.* Nature Chem., 2010. **2**(5): p. 400-405.
175. Hirao, H., D. Kumar, L. Que, Jr., and S. Shaik, *Two-state reactivity in alkane hydroxylation by non-heme iron-oxo complexes.* J. Am. Chem. Soc., 2006. **128**(26): p. 8590-606.
176. Decker, A., J.-U. Rohde, E.J. Klinker, S.D. Wong, L. Que, Jr., and E.I. Solomon, *Spectroscopic and quantum chemical studies on low-spin FeIV:O complexes: Fe-O bonding and its contributions to reactivity.* J. Am. Chem. Soc., 2007. **129**(51): p. 15983-15996.

177. Murray, L.J., S.G. Naik, D.O. Ortillo, R. Garcia-Serres, J.K. Lee, B.H. Huynh, and S.J. Lippard, *Characterization of the arene-oxidizing intermediate in ToMOH as a diiron(III) species.* J. Am. Chem. Soc., 2007. **129**(46): p. 14500-14510.
178. Song, W.J. and S.J. Lippard, *Mechanistic studies of reactions of peroxodiiron(III) intermediates in T201 variants of toluene/o-xylene monooxygenase hydroxylase.* Biochemistry, 2011. **50**(23): p. 5391-5399.
179. Wang, D., E.R. Farquhar, A. Stubna, E. Münck, and L. Que, Jr., *A diiron(IV) complex that cleaves strong C-H and O-H bonds.* Nature Chem., 2009. **1**(2): p. 145-150, S145/1-S145/15.
180. Davydov, A., R. Davydov, A. Gräslund, J.D. Lipscomb, and K.K. Andersson, *Radiolytic reduction of methane monooxygenase dinuclear iron cluster at 77 K - EPR evidence for conformational change upon reduction or binding of component B to the diferric state.* J. Biol. Chem., 1997. **272**(11): p. 7022-7026.
181. Fox, B.G., K.K. Surerus, E. Münck, and J.D. Lipscomb, *Evidence for a μ-oxo-bridged binuclear iron cluster in the hydroxylase component of methane monooxygenase. Mössbauer and EPR studies.* J. Biol. Chem., 1988. **263**(22): p. 10553-10556.
182. Fox, B.G. and J.D. Lipscomb, *Purification of a high specific activity methane monooxygenase hydroxylase component from a type II methanotroph.* Biochem. Biophys. Res. Comm., 1988. **154**(1): p. 165-170.
183. Stahl, S.S., W.A. Francisco, M. Merkx, J.P. Klinman, and S.J. Lippard, *Oxygen kinetic isotope effects in soluble methane monooxygenase.* J. Biol. Chem., 2001. **276**(7): p. 4549-4553.
184. Fox, B.G., W.A. Froland, D.R. Jollie, and J.D. Lipscomb, *Methane monooxygenase from Methylosinus trichosporium OB3b.* Methods in Enzymology, 1990. **188**: p. 191-202.
185. Cardy, D.L., V. Laidler, G.P. Salmond, and J.C. Murrell, *The methane monooxygenase gene cluster of Methylosinus trichosporium: cloning and sequencing of the mmoC gene.* Arch. Microbiol., 1991. **156**(6): p. 477-483.
186. Mbughuni, M.M., M. Chakrabarti, J.A. Hayden, E.L. Bominaar, M.P. Hendrich, E. Münck, and J.D. Lipscomb, *Trapping and spectroscopic characterization of an FeIII-superoxo intermediate from a nonheme mononuclear iron-containing enzyme.* Proc. Nat. Acad. Sci. USA, 2010. **107**(39): p. 16788-93.
187. Willson, R.L. and A.J.F. Searle, *Metronidazole (Flagyl) - iron catalyzed reaction with sulfhydryl groups and tumor radiosensitization.* Nature, 1975. **255**(5508): p. 498-500.
188. Searle, A.J.F. and A. Tomasi, *Hydroxyl free radical production in iron-cysteine solutions and protection by zinc.* Journal of Inorganic Biochemistry, 1982. **17**(2): p. 161-166.
189. Barron, E.S.G., L.B. Flexner, and L. Michaelis, *Oxidation-reduction systems of biological significance.* J. Biol. Chem., 1929. **81**(3): p. 743-754.
190. Welch, K.D., T.Z. Davis, and S.D. Aust, *Iron autoxidation and free radical generation: effects of buffers, ligands, and chelators.* Archives of Biochemistry and Biophysics, 2002. **397**(2): p. 360-9.
191. Stadtman, E.R., *Metal ion-catalyzed oxidation of proteins: biochemical mechanism and biological consequences.* Free Radical Biology & Medicine, 1990. **9**(4): p. 315-25.
192. Brazeau, B.J., B.J. Wallar, and J.D. Lipscomb, *Effector proteins from P450cam and methane monooxygenase: lessons in tuning nature's powerful reagents.* Biochem. Biophys. Res. Comm., 2003. **312**(1): p. 143-148.
193. Dworkin, M., S. Falkow, E. Rosenberg, K.-H. Schleifer, and E. Stackebrandt, *The Prokaryotes*. 3 ed. The Prokaryotes. Vol. Proteobacteria: Alpha and Beta Subclasses. 2006: Springer.

194. Prior, S.D. and H. Dalton, *Acetylene as a suicide substrate and active-site probe for methane monooxygenase from Methylococcus-capsulatus (Bath).* FEMS Microbiology Letters, 1985. **29**(1-2): p. 105-109.
195. Lloyd, J.S., R. Finch, H. Dalton, and J.C. Murrell, *Homologous expression of soluble methane monooxygenase genes in Methylosinus trichosporium OB3b.* Microbiology, 1999. **145**(2): p. 461-470.
196. Xing, X.H., H. Wu, M.F. Luo, and B.P. Wang, *Effects of organic chemicals on growth of Methylosinus trichosporium OB3b.* Biochemical Engineering Journal, 2006. **31**(2): p. 113-117.
197. Grosse, S., L. Laramee, K.D. Wendlandt, I.R. McDonald, C.B. Miguez, and H.P. Kleber, *Purification and characterization of the soluble methane monooxygenase of the type II methanotrophic bacterium Methylocystis sp. strain WI 14.* Appl. Environ. Microbiol., 1999. **65**(9): p. 3929-3935.
198. Ali, H., J. Scanlan, M.G. Dumont, and J.C. Murrell, *Duplication of the mmoX gene in Methylosinus sporium: cloning, sequencing and mutational analysis.* Microbiology, 2006. **152**(Pt 10): p. 2931-42.
199. Shu, L.J., Y. Liu, J.D. Lipscomb, and L. Que, *X-ray absorption spectroscopic studies of the methane monooxygenase hydroxylase component from Methylosinus trichosporium OB3b.* J. Biol. Inorg. Chem., 1996. **1**(4): p. 297-304.
200. Kauffmann, K.E., C.V. Popescu, Y. Dong, J.D. Lipscomb, L. Que, Jr., and E. Münck, *Mössbauer evidence for antisymmetric exchange in a diferric synthetic complex and diferric methane monooxygenase.* J. Am. Chem. Soc., 1998. **120**(34): p. 8739-8746.
201. Gross, A.J. and I.W. Sizer, *The oxidation of tyramine, tyrosine, and related compounds by peroxidase.* J. Biol. Chem., 1959. **234**(6): p. 1611-4.
202. Doughty, D.M., K.H. Halsey, C.J. Vieville, L.A. Sayavedra-Soto, D.J. Arp, and P.J. Bottomley, *Propionate inactivation of butane monooxygenase activity in 'Pseudomonas butanovora': biochemical and physiological implications.* Microbiology, 2007. **153**(Pt 11): p. 3722-9.
203. Colby, J. and H. Dalton, *Resolution of the methane monooxygenase of Methylococcus capsulatus (Bath) into three components.* Biochemical Journal, 1978. **171**: p. 461-468.
204. Smith, D.D. and H. Dalton, *Solubilisation of methane monooxygenase from Methylococcus capsulatus (Bath).* Eur. J. Biochem., 1989. **182**(3): p. 667-671.
205. Tinberg, C.E. and S.J. Lippard, *Dioxygen activation in soluble methane monooxygenase.* Acc. Chem. Res., 2011. **44**(4): p. 280-288.
206. Mitić, N., J.K. Schwartz, B.J. Brazeau, J.D. Lipscomb, and E.I. Solomon, *CD and MCD studies of the effects of component B variant binding on the biferrous active site of methane monooxygenase.* Biochemistry, 2008. **47**: p. 8386–8397.
207. Wei, P.P., A.J. Skulan, H. Wade, W.F. DeGrado, and E.I. Solomon, *Spectroscopic and computational studies of the de novo designed protein DF2t: correlation to the biferrous active site of ribonucleotide reductase and factors that affect O_2 reactivity.* J. Am. Chem. Soc., 2005. **127**(46): p. 16098-106.
208. Whittington, D.A. and S.J. Lippard, *Crystal structures of the soluble methane monooxygenase hydroxylase from Methylococcus capsulatus (Bath) demonstrating geometrical variability at the dinuclear iron active site.* J. Am. Chem. Soc., 2001. **123**(5): p. 827-838.
209. Pulver, S., W.A. Froland, B.G. Fox, J.D. Lipscomb, and E.I. Solomon, *Spectroscopic studies of the coupled binuclear non-heme iron active site in the fully reduced hydroxylase component of methane monooxygenase: Comparison to deoxy and deoxy-azide hemerythrin.* J. Am. Chem. Soc., 1993. **115**: p. 12409-12422.

210. Mbughuni, M.M., K.K. Meier, E. Münck, and J.D. Lipscomb, *Substrate-mediated oxygen activation by homoprotocatechuate 2,3-dioxygenase: intermediates formed by a tyrosine 257 variant.* Biochemistry, 2012. **51**(44): p. 8743-54.
211. Marti, M.A., A. Crespo, L. Capece, L. Boechi, D.E. Bikiel, D.A. Scherlis, and D.A. Estrin, *Dioxygen affinity in heme proteins investigated by computer simulation.* Journal of Inorganic Biochemistry, 2006. **100**(4): p. 761-770.
212. Capece, L., M.A. Marti, A. Crespo, F. Doctorovich, and D.A. Estrin, *Heme protein oxygen affinity regulation exerted by proximal effects.* J. Am. Chem. Soc., 2006. **128**(38): p. 12455-12461.
213. Shibata, T., S. Nagao, M. Fukaya, H. Tai, S. Nagatomo, K. Morihashi, T. Matsuo, S. Hirota, A. Suzuki, K. Imai, and Y. Yamamoto, *Effect of heme modification on oxygen affinity of myoglobin and equilibrium of the acid-alkaline transition in metmyoglobin.* J. Am. Chem. Soc., 2010. **132**(17): p. 6091-8.
214. Olea, C., E.M. Boon, P. Pellicena, J. Kuriyan, and M.A. Marletta, *Probing the function of heme distortion in the H-NOX family.* ACS Chemical Biology, 2008. **3**(11): p. 703-10.
215. Chen, H., M. Ikeda-Saito, and S. Shaik, *Nature of the Fe-O2 bonding in oxy-myoglobin: effect of the protein.* J. Am. Chem. Soc., 2008. **130**(44): p. 14778-90.
216. Pikus, J.D., J.M. Studts, C. Achim, K.E. Kauffmann, E. Münck, R.J. Steffan, K. McClay, and B.G. Fox, *Recombinant toluene-4-monooxygenase: Catalytic and Mössbauer studies of the purified diiron and Rieske components of a four-protein complex.* Biochemistry, 1996. **35**: p. 9106-9119.
217. Pulver, S.C., W.H. Tong, J.M. Bollinger, J. Stubbe, and E.I. Solomon, *Circular dichroism and magnetic circular dichroism studies of the fully reduced binuclear non-heme iron active site in the E. coli R2 subunit of ribonucleoside diphosphate reductase.* J. Am. Chem. Soc., 1995. **117**: p. 12664-12678.
218. Yang, Y.-S., J.A. Broadwater, S.C. Pulver, B.G. Fox, and E.I. Solomon, *Circular dichroism and magnetic circular dichroism studies of the reduced binuclear non-heme iron site of stearoyl-ACP Δ^9-desaturase: substrate binding and comparison to ribonucleotide reductase.* J. Am. Chem. Soc., 1999. **121**(12): p. 2770-2783.
219. Wei, P.-p., A.J. Skulan, N. Mitić, Y.-S. Yang, L. Saleh, J.M. Bollinger, Jr., and E.I. Solomon, *Electronic and spectroscopic studies of the non-heme reduced binuclear iron sites of two ribonucleotide reductase variants: comparison to reduced methane monooxygenase and contributions to O_2 reactivity.* J. Am. Chem. Soc., 2004. **126**(12): p. 3777-3788.
220. Logan, D.T., X.D. Su, A. Aberg, K. Regnstrom, J. Hajdu, H. Eklund, and P. Nordlund, *Crystal structure of reduced protein R2 of ribonucleotide reductase - the structural basis for oxygen activation at a dinuclear iron site.* Structure, 1996. **4**(9): p. 1053-1064.
221. Lindqvist, Y., W.J. Huang, G. Schneider, and J. Shanklin, *Crystal structure of Δ^9 stearoyl-acyl carrier protein desaturase from castor seed and its relationship to other diiron proteins.* EMBO, 1996. **15**(16): p. 4081-4092.
222. Li, F.F., K.K. Meier, M.A. Cranswick, M. Chakrabarti, K.M. Van Heuvelen, E. Münck, and L. Que, *Characterization of a high-spin non-heme Fe^{III}-O intermediate and its quantitative conversion to an Fe^{IV} = O complex.* J. Am. Chem. Soc., 2011. **133**(19): p. 7256-7259.
223. Kim, K. and S.J. Lippard, *Structure and Mössbauer spectrum of a (μ-1,2-peroxo)bis(μ-carboxylato)diiron(III) model for the peroxo intermediate in the methane monooxygenase hydroxylase reaction cycle.* J. Am. Chem. Soc., 1996. **118**: p. 4914-4915.

224. Roelfes, G., V. Vrajmasu, K. Chen, R.Y.N. Ho, J.-U. Rohde, C. Zondervan, R.M. la Crois, E.P. Schudde, M. Lutz, A.L. Spek, R. Hage, B.L. Feringa, E. Münck, and L. Que, Jr., *End-on and side-on peroxo derivatives of non-heme iron complexes with pentadentate ligands: models for putative intermediates in biological iron/dioxygen chemistry.* Inorganic Chemistry, 2003. **42**(8): p. 2639-2653.
225. Orville, A.M., N. Elango, J.D. Lipscomb, and D.H. Ohlendorf, *Structures of competitive inhibitor complexes of protocatechuate 3,4-dioxygenase: Multiple exogenous ligand binding orientations within the active site.* Biochemistry, 1997. **36**(33): p. 10039-10051.
226. Orville, A.M., J.D. Lipscomb, and D.H. Ohlendorf, *Crystal structures of substrate and substrate analog complexes of protocatechuate 3,4-dioxygenase: Endogenous Fe^{3+} ligand displacement in response to substrate binding.* Biochemistry, 1997. **36**(33): p. 10052-10066.
227. Dong, Y., S. Yan, J. Young, V. G., and L. Que, Jr., *The crystal structure of a synthetic nonheme diiron-O_2 adduct: insight into oxygen activation.* Angew. Chem. Int. Edit., 1996. **35**(6): p. 618-620.
228. Do, L.H., T. Hayashi, P. Moenne-Loccoz, and S.J. Lippard, *Carboxylate as the protonation site in (Peroxo)diiron(III) model complexes of soluble methane monooxygenase and related diiron proteins.* J. Am. Chem. Soc., 2010. **132**(4): p. 1273-5.
229. Jensen, K.P., C.B. Bell, III, M.D. Clay, and E.I. Solomon, *Peroxo-type intermediates in class I ribonucleotide reductase and related binuclear non-heme iron enzymes.* J. Am. Chem. Soc., 2009. **131**(34): p. 12155-12171.
230. Choudhary, T.V. and V.R. Choudhary, *Energy-efficient syngas production through, catalytic oxy-methane reforming reactions.* Angew. Chem. Int. Edit., 2008. **47**(10): p. 1828-1847.
231. Martyshkin, D.V., R.C. Ahuja, A. Kudriavtsev, and S.B. Mirov, *Effective suppression of fluorescence light in Raman measurements using ultrafast time gated charge coupled device camera.* Review of Scientific Instruments, 2004. **75**(3): p. 630-635.
232. Ogura, T. and T. Kitagawa, *Device for simultaneous measurements of transient Raman and absorption-spectra of enzymatic-reactions - application to compound-I of horseradish-peroxidase.* J. Am. Chem. Soc., 1987. **109**(7): p. 2177-2179.
233. Nesheim, J.C., *Component interactions and catalysis of Methane Monooxygenase: Spectroscopic, kinetic and isotope effect studies.* , in *Biochemistry, Molecular Biology and Biophysics*1998, University of Minnesota: Minneapolis.
234. Grzyska, P.K., E.H. Appelman, R.P. Hausinger, and D.A. Proshlyakov, *Insight into the mechanism of an iron dioxygenase by resolution of steps following the Fe-IV=O species.* Proc. Nat. Acad. Sci. USA, 2010. **107**(9): p. 3982-3987.
235. Mitić, N., M.D. Clay, L. Saleh, J.M. Bollinger, and E.I. Solomon, *Spectroscopic and electronic structure studies of intermediate X in ribonucleotide reductase R2 and two variants: A description of the FeIV-oxo bond in the FeIII-O-FeIV dimer.* J. Am. Chem. Soc., 2007. **129**(29): p. 9049-9065.
236. Sanders-Loehr, J., W.D. Wheeler, A.K. Shiemke, B.A. Averill, and T.M. Loehr, *Electronic and Raman spectroscopic properties of oxo-bridge dinuclear iron centers in proteins and model compounds.* J. Am. Chem. Soc., 1989. **111**: p. 8084-8093.
237. Que, L., Jr. and W.B. Tolman, *Bis(μ-oxo)dimetal "diamond" cores in copper and iron complexes relevant to biocatalysis.* Angew. Chem. Int. Edit., 2002. **41**(7): p. 1114-1137.
238. Sitter, A.J., J.R. Shifflett, and J. Terner, *Resonance Raman spectroscopic evidence for heme iron-hydroxide ligation in peroxidase alkaline forms.* J. Biol. Chem., 1988. **263**(26): p. 13032-8.

239. Zheng, H., Y. Zang, Y. Dong, V.G. Young, Jr., and L. Que, Jr., *Complexes with $FeIII_2(\mu$-$O)(\mu$-$OH)$, $FeIII_2(\mu$-$O)_2$, and $[FeIII_3(\mu_2$-$O)_3]$ cores: Structures, spectroscopy, and core interconversions.* J. Am. Chem. Soc., 1999. **121**(10): p. 2226-2235.
240. Backes, G., M. Sahlin, B.M. Sjöberg, T.M. Loehr, and J. Sanders-Loehr, *Resonance Raman spectroscopy of ribonucleotide reductase. Evidence for a deprotonated tyrosyl radical and photochemistry of the binuclear iron center.* Biochemistry, 1989. **28**(4): p. 1923-1929.
241. Fox, B.G., J. Shanklin, J. Ai, T.M. Loehr, and J. Sanders-Loehr, *Resonance Raman evidence for an Fe-O-Fe center in stearoyl-ACP desaturase. Primary sequence identity with other diiron-oxo proteins.* Biochemistry, 1994. **33**(43): p. 12776-12786.
242. Vu, V.V., T.M. Makris, J.D. Lipscomb, and L. Que, *Active-site structure of a beta-hydroxylase in antibiotic biosynthesis.* J. Am. Chem. Soc., 2011. **133**(18): p. 6938-6941.
243. Shiemke, A.K., T.M. Loehr, and J. Sanders-Loehr, *Resonance Raman study of oxyhemerythrin and hydroxhemerythrin: Evidence for hydrogen bonding of ligands to the Fe-O-Fe center.* J. Am. Chem. Soc., 1986. **108**: p. 2437-2443, and references cited therein.
244. Stone, K.L., R.K. Behan, and M.T. Green, *Resonance Raman spectroscopy of chloroperoxidase compound II provides direct evidence for the existence of an iron(IV)-hydroxide.* Proc. Nat. Acad. Sci. USA, 2006. **103**(33): p. 12307-10.
245. Ogo, S., R. Yamahara, M. Roach, T. Suenobu, M. Aki, T. Ogura, T. Kitagawa, H. Masuda, S. Fukuzumi, and Y. Watanabe, *Structural and spectroscopic features of a cis (hydroxo)-Fe(III)-(carboxylato) configuration as an active site model for lipoxygenases.* Inorganic Chemistry, 2002. **41**(21): p. 5513-20.
246. Groves, J.T., *High-valent iron in chemical and biological oxidations.* Journal of Inorganic Biochemistry, 2006. **100**(4): p. 434-447.
247. Schlichting, I., J. Berendzen, K. Chu, A.M. Stock, S.A. Maves, D.E. Benson, R.M. Sweet, D. Ringe, G.A. Petsko, and S.G. Sligar, *The catalytic pathway of cytochrome P450cam at atomic resolution.* Science, 2000. **287**(5458): p. 1615-1622.
248. Chen, M.M., P.S. Coelho, and F.H. Arnold, *Utilizing terminal oxidants to achieve P450-catalyzed oxidation of methane.* Adv. Synth. Catal., 2012. **354**(6): p. 964-968.
249. Zilly, F.E., J.P. Acevedo, W. Augustyniak, A. Deege, U.W. Hausig, and M.T. Reetz, *Tuning a P450 enzyme for methane oxidation.* Angew. Chem. Int. Edit., 2011. **50**(12): p. 2720-2724.
250. Janardanan, D., Y. Wang, P. Schyman, L. Que, Jr., and S. Shaik, *The fundamental role of exchange-enhanced reactivity in C-H activation by S=2 oxo iron(IV) complexes.* Angew. Chem. Int. Edit., 2010. **49**(19): p. 3342-5.
251. Solomon, E.I., S.D. Wong, L.V. Liu, A. Decker, and M.S. Chow, *Peroxo and oxo intermediates in mononuclear nonheme iron enzymes and related active sites.* Curr. Opin. Chem. Biol. , 2009. **13**(1): p. 99-113.
252. Price, J.C., E.W. Barr, B. Tirupati, J.M. Bollinger, Jr., and C. Krebs, *The first direct characterization of a high-valent iron intermediate in the reaction of an alpha-ketoglutarate-dependent dioxygenase: a high-spin Fe^{IV} complex in taurine/alpha-ketoglutarate dioxygenase (TauD) from Escherichia coli.* Biochemistry, 2003. **42**(24): p. 7497-7508.
253. Proshlyakov, D.A., T.F. Henshaw, G.R. Monterosso, M.J. Ryle, and R.P. Hausinger, *Direct detection of oxygen intermediates in the non-heme Fe enzyme taurine/alpha-ketoglutarate dioxygenase.* J. Am. Chem. Soc., 2004. **126**(4): p. 1022-1023.

254. Panay Aram, J., M. Lee, C. Krebs, J.M. Bollinger, and F. Fitzpatrick Paul, *Evidence for a high-spin Fe(IV) species in the catalytic cycle of a bacterial phenylalanine hydroxylase.* Biochemistry, 2011. **50**(11): p. 1928-33.
255. Ho, R.Y.N., M.P. Mehn, E.L. Hegg, A. Liu, M.J. Ryle, R.P. Hausinger, and L. Que, Jr., *Resonance Raman studies of the iron(II)-α-keto acid chromophore in model and enzyme complexes.* J. Am. Chem. Soc., 2001. **123**(21): p. 5022-5029.
256. Xue, G., A. Pokutsa, and L. Que, Jr., *Substrate-triggered activation of a synthetic [Fe_2(μ-O)2] diamond core for C-H bond cleavage.* J. Am. Chem. Soc., 2011. **133**(41): p. 16657-67.
257. Stubbe, J. and W.A. van der Donk, *Protein radicals in enzyme catalysis.* Chem. Rev., 1998. **98**(2): p. 705-762.
258. Kolberg, M., D.T. Logan, G. Bleifuss, S. Poetsch, B.-M. Sjoeberg, A. Gräslund, W. Lubitz, G. Lassmann, and F. Lendzian, *A new tyrosyl radical on Phe208 as ligand to the diiron center in escherichia coli ribonucleotide reductase, mutant R2-Y122H: Combined X-ray diffraction and EPR/ENDOR studies.* J. Biol. Chem, 2005. **280**(12): p. 11233-11246.